UNIVERSIDADE FEDERAL DE PERNAMBUCO
CENTRO DE CIÊNCIAS EXATAS E DA NATUREZA
PROGRAMA DE PÓS-GRADUAÇÃO EM FÍSICA

Mateus Rattes Lima da Motta

# Four-wave mixing driven by structured light in atomic media: optical mode transfer and spatial correlations

Recife

2024

Mateus Rattes Lima da Motta

# Four-wave mixing driven by structured light in atomic media: optical mode transfer and spatial correlations

Tese apresentada ao Programa de Pós-Graduação em Física da Universidade Federal de Pernambuco, como requisito parcial para a obtenção do título de Doutor em Física.

**Área de Concentração**: Óptica

**Orientador (a)**: Sandra Sampaio Vianna

Recife

2024

Catalogação na fonte
Bibliotecária Nataly Soares Leite Moro, CRB4-1722

M921f Motta, Mateus Rattes Lima da
*Four-wave mixing driven by structured light in atomic media: optical mode transfer and spatial correlations* / Mateus Rattes Lima da Motta. – 2024.
170 f.: il., fig., tab.

Orientadora: Sandra Sampaio Vianna.
Tese (Doutorado) – Universidade Federal de Pernambuco. CCEN, Física, Recife, 2024.
Inclui referências e apêndices.

1. Óptica. 2. Luz estruturada. 3. Óptica não-linear. 4. Vapor atômico. 5. Correlações espaciais. I. Vianna, Sandra Sampaio (orientadora). II. Título.

535.2 CDD (23. ed.) UFPE- CCEN 2024 - 29

**MATEUS RATTES LIMA DA MOTTA**

# FOUR-WAVE MIXING DRIVEN BY STRUCTURED LIGHT IN ATOMIC MEDIA: OPTICAL MODE TRANSFER AND SPATIAL CORRELATIONS

Tese apresentada ao Programa de Pós-Graduação em Física da Universidade Federal de Pernambuco, como requisito parcial para a obtenção do título de Doutor em Física.

Aprovada em: 05/02/2024.

## BANCA EXAMINADORA

Profa. Dra. Sandra Sampaio Vianna
Orientadora
Universidade Federal de Pernambuco

Prof. Dr. Anderson Monteiro Amaral
Examinador Interno
Universidade Federal de Pernambuco

Prof. Dr. Lúcio Hora Acioli
Examinador Interno
Universidade Federal de Pernambuco

Prof. Dr. Felipe Arruda de Araujo Pinheiro
Examinador Externo
Universidade Federal do Rio de Janeiro

Prof. Dr. Raul Celistrino Teixeira
Examinador Externo
Universidade Federal de São Carlos

Prof. Dr. Sebastião José Nascimento de Pádua
Examinador Externo
Universidade Federal de Minas Gerais

# ACKNOWLEDGEMENTS

Agradeço aos meus pais, Maria da Conceição e Flávio Fernando, à minha irmã, Melina, e aos meus avós, Irma e Mateus, pelo carinho e suporte que sempre me deram, desde quando consigo me lembrar, por tudo o que me ensinaram, e por sempre incentivarem as minhas decisões.

À minha companheira da vida, Ana Catarina, por todo o seu amor, por sempre apoiar as minhas escolhas e ser a luz que me orienta. Por compartilhar os bons momentos e me dar forças nas horas mais difíceis.

Agradeço também àqueles com quem compartilhei o ambiente do Departamento de Física da UFPE nos últimos anos.

À professora Sandra Vianna, pela paciência e dedicação que sempre demonstrou, pela confiança no meu trabalho, e por me passar a tranquilidade de saber que a todos os momentos estive bem direcionado na pesquisa.

A todos os colegas e amigos do DF, pela companhia e pelos bons momentos de descontração. A Alexandre, Álvaro e Wellington, agradeço pela amizade que levarei para fora dos corredores do departamento. A Alyson e Raoni, pela simpatia que sempre carregaram e pela disposição em ajudar a todos os momentos. Ao professor José Ferraz, pela parceria na física e nas quadras de tênis.

A todos os familiares e amigos, de perto e de longe, que me apoiaram e contribuíram de alguma forma para que eu pudesse chegar onde estou.

À CAPES pelo suporte financeiro.

*"The agreement of the results seems to show that light and magnetism are affections of the same substance, and that light is an electromagnetic disturbance propagated through the field according to electromagnetic laws."*

James Clerk Maxwell, (MAXWELL, 1865, p. 499).

# ABSTRACT

In this work we present a series of results on four-wave mixing (FWM) processes induced by structured light in atomic media. We start with a theoretical study focusing on a cascade FWM process in rubidium vapor, generating a blue light field at $420\ \mathrm{nm}$. In this setting, we show that in the extended-medium regime the Hermite-Gaussian basis presents a unique property of optical structure transfer. We then exploit this result to show that, by carefully tailoring the structure of the pump beams, one can obtain desired spatial modes with cylindrical and elliptical symmetries with high fidelity at the blue light output. Following that, we consider an experimental configuration where two degenerate FWM signals are generated in different directions of space by the same pump fields. In this setup, we present results in heated rubidium vapor evidencing the simultaneous conservation of orbital angular momentum (OAM) in the two FWM processes. We show that the two-channel setting allows to encode the OAM content of the input beams onto the OAM carried by the two FWM signals. Next, we explore the transverse mode dynamics in the context of optical modes contained in the so-called orbital angular momentum Poincaré sphere (PS). Defined in analogy with a general polarization state, this family of modes is parametrized in terms of polar and azimuthal angles. We show that the two FWM signals can also be described as belonging to Poincaré spheres, and that the angles on the output PS are related to those on the input PS by well-defined symmetries. The predicted FWM intensity profiles, as well as the consequences of the symmetry properties, are in good agreement with our experimental results. We also explore interesting scenarios, such as combinations of different PS modes and the fulfillment of one of the symmetry relations in each sphere independently, and restrictions that arise in the extended-medium regime. In the last part, we study the correlations between the light fields participating in the two-channel FWM configuration. Following our recent work on cold atoms, we investigate the correlations originating from the conversion of phase-noise to amplitude-noise as a result of the light-atom interaction, and discuss our attempts to discriminate transverse spatial dependencies on these correlations. Finally, we outline the quantum theory of FWM, exploring the multi-spatial-mode nature of the generated light state and the associated spatial correlations.

**Keywords**: structured light; nonlinear optics; atomic vapor; spatial correlations.

# RESUMO

Neste trabalho, apresentamos uma série de resultados em mistura de quatro ondas (MQO) induzida por feixes de luz estruturada em meios atômicos. Começamos com um estudo teórico de um processo de MQO em cascata em vapor de rubídio gerando luz azul em $420\ \mathrm{nm}$. Nessa configuração, mostramos que no regime de meio extenso, a base de modos Hermite-Gauss apresenta uma propriedade única de transferência de estrutura óptica. Nós então exploramos esse resultado para mostrar que ao estruturarmos cuidadosamente os feixes de bombeio, podemos obter modos espaciais desejados com simetrias cilíndrica e elíptica com alta fidelidade no sinal de luz azul. Na sequência, passamos a considerar uma configuração experimental onde dois sinais de MQO degenerada são gerados em direções diferentes do espaço, usando os mesmos feixes de bombeio. Nesse caso, apresentamos resultados em vapor aquecido de rubidio que evidenciam a conservação de momento angular orbital (MAO) simultaneamente nos dois processos de MQO. Mostramos que a configuração com dois canais de MQO nos permite codificar o MAO dos feixes incidentes no MAO dos dois sinais de MQO. Na sequência, exploramos a dinâmica de modos transversais no contexto de modos óticos contidos na chamada esfera de Poincaré (EP) de momento angular orbital. Definida em analogia com um estado arbitrário de polarização, essa família de modos é parametrizada em termos dos ângulos polar e azimutal na esfera. Mostramos que os dois sinais de MQO também podem ser descritos como pertencendo a esferas de Poincaré, e que os ângulos nas esferas de *output* e aqueles na EP do modo incidente são relacionados por simetrias bem definidas. Os perfis de intensidade dos feixes de MQO, assim como as consequências das simetrias, concordam bem com nossos resultados experimentais. Além disso, exploramos situações interessantes, como combinações de modos em EPs distintas e o cumprimento de uma das relações de simetria em cada esfera independentemente, e também restrições no regime de meio extenso. Na parte final, estudamos as correlações entre os campos de luz que participam nos dois processos de MQO. Dando sequência a um trabalho recente em átomos frios, investigamos as correlações oriundas da conversão de ruído de fase para ruído de amplitude como resultado da interação luz-átomo e discutimos nossas tentativas de identificar dependências espaciais nessas correlações. Finalmente, apresentamos a teoria quântica de MQO, explorando a natureza multi-modos espaciais do estado quântico da luz gerado no processo, e as correlações espaciais associadas.

**Palavras-chave**: luz estruturada; óptica não-linear; vapor atômico; correlações espaciais.

# LIST OF FIGURES

# LIST OF TABLES

# CONTENTS

# 1 INTRODUCTION

In recent years, the spatial structure of light has seen a significant increase in research interest, both in fundamental studies, and in applications and technological developments (RUBINSZTEIN-DUNLOP et al., 2016). The understanding of effects attributed to the transverse structure of light in optical phenomena, and the ability to control the spatial degrees of freedom of the light field have allowed numerous advances in the optical sciences (FORBES; OLIVEIRA; DENNIS, 2021). We may highlight fundamental properties of electromagnetic radiation, quantum optics, manipulation of matter, holography, information multiplexing, quantum communication, metrology, and nonlinear light-matter interactions.

The starting point of these advances can be traced back to 1992, when the seminal work of Allen *et al.* (ALLEN et al., 1992) established the connection between the orbital angular momentum (OAM) of a Laguerre-Gaussian (LG) light beam and its spatial distribution, more specifically, its helical phase structure. This breakthrough originated the field of light OAM, which over the past three decades has grown immensely, and transformed in such a way as to be recognized today as the more general field of structured light.

Shortly after the initial developments, the investigation of the role played by OAM in nonlinear optical processes started in second-harmonic generation (SHG) (DHOLAKIA et al., 1996; COURTIAL et al., 1997; BERžANSKIS et al., 1998). Four-wave mixing (FWM), a third-order nonlinear optical process that can take place in a variety of systems, such as atomic vapors, cold atoms, and optical fibers, soon started to be employed to study the interaction of OAM with atomic systems (TABOSA; PETROV, 1999). In the past, FWM has allowed the investigation of several optical phenomena, for instance, AC Stark shift, phase conjugation and electromagnetically induced transparency (HARTER; BOYD, 1980; BOYD et al., 1981; YARIV; PEPPER, 1977; ABRAMS; LIND, 1978; FLEISCHHAUER; IMAMOGLU; MARANGOS, 2005), and has become an important method for generating quantum correlated beams (BOYER et al., 2008; BOYER; MARINO; LETT, 2008; MARINO et al., 2008). Today, SHG and other second-order optical phenomena, as well as FWM in its many accessible configurations, offer highly versatile platforms to explore the transverse degrees of freedom of light, both in the classical and quantum regimes.

The fundamental solution to the paraxial wave equation (PWE), the Gaussian beam, encompasses important properties of the actual output of laser sources, such as their characteristic intensity profile and phase distribution, both of which evolve as the beam propagates. One exact higher-order solution to the PWE is the Hermite-Gaussian (HG) mode, which is given in cartesian coordinates and is characterized by lobes of light disposed in a rectangular grid. HG modes are important in the study of laser cavities, as they describe the spatial distribution of the output beams from these light sources (KOGELNIK; LI, 1966). The Laguerre-Gaussian mode is another exact solution to the PWE. It is given in cylindrical coordinates and carries a ring-shaped intensity distribution. Most importantly, LG modes carry well-defined orbital angular momentum in the propagation direction per photon (ALLEN et al., 1992). There are many other higher-order solutions to the PWE that present vastly diverse characteristics and interesting properties (FORBES; OLIVEIRA; DENNIS, 2021).

The above discussion considers the radiation field of light, in its many accessible spatial distributions or modes, propagating in free space. In the present work, we are interested in the nonlinear light-matter interactions taking place in third-order media and in understanding how these interactions affect the structure of the light field. In particular, we will be concerned with different configurations of four-wave mixing induced in atomic samples. One setting that is commonly used to study the nonlinear interaction of structured light with matter is that of FWM induced by amplified spontaneous emission (ASE) in a hot rubidium vapor, with a 3-level cascade system (VERNIER et al., 2010). In this configuration, we may highlight the transfer of OAM and intricate optical structures (WALKER; ARNOLD; FRANKE-ARNOLD, 2012; AKULSHIN et al., 2015; AKULSHIN et al., 2016; CHOPINAUD et al., 2018), the investigation of the number of modes involved in the entangled light state (OFFER et al., 2018), and the fulfillment of the Gouy phase-matching condition in an extended medium (OFFER et al., 2021). In cold atomic samples, FWM was employed to transfer OAM from incident to generated beams in nondegenerate (TABOSA; PETROV, 1999) and degenerate (BARREIRO; TABOSA, 2003) systems, to transfer more complicated phase structures obtained by superimposing LG modes of different orders (BARREIRO et al., 2004), and to store the information carried by the spatial structure of light in the ensemble of atoms, and later retrieve it (MORETTI; FELINTO; TABOSA, 2009; DING et al., 2013).

In this Thesis we present results obtained in the last years from our efforts to understand nonlinear optical phenomena driven by structured light in atomic media, and it is divided as follows. In Chapter 2 we present fundamental concepts necessary for understanding our main results. We outline the description of the light-matter interaction in the linear and nonlinear regimes, and present topics related to paraxial optics. We calculate the so-called overlap integrals in the LG and HG bases, and the associated selection rules that dictate the optical mode transfer in FWM. In Chapter 3 we describe the experimental apparatus used in this work. Namely, we discuss the operation of our heated vapor setup and our magneto-optical trap, as well as the spatial light modulator, the device used to generate the structured light beams.

Chapter 4 is dedicated to results obtained in the rubidium vapor system. We start with a theoretical study of the optical mode conversion in FWM induced by ASE driven by HG modes. We first demonstrate that in the extended-medium regime the HG basis presents a unique property that allows to generate a highly pure HG mode at the blue light output from the wave-mixing of two input HG modes. By analyzing the combined transverse and longitudinal selection rules that dictate the optical structure dynamics, we predict that the indices characterizing the generated mode are given by the sums of the indices of the pump modes. This is similar to what was verified in second-order nonlinear media (PIRES et al., 2020). Next, we show that it is possible to use this effective selection rule to obtain desired modes with cylindrical and elliptical symmetries at the output. This is done by carefully preparing the input beams as superpositions of HG modes with the correct weights. This type of controlled conversion has been demonstrated in second-harmonic generation (PIRES et al., 2019), and we extend the approach to a higher order process.

Our most recent studies were concerned with a relatively unusual configuration, where two degenerate (meaning that all participating fields have the same frequency) FWM signals are generated simultaneously in different directions of space. The two processes are driven by the same pump fields, which when carrying similar power, favor the generation of both signals equally. This arrangement can be employed in both types of systems mentioned above: cold and hot atoms, and we have already studied the spectral characteristics of the process in hot Rb vapor (ALVAREZ; ALMEIDA; VIANNA, 2021), and the cross-correlation between the pairs of transmitted beams and FWM signals in a cold Rb cloud (ALMEIDA; MOTTA; VIANNA, 2023). This two-channel configuration is the focus of the second and third parts of Chapter 4, where we present results on the spatial mode dynamics of both generated light fields. We first investigate the simultaneous transfer of OAM from the input beams to the generated signals, evidencing the fulfillment of the OAM conservation selection rules in both processes (MOTTA; ALMEIDA; VIANNA, 2023). We show that one can encode the information carried by the OAM of the pump beams onto the topological charges of the generated fields.

Following that, we investigate the transverse mode dynamics in the context of the OAM Poincaré sphere (PS) (MOTTA et al., 2024). In analogy with usual polarization Poincaré sphere

(PADGETT; COURTIAL, 1999), an arbitrary mode on the OAM PS is parametrized by the polar and azimuthal angles. Under usual assumptions, we show that both FWM fields can also be represented by modes contained in Poincaré spheres, and that the angles on the output and input spheres are related by well-defined symmetries. Drawing a parallel with three-wave mixing processes in nonlinear crystals, we show that the results presented here are similar to what has been verified in second-harmonic generation (PEREIRA et al., 2017) and in the down-conversion process in parametric amplification (SANTOS et al., 2007; RODRIGUES et al., 2018; RODRIGUES et al., 2022). More specifically, we verify the reflection symmetry of the mode vector on the PS in one of the FWM signals, and the generation of a finite spectrum of radial modes in the other one. This equivalent to what happens in down-conversion and SHG processes, respectively. With this, we extend an approach extensively employed within second-order nonlinear systems to a higher-order nonlinear medium.

A natural lead to these studies, aligned with the current tendency of exploring multi-channel configurations in nonlinear and quantum optics (GUPTA et al., 2016), is the investigation of correlations between the participating fields in the two FWM processes. This is the subject of Chapter 5. We begin this Chapter with an investigation of the intensity fluctuation correlations between the incident beams transmitted through a cold rubidium cloud. In particular, these fluctuations originate from the conversion of the phase-noise inherent to diode lasers, to amplitude-noise as a result of the light-matter interaction (ARIUNBOLD et al., 2010). In a recent work (ALMEIDA; MOTTA; VIANNA, 2023), we attributed the verified oscillatory behaviour of the second-order correlation curves to a signature of the generalized Rabi frequency. As a sequence, here we attempt to identify spatial dependencies on these correlations, or even a cross-talk between the transmitted beams inside the sample. To this end, we employed a spatially resolved detection scheme, consisting on placing pinholes with a single translation degree of freedom in front of the detectors, allowing us to look at the fluctuations of localized regions of the transmitted beams. In the second part of Chapter 5, we outline the quantum description of FWM. We first establish the interaction Hamiltonian that describes the FWM process, and the corresponding time evolution operator in the first-order approximation. This leads to the biphoton state, containing the full multi-spatial-mode distribution of the generated light fields. We then calculate the spatial correlation function and discuss interesting results in different settings, highlighting similarities with what has been verified in parametric-down conversion (WALBORN et al., 2010).

Finally, concluding remarks and perspectives for future work are given in Chapter 6.

# 2 FUNDAMENTALS

In this Chapter we discuss various topics that are relevant for the understanding of our main results. We start with the semi-classical model of the light-matter interaction in the two-level approximation, which we will use in a first moment to discuss general aspects of the atomic response, such as absorption, variation of the index of refraction, and Doppler broadening. We will then discuss topics related to paraxial optics, and establish important general results that will be used throughout the Thesis. At the end, we discuss nonlinear optics and, more specifically, four-wave mixing. We will consider a general description of the FWM process in the semi-classical regime, making use of the equations for the light-atom interaction obtained in the first Section. Finally, we discuss FWM in the context of structured light, taking fully into account the spatial degrees of freedom of the participating light beams. We solve the wave-equation for the FWM field and detail the calculation of the relevant overlap integrals in the Laguerre-Gaussian and Hermite-Gaussian bases. In each case we outline the selection rules that dictate the transverse mode dynamics.

## 2.1 LIGHT-MATTER INTERACTION IN A TWO-LEVEL ATOM

To describe the response of a sample of atoms to the interaction with the oscillating electric field of laser light we employ the density matrix formalism. In many situations, including the ones we are interested in, the interaction involves only two atomic states. This is the case when, for example, the laser beam has a well-defined circular polarization. Thus, the individual atoms may be modeled as simple two-level systems, where the two states are the ground and excited states, $|1\rangle$ and $|2\rangle$, respectively. This problem is treated in many standard textbooks, and here we follow closely Ref. (YARIV, 1989).

Consider a single atom located in a region where a monochromatic light field is present. The Hamiltonian of the system is:

$$\hat{H} = \hat{H}_0 + \hat{V}(t), \tag{2.1}$$

where $\hat{H}_0 = \mathbb{E}_1 |1\rangle \langle 1| + \mathbb{E}_2 |2\rangle \langle 2|$ is the non-perturbed Hamiltonian for the internal degrees of freedom of the atom and $\mathbb{E}_j$ is the energy eigenvalue of state $|j\rangle$. The interaction Hamiltonian

$\hat{V}$ is the electric dipole Hamiltonian:

$$\hat{V}(t) = -\hat{\boldsymbol{\mu}} \cdot \mathbf{E}(t), \tag{2.2}$$

where $\hat{\boldsymbol{\mu}} = e\hat{\mathbf{r}}$ is the electric dipole operator. The electric field $\mathbf{E}(t)$ is given by a monochromatic plane-wave with frequency $\omega$ and wave-vector $\mathbf{k}$, as:

$$\begin{aligned}\mathbf{E}(t) &= \frac{1}{2}\boldsymbol{\epsilon}\mathcal{E}e^{-i(\mathbf{k}\cdot\mathbf{r}-\omega t)} + \text{c.c.}, \\ &= \boldsymbol{\epsilon}E(t) + \text{c.c.},\end{aligned} \tag{2.3}$$

where $\boldsymbol{\epsilon}$ is the polarization direction, $\mathcal{E}$ is the amplitude, and $\text{c.c.}$ means the complex conjugate. In the rotating wave and electric dipole approximations, the matrix elements of the interaction Hamiltonian are written as:

$$\begin{aligned}V_{jk}(t) &= \langle j|\hat{V}(t)|k\rangle, \\ &= -\frac{1}{2}\mu_{jk}\mathcal{E}e^{i\omega t}.\end{aligned} \tag{2.4}$$

where $(j,k) \in \{1,2\}$ and $\mu_{jk} = \langle j|\hat{\boldsymbol{\mu}} \cdot \boldsymbol{\epsilon}|k\rangle$ is the transition dipole moment. Due to the parity of the operator $\hat{\boldsymbol{\mu}}$, the dipole interaction only couples different states, i.e., $\mu_{jj} = 0$. The phases of $|1\rangle$ and $|2\rangle$ can be chosen so that $\mu_{12} = \mu_{21}^* = \mu$ is a real number. We introduce the Rabi frequency $\Omega \equiv \mu\mathcal{E}/2\hbar$, to write:

$$V_{12} = V_{21}^* = -\hbar\Omega e^{i\omega t}. \tag{2.5}$$

In this manner, the Hamiltonian given by Eq. (2.1) can be rewritten as:

$$\hat{H} = \hbar\omega_1 |1\rangle\langle 1| + \hbar\omega_2 |2\rangle\langle 2| - \hbar\Omega e^{i\omega t} |1\rangle\langle 2| - \hbar\Omega^* e^{-i\omega t} |2\rangle\langle 1|, \tag{2.6}$$

where $\omega_{1,2} \equiv \mathbb{E}_{1,2}/\hbar$. We then see that the interaction with the laser field couples the ground and excited states with a time-varying coupling of strength given by the Rabi frequency $\Omega$. The atom's state at time $t$ can be written as the superposition:

$$|\psi(t)\rangle = c_1(t)|1\rangle + c_2(t)|2\rangle, \tag{2.7}$$

where coefficients $\{c_1(t), c_2(t)\} \in \mathbb{C}$ are related to the probabilities of finding the system in the eigenstates $|1\rangle, |2\rangle$ at time $t$ as $P_{1,2}(t) = |c_{1,2}(t)|^2$. Note that this imposes the constraint $|c_1(t)|^2 + |c_2(t)|^2 = 1$. For any initial state of the atom $|\psi(t=0)\rangle$, one may obtain $|\psi(t)\rangle$ at any $t$ using Schrödinger's equation.

However, we are not interested in the behavior of a single atom. When dealing with a system of many atoms, an ensemble, where classical uncertainties forbids the knowledge of the exact state of the system, the density operator formalism is the ideal framework. The density operator of a pure system $|\psi\rangle$ can be defined as $\hat{\rho} = |\psi\rangle\langle\psi|$, and with Eq. (2.7), we may write:

$$\hat{\rho} = |c_1|^2 |1\rangle\langle 1| + |c_2|^2 |2\rangle\langle 2| + c_1 c_2^* |1\rangle\langle 2| + c_1^* c_2 |2\rangle\langle 1| . \tag{2.8}$$

More generally, the density operator can be written as:

$$\hat{\rho} = \sum_{j,k} \rho_{jk} |j\rangle\langle k| , \tag{2.9}$$

where the diagonal elements $\rho_{jj}$ are the populations and represent the probability of finding an atom of the ensemble in the eigenstate $|j\rangle$. This imposes $\sum_j \rho_{jj} = 1$. The off-diagonal elements $\rho_{jk}$ are the coherences and in our case are related to the response of the system due to the light-atom interaction. The density operator is Hermitian, and therefore it must satisfy $\rho_{jk} = \rho_{kj}^*$. In our case, we have $\rho_{11} = |c_1|^2, \rho_{22} = |c_2|^2, \rho_{12} = \rho_{21}^* = c_1^* c_2$. The time evolution of $\hat{\rho}$ is described by Liouville's Equation:

$$\frac{\partial\hat{\rho}}{\partial t} = \frac{i}{\hbar}[\hat{\rho}, \hat{H}], \tag{2.10}$$

where $[\hat{A}, \hat{B}] = \hat{A}\hat{B} - \hat{B}\hat{A}$ is the commutator of the operators $\hat{A}$ and $\hat{B}$. For the two-level system, we can write the equations describing the time evolution of each element of $\hat{\rho}$ as:

$$\dot{\rho}_{11} = \frac{i}{\hbar}\left[\rho_{12}V_{21} - \rho_{21}V_{12}\right], \tag{2.11}$$

$$\dot{\rho}_{22} = \frac{i}{\hbar}\left[\rho_{21}V_{12} - \rho_{12}V_{21}\right], \tag{2.12}$$

$$\dot{\rho}_{12} = \frac{i}{\hbar}\left[V_{12}\left(\rho_{11} - \rho_{22}\right) + \rho_{12}\left(\mathbb{E}_2 - \mathbb{E}_1\right)\right], \tag{2.13}$$

$$\dot{\rho}_{21} = \frac{i}{\hbar}\left[V_{21}\left(\rho_{22} - \rho_{11}\right) + \rho_{21}\left(\mathbb{E}_1 - \mathbb{E}_2\right)\right]. \tag{2.14}$$

We rewrite the above system of coupled equations in the more convenient form:

$$(\dot{\rho}_{22} - \dot{\rho}_{11}) = -\frac{2i}{\hbar}[\rho_{12}V_{21} - \text{c.c.}], \tag{2.15}$$

$$\dot{\rho}_{12} = -\frac{i}{\hbar}\left[V_{12}(\rho_{22} - \rho_{11}) - \rho_{12}\left(\mathbb{E}_2 - \mathbb{E}_1\right)\right], \tag{2.16}$$

where $\rho_{11} + \rho_{22} = 1$ and $\rho_{12} = \rho_{21}^*$ must be satisfied. One aspect that our treatment so far fails to capture is the spontaneous decay of the atoms in the excited state. Rigorously, to encompass this phenomenon, we must account for the coupling with the vacuum modes of the radiation field within a second-quantized framework. Here, however, it suffices to add to Eqs. (2.15) and (2.16) relaxation terms that account for the spontaneous decay process. Let $\Gamma/2\pi$ be the rate at which the atom decays from the excited state[1]. Then, populations and coherences decay at (angular) rates $\Gamma$ and $\Gamma/2$, respectively. We therefore modify Eqs. (2.15) and (2.16) to read:

$$(\Delta\dot{\rho}) = -\frac{2i}{\hbar}[\rho_{12}V_{21} - \text{c.c.}] - \Gamma\left[\Delta\rho - (\Delta\rho)^0\right], \tag{2.17}$$

$$\dot{\rho}_{12} = -\frac{i}{\hbar}\left[V_{12}\Delta\rho - \rho_{12}\left(\mathbb{E}_2 - \mathbb{E}_1\right)\right] - \frac{\Gamma}{2}\rho_{12}, \tag{2.18}$$

where $\Delta\rho = (\rho_{22} - \rho_{11})$ and $(\Delta\rho)^0 = -1$ is the population difference far from the region of interaction. These are the Optical Bloch's Equations (OBEs) for our system. We will be interested in a steady state solution, i.e., for $t$ much larger than the characteristic time scale of the interaction dynamics. We begin by writing the coherence in the slowly varying form:

$$\rho_{12} = \sigma_{12}e^{i\omega t}, \tag{2.19}$$

and substitute $V_{12}$ from (2.4) to arrive at:

$$(\Delta\dot{\rho}) = 2i(\sigma_{12}\Omega^* - \sigma_{21}\Omega) - \Gamma\left[\Delta\rho - (\Delta\rho)^0\right], \tag{2.20}$$

$$\dot{\sigma}_{12} = i\Omega\Delta\rho - \sigma_{12}\left(i\delta + \frac{\Gamma}{2}\right), \tag{2.21}$$

where $\omega_o = (\mathbb{E}_2 - \mathbb{E}_1)/\hbar = \omega_2 - \omega_1$ is the resonance frequency and $\delta = \omega - \omega_o$ is the detuning from resonance. In the steady state, we have:

$$\Delta\rho = (\Delta\rho)^0 + \frac{2i}{\Gamma}[\sigma_{12}\Omega^* - \sigma_{21}\Omega], \tag{2.22}$$

$$\sigma_{12} = i\frac{\Omega\Delta\rho}{i\delta + \Gamma/2}. \tag{2.23}$$

Substituting the second equation into the first, we get the population difference:

$$\Delta\rho = \frac{(\Delta\rho)^0}{1 + \dfrac{2|\Omega|^2}{\delta^2 + \Gamma^2/4}}. \tag{2.24}$$

Then, the steady state solution to $\sigma_{12}$ is thus readily found as:

$$\sigma_{12} = -\frac{\Omega\left(\delta + i\Gamma/2\right)}{\delta^2 + \Gamma^2/4 + 2|\Omega|^2}, \tag{2.25}$$

---

[1] For the $\mathrm{D}_2$ line of $^{87}\mathrm{Rb}$, we have $\Gamma/2\pi \approx 6\,\mathrm{MHz}$ (STECK, 2001), for example.

where the presence of $|\Omega|^2$ in the denominator is related to saturation effects and power broadening.

The response of the atomic ensemble is governed by the macroscopic polarization, given by $\mathbf{P} = \mathcal{N}\langle\hat{\boldsymbol{\mu}}\rangle = \mathcal{N}\mathrm{tr}(\hat{\rho}\hat{\boldsymbol{\mu}})$, where $\mathcal{N}$ is the atomic density. It is also related to the incident field by the electric susceptibility $\chi$ via $\mathbf{P} = \varepsilon_0\chi\boldsymbol{\epsilon}E + \mathrm{c.c.}$, where $\varepsilon_0$ is the electric permittivity of free space. Projecting both expressions for $\mathbf{P}$ onto the oscillation direction of the field $\boldsymbol{\epsilon}^*$, one obtains:

$$\varepsilon_0\chi E = \mathcal{N}\mathrm{tr}[\hat{\rho}(\hat{\boldsymbol{\mu}}\cdot\boldsymbol{\epsilon}^*)]. \tag{2.26}$$

It is interesting to note that in the above equation, the left-hand side comes from the classical macroscopic response of the medium to a propagating field, while the right-hand side comes from the quantum description of the atomic response to the interaction with the field. The trace is the dipole moment per atom and can be readily found as $\mathrm{tr}[\hat{\rho}(\hat{\boldsymbol{\mu}}\cdot\boldsymbol{\epsilon}^*)] = (\mu\sigma_{12}e^{i\omega t} + \mathrm{c.c.})$. Substituting (2.25), we find the effective electric susceptibility as:

$$\chi = -\frac{\mathcal{N}|\mu|^2}{\hbar\varepsilon_0}\frac{\delta + i\Gamma/2}{\delta^2 + \Gamma^2/4 + 2|\Omega|^2}. \tag{2.27}$$

For small field intensities we obtain (BOYD, 2020):

$$\begin{aligned}\chi &\approx -\frac{\mathcal{N}|\mu|^2}{\hbar\varepsilon_0}\left(\frac{1}{\delta - i\Gamma/2} - \frac{2(\delta + i\Gamma/2)}{(\delta^2 + \Gamma^2/4)^2}|\Omega|^2\right),\\ &= \chi^{(1)} + 3\chi^{(3)}|E|^2,\end{aligned} \tag{2.28}$$

where:

$$\chi^{(1)}(\delta) = -\frac{\mathcal{N}|\mu|^2}{\hbar\varepsilon_0}\frac{1}{\delta - i\Gamma/2}, \tag{2.29}$$

$$\chi^{(3)}(\delta) = \frac{2\mathcal{N}|\mu|^4}{3\hbar^3\varepsilon_0}\frac{\delta + i\Gamma/2}{(\delta^2 + \Gamma^2/4)^2} \tag{2.30}$$

are the first- and third-order electric susceptibilities. The first-order susceptibility is related to the linear absorption and the variation of the refractive index. The third-order susceptibility is related to nonlinear phenomena, such as the Kerr effect, also known as self-phase modulation. The complex index of refraction in the medium is $\tilde{n} = (1 + \chi^{(1)})^{1/2}$, which for $\chi^{(1)} \ll 1$ can be approximated as $\tilde{n} \simeq 1 + \chi^{(1)}/2$. We then define:

$$\tilde{n} \equiv n + i\frac{c}{2\omega}\alpha, \tag{2.31}$$

where $n$ is the index of refraction in the medium and $\alpha$ is the absorption coefficient. We can therefore write:

$$n = 1 - \frac{\mathcal{N}|\mu|^2}{2\hbar\varepsilon_0}\frac{\delta}{\delta^2 + \Gamma^2/4}, \tag{2.32}$$

$$\alpha = -\frac{\Gamma k\mathcal{N}|\mu|^2}{2\hbar\varepsilon_0}\frac{1}{\delta^2 + \Gamma^2/4}. \tag{2.33}$$

Figure 1 shows $n$ and $\alpha$ as functions of the detuning from resonance $\delta$.

**Figure 1** – Dependence of (a) the index of refraction $n$ and (b) the absorption coefficient $\alpha$ with the detuning from resonance. $\Gamma/2\pi = 6\,\mathrm{MHz}$, corresponding to the closed transition of the $\mathrm{D}_2$ line of $^{87}\mathrm{Rb}$.

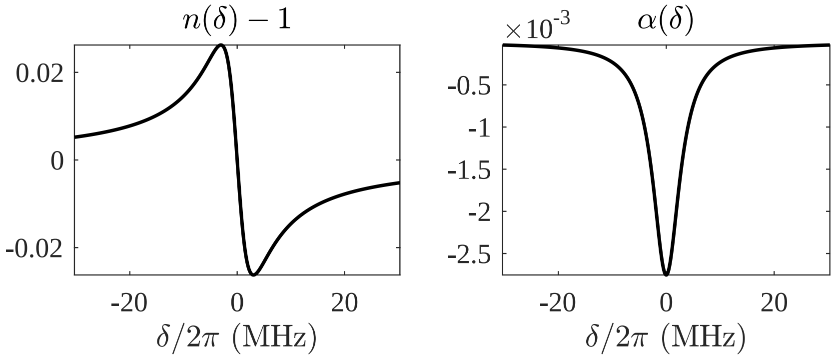

**Source:** The author (2024).

The intensity of the incident wave propagating inside the medium in the $z$ direction decays with $e^{-|\alpha|z}$. Thus, with Eq. (2.33), we can estimate the density of atoms $\mathcal{N}$ inside a dilute cloud of cold atoms, for example. This can be done by measuring the transmission of a weak probe passing through the sample as a function of the detuning, and fitting the detected absorption profile to the curve:

$$I(\delta) = I_0 \exp\left(-\frac{\mathrm{OD}}{1 + (2\delta/\Gamma)^2}\right), \tag{2.34}$$

where $I_0$ is the intensity of the beam before passing through the sample, and $\mathrm{OD}$ is the optical depth of the sample. The $\mathrm{OD}$ can then be found as:

$$\mathrm{OD} = \ln(2)\left[1 + (\Delta/\Gamma)^2\right], \tag{2.35}$$

where $\Delta$ is the full width at half maximum $(\mathrm{FWHM})$. Then, for a sample of size $L$, we may estimate $\mathcal{N}$ via:

$$\mathcal{N} = \frac{\mathrm{OD}}{2L}\frac{\Gamma\hbar\varepsilon_0}{k|\mu|^2}. \tag{2.36}$$

Due to the Doppler effect and the atomic motion at room temperature, atoms see an incoming light field with frequency $\omega' = \omega - \mathbf{k}\cdot\mathbf{v}$, where $\mathbf{k}$ is the wave-vector of the photon and $\mathbf{v}$ is the velocity of the atom. Considering the movement in 1D, the linear response of a large number of atoms in the velocity group $v$ is $\chi^{(1)}(\delta - kv)$. To account for all velocity groups, we average the susceptibility over all possible values of $v$:

$$\chi_D^{(1)}(\delta) = \int_{-\infty}^{\infty} \chi^{(1)}(\delta - kv) f(v) dv. \tag{2.37}$$

The weighting factor is the Maxwell-Boltzmann distribution $f(v) = \frac{1}{\sqrt{\pi}u} e^{-v^2/u^2}$, where $u = \sqrt{2k_B T/m}$ is the most probable velocity at a given temperature $T$. The absorption profile becomes:

$$\alpha_D(\delta) = -\frac{\Gamma k \mathcal{N} |\mu|^2}{2\hbar\varepsilon_0} g(\delta), \tag{2.38}$$

where $g(\delta)$ is the lineshape function, with a Voigt profile, which is the convolution between the Lorentzian and Gaussian lineshapes:

$$g(\delta) = \frac{1}{\sqrt{\pi}u} \int_{-\infty}^{\infty} \frac{e^{-v^2/u^2}}{(\delta - kv)^2 + \Gamma^2/4} dv. \tag{2.39}$$

Figure 2 shows a Lorentzian lineshape and the Voigt profile considering an atomic sample at $T \approx 500\,\mathrm{mK}$. We see that the motion of atoms at this relatively low temperature leads to a significant broadening of the absorption lines. At room temperature, $T \approx 300\,\mathrm{K}$, the Doppler broadening is much greater than many natural linewidths, and it forbids the observation of the hyperfine transitions of an atom by looking at the absorption of a single probe beam. In this situation, $ku \gg \Gamma$, and the lineshape function can be approximated by a Gaussian distribution

$$g(\delta) \simeq \frac{2\sqrt{\pi}}{\Gamma k u} e^{-\frac{\delta^2}{k^2 u^2}}. \tag{2.40}$$

**Figure 2** – Lorentzian and Voigt profiles considering a sample of atoms at $T \approx 500$ mK ($u \approx 10\,\mathrm{m/s}$).

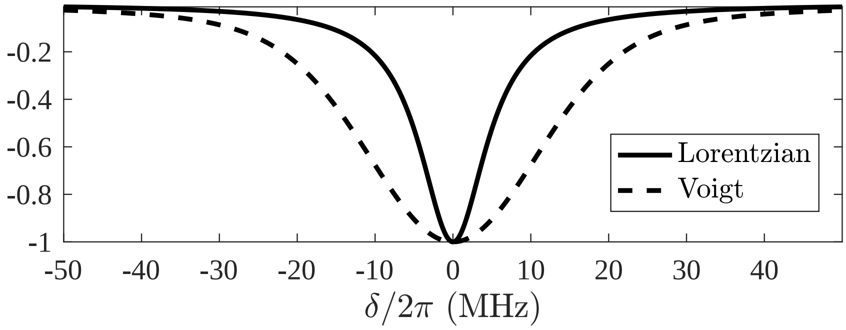

**Source:** The author (2024).

## 2.2 PARAXIAL OPTICS AND WAVE PROPAGATION IN THE PARAXIAL REGIME

Most of our results revolve around operations with paraxial modes, which are exact solutions to the paraxial wave-equation (PWE). The PWE is an approximate wave-equation that is suitable to describe the propagation of electromagnetic fields in vacuum. The so-called paraxial approximation is valid for most conditions encountered in real experimental scenarios. Within this approximation, it is also possible to adequately describe the propagation of light inside matter. To obtain the PWE, we start with Maxwell's equations in vacuum with no sources (JACKSON, 1999):

$$\nabla \cdot \mathbf{E} = 0, \tag{2.41}$$

$$\nabla \cdot \mathbf{B} = 0, \tag{2.42}$$

$$\nabla \times \mathbf{E} = -\frac{\partial \mathbf{B}}{\partial t}, \tag{2.43}$$

$$\nabla \times \mathbf{B} = \varepsilon_0 \mu_0 \frac{\partial \mathbf{E}}{\partial t}, \tag{2.44}$$

where $\mathbf{E}$ and $\mathbf{B}$ are the electric and magnetic fields, respectively, $\nabla = \sum_i \mathbf{e}_i \frac{\partial}{\partial x_i}$ is the gradient operator, and $\mu_0$ is the vacuum magnetic permeability. It is a straightforward matter to decouple Eqs. (2.41)-(2.44) and arrive at the wave-equation for the electric field $\mathbf{E}$ of a traveling light beam:

$$\nabla^2 \mathbf{E} - \frac{1}{c^2}\frac{\partial^2 \mathbf{E}}{\partial t^2} = 0, \tag{2.45}$$

where $\nabla^2 = \sum_i \frac{\partial^2}{\partial x_i^2}$ is the Laplacian, and $c = 1/\sqrt{\varepsilon_0 \mu_0}$ is the speed of light in vacuum. As we have done in Section 2.1, we suppose that $\mathbf{E}$ is a monochromatic beam propagating in the $z$ direction. However, as we are now interested in the spatial form of the light field, we make explicit its position dependence as:

$$\begin{aligned} \mathbf{E}(\mathbf{r}, t) &= \frac{1}{2}\boldsymbol{\epsilon}\mathcal{E}(\mathbf{r})e^{-i(kz-\omega t)} + \text{c.c.}, \\ &= \boldsymbol{\epsilon}E(\mathbf{r}, t) + \text{c.c.}, \end{aligned} \tag{2.46}$$

where $\boldsymbol{\epsilon}$ is the polarization direction, $\mathcal{E}(\mathbf{r}) = \mathcal{E}_0 u(\mathbf{r})$, $u(\mathbf{r})$ being a complex amplitude that describes the transverse distribution of the field at each $z$ plane, $k$ is the wave-number, and $\omega = ck$ is the frequency. Projecting Eq. (2.45) onto the direction $\boldsymbol{\epsilon}^*$, we obtain the scalar equation for the field amplitude $E(\mathbf{r}, t)$

$$\nabla_\perp^2 E + \frac{\partial^2 E}{\partial z^2} + k^2 E = 0, \tag{2.47}$$

where $\nabla_\perp^2 = \frac{\partial^2}{\partial x^2} + \frac{\partial^2}{\partial y^2}$ is the transverse Laplacian. Performing the $z$ derivatives, we obtain the equation satisfied by the envelope $u(\mathbf{r})$:

$$\nabla_\perp^2 u + \frac{\partial^2 u}{\partial z^2} - 2ik\frac{\partial u}{\partial z} = 0. \tag{2.48}$$

We now consider that the variation of $u(\mathbf{r})$ with the longitudinal coordinate is slow, in such a way that:

$$\left|\frac{\partial^2 u}{\partial z^2}\right| \ll \left|k\frac{\partial u}{\partial z}\right|, \tag{2.49}$$

and neglect the second derivative in $z$. This is known as the slowly varying envelope approximation. We then arrive at the paraxial wave-equation (PWE):

$$\nabla_\perp^2 u - 2ik\frac{\partial u}{\partial z} = 0. \tag{2.50}$$

The PWE describes the evolution of the transverse distribution of the radiation field of light in vacuum. The lowest order solution to the PWE is the well-known Gaussian beam, and it faithfully represents the characteristics of real laser beams. Numerous other solutions are known and experimentally attainable, such as the already mentioned Hermite- and Laguerre-Gaussian modes, the Bessel, Mathieu and Airy beams, to cite a few (FORBES; OLIVEIRA; DENNIS, 2021).

It is interesting to note that the PWE is mathematically equivalent to the $2\mathrm{D}$ Schrödinger equation for a free particle, and therefore similarities may be drawn between classical optics and quantum mechanics. In fact, these similarities were noted since the early days of quantum mechanics. Exact solutions to the PWE are named paraxial modes, and we shall denote a general paraxial mode by $u_{m,n}(\mathbf{r}_\perp, z)$, where the pair of indices $(m,n)$ determine their transverse spatial distribution, $\mathbf{r}_\perp$ is the transverse position vector in a particular coordinate system, and $z$ is the longitudinal coordinate. The set of all modes $\{u_{m,n}\}$ form complete orthonormal sets of functions, bases, on the transverse plane. In upcoming sections, we will present different families of modes and discuss their characteristics. Here we outline general properties shared by these families. The orthogonality and completeness relations read:

$$\iint u_{m,n}u^*_{m',n'}d^2\mathbf{r}_\perp = \delta_{m,m'}\delta_{n,n'}, \tag{2.51}$$

$$\sum_{m,n} u_{m,n}(\mathbf{r}_\perp, z)u^*_{m,n}(\mathbf{r}'_\perp, z) = \delta(\mathbf{r}_\perp - \mathbf{r}'_\perp). \tag{2.52}$$

This allows to write any scalar optical field as a superposition of the form:

$$U(\mathbf{r}_\perp, z) = \sum_{m,n} c_{m,n}(z)u_{m,n}(\mathbf{r}_\perp, z). \tag{2.53}$$

The expansion coefficients $c_{m,n}(z)$ can be seen as power control parameters. If we call $P_{m,n} = |c_{m,n}|^2$ the power allocated to the mode $u_{m,n}$, then the total power carried by the field $U$ is $P = \sum_{m,n} P_{m,n} = \sum_{m,n} |c_{m,n}|^2$. We may define the normalized mode weight as $\eta_{m,n} \equiv |c_{m,n}|^2/P$. It is important to note that $c_{m,n}(z)$ can be complex.

If we multiply Eq. (2.50) by $u^*$, where $u$ is any paraxial mode, and add to the resulting equation its complex conjugate, we obtain the continuity equation:

$$\frac{\partial |u|^2}{\partial z} + \boldsymbol{\nabla}_\perp \cdot \mathbf{j} = 0, \tag{2.54}$$

where the current is $\mathbf{j} = \frac{i}{2k}(u^* \boldsymbol{\nabla}_\perp u - u \boldsymbol{\nabla}_\perp u^*)$. Now we integrate Eq. (2.54) over a surface $\mathbb{S}$ on the transverse plane, and use 2D Gauss' theorem on the divergence term, to obtain:

$$\frac{dP_\mathrm{c}}{dz} + \Phi_\mathrm{b} = 0, \tag{2.55}$$

where $P_\mathrm{c} = \iint_\mathbb{S} |u|^2 d^2\mathbf{r}_\perp$ is the power contained in the surface $\mathbb{S}$, and $\Phi_\mathrm{b} = \int_{\partial\mathbb{S}} (\mathbf{j} \cdot \mathbf{n}) dl$, with $\mathbf{n}$ being a unit vector normal to the contour $\partial\mathbb{S}$ pointing outward, is the flux of the current $\mathbf{j}$ through the boundary of the surface. If we extend the surface $\mathbb{S}$ to be the infinite transverse plane, $P_\mathrm{c}$ becomes the total power carried by the light beam, $P$, and the flux term goes to $0$. We then obtain:

$$\frac{dP}{dz} = 0, \tag{2.56}$$

and conclude that the total power carried by a paraxial beam is conserved upon free-space propagation.

The Fourier transform (FT) or the angular spectrum of a paraxial mode gives the field amplitude as a function of the transverse wave-vector $\mathbf{q}$, and can be useful for many computations. For an arbitrary paraxial mode $u_{m,n}$, we may write the FT as:

$$\begin{aligned} \mathcal{U}_{m,n}(\mathbf{q}, z) &= \mathcal{F}\{u_{m,n}(\mathbf{r}_\perp, z)\}, \\ &= \frac{1}{2\pi} \iint u_{m,n}(\mathbf{r}_\perp, z) e^{i\mathbf{q}\cdot\mathbf{r}_\perp} d^2\mathbf{r}_\perp, \end{aligned} \tag{2.57}$$

The angular spectrum satisfies the PWE in wave-vector space, obtained by applying the FT to Eq. (2.50):

$$\left(-i\frac{|\mathbf{q}|^2}{2k} + \frac{\partial}{\partial z}\right) \mathcal{U}_{m,n}(\mathbf{q}, z) = 0. \tag{2.58}$$

From Eq. (2.58) the evolution of $\mathcal{U}_{m,n}(\mathbf{q})$ with the longitudinal coordinate can be found as:

$$\mathcal{U}_{m,n}(\mathbf{q}, z) = \mathcal{U}_{m,n}(\mathbf{q}, 0) e^{ik\vartheta_\mathbf{k}^2 z}, \tag{2.59}$$

where we have defined the parameter $\vartheta_{\mathbf{k}} \equiv |\mathbf{q}|/\sqrt{2}k$, which can be seen as a measure of the degree of paraxiality. In the paraxial limit, $|\mathbf{q}| \ll k$, and $\vartheta_{\mathbf{k}} \ll 1$. It can be noted that the $z$ dependence of the angular spectrum is much simpler than that of the mode in position space. Also, the squared modulus of $\mathcal{U}$ is invariant with the propagation distance $z$, $|\mathcal{U}(\mathbf{q}, z)|^2 = |\mathcal{U}(\mathbf{q}, 0)|^2$. Equation (2.59) gives a general recipe to propagate an arbitrary paraxial field $\mathcal{E}(\mathbf{r}_\perp, z_0)$ up to a position $z$:

$$\mathcal{E}(\mathbf{r}_\perp, z) = \mathcal{F}^{-1}\left\{\tilde{\mathcal{E}}(\mathbf{q}, z_0) e^{i\frac{|\mathbf{q}|^2}{2k}(z-z_0)}\right\}, \tag{2.60}$$

where we defined $\tilde{\mathcal{E}}(\mathbf{q}, z_0) \equiv \mathcal{F}\left\{\mathcal{E}(\mathbf{r}_\perp, z_0)\right\}$.

Two important constructions in paraxial optics are the propagator and the Green's function (LANNING et al., 2017):

$$K(\mathbf{r}_\perp, z; \mathbf{r}'_\perp, z') = \sum_{m,n} u_{m,n}(\mathbf{r}_\perp, z) u^*_{m,n}(\mathbf{r}'_\perp, z'), \tag{2.61}$$

$$G(\mathbf{r}_\perp, z; \mathbf{r}'_\perp, z') = \Theta(z - z') K(\mathbf{r}_\perp, z; \mathbf{r}'_\perp, z'), \tag{2.62}$$

where $\Theta(\cdot)$ is the Heaviside step function. The propagator $K$ receives this name because it propagates a mode from an initial position $z'$ to a final position $z$ as:

$$\iint K(\mathbf{r}_\perp, z; \mathbf{r}'_\perp, z') u_{m,n}(\mathbf{r}'_\perp, z') d^2\mathbf{r}'_\perp = u_{m,n}(\mathbf{r}_\perp, z), \tag{2.63}$$

and the Green's function $G$ is useful to solve non-homogeneous paraxial wave-equations of the form:

$$\hat{\mathcal{D}}_k \mathcal{E}(\mathbf{r}) = \wp(\mathbf{r}), \tag{2.64}$$

where $\hat{\mathcal{D}}_k \equiv (i\nabla^2_\perp/2k + \partial/\partial z)$ is the PWE differential operator, and $\wp(\mathbf{r})$ is the source term, defined in a region $\mathbb{V}$ of space. It is straightforward to show that $G$ satisfies:

$$\hat{\mathcal{D}}_k G(\mathbf{r}_\perp, z; \mathbf{r}'_\perp, z') = \delta^{(2)}(\mathbf{r}_\perp - \mathbf{r}'_\perp)\delta(z - z'), \tag{2.65}$$

and given that the field at the initial position $z_0$, $\mathcal{E}(\mathbf{r}_\perp, z_0) = \mathcal{E}_0(\mathbf{r}_\perp)$, is known, the general solution to the non-homogeneous PWE with source term $\wp(\mathbf{r})$ can be found as (LANNING et al., 2017):

$$\mathcal{E}(\mathbf{r}_\perp, z) = \iint \left\{K(\mathbf{r}_\perp, z; \mathbf{r}'_\perp, z_0)\mathcal{E}(\mathbf{r}'_\perp, z_0) + \int G(\mathbf{r}_\perp, z; \mathbf{r}'_\perp, z')\wp(\mathbf{r}'_\perp, z')dz'\right\} d^2\mathbf{r}'_\perp. \tag{2.66}$$

The first term is associated with the free-propagation of the input field from $z_0$ to $z$, while the second term is related to effects due to the source. For a field that is generated as the result of some process taking place inside the region $\mathbb{V}$, the initial condition is $\mathcal{E}(\mathbf{r}_\perp, z_0) = 0$, and the solution to $\mathcal{E}$ at $z$ fully determined by the second term in Eq. (2.66). In general, the source term is itself affected by the changing field distribution, $\mathcal{E}(\mathbf{r}_\perp, z)$, but to take this into account makes the situation very complicated. A good approximation is to consider that $\wp(\mathbf{r}_\perp)$ is only affected by the initial field distribution $\mathcal{E}_0(\mathbf{r}_\perp)$. Substituting expression (2.62) into Eq. (2.66), we obtain:

$$\mathcal{E}(\mathbf{r}_\perp, z) = \sum_{m,n} \mathcal{A}_{m,n}(z) u_{m,n}(\mathbf{r}_\perp, z), \tag{2.67}$$

where:

$$\begin{aligned}\mathcal{A}_{m,n}(z) &= \int_{\mathbb{R}^3} \Theta(z - z')\wp(\mathbf{r}'_\perp, z')u^*_{m,n}(\mathbf{r}'_\perp, z')d^3\mathbf{r}', \\ &= \int_{-\infty}^{z} \iint_{\mathbb{R}^2} \wp(\mathbf{r}'_\perp, z')u^*_{m,n}(\mathbf{r}'_\perp, z')d^2\mathbf{r}'_\perp dz'. \end{aligned} \tag{2.68}$$

Usually the source term is nonzero only in a limited region of space. In the $z$ direction, we may consider that it exists between $z = -L/2$, and $z = L/2$, and is zero everywhere else. We may represent it as:

$$\wp(\mathbf{r}'_\perp, z') = S(\mathbf{r}'_\perp, z')[\Theta(z' + L/2) - \Theta(z' - L/2)], \tag{2.69}$$

where $\Theta(\cdot)$ is the Heaviside function, and $S$ carries any other spatial distribution of the source term. We may thus write:

$$\mathcal{A}_{m,n}(z) = \int_{-L/2}^{z_<} \iint S(\mathbf{r}'_\perp, z')u^*_{m,n}(\mathbf{r}'_\perp, z')d^2\mathbf{r}'_\perp dz', \tag{2.70}$$

where $z_< = \min[z, L/2]$. Note that this expression encompasses the solution for the field $\mathcal{E}$ both inside and outside the region where the source term is defined. As we shall see, assuming an ansatz for $\mathcal{E}$ in the form of an arbitrary superposition of paraxial modes, as in Eq. (2.53), yields the same solution as obtained with the Green's function introduced in (LANNING et al., 2017).

### 2.2.1 The Laguerre-Gaussian mode

We will be interested in problems that involve the OAM of light, and for this reason we consider the Laguerre-Gaussian (LG) basis, which is also convenient when dealing with circularly symmetric light fields. LG modes are solutions to the PWE in cylindrical coordinates:

$$\frac{\partial^2 u}{\partial r^2} + \frac{1}{r}\frac{\partial u}{\partial r} + \frac{1}{r^2}\frac{\partial^2 u}{\partial \phi^2} - 2ik\frac{\partial u}{\partial z} = 0, \tag{2.71}$$

and are denoted as

$$u_{\ell,p}(\mathbf{r}) = \frac{C_{\ell,p}}{w(z)}\left(\frac{\sqrt{2}r}{w(z)}\right)^{|\ell|} L_p^{|\ell|}\left(\frac{2r^2}{w^2(z)}\right) e^{-r^2/w^2(z)} \times e^{i\ell\phi}\exp\left(-i\frac{kr^2}{2R(z)} + i\Psi_{\mathrm{G}}(z)\right), \tag{2.72}$$

where $C_{\ell,p} = \sqrt{2p!/\pi(p+|\ell|)!}$ is the normalization constant, $L_p^{|\ell|}(\cdot)$ is the associated Laguerre polynomial, $w(z) = w_0\sqrt{1+(z/z_R)^2}$ is the beam width, $R(z) = z\left[1+(z_R/z)^2\right]$ is the curvature radius, $\Psi_{\mathrm{G}}(z) = (N_{\ell,p}+1)\tan^{-1}(z/z_R)$ is the Gouy phase shift, with the total mode order defined as $N_{\ell,p} = 2p+|\ell|$, $z_R = kw_0^2/2$ is the Rayleigh range and $w_0$ is the beam waist. The waist $w_0$ and Rayleigh range $z_R$ are the transverse and longitudinal characteristic lengths of the LG mode, respectively. Note that they are related by the wave-number, which is usually a stronger constraint in the experimental setup. To determine the mode functions $\{u_{\ell,p}\}$, one must specify either $w_0$ or $z_R$, but generally it is more convenient to think about the beam waist.

A light beam described by an LG mode carries well-defined OAM in the $z$-direction, which is related to the azimuthal phase factor $e^{i\ell\phi}$, where integer $\ell \in (-\infty,\infty)$, called the topological charge, defines the OAM per photon in the beam (ALLEN et al., 1992). This term introduces a phase singularity, an optical vortex (OV), at the center of the beam, where the intensity is zero. The phase-fronts of LG beams are twisted around the propagation axis (see Fig. 3), with the number and handedness of the helices defined by the magnitude and sign of $\ell$, respectively. The Poynting vector, which is normal to the phase-fronts at all positions, spirals around the beam axis (ALLEN et al., 1992). The linear momentum density thus possesses an off-axis azimuthal component, that gives rise to the angular momentum of the beam (YAO; PADGETT, 2011). The other index characterizing the mode, $p \in [0,\infty)$, is called the radial index. It is related to the number of dark rings in the intensity profile of $u_{\ell,p}$, but does not have a straightforward connection with a physical quantity as is the case for $\ell$. In recent years, however, the radial index has been the subject of theoretical works (KARIMI et al., 2014; PLICK; KRENN, 2015) that have enlightened its significance. In Fig. 4 we show the intensity and phase distributions of LG modes with different orders at the focal plane $z = 0$.

One last remark is that the LG mode possesses the interesting property that its Fourier transform at $z = 0$, $\mathcal{L}_{\ell,p}(\mathbf{q},0) \equiv \mathcal{F}\{u_{\ell,p}(\mathbf{r}_\perp,0)\}$, has the same form as the mode itself. In cylindrical coordinates, we have:

$$\mathcal{L}_{\ell,p}(\rho,\varphi,0) = \frac{1}{2\pi}\iint u_{\ell,p}(r,\phi,0)e^{ir\rho\cos(\varphi-\phi)}rdrd\phi, \tag{2.73}$$

**Figure 3** – Phase fronts of (a) a plane wave, $\ell = 0$, and LG beams with (b) $\ell = 1$, (c) $\ell = 2$ and (d) $\ell = 3$.

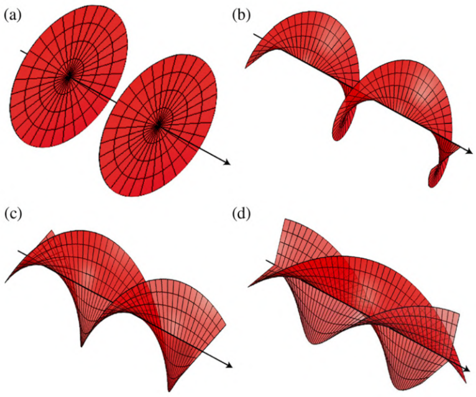

**Source:** Taken from reference (YAO; PADGETT, 2011).

where $(\rho\cos\varphi, \rho\sin\varphi) = (q_x, q_y) = \mathbf{q}$ is transverse wave-vector. We can then obtain:

$$\mathcal{L}_{\ell,p}(\mathbf{q},0) = C_{\ell,p}\frac{w_0}{2}\left(\frac{\rho w_0}{\sqrt{2}}\right)^{|\ell|} L_p^{|\ell|}\left(\frac{\rho^2 w_0^2}{2}\right) e^{-\rho^2 w_0^2/4} e^{i\ell\varphi} \exp\left[i\frac{\pi}{2}(2p+|\ell|)\right]. \tag{2.74}$$

As we have already seen, the evolution of the LG angular spectrum with the longitudinal coordinate $z$ is given by Eq. (2.59), $\mathcal{L}_{\ell,p}(\mathbf{q},z) = \mathcal{L}_{\ell,p}(\mathbf{q},0)e^{ik\vartheta_{\mathbf{k}}^2 z}$.

To show that the LG mode does indeed carry well-defined OAM in the propagation direction, we recur to the Lorenz gauge, in which the vector potential $\mathbf{A}$ satisfies the wave-equation. We describe it as a linearly polarized wave traveling in the $z$ direction, with its positive fre-

**Figure 4** – Intensity profiles and phase distributions of LG modes of different orders $\ell = -1, 0, 1, 3$, $p = 0, 1, 2$.

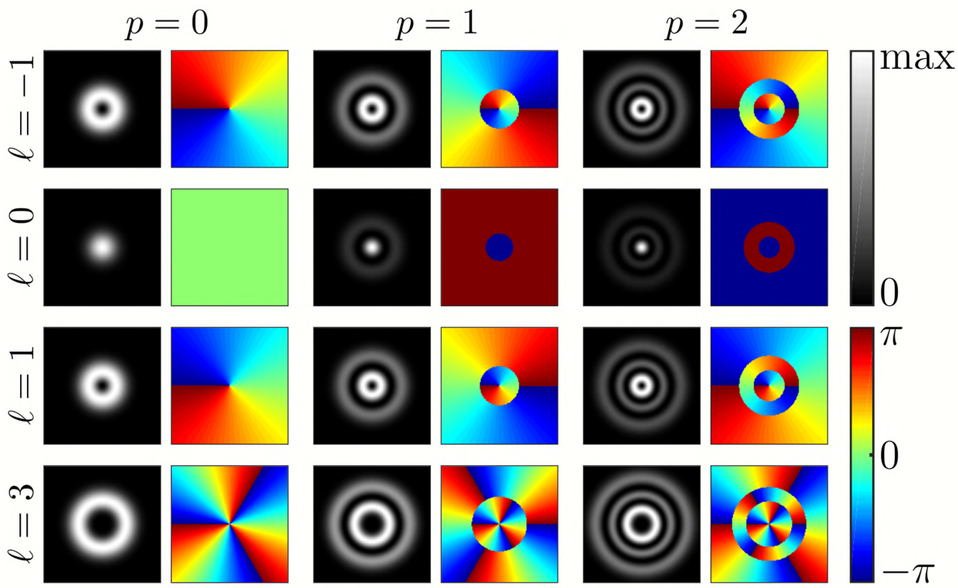

**Source:** The author (2024).

quency component written as (ALLEN et al., 1992):

$$\mathbf{A}(\mathbf{r},t) = \mathbf{e}_x u(\mathbf{r}) e^{-i(kz-\omega t)}, \tag{2.75}$$

where $u(\mathbf{r})$ satisfies the PWE. The electric and magnetic fields in this case are written as (ANDREWS; BABIKER, 2012; MOLINA-TERRIZA; TORRES; TORNER, 2007)

$$\mathbf{E} = -\frac{\omega}{k}\left(\mathbf{e}_x iku + \mathbf{e}_z \frac{\partial u}{\partial x}\right) e^{-i(kz-\omega t)}, \tag{2.76}$$

$$\mathbf{B} = -\left(\mathbf{e}_y iku + \mathbf{e}_z \frac{\partial u}{\partial y}\right) e^{-(ikz-\omega t)}. \tag{2.77}$$

To obtain these forms, we neglected $\partial^2 u/\partial y\partial x$ and considered $|\partial u/\partial z| \ll |ku|, |\partial^2 u/\partial x^2| \ll |k^2 u|$. We see that the electromagnetic wave described by Eq. (2.76) is not purely transverse. The longitudinal components of $\mathbf{E}$ and $\mathbf{B}$, although much smaller than the transverse components, are essential to obtain the result we want. The time average of the linear momentum density is (ALLEN et al., 1992):

$$\begin{aligned}\langle\mathbf{p}\rangle &= \varepsilon_0\langle\mathbf{E}\times\mathbf{B}\rangle,\\ &= \frac{\varepsilon_0}{2}\mathrm{Re}\{\mathbf{E}\times\mathbf{B}^*\},\\ &= i\omega\frac{\varepsilon_0}{2}\left(u^*\boldsymbol{\nabla}_\perp u - u\boldsymbol{\nabla}_\perp u^*\right) + \omega k\varepsilon_0|u|^2\mathbf{e}_z. \end{aligned}\tag{2.78}$$

Specializing to cylindrical coordinates, the longitudinal component of the time averaged angular momentum, $J_z = \iint(\mathbf{r}\times\langle\mathbf{p}\rangle)_z d^2\mathbf{r}_\perp$, can be found as:

$$J_z = -\omega\varepsilon_0 \iint \mathrm{Im}\left\{u^*\partial_\phi u\right\} d^2\mathbf{r}_\perp. \tag{2.79}$$

Using the expression for the LG mode $u = u_{\ell,p}$, we can write $J_z$ as:

$$J_z = \omega\varepsilon_0\ell. \tag{2.80}$$

Moreover, since the total energy per unit length carried by the radiation field is $W \simeq \varepsilon_0\omega^2$, the ratio between the angular momentum along the beam axis and the field energy is found as:

$$\frac{J_z}{W} = \frac{\ell}{\omega}. \tag{2.81}$$

This result can be generalized to the case of a field with circular polarization (ALLEN et al., 1992), where we obtain:

$$\frac{J_z}{W} = \frac{\ell + \sigma_z}{\omega}, \tag{2.82}$$

where $\sigma_z = \pm 1$ for left- or right-circular polarizations. It is known that a photon from a circularly polarized light beam possesses an angular momentum given by:

$$S_z = \sigma_z \hbar, \tag{2.83}$$

which is regarded as the spin of the photon. Thus, Eq. (2.82) suggests that the orbital angular momentum in the $z$ direction per photon in a Laguerre-Gaussian beam is

$$L_z = \ell \hbar. \tag{2.84}$$

Contrary to the spin component of the angular momentum of a photon, its OAM can assume an infinite number of values. This high dimensionality represents a useful tool for information multiplexing in optical communications exploring the transverse degrees of freedom of light, and also for quantum optics and quantum information.

### 2.2.2 Three families of paraxial solutions: LG, HG, and IG

One can also work with the parity-defined LG (PDLG) modes, which do not carry well-defined OAM, $u^{\sigma}_{\ell,p}$, where $\sigma = e, o$ corresponds to the *even* and *odd* parity modes, respectively. They are given by:

$$u^{e,o}_{\ell,p}(r,\phi,z) = \sqrt{\frac{2}{(1+\delta_{\ell,0})}} V_p^{|\ell|}(r,z) \begin{Bmatrix} \cos \ell\phi \\ \sin \ell\phi \end{Bmatrix}, \tag{2.85}$$

where $V_p^{|\ell|}(r,z)$ is defined via $u_{\ell,p} = V_p^{|\ell|}(r,z)e^{i\ell\phi}$. Instead of the characteristic ring-shaped profile carried by helical LG beams, PDLG modes present a flowerlike pattern with $2|\ell|$ light petals (GRYNBERG; MAÎTRE; PETROSSIAN, 1994).

The Hermite-Gaussian (HG) mode is another commonly used solution to the paraxial wave-equation in numerous applications. HG modes are given in cartesian coordinates and are denoted as:

$$\begin{aligned} u^{\mathrm{HG}}_{n_x,n_y}(x,y,z) = {} & \sqrt{\frac{2}{\pi}} \frac{B_{n_x,n_y}}{w(z)} H_{n_x}\left(\frac{\sqrt{2}x}{w(z)}\right) H_{n_y}\left(\frac{\sqrt{2}y}{w(z)}\right) \\ & \times e^{-\frac{x^2+y^2}{w^2(z)}} \exp\left(-ik\frac{x^2+y^2}{2R(z)} + i\Psi_{\mathrm{HG}}(z)\right), \end{aligned} \tag{2.86}$$

where $B_{n_x,n_y} = \sqrt{2^{-(n_x+n_y)}/n_x!n_y!}$ is a normalization constant, $H_m(\cdot)$ is the Hermite polynomial of order $m$, $\Psi_{\mathrm{HG}}(z) = (1+N_{n_x n_y})\tan^{-1}(z/z_R)$, with $N_{n_x,n_y} = n_x+n_y$, is the Gouy phase and $w(z)$ and $R(z)$ are the beam waist and radius of curvature. The indices $n_x, n_y = 0, 1, 2, ...$ characterize the field distribution in the $x$ and $y$ directions, respectively. The intensity profile of HG modes is composed of $(m+1) \times (n+1)$ lobes of light disposed in a rectangular grid with $(n+1)$ rows and $(m+1)$ columns. The correspondence between the HG and LG families of solutions is well established both in theory and in practice (ALLEN et al., 1992; KIMEL; ELIAS, 1993).

Ince-Gaussian (IG) modes, on the other hand, are not found so easily in text-books. They possess elliptical symmetry, are parity defined and require an extra parameter to be fully characterized: the ellipticity or eccentricity $\varepsilon$. The IG mode transverse distribution is described by Ince polynomials (BANDRES; GUTIéRREZ-VEGA, 2004). What is perhaps most interesting, is that HG and LG modes are limiting cases of the IG mode when the ellipticity goes to $\infty$ and $0$, respectively. We might represent these mode transitions symbolically as (BANDRES; GUTIéRREZ-VEGA, 2004):

$$\mathrm{LG}^{\sigma}_{(q-m)/2,m} \underset{(\varepsilon\to 0)}{\longleftarrow} \mathrm{IG}^{\sigma}_{q,m}(\varepsilon) \underset{(\varepsilon\to\infty)}{\longrightarrow} \begin{cases} \mathrm{HG}_{m,q-m} & (\sigma = e), \\ \mathrm{HG}_{m-1,q-m+1} & (\sigma = o). \end{cases} \tag{2.87}$$

Lastly, since all three families of solutions form bases of functions on the transverse plane, each one can be decomposed in terms of the other (KIMEL; ELIAS, 1993; BANDRES; GUTIéRREZ-VEGA, 2004; BANDRES; GUIZAR-SICAIROS, 2009).

The interplay between the three families has been explored in second-order nonlinear optical processes to demonstrate optical mode conversion in crystals (PIRES et al., 2019), and the HG basis was shown to present an advantage in this kind of manipulation of optical structure, in comparison with the LG basis (PIRES et al., 2020). More recently, we showed that the HG basis also presents a unique property of spatial structure transfer in the context of a nondegenerate cascade FWM process in Rb vapor generating blue light, and that this property allows for optical mode conversion in a similar fashion (ROCHA et al., 2022). It was predicted that by performing the wave-mixing of two HG modes $u^{\mathrm{HG}}_{m,n}$ and $u^{\mathrm{HG}}_{m',n'}$, a nearly pure[2] $u^{\mathrm{HG}}_{m+m',n+n'}$ emerges at the FWM blue light output. This can be exploited to obtain at the output desired LG and IG modes with high fidelity. It is numerically demonstrated that this is valid in an extended-medium setting, i.e., if the interaction medium length is much larger than the Rayleigh range of the participating beams, $L/z_R \gg 1$. This subject is discussed in Chapter 4.

---

[2] In contrast, the sum-frequency generation in a $\chi^{(2)}$ medium with HG modes only results in a *dominant* contribution of the HG mode with summed indices, meaning that other modes may contribute sensibly to the output superposition.

### 2.2.3 The tilted-lens technique

The tilted lens (TL) technique (VAITY; BANERJI; SINGH, 2013) is a simple but extremely useful method to measure the topological charge $\ell$ of a laser beam. It consists of a convex lens tilted by a small angle with respect to the propagation axis of the beam. The effect of such an arrangement is to perform an astigmatic transformation onto the optical mode. The resulting intensity profile formed near the focal plane possesses an HG distribution with the number of dark valleys equal to the topological charge magnitude $|\ell|$, rotated by $\sim \mathrm{sgn}(\ell)45°$, where $\mathrm{sgn}(\cdot)$ is the sign function, as illustrated in Fig. 5. Therefore, with this method we can identify both the magnitude and the helicity of an optical vortex.

This is not the only use for the method. Recently it has been applied within a machine learning framework to successfully identify superpositions of LG modes (SILVA et al., 2021b), and to investigate families of modes that are unaffected by the transformation (BUONO et al., 2022). Another interesting aspect we are currently investigating is the fact that the TL transformation is related to the Wigner distribution (CALVO, 2005) of the optical mode, and therefore it allows to access information regarding the 4D optical phase-space in the $(\mathbf{r}_\perp, \mathbf{q})$ coordinates. In this section we discuss methods for calculating the tilted lens profiles.

**Figure 5** – Schematic description of the tilted lens transformation for LG modes with topological charges $\ell = -1, 0, 1, 2$ (from top to bottom). The intensity (Int.) and tilted lens (TL) profiles of each mode are shown. The number of dark valleys and the orientation of the TL pattern indicate, respectively, the magnitude $|\ell|$ and the relative helicity $\mathrm{sgn}(\ell)$. On the right we show the corresponding experimental profiles.

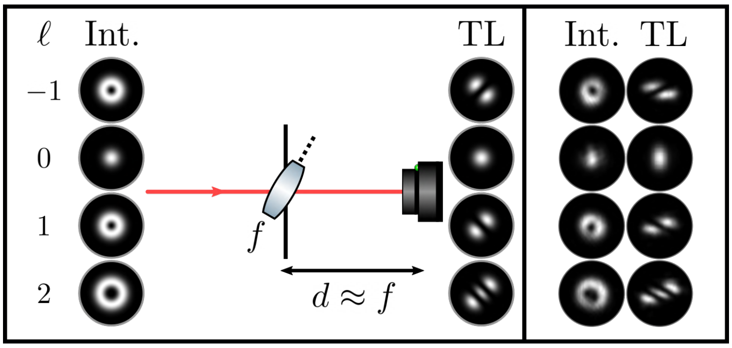

**Source:** The author (2024).

#### 2.2.3.1 *The tilted-lens as a misaligned ABCD system*

Here we briefly mention the basics of beam transformation via diffraction integrals. The evolution of a paraxial optical field $\mathcal{E}(\mathbf{r})$ through any effective ABCD optical system can be evaluated via the integral:

$$\mathcal{E}(\mathbf{r}_\perp, z) = \frac{i}{\lambda \mathrm{B}} \iint \mathcal{E}(\mathbf{r}'_\perp, z_0) e^{-ik\mathcal{S}(\mathbf{r}_\perp, \mathbf{r}'_\perp)} d^2\mathbf{r}'_\perp, \tag{2.88}$$

where $\mathcal{S} = \mathcal{S}(\mathbf{r}_\perp, \mathbf{r}'_\perp, z - z_0; \mathbf{M})$ is the optical path between the planes $z$ and $z_0$ and $\mathbf{M} = (\mathrm{A}, \mathrm{B}; \mathrm{C}, \mathrm{D})$ is the appropriate ABCD matrix of the system. In cylindrical coordinates we have:

$$\mathcal{S} = (z - z_0) + \frac{1}{2\mathrm{B}}(\mathrm{A}r'^2 - 2rr'\cos(\phi' - \phi) + \mathrm{D}r^2). \tag{2.89}$$

For a pure LG mode the integral given by Eq. (2.88) with $\mathcal{S}$ given by Eq. (2.89) can be solved exactly, and the usual ABCD law for Gaussian beams applies (TACHÉ, 1987). Consider the ABCD matrices for a thin convex lens of focal length $f$ and for the free propagation over a distance $D$:

$$\mathbf{M}_{\text{lens}} = \begin{pmatrix} 1 & 0 \\ -1/f & 1 \end{pmatrix}, \qquad \mathbf{M}_D = \begin{pmatrix} 1 & D \\ 0 & 1 \end{pmatrix}. \tag{2.90}$$

The total ABCD matrix accounting for the propagation distances of $d_0$ before, and $d$ after passing through the lens is:

$$\mathbf{M}_{\text{total}} = \mathbf{M}_d \mathbf{M}_{\text{lens}} \mathbf{M}_{d_0} = \begin{pmatrix} 1 - d/f & d_0(1 - d/f) + d \\ -1/f & 1 - d_0/f \end{pmatrix}. \tag{2.91}$$

For distances $d_0$ and $d$ equal to the focal length $d = d_0 = f$, $\mathrm{A} = \mathrm{D} = 0$, $\mathrm{B} = f$, and $\mathrm{C} = -1/f$. Given that the field at $z = z_0$, $\mathcal{E}(\mathbf{r}_\perp, z_0)$ is known, we can write the field at the focal plane as:

$$\mathcal{E}(\mathbf{r}_\perp, z_0 + 2f) = \frac{i}{kf} e^{-ikf} \iint \mathcal{E}(\mathbf{r}'_\perp, z_0) e^{i\frac{k}{f}rr'\cos(\phi' - \phi)} d^2\mathbf{r}'_\perp. \tag{2.92}$$

The integral can be identified as the Fourier transform of the field $\mathcal{E}$. We conclude that the intensity profile of a paraxial optical field at the focal plane of a lens is proportional to the squared modulus of its Fourier transform at $z = z_0$:

$$|\mathcal{E}(r, \phi, z_0 + 2f)|^2 \propto |\tilde{\mathcal{E}}(rk/f, \phi, z_0)|^2, \tag{2.93}$$

where $\tilde{\mathcal{E}} \equiv \mathcal{F}\{\mathcal{E}\}$ is the Fourier transform of $\mathcal{E}$.

In the case of a misaligned optical element, $\mathbf{M}$ is a $4 \times 4$ matrix, $\mathbf{M} = (\mathbf{A}, \mathbf{B}; \mathbf{C}/f, \mathbf{D})$, where now each element is a $2 \times 2$ matrix. We may rewrite the propagation integral as:

$$\mathcal{E}(\mathbf{r}_\perp, z) = \frac{i}{\lambda\sqrt{\det \mathbf{B}}} \iint \mathcal{E}(\mathbf{r}'_\perp, z_0) e^{-ik\mathcal{S}_{\text{mis}}} d^2\mathbf{r}'_\perp, \tag{2.94}$$

where now the optical path is written as (VAITY; BANERJI; SINGH, 2013):

$$\mathcal{S}_{\mathrm{mis}} = (z - z_0) + \frac{1}{2}\mathbf{r}'_{\perp}\mathbf{B}^{-1}\mathbf{A}\mathbf{r}'_{\perp} + \frac{1}{2}\mathbf{r}_{\perp}\mathbf{D}\mathbf{B}^{-1}\mathbf{r}_{\perp} - \mathbf{r}'_{\perp}\mathbf{B}^{-1}\mathbf{r}_{\perp}. \tag{2.95}$$

For a convex lens tilted by an angle $\theta$ with respect to the axis perpendicular to the propagation plane of the light beam, the matrices are:

$$\mathbf{A} = \begin{pmatrix} 1 - d\sec\theta/f & 0 \\ 0 & 1 - d\cos\theta/f \end{pmatrix}, \tag{2.96}$$

$$\mathbf{B} = \begin{pmatrix} d_0 + d(1 - d_0\sec\theta/f) & 0 \\ 0 & d_0 + d(1 - d_0\cos\theta/f) \end{pmatrix}, \tag{2.97}$$

$$\mathbf{C} = \begin{pmatrix} \sec\theta & 0 \\ 0 & \cos\theta \end{pmatrix}, \tag{2.98}$$

$$\mathbf{D} = \begin{pmatrix} 1 - d_0\sec\theta/f & 0 \\ 0 & 1 - d_0\cos\theta/f \end{pmatrix}. \tag{2.99}$$

By carrying the integration given by Eq. (2.94), with propagation distances $d$ and $d_0$ equal to the focal length $f$, we can obtain the tilted lens intensity profile of the incoming field $\mathcal{E}$. For more details on the propagation of optical fields through misaligned elements, see Ref. (WEBER, 2006). An alternative method, which is based on group theory and bypasses the direct evaluation of integrals of the form (2.88) and (2.94) is given in Ref. (BANDRES; GUIZAR-SICAIROS, 2009).

### 2.2.3.2 *The tilted lens operator*

Here we borrow the ket notation and use it to represent paraxial modes and transformations acting on these modes in a convenient form. We can define the astigmatic transformation performed by the tilted lens (including the free propagation before and after the lens) as the action of the operator (BUONO et al., 2022):

$$\hat{O}_{TL} = \sum_{k=0}^{N_{\max}} \sum_{s=0}^{k} e^{i(k-2s)\pi/4} \left|\mathrm{HG}_{k-s,s}\right\rangle \left\langle\mathrm{HG}_{k-s,s}\right|, \tag{2.100}$$

where $N_{\max}$ is the maximum mode order contained in the paraxial mode expansion of the optical field being considered. Using an arbitrary basis of modes $\{u_{l,q}\}$, we can write $|\Psi\rangle =$

$\sum_{l,q} c_{l,q} \left| u_{l,q} \right\rangle$, and the transformed field amplitude $\Psi'(\mathbf{r}_\perp) = \langle \mathbf{r}_\perp | \Psi' \rangle = \langle \mathbf{r}_\perp | \hat{O}_{TL} | \Psi \rangle$ is:

$$\Psi'(\mathbf{r}_\perp) = \sum_{k=0}^{N_{\max}} \sum_{s=0}^{k} e^{i(k-2s)\pi/4} \mathcal{C}_{k,s} u^{\mathrm{HG}}_{k-s,s}(\mathbf{r}_\perp), \tag{2.101}$$

with the coefficients $\mathcal{C}_{k,s}$ given by:

$$\mathcal{C}_{k,s} = \sum_{l,q} c_{l,q} \left\langle \mathrm{HG}_{k-s,s} | u_{l,q} \right\rangle . \tag{2.102}$$

The inner product $\langle \mathrm{HG}_{k-s,s} | u_{l,q} \rangle \equiv \iint (u^{\mathrm{HG}}_{k-s,s})^* u_{l,q} d^2\mathbf{r}_\perp$ can be readily computed. This gives a much more straightforward recipe to calculate the tilted lens complex field amplitude, $\Psi'(\mathbf{r}_\perp)$, and intensity profile, $I_{TL} = |\Psi'(\mathbf{r}_\perp)|^2$, near the lens focal position.

Remarkably, if the incident field is a pure HG mode, $|\Psi\rangle = |\mathrm{HG}_{m'n'}\rangle$, then $\mathcal{C}_{k,s} = \delta_{k-s,m'}\delta_{s,n'}$, and we obtain:

$$\hat{O}_{TL} \left| \mathrm{HG}_{m',n'} \right\rangle = e^{i(m'-n')\pi/4} \left| \mathrm{HG}_{m',n'} \right\rangle . \tag{2.103}$$

We then see that pure $\mathrm{HG}_{m,n}$ modes are eigenstates of the operator $\hat{O}_{TL}$ with eigenvalues $\lambda_{m,n} = e^{i(m-n)\pi/4}$, and are therefore unaffected after passing by a tilted lens. More interestingly, superpositions of HG modes carrying the same eigenvalue $\lambda_{m,n}$ (same value for $m-n$) are also eigenstates of $\hat{O}_{TL}$, and families of such invariant optical modes were studied in Ref. (BUONO et al., 2022).

## 2.3 NONLINEAR OPTICS

Nonlinear optics studies the interaction of strong light fields with matter, such that the medium response depends nonlinearly on the electric field of the incident light beam. Second harmonic generation (SHG), where two photons with frequency $\omega$ interact nonlinearly inside a crystal to create a photon with frequency $2\omega$, was the first nonlinear optical process to be experimentally demonstrated (FRANKEN et al., 1961). It was achieved using a ruby laser and a quartz crystal, only one year after the construction of the first laser by Maiman, in 1960 (MAIMAN, 1960).

Inside matter, Maxwell's macroscopic equations (JACKSON, 1999) lead to the non homogeneous wave-equation for the electric field $\mathbf{E}$ of light

$$\nabla^2\mathbf{E} - \frac{1}{c^2}\frac{\partial^2\mathbf{E}}{\partial t^2} = \mu_0\frac{\partial^2\mathbf{P}}{\partial t^2}, \tag{2.104}$$

where $\mathbf{P}$ is the macroscopic polarization vector, which describes the medium response to the incident radiation field. It can be separated in a linear part and a nonlinear part, $\mathbf{P} = \mathbf{P}_L + \mathbf{P}_{NL}$, where

$$\mathbf{P}_L = \varepsilon_0\chi^{(1)}\cdot\mathbf{E}, \tag{2.105}$$

$$\mathbf{P}_{NL} = \varepsilon_0\left(\chi^{(2)} : \mathbf{EE} + \chi^{(3)} \vdots\, \mathbf{EEE} + \cdots\right). \tag{2.106}$$

The linear susceptibility, $\chi^{(1)}$, is related to linear absorption and the variation of the index of refraction, while the multiple nonlinear susceptibilities $\chi^{(n)}$ in the expansion of $\mathbf{P}_{NL}$ are responsible for all nonlinear optical phenomena that occur in the medium. The $\chi^{(n)}$ are tensors of rank $(n+1)$ and the products of fields that go along with these quantities are tensorial products. The leading term in the nonlinear polarization, described by the second-order susceptibility $\chi^{(2)}$, is associated with a multitude of optical phenomena such as second-harmonic and sum-frequency generation, spontaneous and stimulated parametric down-conversion, and parametric oscillation. Symmetries of the medium reduce the number of independent elements of $\chi^{(n)}$ one must account for. For instance, in centrosymmetric media, such as atomic samples, all even order susceptibilities are null, $\chi^{(2n)} = 0$, and the nonlinearity of lowest order is given by the third-order susceptibility $\chi^{(3)}$. This contribution is related to effects such as self-phase modulation and four-wave mixing.

The nonhomogenous wave-equation (2.104) together with the source term given by the total medium response including contributions from Eqs. (2.105) and (2.106), is an essential part of the description of nonlinear optical phenomena in various configurations and regimes. Let us consider a general four-wave mixing (FWM) scheme, where three fields $\mathbf{E}_a$, $\mathbf{E}_b$ and $\mathbf{E}_{a'}$ with frequencies $\omega_a$, $\omega_b$ and $\omega_{a'}$, and propagation directions $\mathbf{k}_a$, $\mathbf{k}_b$ and $\mathbf{k}_{a'}$, interact with a sample of atoms – which constitutes an isotropic and centrosymmetric nonlinear medium – to generate the field $\mathbf{E}_s$. For the moment we shall not concern ourselves with polarization, and we assume that the FWM process is allowed by the selection rules imposed by the internal structure of the atoms. Due to the requirement of the conservation of energy and conservation of linear momentum in the interaction, the field $\mathbf{E}_s$ emerges with frequency $\omega_s = \omega_a + \omega_{a'} - \omega_b$, and with propagation direction $\mathbf{k}_s = \mathbf{k}_a + \mathbf{k}_{a'} - \mathbf{k}_b$. It can be shown that the scalar wave-equation for the generated field complex amplitude $E_s = \mathcal{E}_s e^{-i(\mathbf{k}_s \cdot \mathbf{r} - \omega_s t)}$ takes the form:

$$\nabla^2 E_s + k_s^2 E_s = -\frac{\omega_s^2}{c^2}\left(i\mathrm{Im}\{\chi^{(1)}(\omega_s)\}E_s + \chi^{(3)}(\omega_s)E_a E_{a'} E_b^*\right), \qquad (2.107)$$

where $k_s = \omega_s n_s / c$, and $n_s^2 = 1 + \mathrm{Re}\{\chi^{(1)}(\omega_s)\}$ is the index of refraction in the medium at frequency $\omega_s$. Here $\chi^{(1)}(\omega_s)$ and $\chi^{(3)}(\omega_s = \omega_a + \omega_{a'} - \omega_b)$ are both scalars and their detailed forms, related to the type of the atomic system considered, can be obtained by solving the adequate set of optical Bloch's equations, as we have done in Section 2.1 for a two-level system. Note that in Eq. (2.107) both terms on the right-hand side are associated with macroscopic polarization vectors with the same direction and frequency of the generated field, $\mathbf{P} \sim e^{-i(\mathbf{k}_s \cdot \mathbf{r} - \omega_s t)}$. The wave-equations that describe the evolution of the incident fields can be found in a similar form. In Ref. (BOYD et al., 1981), where the field $E_a = E_{a'}$ is the strong (or pump) field, a solution is given for the coupled evolution of the weak (or probe) field $E_b$, and the generated FWM field, $E_s$.

Let us consider the wave-equation for $E_s$ uncoupled from the equations for $E_a, E_b$, and, for the moment, plane wave-fronts for all fields. The solution in this case is well known and easily obtained. If we neglect the transverse derivatives of $\mathcal{E}_s$, we arrive at:

$$\frac{\partial \mathcal{E}_s}{\partial z} = -\alpha \mathcal{E}_s + \kappa \mathcal{E}_a \mathcal{E}_{a'} \mathcal{E}_b^* e^{-i\Delta \mathbf{k} \cdot \mathbf{r}}, \qquad (2.108)$$

where

$$\alpha = -\frac{\omega_s}{2cn_s}\mathrm{Im}\{\chi^{(1)}(\omega_s)\} \qquad (2.109)$$

is the absorption coefficient,

$$\kappa = -i\frac{\omega_s}{2cn_s}\chi^{(3)}(\omega_s) \qquad (2.110)$$

is the nonlinear coupling and, $\Delta\mathbf{k} = \mathbf{k}_a + \mathbf{k}_{a'} - \mathbf{k}_b - \mathbf{k}_s$ is the phase mismatch (see Fig. 6). Making the substitution $\tilde{\mathcal{E}}_s = \mathcal{E}_s e^{\alpha z}$, we get

**Figure 6** – (a) Spatial orientation of the wave-vectors of three fields which interact in a third-order nonlinear medium to generate a fourth field. (b) Schematic representation of the FWM process in a two-level atom evidencing the energy conservation, $\omega_a + \omega_{a'} = \omega_b + \omega_s$. (c) Wave-vector of the generated field resulting from the conservation of momentum in the interaction, and the associated phase-mismatch vector $\Delta\mathbf{k}$. In this example, $\omega_b > \omega_a > \omega_{a'}$.

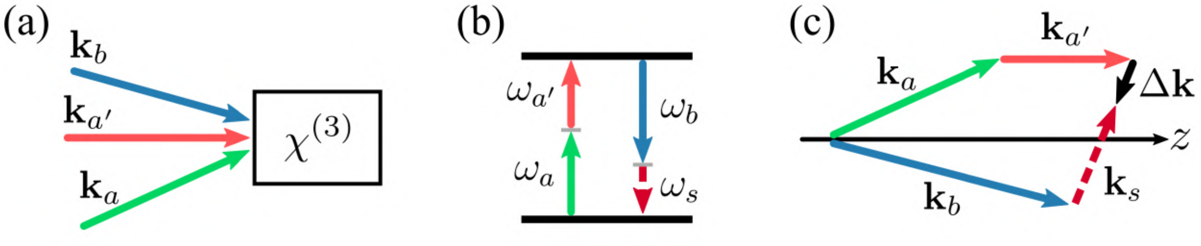

**Source:** The author (2024).

$$\frac{\partial \tilde{\mathcal{E}}_s}{\partial z} = \kappa \mathcal{E}_a \mathcal{E}_{a'} \mathcal{E}_b^* e^{\alpha z - i\Delta k z}. \tag{2.111}$$

With the initial condition $\tilde{\mathcal{E}}_s(0) = \mathcal{E}_s(0) = 0$, the solution to the FWM field $\mathcal{E}_s(z)$ is

$$\mathcal{E}_s(z) = \kappa \mathcal{E}_a \mathcal{E}_{a'} \mathcal{E}_b^* \left( \frac{e^{-i\Delta k z} - e^{-\alpha z}}{\alpha - i\Delta k} \right). \tag{2.112}$$

From this result one can infer many aspects of the nonlinear signal generation process. For example, the nonlinear signal power output is proportional to the intensities of the driving fields, and to the square of the nonlinear susceptibility $\chi^{(3)}$, and consequently to the square of the density of atoms. Also, in a medium with extension $L$, in a case where the linear absorption can be neglected (low atomic densities, or far off-resonant interaction, for example), we obtain the well-known result:

$$P_s \propto \mathrm{sinc}^2\left(\frac{\Delta k L}{2}\right), \tag{2.113}$$

which tells us that for an efficient signal generation, a small phase-mismatch is desired. For this reason, the angles between the driving laser beams are usually very small.

### 2.3.1 Four-wave mixing in a two-level atom

In this section we will obtain the third-order susceptibility $\chi^{(3)}$ associated with a degenerate FWM process in a two-level atom, by solving an appropriate form of the optical Bloch's equations. The susceptibility describes the response of the atomic medium and the resulting nonlinear signal generation. We will also discuss the role of this susceptibility when the optical fields carry non uniform spatial structures.

**Figure 7** – (a) Spatial orientation of incident and FWM fields. (b) Depiction of the parametric processes that generate signals $S_1$ and $S_2$ in a two-level atom. (c) Wave-vectors of the incident and generated fields and the phase-mismatches associated with the FWM processes.

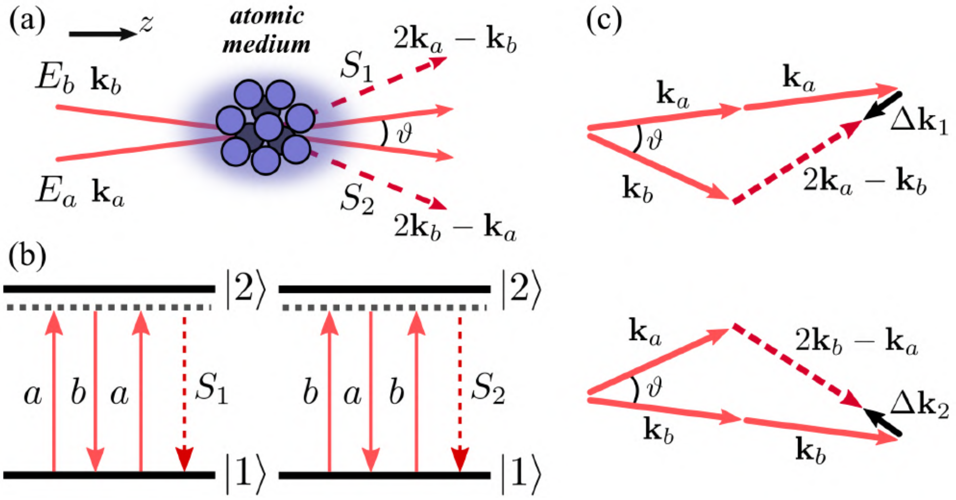

**Source:** The author (2024).

We will focus in two processes of degenerate four-wave mixing, driven by two fields, $\mathbf{E}_a$ and $\mathbf{E}_b$[3], with wave-vectors $\mathbf{k}_a$ and $\mathbf{k}_b$. The two signals, which we name $S_1$ and $S_2$ are detected in the $2\mathbf{k}_a - \mathbf{k}_b$ and $2\mathbf{k}_b - \mathbf{k}_a$ directions, as represented in Fig. 7(a). We employ the density operator formalism outlined in Section 2.1 to calculate the atomic medium response related to the nonlinear processes represented in Fig. 7(b). As before, the total Hamiltonian is $\hat{H} = \hat{H}_0 + \hat{V}$, where $\hat{H}_0$ is the free-atom Hamiltonian, and $\hat{V} = -\hat{\boldsymbol{\mu}}\cdot\mathbf{E}$ is the dipole interaction Hamiltonian. Now $\mathbf{E}$ is the total electric field, given by $\mathbf{E}(\mathbf{r},t) = \sum_\upsilon \mathbf{E}_\upsilon(\mathbf{r},t)$, $\upsilon \in \{a,b\}$,

$$\begin{aligned}\mathbf{E}_\upsilon(\mathbf{r},t) &= \frac{1}{2}\boldsymbol{\epsilon}_\upsilon \mathcal{E}_\upsilon(\mathbf{r})\, e^{-i(\mathbf{k}_\upsilon\cdot\mathbf{r}-\omega_\upsilon t)} + \text{c.c.},\\ &= \boldsymbol{\epsilon}_\upsilon E_\upsilon(\mathbf{r},t) + \text{c.c.},\end{aligned} \tag{2.114}$$

where $\mathbf{k}_\upsilon$ is the wave-vector, $\omega_\upsilon$ is the frequency, $\boldsymbol{\epsilon}_\upsilon$ is the polarization direction, the amplitudes $\mathcal{E}_\upsilon(\mathbf{r})$ satisfy the paraxial wave-equation, and $\text{c.c.}$ means the complex conjugate. We consider a quasi co-propagating configuration, where the angle $\vartheta$ between $\mathbf{k}_a$ and $\mathbf{k}_b$ [Fig. 7(a)] is very small, making $\mathbf{k}_\upsilon\cdot\mathbf{r} \simeq k_\upsilon z$, where $k_\upsilon = |\mathbf{k}_\upsilon| = \omega_\upsilon n_\upsilon/c$ and $n_\upsilon$ is the index of refraction at frequency $\omega_\upsilon$. This angle is important in the experimental configuration to allow us to separate the beams, and since we consider a degenerate setting, there will be phase mismatches inherently associated with both FWM processes, as indicated in Fig. 7(c).

The polarization directions $\boldsymbol{\epsilon}_a$ and $\boldsymbol{\epsilon}_b$ of input beams $\mathbf{E}_a$ and $\mathbf{E}_b$, respectively, determine the number of atomic states involved in the nonlinear process. We are interested in the case

---

[3] With respect to the general example treated in the previous Section, we made $\mathbf{E}_{a'} \to \mathbf{E}_a$.

where $\boldsymbol{\epsilon}_a$ and $\boldsymbol{\epsilon}_b$ are parallel circular polarizations, and therefore only two Zeeman sublevels are coupled by the external light field. Thus, the light-atom interaction can be described in terms of a two-level system, and we can use the same density operator equations obtained in Section 2.1. The difference will be the interaction Hamiltonian matrix elements, which now read

$$V_{12} = V_{21}^* = -\hbar \sum_v \Omega_v e^{-i(k_v z - \omega_v t)} + \text{c.c.}, \tag{2.115}$$

where $\Omega_v = \mu \mathcal{E}_v(\mathbf{r})/2\hbar$ is the Rabi frequency associated with field $\mathbf{E}_v$. The nonlinear interaction leads to the generation of signal $S_1$, due to the absorption of two photons from beam $\mathbf{E}_a$ and the stimulated emission of one photon from beam $\mathbf{E}_b$; and signal $S_2$, due to the absorption of two photons from $\mathbf{E}_b$ and the stimulated emission of one photon from $\mathbf{E}_a$. Figure 7(b) illustrates these processes schematically. The electric fields of the FWM fields $S_1$ and $S_2$ are $\mathbf{E}_1$ and $\mathbf{E}_2$, respectively.

We may rewrite the optical Bloch's equations (OBEs) for the two-level system as we have already encountered previously [see Section 2.1, Eqs. (2.17) and (2.18)]

$$(\Delta\dot{\rho}) = -\frac{2i}{\hbar}[\rho_{12}V_{21} - \text{c.c.}] - \Gamma\left[\Delta\rho - (\Delta\rho)^0\right], \tag{2.116}$$

$$\dot{\rho}_{12} = -\frac{i}{\hbar}\left[V_{12}\Delta\rho - \rho_{12}\left(\mathbb{E}_2 - \mathbb{E}_1\right)\right] - \frac{\Gamma}{2}\rho_{12}, \tag{2.117}$$

where $\Delta\rho = (\rho_{22} - \rho_{11})$ is the population difference and $(\Delta\rho)^0$ is the population difference far from the region of interaction with fields $\mathbf{E}_a$ and $\mathbf{E}_b$. The problem of a two-level system interacting with two strong fields has been addressed in Refs. (AGARWAL; NAYAK, 1986; FRIEDMANN; WILSON-GORDON, 1987; WILSON-GORDON; FRIEDMANN, 1988), and Eqs. (2.116) and (2.117) are solved for arbitrary pump intensities assuming that the elements of the density operator oscillate with an infinite number of frequencies. In these works, the nonlinear coherence associated with the FWM process at frequency $2\omega_a - \omega_b$ is found in terms of a recursive formula. Here, we employ a simpler solution method, similar to the treatment found in (BOYD et al., 1981), to obtain a closed expression to the relevant nonlinear coherence. To establish the validity of this approach, we will compare FWM spectra for different intensities obtained with our solution and with that of Ref. (FRIEDMANN; WILSON-GORDON, 1987; WILSON-GORDON; FRIEDMANN, 1988). Considering signal $S_1$, we assume that the coherence $\rho_{12}$ oscillates with frequencies $\omega_a$, $\omega_b$ and $2\omega_a - \omega_b$ (BOYD et al., 1981; HARTER; BOYD, 1980)

$$\rho_{12} = \sigma_{12}^a e^{i\omega_a t} + \sigma_{12}^b e^{i\omega_b t} + \sigma_{12}^{2a-b} e^{i(2\omega_a - \omega_b)t}, \tag{2.118}$$

where $\sigma_{ij}$ are the slowly varying coherences. The $2\omega_a - \omega_b$ component is responsible for the FWM process that generates the signal $S_1$. The population difference $\Delta\rho$ has a stationary component and one oscillating at $|\omega_a - \omega_b|$ (HARTER; BOYD, 1980),

$$\Delta\rho = (\Delta\rho)^{\mathrm{dc}} + \left[(\Delta\rho)^{a-b} e^{i(\omega_a - \omega_b)t} + \mathrm{c.c.}\right]. \tag{2.119}$$

We now substitute equations (2.115), (2.118) and (2.119) into Eqs. (2.116) and (2.117), perform the rotating wave approximation and collect terms that oscillate with the same frequency. Then, in the steady state regime we arrive at the set of algebraic equations for the slowly varying coherences and population differences

$$(\Delta\rho)^{a-b} = \frac{2i\widetilde{\Omega}_a^* \sigma_{12}^{2a-b} + 2i\widetilde{\Omega}_b^* \sigma_{12}^{a} - 2i\widetilde{\Omega}_a \sigma_{12}^{b*}}{(i\delta_a - i\delta_b + \Gamma)}, \tag{2.120}$$

$$(\Delta\rho)^{\mathrm{dc}} = (\Delta\rho)^0 - \frac{4}{\Gamma}(\mathrm{Im}[\Omega_a^* \sigma_{12}^a] + \mathrm{Im}[\Omega_b^* \sigma_{12}^b]), \tag{2.121}$$

$$\sigma_{12}^a = \frac{i\widetilde{\Omega}_a (\Delta\rho)^{\mathrm{dc}} + i\widetilde{\Omega}_b (\Delta\rho)^{a-b}}{(i\delta_a + \Gamma/2)}, \tag{2.122}$$

$$\sigma_{12}^b = \frac{i\widetilde{\Omega}_b (\Delta\rho)^{\mathrm{dc}} + i\widetilde{\Omega}_a \left[(\Delta\rho)^{a-b}\right]^*}{(i\delta_b + \Gamma/2)}, \tag{2.123}$$

$$\sigma_{12}^{2a-b} = \frac{i\widetilde{\Omega}_a (\Delta\rho)^{a-b}}{(2i\delta_a - i\delta_b + \Gamma/2)}. \tag{2.124}$$

One could add to Eq. (2.118) the coherence $\rho_{12}^{2b-a} = \sigma_{12}^{2b-a} e^{i(2\omega_b - \omega_a)t}$, related to the FWM process at frequency $2\omega_b - \omega_a$. This would lead to an additional equation for the slow coherence $\sigma_{12}^{2b-a}$, and Eq. (2.120), for the population difference $(\Delta\rho)^{a-b}$, would be modified. However, terms which would appear in our final solution due to these changes are related to higher-order nonlinear processes in the direction $2\mathbf{k}_a - \mathbf{k}_b$, and we do not keep them. In other words, we assume that we can solve for the coherences related to the two nonlinear processes separately.

Defining $\widetilde{\Omega}_v \equiv \Omega_v e^{-ik_v z}$, $\delta_v \equiv \omega_v - \omega_o$ as the detuning from resonance of field $\Omega_v$ and $\omega_o \equiv (\mathbb{E}_2 - \mathbb{E}_1)/\hbar$ as the resonance frequency, with a direct substitution method we obtain for the coherence $\sigma_{12}^{2a-b}$, related to the generation of signal $S_1$,

$$\sigma_{12}^{2a-b} = \frac{-2i\widetilde{\Omega}_a^2 \widetilde{\Omega}_b^* (\Delta\rho)^{\mathrm{dc}} (1/\Delta_a + 1/\Delta_b)}{(\Delta_a + \Delta_b)(2i\delta_a - i\delta_b + \Gamma/2) + 2|\Omega_a|^2}, \tag{2.125}$$

where $\Delta_a = i\delta_a + \Gamma/2$, $\Delta_b = -i\delta_b + \Gamma/2$ and

$$(\Delta\rho)^{\mathrm{dc}} = \frac{(\Delta\rho)^0}{1 + \dfrac{2|\Omega_a|^2}{\delta_a^2 + \Gamma^2/4} + \dfrac{2|\Omega_b|^2}{\delta_b^2 + \Gamma^2/4}}. \tag{2.126}$$

A similar result is found for the coherence $\sigma_{12}^{2b-a}$, related to the generation of signal $S_2$ in the direction $(2\mathbf{k}_b - \mathbf{k}_a)$. In fact, under the approximations considered, $\sigma_{12}^{2b-a}$ has the same form as $\sigma_{12}^{2a-b}$ with the exchange of labels $a \leftrightarrow b$. For Rabi frequencies up to $\Omega_{a,b} = \Gamma$, the FWM spectra calculated with the coherence given by Eq. (2.125) are in good agreement with the more general solution for a two-level system driven by two strong pumps. This is evidenced in Fig. 8, which shows the spectra contained in Fig. 4 of Ref. (WILSON-GORDON; FRIEDMANN, 1988) calculated with the recursive formula and with Eq. (2.125). For Rabi frequencies up to $\Omega = \Gamma$, the FWM spectra calculated by the two methods are similar. For $\Omega = 4\Gamma$, we can see that the correspondence is not so good and that our solution does not reproduce the finer details in the spectrum. For the higher Rabi frequency, $\Omega = 7\Gamma$, the two solutions differ considerably. In light of these results, we believe that our solution is suitable for lower intensities, at least until $\Omega = \Gamma$. For higher intensities, higher-order processes must be taken into account, and a different solution becomes necessary.

**Figure 8** – Normalized FWM spectra calculated using the solution to the nonlinear coherence given in (WILSON-GORDON; FRIEDMANN, 1988) (blue line) and the one obtained with Eq. (2.125) (red dashed line) for different Rabi frequencies. In all graphs $\delta_a = -10\Gamma = -20/T_2$ ($T_2 = 2/\Gamma$), $\Omega_a = \Omega_b$ and $\delta = \delta_b - \delta_a$. Also, $V_1 = \Omega_a$ and $V_2 = \Omega_b$.

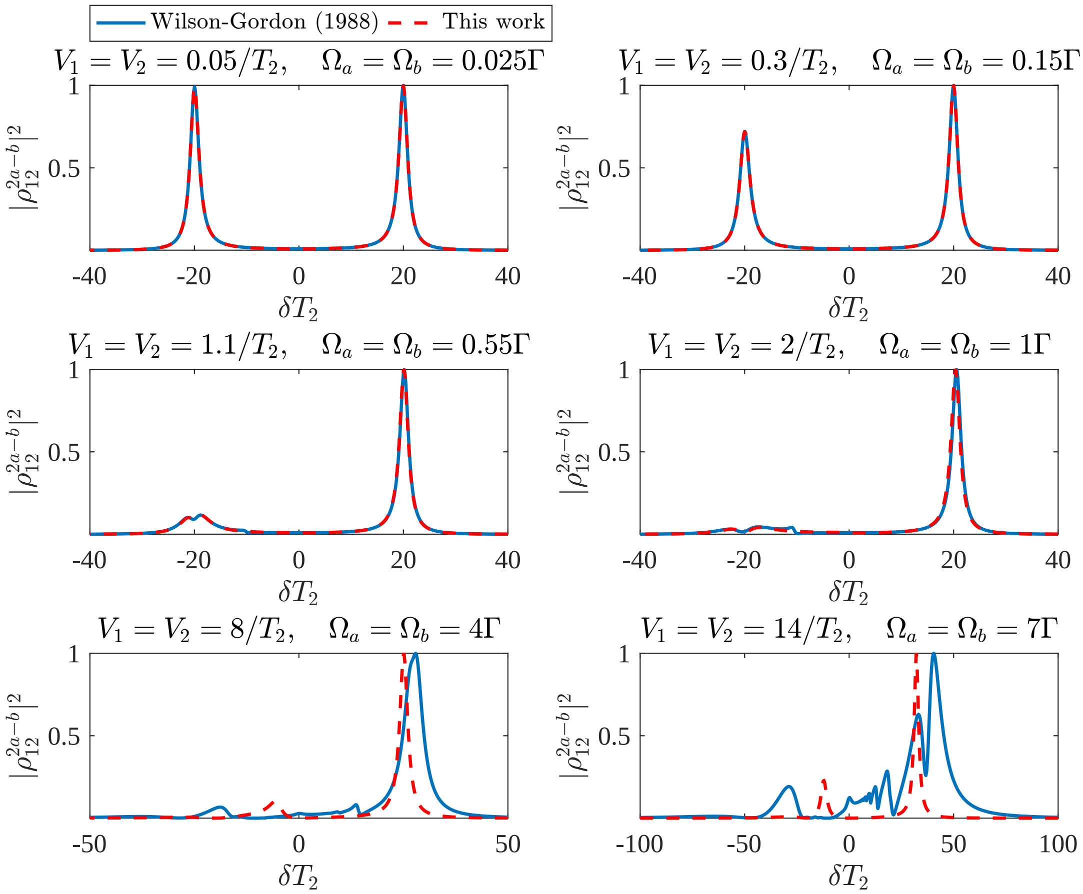

**Source:** The author (2024).

We rewrite the coherence given by Eqs. (2.125) as

$$\sigma_{12}^{2a-b} = X^{2a-b}\widetilde{\Omega}_a^2\widetilde{\Omega}_b^*, \tag{2.127}$$

where $X^{2a-b}$, is the coupling associated with the processes in directions $(2\mathbf{k}_a - \mathbf{k}_b)$, and it carries the spectral response of the medium. This coupling factor also depends on the field amplitudes $|\Omega_{a,b}|^2$, and thus the corresponding susceptibilities contain information about power broadening and saturation effects. We define the effective susceptibility

$$\begin{aligned}\chi^{2a-b} &= \frac{\mathcal{N}|\mu_{12}|^4}{\varepsilon_0\hbar^3}X^{2a-b}, \\ &= \frac{-2i\mathcal{N}|\mu_{12}|^4(\Delta\rho)^{\mathrm{dc}}(1/\Delta_a + 1/\Delta_b)/\varepsilon_0\hbar^3}{(\Delta_a+\Delta_b)\left(2i\delta_a - i\delta_b + \Gamma/2\right) + 2|\Omega_a|^2},\end{aligned} \tag{2.128}$$

where $\mathcal{N}$ is the atomic density. Our investigations were conducted in two types of atomic systems: cold atoms and hot atomic vapors. When working with cold atom samples, where the atoms can be considered stationary, we do not need to include the effect of Doppler broadening. However, in order to accurately describe phenomena that occur in hot vapors, rigorously one needs to account for the contributions of the multiple velocity groups. This is paramount when dealing, for example, with the spectral response of the system, but, as we hope to become clear throughout this work, when the focus lies in the spatial degrees of freedom of the light field, the effects associated with the atomic coherence built inside the medium can – to some extent – be looked-over.

### 2.3.2 Structured FWM field

In this Section we establish the common ground for most of our results: the solution to the non homogeneous wave-equation describing the generation of the FWM field $\mathbf{E}_s$, with the source term determined by the macroscopic polarization $\mathbf{P}$, taking fully into account the non-trivial spatial structures of the participating light beams. Once again, we start with the Maxwell's wave-equation (JACKSON, 1999):

$$\nabla^2\mathbf{E}_s - \frac{1}{c^2}\frac{\partial^2\mathbf{E}_s}{\partial t^2} = \mu_o\frac{\partial^2\mathbf{P}}{\partial t^2}, \tag{2.129}$$

where $\mathbf{E}_s$ is written as in Eq. (2.114). What changes here is the fact that we cannot neglect the transverse derivative terms. We will focus on signal $S_1$, since the equations for $S_2$ are obtained and solved in the same way. The nonlinear macroscopic polarization $\mathbf{P}$ can be divided in two components: $\mathbf{P}_{2a-b}$, which describes the generation process of the FWM field $\mathbf{E}_s$; and $\mathbf{P}_{ab}$, associated with the propagation of the generated field inside the medium affected by the strong fields $\mathbf{E}_a$ and $\mathbf{E}_b$. We can write the total polarization as $\mathbf{P} = \mathbf{P}_{ab} + \mathbf{P}_{2a-b}$, and its projection onto the oscillation direction of the generated field is

$$(\mathbf{P} \cdot \boldsymbol{\epsilon}_s^*) = \varepsilon_0 \chi^{ab} E_s + \varepsilon_0 \chi^{2a-b} E_a^2 E_b^*, \tag{2.130}$$

where the amplitudes are $E_i(\mathbf{r}, t) = \mathcal{E}_i(\mathbf{r}) e^{-i(k_i z - \omega_i t)}$. It is possible to carry the calculations further with both terms in Eq. (2.130), but for simplicity, in what follows and throughout the rest of this work, we neglect the first term on the right-hand side. We justify this approximation based on the thin-medium assumption, such that effects associated with the propagation of the generated field inside the sample are negligible. This seems reasonable in a cold atom cloud, but in the case of a heated Rb vapor system, one may argue that effects such as the absorption of the FWM field should not be neglected. This is certainly true when we look at the spectral degrees of freedom, for example. In any case, we shall assume that the linear term in $E_s$ does not significantly affect the spatial degrees of freedom of the generated light field. Under the rotating wave and paraxial approximations, we obtain

$$\left( \frac{i}{2k_s} \nabla_\perp^2 + \frac{\partial}{\partial z} \right) \mathcal{E}_s = \kappa u_a^2 u_b^* e^{-i\Delta k z}, \tag{2.131}$$

where $u_a(\mathbf{r})$ and $u_b(\mathbf{r})$ are mode functions normalized to unity giving the spatial distributions of the incident fields, such that $\Omega_{a,b}(\mathbf{r}) = \Omega_{a,b}^0 u_{a,b}(\mathbf{r})$, $\nabla_\perp^2$ is the transverse Laplacian, the phase mismatch can be written as (see Fig. 7):

$$\begin{aligned} \Delta k &= |2\mathbf{k}_a - \mathbf{k}_b - \mathbf{k}_s|, \\ &\simeq (2k_a - k_b) \cos \frac{\vartheta}{2} - k_s \cos \frac{3\vartheta}{2}, \end{aligned} \tag{2.132}$$

and $\kappa$ is the nonlinear coupling, given by

$$\kappa(\mathbf{r}; \delta) = -i \frac{\omega_s \hbar^3 \Omega^0}{2c\mu_{12} |\mu_{12}|^2} \chi^{2a-b}(\mathbf{r}; \delta), \tag{2.133}$$

with $\Omega^0 = (\Omega_a^0)^2 (\Omega_b^0)^*$. In Eq. (2.133), $\delta$ represents $\delta_a$ and $\delta_b$. We highlight that the dependence of the nonlinear coupling $\kappa$ with the position comes from the dependence of the input field contributing with the square of the field amplitude [see the denominator in Eqs. (2.125),(2.128)]. But there is an additional, implicit, dependence of $\kappa$ with the $z$ coordinate: it exists only inside the interaction region, between $z = -L/2$ and $z = L/2$, and is zero everywhere else in the $z$-axis. Thus, Eq. (2.131) describes the nonlinear signal generation process inside the sample. There is no nonlinear signal at positions $z \leq -L/2$, and so the boundary condition is $\mathcal{E}_s(\mathbf{r}_\perp, -L/2) = 0$. For $z > L/2$, where the generated beam propagates in free space, $\mathcal{E}_s$ must satisfy the homogeneous paraxial wave-equation, $(i\nabla_\perp^2/2k_s + \partial/\partial z)\mathcal{E}_s = 0$, with the boundary condition given by the solution of Eq. (2.131) at $z = L/2$, $\mathcal{E}_s(\mathbf{r}_\perp, L/2)$.

We write the generated field amplitude $\mathcal{E}_s$ as the superposition of paraxial modes:

$$\mathcal{E}_s(\mathbf{r}) = \sum_{m,n} \mathcal{A}_{m,n}(z) u_{m,n}(\mathbf{r}). \tag{2.134}$$

The specific basis of modes $\{u_{m,n}\}$ shall be chosen according to the specific situation considered. For example, when working with light beams that present cylindrical symmetry, or OAM carrying beams, a convenient choice is the LG basis. In any case, the problem becomes that of finding the set of relevant coefficients $\{\mathcal{A}_{m,n}\}$. Substituting Eq. (2.134) into Eq. (2.131) and employing the orthogonality relation of $u_{m,n}$ [Eq. (2.51)], we obtain an equation for $\mathcal{A}_{m,n}(z)$.

$$\frac{\partial \mathcal{A}_{m,n}(z)}{\partial z} = \Lambda_{m,n}(z) e^{-i\Delta k z}, \tag{2.135}$$

where

$$\Lambda_{m,n}(z) = \iint \kappa(\mathbf{r}; \delta) u_a^2 u_b^* u_{m,n}^* d^2\mathbf{r}_\perp, \tag{2.136}$$

is the projection of the spatially dependent nonlinear source term onto the chosen paraxial basis, called the transverse overlap integral. It is important to note that the position dependence of $\kappa$ couples the spatial and spectral degrees of freedom. In all cases we consider, Eq. (2.136) is calculated assuming parallel transverse planes for all beams, which is reasonable for small angles $\vartheta$ (LANNING et al., 2017). We then integrate Eq. (2.135) on the longitudinal coordinate to find the FWM field expansion coefficients as

$$\mathcal{A}_{m,n}(z) = \int_{-L/2}^{z_<} \Lambda_{m,n}(z') e^{-i\Delta k z'} dz', \tag{2.137}$$

where $z_< = \min[z, L/2]$. Equation (2.137) is called the full spatial overlap, which encompasses all of the dynamics of the spatial degrees of freedom under the nonlinear interaction. This solution is suitable for both regions of space: $-L/2 < z \leq L/2$ and $z > L/2$. We are most interested in the FWM beam outside the medium, where it can be detected, and thus seek to evaluate $\mathcal{A}_{m,n}(L/2)$.

This is a good moment to stop and discuss the role of the spatially dependent nonlinear coupling $\kappa$ inside the integral in Eq. (2.136). In a recent work, considering a degenerate FWM process driven by Gaussian beams in a thin sample of cold atoms (MOTTA; ALMEIDA;

VIANNA, 2022), we showed that by taking fully into account this position dependency, effects of the structured atomic coherence on the FWM field structure arise. The first one is that the total power of incident beams affects the transverse distribution and propagation of the FWM signals, and the second is the influence of the spectral characteristics of the medium on the longitudinal profile (measured by the so-called root mean square quantities (VALLONE et al., 2016)) of both generated signals upon free propagation. We argue that the first effect can be seen as a saturation of the medium in regions of higher intensity, while the second can be understood as the result of a nonlinear contribution to the refractive index inside the atomic sample. They can be symmetric between the two signals, with asymmetries induced by different detunings from resonance of the incident fields. Also, when the driving beams carry optical vortices, the transverse phase distributions of the FWM fields are twisted when the detunings vary around resonance, and the phase discontinuities inherent to vortex beams are the features that reveal this twisting effect (HAMEDI; RUSECKAS; JUZELIŪNAS, 2018; MALLICK; DEY, 2020; YU; WANG, 2021; ZHOU; WANG, 2023). However, these effects manifest most strongly near the atomic resonance and for higher intensities. For lower Rabi frequencies (below $\Gamma$), the contribution of the structured coupling $\kappa$ in Eq. (2.136) becomes less relevant. We may therefore rewrite the transverse overlap, given by Eq. (2.136), as:

$$\Lambda_{m,n}(z) \simeq \overline{\kappa}(\delta) \iint u_a^2 u_b^* u_{m,n}^* d^2\mathbf{r}_\perp, \tag{2.138}$$

where $\overline{\kappa}$ is an effective nonlinear coupling. With this, we have decoupled the spatial and spectral degrees of freedom. Also, since $\overline{\kappa}$ is a common factor to all the coefficients $\mathcal{A}_{m,n}$, we don't need to carry it further. Under these assumptions, the overlap integral, and consequently the FWM mode superposition, are determined solely by the product of incident fields $u_a^2 u_b^*$ (for $S_1$). Indeed, this is usually assumed in the description of nonlinear processes involving beams with arbitrary transverse structures. In many references that focus on second-order nonlinearities (parametric oscillation, second-harmonic generation, sum-frequency generation) (SCHWOB et al., 1998; PEREIRA et al., 2017; ALVES et al., 2018; BUONO et al., 2020), and in those that treat FWM (WALKER; ARNOLD; FRANKE-ARNOLD, 2012; OFFER et al., 2018; OFFER et al., 2021; ROCHA et al., 2022), the relevant mode weights are overlap integrals of three ($\chi^{(2)}$) and four ($\chi^{(3)}$) paraxial modes.

The characteristic length of $\Lambda_{m,n}(z)$ is given by the Rayleigh ranges of the beams that participate in the FWM process, $z_R$. Most of the results presented in this thesis focus on a thin-medium regime, characterized by a medium extension much smaller than the Rayleigh

**Figure 9** – Normalized conversion efficiency factor $|T|^2$ as a function of the separation angle $\vartheta$. The medium extension is $L = 3\,\mathrm{mm}$.

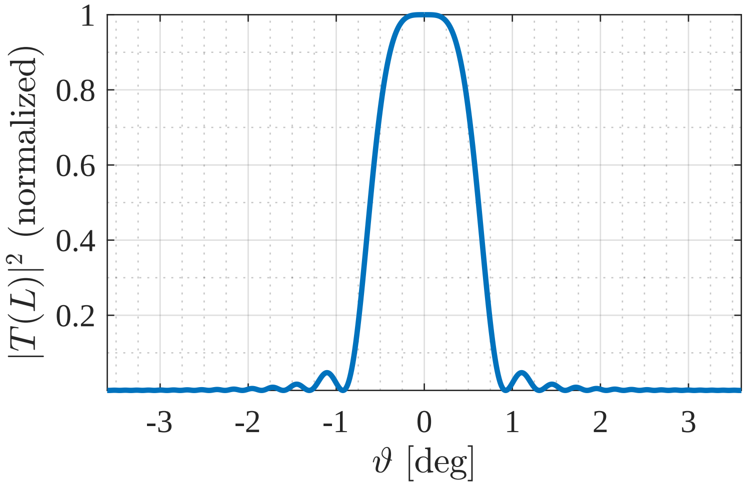

**Source:** The author (2024).

range of the participating optical fields, $L \ll z_R$. In this case, we can neglect the variation of $\Lambda_{m,n}(z)$ inside the interaction region and take its value at $z = 0$. This allows to remove the transverse overlap from the $z$ integral in Eq. (2.137) and write the approximate form

$$\begin{aligned} \mathcal{A}_{m,n}(L/2) &\simeq \Lambda_{m,n}(0) \int_{-L/2}^{L/2} e^{-i\Delta k z'} dz', \\ &= \Lambda_{m,n}(0) T(L), \end{aligned} \tag{2.139}$$

where

$$\begin{aligned} T(L) &= \frac{\sin(\Delta k L/2)}{\Delta k/2}, \\ &= L \,\mathrm{sinc}\left(\frac{\Delta k L}{2}\right), \end{aligned} \tag{2.140}$$

can be regarded as an efficiency measure of the signal generation process inside the medium. It takes into account the phase-mismatch and is a common factor to all $\mathcal{A}_{m,n}$. It can be used to estimate the range of values of the angle $\vartheta$ for which one may expect to have a good conversion efficiency. As an example, we show in Fig. 9 a plot of $|T|^2$ as a function of $\vartheta$, using $\Delta k$ given in Eq. (2.132). It can be seen that even for $\vartheta < 1^\circ$, there is already a sensible decrease in efficiency.

With this, we see that in the thin-medium regime, all the information of the nonlinear wave mixing process is contained in the transverse overlap integral evaluated at $z = 0$, $\Lambda_{m,n}(0)$, and most of the intuition of the transverse phenomena can be built upon the physical overlap of the incident beams. In contrast, in an extended-medium regime, characterized by a ratio $L/z_R \gg 1$, the matching of the Gouy phases of the participating fields across the medium extension plays an important role (WALKER; ARNOLD; FRANKE-ARNOLD, 2012; OFFER et al., 2021; ROCHA et al., 2022). In this case, the factorization performed in Eq. (2.139) is not applicable, and the longitudinal integral is performed including the $z$ dependence of the transverse overlap $\Lambda(z)$. As we will see in upcoming sections, this condition results in a selection rule for the mode structure transfer that involves the total mode order. These are two extreme configurations, with distinct predicted outputs, both qualitatively and quantitatively. The thin-medium regime is more easily accessible in the experiment, and we shall comment on the difficulties associated with the achievability of an extended-medium regime in the next Chapter.

### 2.3.3 The LG overlap integral

We now specialize to the LG basis, and obtain an analytical expression for the full overlap integral in a phase-matched setting, $\Delta k = 0$. Here we consider a more general situation where we have three possibly independent incident fields: the fields $u_a, u_b$, and also the field $u_{a'}$, written as

$$u_a = \sum_{l,q} \alpha_{l,q} u_{l,q}, \tag{2.141}$$

$$u_{a'} = \sum_{l',q'} \beta_{l',q'} u_{l',q'}, \tag{2.142}$$

$$u_b = \sum_{m,n} \gamma_{m,n} u_{m,n}. \tag{2.143}$$

Consider the FWM process induced by the absorption of one photon from field $a$, one photon from field $a'$, and the stimulated emission of a photon from field $b$[4]. The transverse overlap integral in this case is:

$$\Lambda_p^{\ell}(z) = \iint u_a u_{a'} u_b^* u_{\ell,p}^* d^2\mathbf{r}_\perp, \tag{2.144}$$

$$= \sum_{l,q} \sum_{l',q'} \sum_{m,n} K_{qq'n}^{ll'm} \Lambda_{qq'np}^{ll'm\ell}(z), \tag{2.145}$$

where $K_{qq'n}^{ll'm} = \alpha_{l,q}\beta_{l',q'}\gamma_{m,n}^*$, and the transverse overlap with additional indices is:

$$\Lambda_{qq'np}^{ll'm\ell}(z) = \iint u_{l,q} u_{l',q'} u_{m,n}^* u_{\ell,p}^* d^2\mathbf{r}_\perp. \tag{2.146}$$

---

[4] Evidently, to treat signal $S_1$, we simply make $u_{a'} \to u_a$.

The full spatial overlap is thus

$$\mathcal{A}^{\ell}_{p} = \sum K^{ll'm}_{qq'n} \mathcal{A}^{ll'm\ell}_{qq'np}, \tag{2.147}$$

where the sum is performed over all repeated indices, and

$$\mathcal{A}^{ll'm\ell}_{qq'np} = \int_{-L/2}^{L/2} \Lambda^{ll'm\ell}_{qq'np}(z) dz. \tag{2.148}$$

To calculate $\mathcal{A}^{ll'm\ell}_{qq'np}$, we consider that all modes $u$ inside the integral have the same Rayleigh range $z_R$. This assumption is referred to as the Boyd criterion, and it maximizes the conversion efficiency (BOYD; KLEINMAN, 1968). As will become evident, it also greatly simplifies our calculations. In general the light fields that participate in the FWM process possess different wavelengths, $\lambda_j$. Thus, to match their Rayleigh ranges, they must possess different waists $w_{0,j}$. We write

$$\begin{aligned}
\mathcal{A}^{ll'm\ell}_{qq'np} = \mathcal{C}^{ll'm\ell}_{qq'np} \int_{\mathbb{V}} & \frac{1}{w_a w_{a'} w_b w_s} \frac{(\sqrt{2}r)^{|l|+|l'|+|m|+|\ell|}}{w_a^{|l|} w_{a'}^{|l'|} w_b^{|m|} w_s^{|\ell|}} \\
& \times L_q^{|l|}\left(\frac{2r^2}{w_a^2}\right) L_{q'}^{|l'|}\left(\frac{2r^2}{w_{a'}^2}\right) L_n^{|m|}\left(\frac{2r^2}{w_b^2}\right) L_p^{|\ell|}\left(\frac{2r^2}{w_s^2}\right) \\
& \times e^{-i(l+l'-m-\ell)\phi} e^{-r^2(1/w_a^2+1/w_{a'}^2+1/w_b^2+1/w_s^2)} \\
& \times \exp\left[i\Delta\Psi(z) - i\delta\Phi_{\mathrm{C}}(r,z)\right] d^3\mathbf{r},
\end{aligned} \tag{2.149}$$

where $\mathbb{V}$ is the interaction volume, $\mathcal{C}^{ll'm\ell}_{qq'np} = C_{l,q} C_{l',q'} C_{m,n} C_{\ell,p}$ is the product of LG normalization constants, $w_j = w_j(z) = w_{0,j}\sqrt{1+(z/z_R)^2}$, the waists are $w_{0,j} = \sqrt{2z_R/k_j} = \sqrt{\lambda_j z_R / n_j \pi}$, with $n_j$ the index of refraction at frequency $\omega_j$,

$$\Delta\Psi(z) = -2Q\tan^{-1}(z/z_R), \tag{2.150}$$

is the difference between the Gouy phases, with the factor $Q$ defined as:

$$Q \equiv \frac{1}{2}(N_{\ell,p} + N_{m,n} - N_{l,q} - N_{l',q'}), \tag{2.151}$$

and

$$\begin{aligned}
\delta\Phi_{\mathrm{C}}(r,z) &= \frac{r^2}{2R(z)}(k_a + k_{a'} - k_b - k_s), \\
&= \frac{\pi r^2}{R(z)}\left(\frac{1}{\lambda_a} + \frac{1}{\lambda_{a'}} - \frac{1}{\lambda_b} - \frac{1}{\lambda_s}\right)
\end{aligned} \tag{2.152}$$

is the difference between the phases related to curvature. Note that the expression (2.152) is only valid because we considered the Boyd criterion. Otherwise, we would have different radii of curvature $R_j(z)$ multiplying each $\lambda_j$ on the denominators inside the parentheses. In the following lines, it will become apparent how this condition simplifies the evaluation of the overlap integral. We also considered that the index of refraction at all frequencies is approximately unity, $n_j \approx 1$. Due to the energy conservation in the nonlinear process, we must have

$$\frac{1}{\lambda_a} + \frac{1}{\lambda_{a'}} = \frac{1}{\lambda_b} + \frac{1}{\lambda_s}, \tag{2.153}$$

and thus $\delta\Phi_{\mathrm{C}}(r,z) = 0$. If we had considered different Rayleigh ranges, this would in general not be satisfied, and we would have to account for a phase factor that couples the integrals in the transverse plane and in $z$. Moreover, $\delta\Phi_{\mathrm{C}}(r,z) \sim k_j$, which are large numbers. A small imbalance in equation (2.152) makes the phase factor $\exp\left(-i\delta\Phi_{\mathrm{C}}(r,z)\right)$ a highly oscillating function of the coordinates $r$ and $z$. Thus, the presence of such a term would lead to a reduced magnitude of $\mathcal{A}^{ll'm\ell}_{qq'np}$ or, in other words, reduced conversion efficiency. Also, equation (2.153) implies

$$\frac{1}{w_{0,a}^2} + \frac{1}{w_{0,a'}^2} = \frac{1}{w_{0,b}^2} + \frac{1}{w_{0,s}^2}, \tag{2.154}$$

which is allowed since we have not yet defined the waist of the modes in the superposition $\mathcal{E}_s$. Defining $W(z) = w_0\sqrt{1+(z/z_R)^2}$, where the waist $w_0$ is a reference beam waist, that we control, $\lambda_0$ as a reference wavelength, associated with $w_0$, the ratios $\xi_j = W(z)/w_j(z) = w_0/w_{0,j} = \sqrt{\lambda_0/\lambda_j}$ and $\rho(r,z) = \sqrt{2}r/W(z)$, the full overlap integral becomes:

$$\begin{aligned}
\mathcal{A}^{ll'm\ell}_{qq'np} = {} & \frac{\mathcal{C}^{ll'm\ell}_{qq'np}}{2w_0^2}\xi_a^{|l|+1}\xi_{a'}^{|l'|+1}\xi_b^{|m|+1}\xi_s^{|\ell|+1} \\
& \times \int_0^\infty \rho^{|l|+|l'|+|m|+|\ell|} L_q^{|l|}(\xi_a^2\rho^2) L_{q'}^{|l'|}(\xi_{a'}^2\rho^2) L_n^{|m|}(\xi_b^2\rho^2) L_p^{|\ell|}(\xi_s^2\rho^2) e^{-\rho^2(\xi_a^2+\xi_{a'}^2)}\rho d\rho \\
& \times \int_0^{2\pi} e^{-i(l+l'-m-\ell)\phi} d\phi \\
& \times \int_{-L/2}^{L/2} \frac{e^{-i2Q\tan^{-1}(z/z_R)}}{1+(z/z_R)^2} dz.
\end{aligned} \tag{2.155}$$

### 2.3.3.1 *Conservation of orbital angular momentum*

The first selection rule that arises is the topological charge selection rule, imposed by the azimuthal integral:

$$\int_0^{2\pi} e^{-i(l+l'-m-\ell)\phi} d\phi = 2\pi\delta_{\ell,l+l'-m}. \tag{2.156}$$

Thus, the only LG modes that can be generated are those that satisfy

$$\ell = l + l' - m. \tag{2.157}$$

This is a statement of the conservation of OAM in the FWM process and always holds. Note that Eq. (2.157) ensures that $Q$ is an integer. We can then write

$$\mathcal{A}_{qq'np}^{ll'm\ell} = \frac{\pi}{w_0^2}\mathcal{C}_{qq'np}^{ll'm\ell}\,\xi_a^{|l|+1}\xi_{a'}^{|l'|+1}\xi_b^{|m|+1}\xi_s^{|\ell|+1}\delta_{\ell,l+l'-m}\mathcal{R}_{qq'np}^{ll'm\ell}\mathcal{I}_Q(L), \tag{2.158}$$

where $\mathcal{R}_{qq'np}^{ll'm\ell}$ and $\mathcal{I}_Q(L)$ are the radial and longitudinal integrals, respectively.

#### 2.3.3.2 Radial integral

Using the series expansion of the associated Laguerre polynomials $L_p^{|\ell|}(x) = \sum_{k=0}^{p} c_k^{p|\ell|}x^k$, with coefficients given by $c_k^{p|\ell|} = \frac{(-1)^k}{k!}\frac{(p+|\ell|)!}{(|\ell|+k)!\,(p-k)!}$, we get

$$\begin{aligned}\mathcal{R}_{qq'np}^{ll'm\ell} = &\sum_{k_1,k_2}^{q,q'}\sum_{k_3,k_4}^{n,p} c_{k_1}^{q|l|}c_{k_2}^{q'|l'|}c_{k_3}^{n|m|}c_{k_4}^{p|\ell|}\xi_a^{2k_1}\xi_{a'}^{2k_2}\xi_b^{2k_3}\xi_s^{2k_4}\\ &\times\int_0^\infty \rho^{|l|+|l'|+|m|+|\ell|+2(k_1+k_2+k_3+k_4)}e^{-\rho^2(\xi_a^2+\xi_{a'}^2)}\rho d\rho.\end{aligned} \tag{2.159}$$

This leads to the general expression in terms of finite sums

$$\mathcal{R}_{qq'np}^{ll'm\ell} = \frac{1}{2(\xi_a^2+\xi_{a'}^2)}\sum_{k_1,k_2}^{q,q'}\sum_{k_3,k_4}^{n,p} c_{k_1}^{q|l|}c_{k_2}^{q'|l'|}c_{k_3}^{n|m|}c_{k_4}^{p|\ell|}\frac{\xi_a^{2k_1}\xi_{a'}^{2k_2}\xi_b^{2k_3}\xi_s^{2k_4}}{(\xi_a^2+\xi_{a'}^2)^G}\Gamma(G+1), \tag{2.160}$$

where $\Gamma(\cdot)$ is the Gamma function and $G = (|l|+|l'|+|m|+|\ell|)/2+k_1+k_2+k_3+k_4$. In the case of degenerate FWM, all wavelengths $\lambda_j$ are equal to $\lambda_0$, making all waists $w_{0,j}$ also equal to $w_0$, and with this, $\xi_j \to 1,\ \forall j$, and we get:

$$\mathcal{R}_{qq'np}^{ll'm\ell} = \frac{1}{2}\sum_{k_1,k_2}^{q,q'}\sum_{k_3,k_4}^{n,p} c_{k_1}^{q|l|}c_{k_2}^{q'|l'|}c_{k_3}^{n|m|}c_{k_4}^{p|\ell|}2^{-G}\Gamma(G+1), \tag{2.161}$$

In upcoming sections we will look at particular cases where the radial integral can be evaluated to give a closed form expression.

#### 2.3.3.3 Longitudinal integral and Gouy phase-matching

The second selection rule comes from the longitudinal integral, $\mathcal{I}_Q(L)$, when the extended-medium condition is fulfilled, i.e., $L/z_R \gg 1$. It is related to the matching of the Gouy phases of the various modes inside the overlap integral and does not depend on the type of system considered, if it is a degenerate or a non-degenerate configuration. It is also independent of the chosen paraxial basis. The longitudinal integral is:

$$\begin{aligned}\mathcal{I}_Q(L) &= \int_{-L/2}^{L/2} \frac{e^{-i2Q\tan^{-1}(z/z_R)}}{1+(z/z_R)^2}dz,\\ &= \int_{-L/2}^{L/2} \frac{1}{1+(z/z_R)^2}\left(\frac{1-iz/z_R}{1+iz/z_R}\right)^Q dz,\\ &= \int_{-L/2}^{L/2} f_Q(z)dz. \end{aligned} \tag{2.162}$$

It is easy to show that for integer $Q$, the imaginary part of $f_Q(z)$ is an odd function of $z$, and therefore $\mathcal{I}_Q \in \mathbb{R}$ for $Q \in \mathbb{Z}$. The integral can be solved to find:

$$\mathcal{I}_Q(L) = \begin{cases} 2z_R\tan^{-1}(L/2z_R) & , \quad Q=0,\\ \dfrac{iz_R}{2Q}\left(g_L^Q - g_L^{-Q}\right) & , \quad Q\neq 0, \end{cases} \tag{2.163}$$

where $g_L = (i+L/2z_R)(i-L/2z_R)^{-1}$. In the extended medium limit, $L/z_R \to \infty$, we obtain

$$\mathcal{I}_Q \underset{L/z_R\to\infty}{\longrightarrow} \begin{cases} \pi z_R & , \; Q=0,\\ 0 & , \; Q\neq 0. \end{cases} \tag{2.164}$$

We conclude that the only modes that survive the wave mixing process in an extended medium are those that satisfy $Q=0$, or equivalently:

$$N_{\ell,p} + N_{m,n} = N_{l,q} + N_{l',q'}, \tag{2.165}$$

which is the Gouy phase-matching (GPM) condition (WALKER; ARNOLD; FRANKE-ARNOLD, 2012; CHOPINAUD et al., 2018; OFFER et al., 2021; ROCHA et al., 2022). We can also express this requirement as:

$$2p + |\ell| = 2(q+q'-n) + (|l| + |l'| - |m|). \tag{2.166}$$

This selection rule restricts the output radial spectrum, and further reduces the number of modes we need to account for. Most importantly, it involves both indices $\ell$ and $p$, introducing a controlled coupling between the angular and radial degrees of freedom that cannot be achieved in a thin medium. It is interesting to note that the GPM condition does not depend on the chosen basis of paraxial modes, neither on the type of process (degenerate or non-degenerate). In Fig. 10 we show the behavior of $\mathcal{I}_Q(L)$ for different values of $Q$.

Experimentally, the restrictions imposed by the GPM condition were verified in situations where the medium length was $\sim 10$ times the Rayleigh range (OFFER et al., 2018; OFFER et al., 2021). In these references, the FWM configuration was that of amplified spontaneous emission, generating blue light.

**Figure 10** – Longitudinal integral $\mathcal{I}_Q(L)$ over the medium extension $L$ for different values of $Q$. For an extended medium, $L/z_R \gg 1$, $\mathcal{I}_0(L) \to \pi z_R$, and $\mathcal{I}_Q(L) \to 0$, $Q \neq 0$.

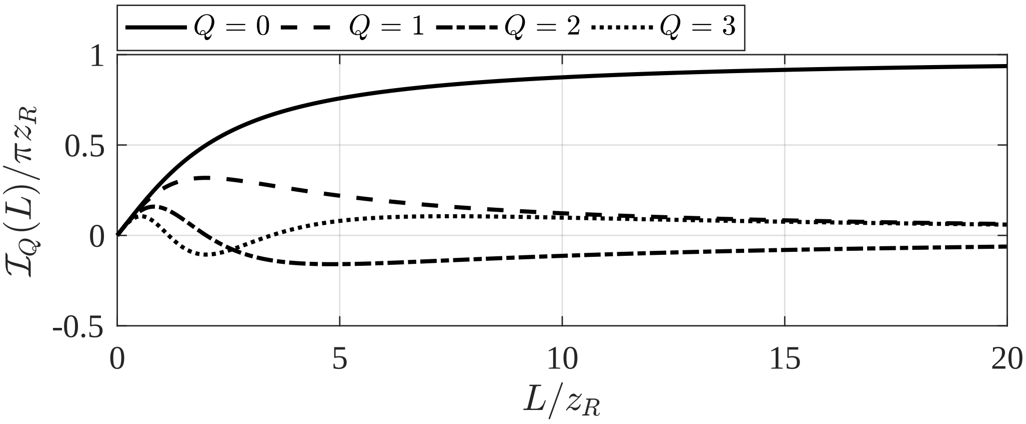

**Source:** The author (2024).

### 2.3.3.4 *Angular-radial mode coupling*

One particularly interesting result in the GPM setting is the direct transfer of radial indices and topological charges from incident fields to the radial index of the generated signal. This was achieved in a non degenerate cascade FWM process generating blue light (OFFER et al., 2021). The selection rule given by Eq. (2.166) imposes for the output modes:

$$\begin{aligned} p &= q + q' - n + \frac{1}{2}(|l| + |l'| - |m| - |\ell|), \\ &= q + q' - n + \frac{1}{2}(|l| + |l'| - |m| - |l + l' - m|). \end{aligned} \tag{2.167}$$

Considering $m = n = 0$ ($u_b$ Gaussian), the OAM conservation requires $\ell = l + l'$, and

$$p = q + q' + \frac{1}{2}(|l| + |l'| - |l + l'|). \tag{2.168}$$

Here the relative helicities of the OAM of fields $u_a$ and $u_{a'}$ become important, i.e., whether we have co-rotating ($l \cdot l' \geq 0$) or counter-rotating ($l \cdot l' < 0$) vortices. We may therefore rewrite Eq. (2.168) as:

$$p = \begin{cases} q + q' & , \quad l \cdot l' \geq 0, \\ q + q' + \min(|l|, |l'|) & , \quad l \cdot l' < 0, \end{cases} \tag{2.169}$$

and the only possible modes at the output are:

$$\begin{aligned} &u_{l+l',q+q'}, && l \cdot l' \geq 0, \\ &u_{l+l',q+q'+\min(|l|,|l'|)}, && l \cdot l' < 0. \end{aligned} \tag{2.170}$$

**Figure 11** – Normalized mode weights (a) $\eta_{0,p} = |\mathcal{A}^{0000}_{ss0p}|$, in the co-rotating case, and (b) $\eta_{0,p} = |\mathcal{A}^{2,-200}_{1s0p}|$, in the counter-rotating case, for $s = 1, 2, 3$. In each situation, as the ratio $L/z_R$ increases, the GPM condition imposes the restrictions given by Eq. (4.9). Namely $\eta_{0,p} \to \delta_{p,2s}$ for (a), and $\eta_{0,p} \to \delta_{p,3+s}$ for (b). The calculations were performed in the degenerate FWM setting.

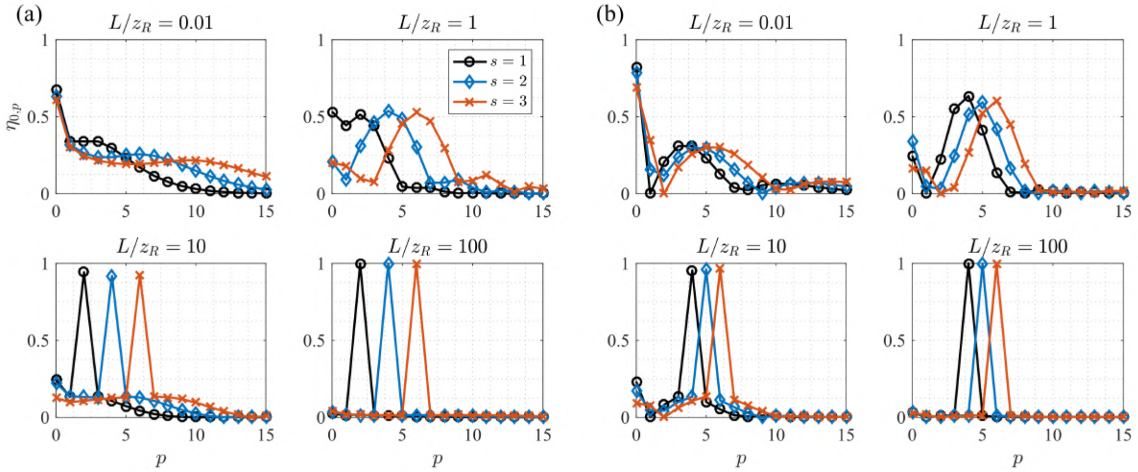

**Source:** The author (2024).

What Eq. (2.170) tells us is that under these assumptions, it is possible to transfer the radial indices of the two input fields to the generated field radial index; and that when $u_a, u_{a'}$ possess counter-rotating vorticities, it is possible to increase the generated radial index by the minimum value among $|l|, |l'|$. Furthermore, when $q = q' = 0$, we see that one can generate radial modes at the output, from incident modes that only carry topological charge, and if $l = -l'$, the generated radial mode will carry no TC (complete transfer of angular to radial charge).

To exemplify these rules, and illustrate what one would get at the output, consider the FWM process induced by the modes $u_a = u_{a'} = u_{0,s}$, and $u_b = u_{0,0}$, for the co-rotating case; and by the modes $u_a = u_{2,1}$, $u_{a'} = u_{-2,s}$, $u_b = u_{0,0}$, for the counter-rotating case. The normalized mode weights are shown in Fig. 11 for different ratios $L/z_R$, and values of $s$. We see that as the ratio $L/z_R$ increases, the GPM condition imposes the restriction on the $p$ orders, following Eq. (4.9). In (a) the output mode emerges with a radial index equal to the sum of the input radial orders, $p = 2s$; and in (b) the output radial order is $p = 3 + s$. This result is valid both for the degenerate and non-degenerate configurations.

Let us now focus on the degenerate FWM process ($\xi_j = 1$). The radial integral, taking into account the GPM condition, can be written:

$$\mathcal{R}^{ll'0(l+l')}_{0000} = \int_0^\infty \rho^{2(|l|+|l'|)} L_0^{|l|+|l'|}(\rho^2) e^{-2\rho^2} \rho d\rho, \qquad l \cdot l' \geq 0, \tag{2.171}$$

and

$$\mathcal{R}^{ll'0(l+l')}_{000\,\min(|l|,|l'|)} = \int_0^\infty \rho^{|l|+|l'|+|l+l'|} L^{|l+l'|}_{\min(|l|,|l'|)}(\rho^2) e^{-2\rho^2} \rho d\rho, \qquad l \cdot l' < 0. \tag{2.172}$$

For the co-rotating case, $l \cdot l' \geq 0$, we have simply:

$$\begin{aligned}
\mathcal{R}^{ll'0(l+l')}_{0000} &= \int_0^\infty \rho^{2(|l|+|l'|)} e^{-2\rho^2} \rho d\rho, \\
&= \frac{1}{4} \frac{(|l|+|l'|)!}{2^{|l|+|l'|}}, \\
&\xrightarrow{l=-l'} \frac{(2|l|)!}{4^{|l|+1}}.
\end{aligned} \tag{2.173}$$

But something a little more interesting happens in the counter-rotating case with $l = -l'$: the radial integral given by Eq. (2.172) is nonzero only if $|l|$ is even. To show this, we write:

$$\begin{aligned}
\mathcal{R}^{l-l00}_{000|l|} &= \int_0^\infty \rho^{2|l|} L^0_{|l|}(\rho^2) e^{-2\rho^2} \rho d\rho, \\
&= |l|! \sum_{k=0}^{|l|} \frac{(-1)^k}{k!} \frac{1}{k!(|l|-k)!} \int_0^\infty \rho^{2(|l|+k)} e^{-2\rho^2} \rho d\rho, \\
&= \frac{1}{4} \frac{|l|!}{2^{|l|}} \sum_{k=0}^{|l|} \frac{(-1)^k}{2^k (k!)^2} \frac{(|l|+k)!}{(|l|-k)!}.
\end{aligned} \tag{2.174}$$

The above finite sum can be cast in terms of the Gamma function, as

$$\mathcal{R}^{l-l00}_{000|l|} = \frac{1}{4} \frac{\Gamma\left(\dfrac{1+|l|}{2}\right)}{\Gamma\left(\dfrac{1-|l|}{2}\right)}. \tag{2.175}$$

Note that for odd $l$, $|l| = 2n+1$, with integer $n \geq 0$, we get

$$\mathcal{R}^{l-l00}_{000|l|} = \frac{1}{4} \frac{\Gamma(1+n)}{\Gamma(-n)}. \tag{2.176}$$

The reciprocal of the Gamma function evaluated at zero and at negative integer values is equal to zero (DENNERY; KRZYWICKI, 1996). Thus, for odd $l$, the radial integral is identically zero:

$$\mathcal{R}^{l-l00}_{000|l|} \overset{\text{odd}\, l}{=} 0. \tag{2.177}$$

This result is not obtained in a non degenerate configuration, since the Gaussian exponential $e^{-\rho^2(\xi_a^2+\xi_{a'}^2)}$ inside the integral in (2.174) would carry a factor $(\xi_a^2 + \xi_{a'}^2) \neq 2$, and therefore the exact expression for the radial integral would not be found. This indicates that some cases reported in Ref. (OFFER et al., 2021) are not reproducible in a degenerate FWM scheme. Also, when incident fields consist of a superposition of odd $\pm l$, one of the mode components of the output field is suppressed in the limit $L/z_R \to \infty$, and one obtains results different from those in Ref. (WALKER; ARNOLD; FRANKE-ARNOLD, 2012). We shall return to this point in Chapter 4.

### 2.3.4 The HG overlap integral

When dealing with the Hermite-Gaussian basis, it will be necessary to calculate the overlap integral of four HG modes

$$\mathcal{A}_{mm'm''m'''}^{nn'n''n'''} = \int_{-L/2}^{L/2} \int_{-\infty}^{\infty} \int_{-\infty}^{\infty} u_{m',n'}^{\mathrm{HG}} u_{m'',n''}^{\mathrm{HG}} u_{m''',n'''}^{\mathrm{HG}*} u_{m,n}^{\mathrm{HG}*} dx dy dz. \tag{2.178}$$

As in the case with the LG basis, depending on the incident field superpositions, there may be several integrals of this kind to be evaluated for a given FWM process, and the selection rules that arise from Eq. (2.178) aid in the task of accounting for all possible combinations of indices.

As in the case with LG modes, we consider that all beams are given by modes with the same Rayleigh range $z_R$. Then, we can write explicitly the integral of four HG modes (to avoid the repetition of lengthy sub- and superscripts, we define $\boldsymbol{m} \equiv \{m, m', m'', m'''\}$ and $\boldsymbol{n} \equiv \{n, n', n'', n'''\}$), to write:

$$\begin{aligned}
\mathcal{A}_{\boldsymbol{m}}^{\boldsymbol{n}} = \frac{4}{\pi^2} \mathcal{M}_{\boldsymbol{m}}^{\boldsymbol{n}} \int_{\mathbb{V}} & \frac{1}{w_a w_{a'} w_b w_s} e^{-r^2(1/w_a^2 + 1/w_{a'}^2 + 1/w_b^2 + 1/w_s^2)} \\
& \times H_{m'}\left(\frac{\sqrt{2}x}{w_a}\right) H_{m''}\left(\frac{\sqrt{2}x}{w_{a'}}\right) H_{m'''}\left(\frac{\sqrt{2}x}{w_b}\right) H_{m}\left(\frac{\sqrt{2}x}{w_s}\right) \\
& \times H_{n'}\left(\frac{\sqrt{2}y}{w_a}\right) H_{n''}\left(\frac{\sqrt{2}y}{w_{a'}}\right) H_{n'''}\left(\frac{\sqrt{2}y}{w_b}\right) H_{n}\left(\frac{\sqrt{2}y}{w_s}\right) \\
& \times \exp\Big[-i2Q \tan^{-1}(z/z_R) + i\delta\Phi_{\mathrm{C}}(r, z)\Big] d^3\mathbf{r},
\end{aligned} \tag{2.179}$$

where $\mathcal{M}_{\boldsymbol{m}}^{\boldsymbol{n}} = M_{m,n} M_{m',n'} M_{m'',n''} M_{m''',n'''}$ is the product of HG normalization constants, $w_j = w_j(z) = w_{0,j}\sqrt{1 + (z/z_R)^2}$ is the waist of each beam, $2Q$ is now the difference in total mode orders $N_{m,n} = m + n$, and $\delta\Phi_{\mathrm{C}}(r, z) = 0$, since we assume the Boyd criterion to be fulfilled. Defining the ratios as before $\xi_j \equiv w_0/w_{0,j}$ with $w_0$ being a reference waist, and $\rho_x(z) = \sqrt{2}x/W(z)$, $\rho_y(z) = \sqrt{2}y/W(z)$, with $W(z) = w_0\sqrt{1 + (z/z_R)^2}$, we can rewrite the integral as

$$\begin{aligned}
\mathcal{A}_{\boldsymbol{m}}^{\boldsymbol{n}} = {} & \frac{4}{\pi^2} \frac{\mathcal{M}_{\boldsymbol{m}}^{\boldsymbol{n}}}{2w_0^2} \xi_a \xi_{a'} \xi_b \xi_s \\
& \times \int_{-\infty}^{\infty} H_{m'}(\xi_a \rho_x) H_{m''}(\xi_{a'} \rho_x) H_{m'''}(\xi_b \rho_x) H_m(\xi_s \rho_x) e^{-\rho_x^2(\xi_a^2 + \xi_{a'}^2)} d\rho_x \\
& \times \int_{-\infty}^{\infty} H_{n'}(\xi_a \rho_y) H_{n''}(\xi_{a'} \rho_y) H_{n'''}(\xi_b \rho_y) H_n(\xi_s \rho_y) e^{-\rho_y^2(\xi_a^2 + \xi_{a'}^2)} d\rho_y \\
& \times \int_{-L/2}^{L/2} \frac{e^{-i2Q \tan^{-1}(z/z_R)}}{1 + (z/z_R)^2} dz,
\end{aligned} \tag{2.180}$$

or

$$\mathcal{A}_{m}^{n} = \frac{2}{\pi^2 w_0^2} \xi_a \xi_{a'} \xi_b \xi_s \mathcal{M}_{m}^{n} \mathcal{X}_{m} \mathcal{Y}^{n} \mathcal{I}_Q(L), \tag{2.181}$$

where $\mathcal{X}_m$ and $\mathcal{Y}^n$ are the integrals in $\rho_x$ and $\rho_y$, respectively, and $\mathcal{I}_Q(L)$ is the longitudinal integral.

#### *2.3.4.1 Transverse overlap*

The transverse integrals are

$$\mathcal{X}_m = \int_{-\infty}^{\infty} H_{m'}(\xi_a \rho_x) H_{m''}(\xi_{a'} \rho_x) H_{m'''}(\xi_b \rho_x) H_m(\xi_s \rho_x) e^{-\rho_x^2(\xi_a^2 + \xi_{a'}^2)} d\rho_x, \tag{2.182}$$

$$\mathcal{Y}^n = \int_{-\infty}^{\infty} H_{n'}(\xi_a \rho_y) H_{n''}(\xi_{a'} \rho_y) H_{n'''}(\xi_b \rho_y) H_n(\xi_s \rho_y) e^{-\rho_y^2(\xi_a^2 + \xi_{a'}^2)} d\rho_y. \tag{2.183}$$

We see that for the full transverse integral to be nonzero, both products of Hermite polynomials in the $\mathcal{X}$ and $\mathcal{Y}$ integrals must be even. Since $H_m(\cdot)$ is even if $m$ is even, and odd if $m$ is odd, it can be verified that a sufficient general requirement to produce nonzero transverse overlap is that the sum of the indices characterizing the Hermite polynomials associated with each direction must be *even*. This constitutes the first selection rule contained in $\mathcal{A}_m^n$, which is associated with the transverse spatial degrees of freedom: the only modes $u_{mn}^{\mathrm{HG}}$ that are generated in the FWM process are those that, considering all combinations, satisfy

$$\mathrm{mod}(N_x, 2) = 0, \tag{2.184}$$

$$\mathrm{mod}(N_y, 2) = 0, \tag{2.185}$$

where $N_x = m' + m'' + m''' + m$ and $N_y = n' + n'' + n''' + n$ are the total mode numbers associated with the $x$ and $y$ distributions, respectively, and are strictly positive. We emphasize that, due to the separability of the transverse integral into two integrals, the selection rules in $x$ and $y$ are independent. Note that Eq. (2.184) does not determine the values of $m$ and $n$, rather, it reduces the number of nonzero coefficients we have to worry about. If $m' + m'' + m'''$ is even (odd), $m$ will assume only even (odd) values. The same can be said about the sum $n' + n'' + n'''$ and $n$. Furthermore, the integrals $\mathcal{X}_m$ and $\mathcal{Y}^n$ are almost identical, the only difference being the set of indices that determine the orders of the Hermite polynomials. Using the series expansion of the Hermite polynomials, $H_m(x) = \sum_{k=0}^{\lfloor m/2 \rfloor} c_k^m x^{m-2k}$, where $\lfloor \cdot \rfloor$ is the floor function, and the coefficients are $c_k^m = (-1)^k \frac{m!}{k!} \frac{2^{m-2k}}{(m-2k)!}$, we get

$$\mathcal{X}_{\boldsymbol{m}} = \sum_{k_1=0}^{\lfloor m'/2 \rfloor} \sum_{k_2=0}^{\lfloor m''/2 \rfloor} \sum_{k_3=0}^{\lfloor m'''/2 \rfloor} \sum_{k_4=0}^{\lfloor m/2 \rfloor} c_{k_1}^{m'} c_{k_2}^{m''} c_{k_3}^{m'''} c_{k_4}^{m} \xi_a^{m'-2k_1} \xi_{a'}^{m''-2k_2} \xi_b^{m'''-2k_3} \xi_s^{m-2k_4}$$
$$\times \int_{-\infty}^{\infty} \rho_x^{m'+m''+m'''+m-2(k_1+k_2+k_3+k_4)} e^{-\rho_x^2(\xi_a^2+\xi_{a'}^2)} d\rho_x. \tag{2.186}$$

Note that $G = m' + m'' + m''' + m - 2(k_1 + k_2 + k_3 + k_4) \geq 0$ is always even. Using a standard Gaussian integral result, we arrive at the expression

$$\mathcal{X}_{\boldsymbol{m}} = \sqrt{\pi} \frac{\xi_a^{m'} \xi_{a'}^{m''} \xi_b^{m'''} \xi_s^{m}}{\sqrt{\xi_a^2 + \xi_{a'}^2}} \sum_{k_1,k_2} \sum_{k_3,k_4} \frac{c_{k_1}^{m'} c_{k_2}^{m''} c_{k_3}^{m'''} c_{k_4}^{m}}{\xi_a^{2k_1} \xi_{a'}^{2k_2} \xi_b^{2k_3} \xi_s^{2k_4}} \frac{2^{-G/2}(G-1)!!}{(\xi_a^2 + \xi_{a'}^2)^{G/2}}, \tag{2.187}$$

where $(\cdot)!!$ is the double factorial. The integral $\mathcal{Y}^{\boldsymbol{n}}$ can be calculated using the same formula, with the change of indices $\boldsymbol{m} \to \boldsymbol{n}$.

#### 2.3.4.2 *Longitudinal integral and Gouy phase-matching*

The second selection rule comes from the longitudinal integral, $\mathcal{I}_Q(L)$, when the extended-medium condition is fulfilled, i.e., $L/z_R \gg 1$, imposing the GPM condition. We obtain the same result as in Eq. (2.163), and in the extended-medium limit, $L/z_R \to \infty$, $\mathcal{I}_Q(L) \to \pi z_R \delta_{Q,0}$. The only modes that survive the mixing process in an extended medium are those that satisfy

$$N_{m'n'} + N_{m''n''} = N_{m'''n'''} + N_{mn}, \tag{2.188}$$

or, alternatively,

$$m + n = (m' + m'' - m''') + (n' + n' - n'''). \tag{2.189}$$

#### 2.3.4.3 *Gaussian IR field and effective selection rule - the index-sum rule*

In a degenerate FWM process, where all fields possess the same wavelength, we have $\xi_j = 1$. However, we consider here a cascade FWM process induced by amplified spontaneous emission (ASE). In this setting, two fields at $780$ nm and $776$ nm interact in a heated sample of $^{85}\mathrm{Rb}$ atoms to generate a signal at $\lambda_{\mathrm{B}} = 420$ nm, with an emission also at $\lambda_{\mathrm{IR}} = 5.23$ µm. In this situation, making the reference wavelength $\lambda_0 = 780$ nm, we have $\xi_a = \xi_{780} = 1$, $\xi_{a'} = \xi_{776} = \sqrt{780/776} \approx 1$. The other ratios $\xi$ are also determined based on this value, $\xi_b = \xi_{\mathrm{IR}} = \sqrt{780/5230}$, $\xi_s = \xi_{\mathrm{B}} = \sqrt{780/420}$. It is well known that, when the ASE FWM is induced by transversely structured beams, the spontaneously emitted IR beam is predominantly Gaussian. This ensures maximum efficiency in the process. We can write $u_{\mathrm{IR}} = u_{00}^{\mathrm{HG}}$, and in all of the expressions we make $m''' = n''' = 0$. The full overlap is thus characterized by the six remaining possibly nonzero indices:

$$\mathcal{A}_{mm'm''m'''}^{nn'n''n'''} \to \mathcal{A}_{mm'm''0}^{nn'n''0} = \mathcal{A}_{mm'm''}^{nn'n''}. \tag{2.190}$$

Furthermore, the transverse integrals, given by Eq. (2.187), can now be written in the approximate form

$$\mathcal{X}_{\boldsymbol{m}} \simeq \sqrt{\frac{\pi}{2}}\,\xi_{\mathrm{B}}^{m} \sum_{k_1,k_2} \sum_{k_4} \frac{c_{k_1}^{m'} c_{k_2}^{m''} c_{k_4}^{m}}{\xi_{\mathrm{B}}^{2k_4}} 2^{-G} (G-1)!!, \tag{2.191}$$

and we see that the ratio $\xi_{\mathrm{B}}$, between the waists of the incident beams and the generated blue light beam, is the only one with a significant contribution to the results. Now, considering a extended-medium regime (which is well suited for the situations we are interested in), the generated $m$ and $n$ must simultaneously satisfy the transverse (2.184) and longitudinal (2.189) selection rules,

$$\operatorname{mod}(m + m' + m'', 2) = 0, \tag{2.192}$$

$$\operatorname{mod}(n + n' + n'', 2) = 0, \tag{2.193}$$

$$(m' + m'') + (n' + n'') = m + n. \tag{2.194}$$

Now, consider the indices given by:

$$\begin{aligned} m(q) &= m' + m'' \pm q, \\ n(q) &= n' + n'' \mp q, \end{aligned} \tag{2.195}$$

where $q$ is an *even* positive integer. Although these are not the only allowed values, it is clear that they comply with all of the conditions (2.192)-(2.194). Without further restrictions to $q$, equations (2.195) can give negative $m$ or $n$, which is not allowed. Evidently, these possibilities must be ruled out if encountered. In any case, it is possible to establish the total number of modes $u_{m,n}^{\mathrm{HG}}$ that can, in principle, be generated. Here we highlight that in the ASE FWM process in a extended-medium, it can be shown that $\mathcal{A}_{m(q),m'm''}^{n(q),n'n''}$ possesses negligible values for $q \neq 0$. In fact, in all cases we consider, we may assume that

$$\mathcal{A}_{mm'm''}^{nn'n''} = \delta_{m,m'+m''} \delta_{n,n'+n''} \mathcal{A}_{m'+m'',m'm''}^{n'+n'',n'n''} \tag{2.196}$$

are the only relevant coefficients in the generated field mode expansion. We name this effective selection rule the "index-sum rule", and it is the key property that allowed to demonstrate the optical mode conversion explored in Ref. (ROCHA et al., 2022). We will come back to this in Chapter 4.

To illustrate the index-sum rule, we show in Fig. 12 how the distribution of normalized expansion coefficients changes as a function of the ratio $z_R/L$, which characterizes a thin- or extended-medium regime, and how it differs between the degenerate and non-degenerate cases, determined by $\xi_j = 1$ and $\xi_{\mathrm{B}} = \sqrt{780/420}$, respectively. We consider the situation $u_{780} = u_{12}^{\mathrm{HG}}$ and $u_{776} = u_{01}^{\mathrm{HG}}$. For larger $z_R/L$ (or conversely, smaller $L/z_R$), closer to a thin-medium regime, many modes can be generated both in the degenerate and non-degenerate situations. It can be noted that there is a strong influence of the ratio $\xi_{\mathrm{B}}$ on the distributions. In the non-degenerate setting ($\xi_{\mathrm{B}} = \sqrt{780/420}$) there is a smaller number of modes generated with relevant amplitudes. This can be seen as a selection performed by the parameter $\xi_{\mathrm{B}}$. As we move to an extended-medium regime, for decreasing $z_R/L$, the Gouy phase-matching condition restricts the modes that can be generated, according to Eq. (2.166). In the non-degenerate configuration, due to the restriction imposed by $\xi_{\mathrm{B}}$, the mode that carries the sum of indices, $m = m' + m''$ and $n = n' + n''$, dominates. As a final remark, note that the nonzero coefficients on the $m \times n$ plane are disposed in diagonal lines corresponding to constant total order $N_{m,n}$, and that no neighboring modes are populated, i.e., they are always spaced by at least $1$ square both in the $m$ and $n$ directions.

**Figure 12** – Distribution of normalized output mode coefficients for $z_R/L = 1, 0.2, 0.1$ (from left to right columns) and $\xi_\mathrm{j} = 1$ (lower row) and $\xi_\mathrm{B} = \sqrt{780/420}$ (upper row), representing the degenerate and non-degenerate processes, respectively. Incident fields are $u_{780} = \mathrm{HG}_{12}$ and $u_{776} = \mathrm{HG}_{01}$. In the top right plot, which represents the result obtained for the non-degenerate FWM process in an extended-medium, we see that the major contribution is from the mode with $m = m' + m''$, $n = n' + n''$, corresponding to $q = 0$. This indicates the validity of the index-sum rule. Insets show the resulting intensity profile of the FWM beam in each configuration.

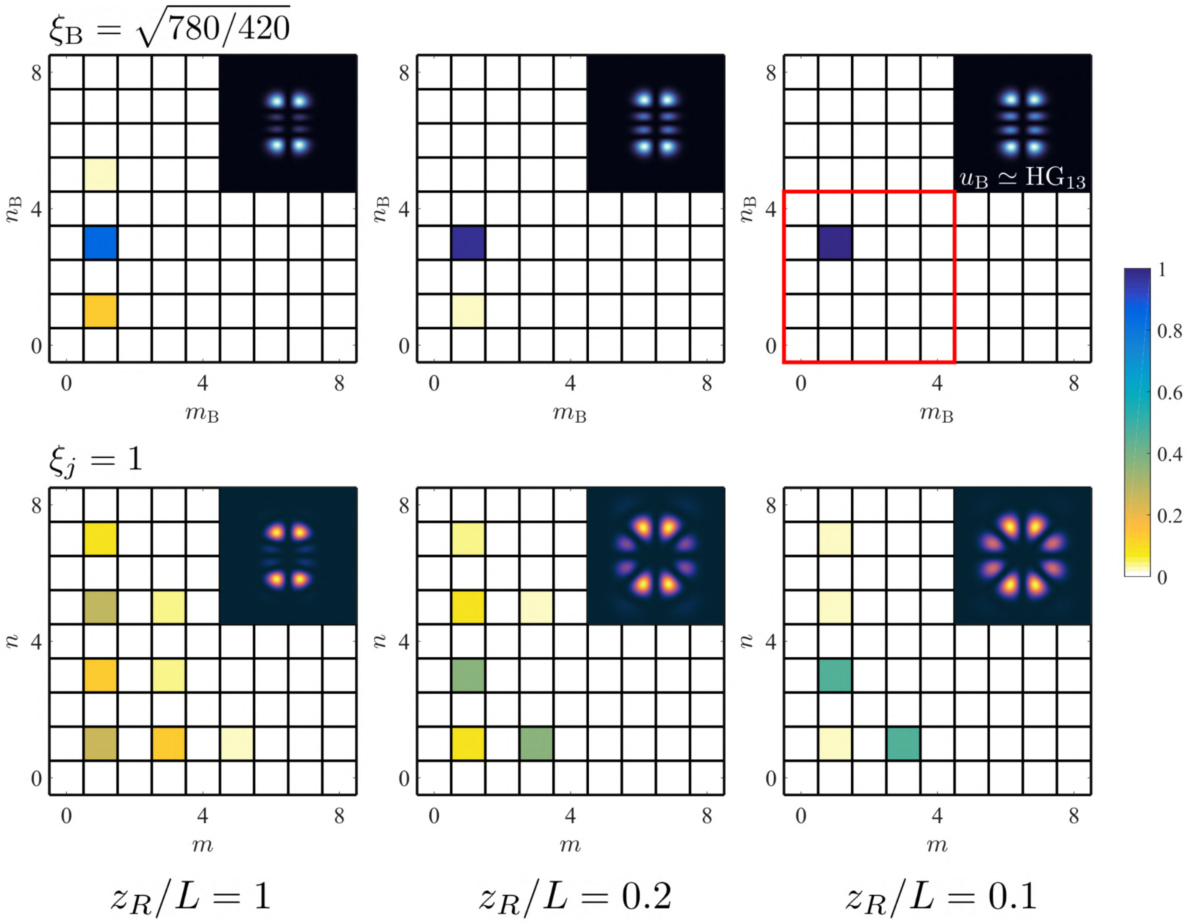

**Source:** Taken from Ref. (ROCHA et al., 2022).

# 3 EXPERIMENTAL DETAILS

In this Chapter we describe the experimental apparatus used in our studies. We worked with two types of atomic systems: cold atoms obtained with our magneto-optical trap, and heated rubidium vapor. We discuss the components and operation of both systems, and also how we used the spatial light modulator (SLM) to generate the structured light beams.

## 3.1 HYPERFINE STRUCTURE OF RUBIDIUM AND SATURATED ABSORPTION SPECTROSCOPY

Alkali atoms possess a single valence electron orbiting a core composed of the nucleus and the electrons of the closed subshells, which shield the nuclear charge. Due to the shielding effect, an excited outermost electron experiences the potential of a nuclear charge of $+e$. In this case, its energy is essentially hydrogenic, $\mathbb{E}_n^{\mathrm{alk}} \simeq \mathbb{E}_1^{\mathrm{H}}/n^2$, where $\mathbb{E}_1^{\mathrm{H}}$ is the ground state energy of hydrogen and $n$ is the principal quantum number. For an $\mathrm{s}$ valence electron (an electron with an orbital angular momentum quantum number $L = 0$), however, the shielding is not as effective, and it sees a greater nuclear charge. Because of this, $\mathrm{s}$ electrons have lower energies than $\mathrm{d}$ electrons ($L = 2$) with the same principal quantum number. The quantum defect $\delta_L$ is a quantity subtracted from the principal quantum number $n$ of the alkalis to account for this effect. The subscript $L$ indicates the dependence of the quantum deffect on the orbital angular momentum quantum number. The effective principal quantum number is $n^* = n - \delta_L$, and the energies of alkali atoms are well described by the modified form of Bohr's formula $\mathbb{E}_{n^*}^{\mathrm{alk}} = \mathbb{E}_1^{\mathrm{H}}/(n^*)^2$.

The fine structure of atoms is a result of the spin-orbit coupling. The total angular momentum of the outer electron is given by $\hat{\mathbf{J}} = \hat{\mathbf{L}} + \hat{\mathbf{S}}$, where $\hat{\mathbf{L}}$ and $\hat{\mathbf{S}}$ are the orbital and spin angular momentum operators, respectively. From the quantum mechanical theory of addition of angular momenta, the corresponding quantum number $J$ is such that $|L-S| \leq J \leq L+S$. Further, the associated magnetic quantum number $m_J$ assumes all integer or half-integer values in the range $-J \leq m_J \leq J$.

The hyperfine structure is a result of the coupling between $\hat{\mathbf{J}}$ and the nuclear angular momentum $\hat{\mathbf{I}}$. The total atomic angular momentum is given by $\hat{\mathbf{F}} = \hat{\mathbf{J}} + \hat{\mathbf{I}}$ and likewise, the quantum numbers $F$ and $m_F$ must satisfy $|J - I| \leq F \leq J + I$ and $-F \leq m_F \leq F$, respectively. The total energy shift due to these effects can be written as

$$\begin{aligned}\Delta E &= \Delta E_{\mathrm{s-o}} + \Delta E_{\mathrm{hfs}},\\ &= A_{\mathrm{s-o}}\langle \hat{\mathbf{L}} \cdot \hat{\mathbf{S}} \rangle + A_{\mathrm{hfs}}\langle \hat{\mathbf{J}} \cdot \hat{\mathbf{I}} \rangle, \end{aligned} \tag{3.1}$$

where $A_{\mathrm{s-o}}$, $A_{\mathrm{hfs}}$ are the spin-orbit and hyperfine structure coupling factors, which can be calculated following standard atomic physics text books (FOOT, 2005; BRANSDEN; JOACHAIN, 2003), and the expectation values are:

$$\langle \hat{\mathbf{L}} \cdot \hat{\mathbf{S}} \rangle = \frac{\hbar^2}{2}\left[J(J+1) - L(L+1) - S(S+1)\right], \tag{3.2}$$

$$\langle \hat{\mathbf{J}} \cdot \hat{\mathbf{I}} \rangle = \frac{\hbar^2}{2}\left[F(F+1) - J(J+1) - I(I+1)\right]. \tag{3.3}$$

The energy shift due to the spin orbit interaction is of the order $\alpha^2\mathbb{E}_{n^*}$, where $\alpha = e^2/4\pi\varepsilon_0\hbar c \simeq 1/137$ is the fine structure constant. The second term on the right-hand side of Eq. (3.1) leads to smaller corrections because the magnetic moment of the nucleus is much smaller than the magnetic moment of the electron (BRANSDEN; JOACHAIN, 2003).

Rubidium has two stable isotopes, $^{85}\mathrm{Rb}$ and $^{87}\mathrm{Rb}$, that are found with abundances of $72.2\%$ and $27.8\%$, respectively. For its ground state, $n = 5$, $L = 0$, $S = 1/2$ and $J = 1/2$. In the first excited, $L = 1$, $S = 1/2$ and $J$ can assume the values $J = 1/2, 3/2$. The spin-orbit interaction thus splits the energy levels of p electrons into two. The transitions $|L = 0, J = 1/2\rangle \to |L = 1, J = 1/2\rangle$ and $|L = 0, J = 1/2\rangle \to |L = 1, J = 3/2\rangle$ are referred to as the $\mathrm{D}_1$ and $\mathrm{D}_2$ lines, respectively. The $\mathrm{D}_2$ lines of both isotopes contain cycling transitions that are of uttermost importance to the trapping and cooling of these atoms. The nuclear spin of $^{87}\mathrm{Rb}$ is $I = 3/2$. The ground state ($J = 1/2$, $I = 3/2$) is split into two, $F = 1, 2$, while the first excited state ($J = 3/2$, $I = 3/2$) is split into four hyperfine levels, $F = 0, 1, 2, 3$. The cyclic transition of the $\mathrm{D}_2$ line is $|J = 1/2, F = 2\rangle \to |J = 3/2, F = 3\rangle$. A similar analysis can be made for $^{85}\mathrm{Rb}$, which has a nuclear spin of $I = 5/2$. Figure 13 shows the hyperfine energy levels of the $\mathrm{D}_2$ lines of $^{87}\mathrm{Rb}$ and $^{85}\mathrm{Rb}$.

As we have seen in Chapter 2, the motion of atoms at room temperature leads to a significant broadening of the absorption lines due to the Doppler effect. For this reason, the hyperfine transitions of Rb cannot be resolved by ordinary absorption. In order to eliminate the Doppler broadening and reveal the hyperfine structure, one must perform a saturated absorption (SA) experiment. The setup is as follows. Two counter-propagating beams, a strong pump and a weak probe, that originate from a single laser (and thus have the same frequency

**Figure 13** – Hyperfine energy levels of the $D_2$ lines of (a) $^{87}\mathrm{Rb}$ and (b) $^{85}\mathrm{Rb}$.

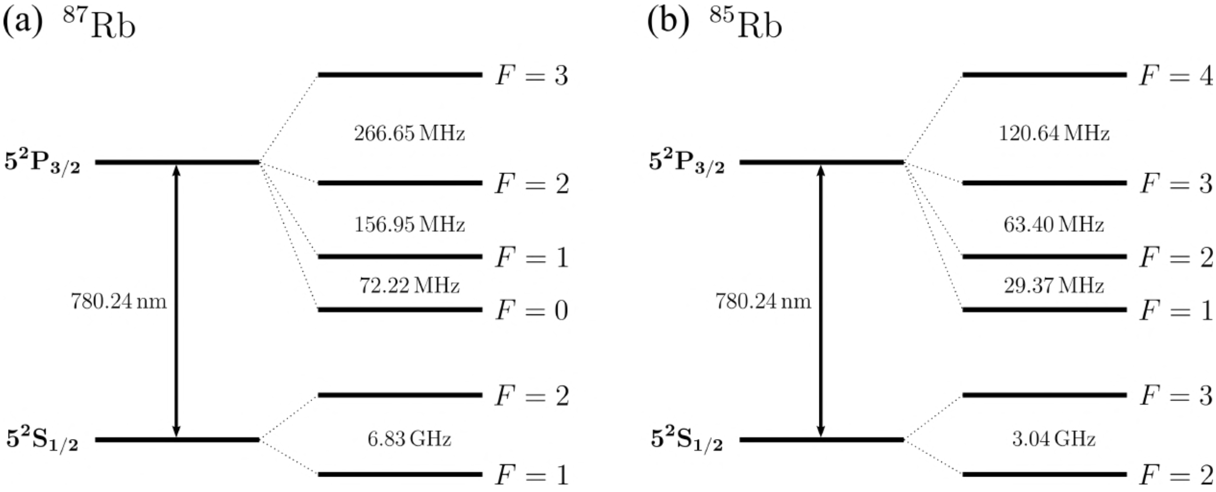

**Source:** Modified from (STECK, 2001).

at all times) are superimposed in a region where the atoms are located. The frequency is made to vary around a hyperfine transition. Off resonance, pump and probe interact with different velocity groups and both beams are absorbed. Precisely at resonance, both beams interact with atoms in the velocity group $v = 0$. The intense pump saturates the medium and thus the probe beam cannot be absorbed, leading to a peak on the probe transmission at resonance. Figure 14 illustrates the process.

**Figure 14** – Depiction of the saturated absorption process. (a) Off resonance, pump and probe interact with atoms at different velocity groups. Exactly at resonance, both beams interact with the velocity group $v = 0$ and the probe is not absorbed. This leads to a peak at a hyperfine resonance frequency in the probe transmission (b).

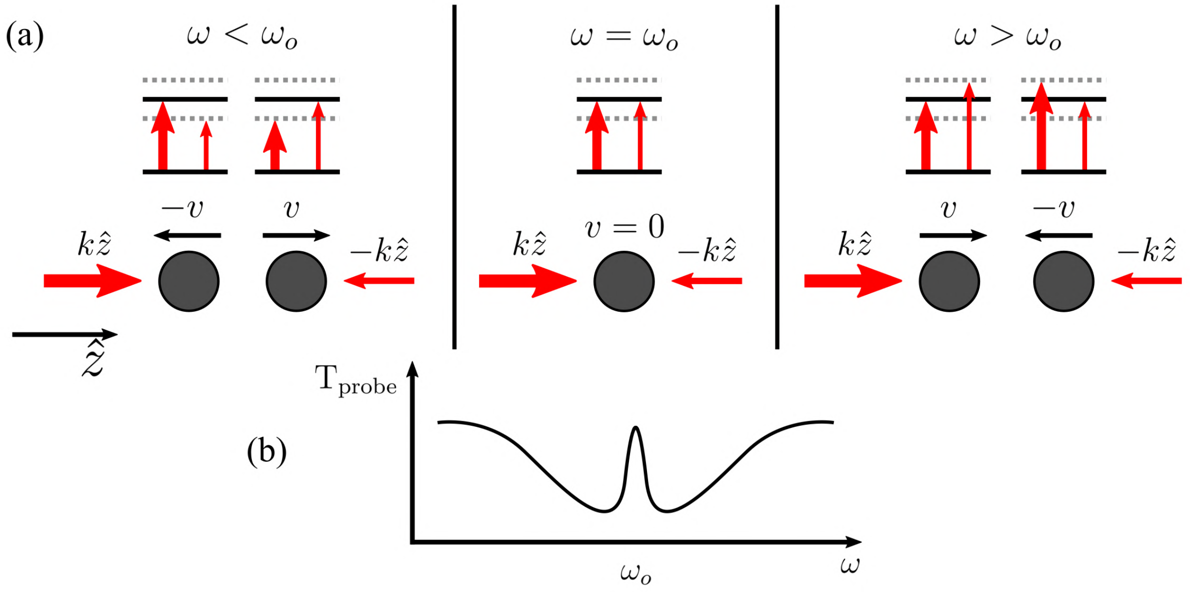

**Source:** The author (2024).

**Figure 15** – Cross-over (CO) resonances in the saturated absorption spectrum. (a) Energy levels involved in the process and associated transition frequencies. (b) Exactly when $\omega = \varpi$ the pump saturates the atoms in the velocity groups $\pm v'$. As a consequence, the probe cannot interact with these atoms and it is transmitted through the medium. This leads to a peak halfway between the two expected resonances at $\omega_1$ and $\omega_2$ in the probe transmission (c).

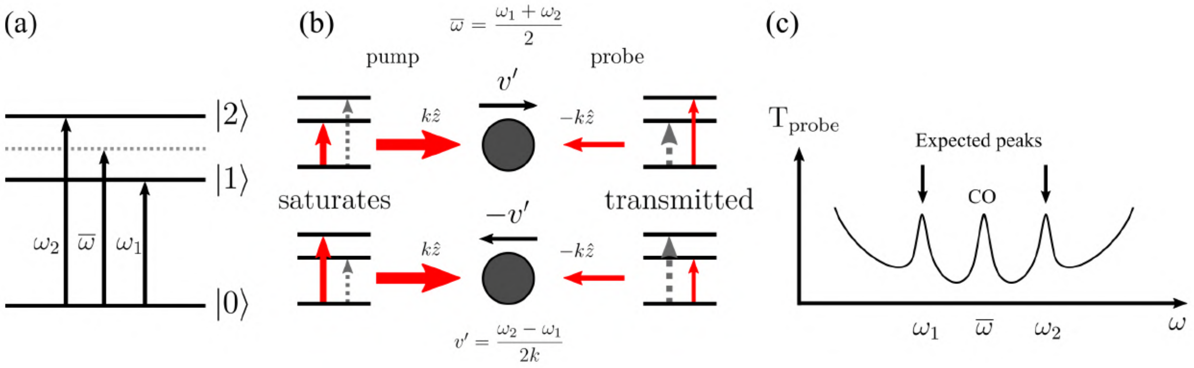

**Source:** The author (2024).

When we have two hyperfine transitions with a common ground state, an additional peak will appear halfway between the two expected peaks in the SA spectrum. These are called cross-over resonances, and arise because when the frequency of the beams is $\omega = \varpi = (\omega_1 + \omega_2)/2$, where $\omega_1 < \omega_2$ are the frequencies corresponding to the two transitions, pump and probe interact with the same velocity groups $\pm v' = \pm(\omega_2 - \omega_1)/2k$, where $k$ is the wave-number. In the reference frame considered [figure 15(b)], atoms with positive (negative) velocity will be promoted to states $|1\rangle$ ($|2\rangle$) by the pump, and become saturated. At the same time the probe would also interact with these velocity groups, but atoms with positive (negative) velocity would be promoted to $|2\rangle$ ($|1\rangle$) in an unsaturated medium. This leads to a peak on the probe transmission at $\varpi$. Figure 15 illustrates the process.

A saturated absorption spectrum can be used as a reference signal to lock the frequency of a tunable diode laser at desired hyperfine transitions using a control system. The setup to obtain the SA signal can be implemented using only a fraction of the total output power of conventional diode lasers and a few optical components, as illustrated in Fig. 16. Figure 17 shows the saturated absorption spectrum of Rb obtained with such an arrangement. In the close up, showing the transitions from $F_g = 2$ of $^{87}\mathrm{Rb}$, we see three well defined peaks, corresponding to the cyclic transition $F_g = 2 \to F_e = 3$, centered at zero, and two cross-over resonances. There are three other peaks that cannot be seen, corresponding to $F_g = 2 \to F_e = 1, 2$ and a third cross-over.

**Figure 16** – Basic setup of a saturation absorption experiment. OI is an optical isolator, F represents filters, PD is a photodiode detector.

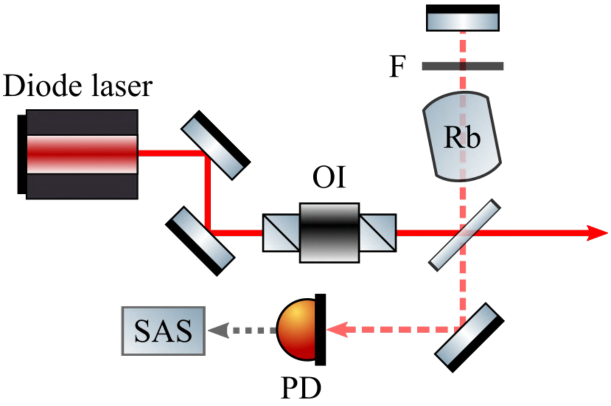

**Source:** The author (2024).

**Figure 17** – Saturated absorption spectrum of Rb. The peak at $\delta = 0$ represents the $F_g = 2 \rightarrow F_e = 3$ hyperfine transition. The inset shows region inside dashed box, highlighting the $|5^2\mathrm{S}_{1/2}, F_g = 2\rangle \rightarrow |5^2\mathrm{P}_{3/2}\rangle$ transition. $\mathrm{CO}(X, Y)$ denotes the cross-over transition involving excited states with $F = X$ and $F = Y$.

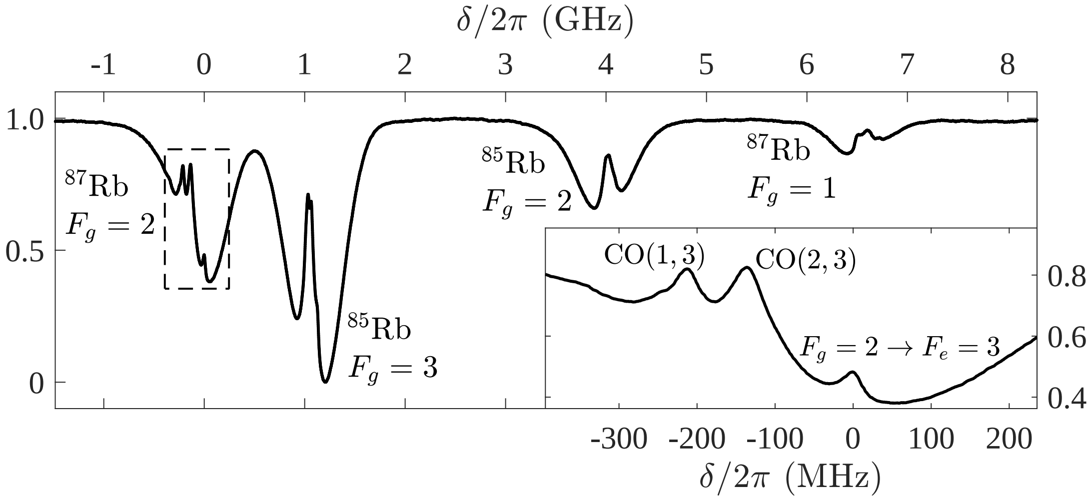

**Source:** The author (2024).

## 3.2 MAGNETO-OPTICAL TRAP SETUP

In this Section we describe the basic aspects of our Rb magneto-optical trap. Figure 18 shows the complete setup of the MOT. The cooling laser is a DL Pro, a grating stabilized tunable single-mode diode laser, from Toptica; and the repump laser is a tunable diode laser from Sanyo, model DL7140-201S, with homemade electronics for current and temperature control. The DL Pro, with a power output of about $100\,\mathrm{mW}$, is set to excite the $|5\mathrm{S}_{1/2}; F_g = 2\rangle \rightarrow |5\mathrm{P}_{3/2}; F_e = 3\rangle$ hyperfine cyclic transition of $^{87}\mathrm{Rb}$. With its dedicated controller, the DLC Pro, also from Toptica, we lock its frequency to the cross-over transition between $|F_e = 1\rangle$ and $|F_e = 3\rangle$, $212$ MHz below resonance. A single-pass acousto-optic modulator (AOM) then introduces a frequency shift of $200$ MHz, leaving it approximately $12$ MHz below the desired resonance frequency. The AOM is also important because it allows to switch the lasers on and off at the rate necessary for our temporal control scheme. The zeroth order diffracted from the AOM is used as a guide beam for other parts of the experiment. The first order is sent into a Toptica Boosta amplifier. The amplified beam is coupled to an optical fiber using a Fiber Dock and the output beam is divided in two. One of the beams goes directly to the main Rb cell via an optical fiber and becomes the $z$ (vertical) arm of the MOT. The other beam is mixed with the repump beam via a fused fiber coupler (FFC). The FFC has two outputs, containing light from cooling and repump lasers, that become the $x$ and $y$ arms of the MOT.

The cooling laser may promote atoms to $|5\mathrm{P}_{3/2}; F_e = 2\rangle$, instead of $F_e = 3$, and these atoms can decay to $|5\mathrm{S}_{1/2}; F_g = 1\rangle$. At this point, they can no longer interact with the cooling laser. For this reason, the repump laser is tuned to the $|5\mathrm{S}_{1/2}; F_g = 1\rangle \rightarrow |5\mathrm{P}_{3/2}; F_e = 2\rangle$ transition and it is responsible for emptying the population of the state $|5\mathrm{S}_{1/2}; F_g = 1\rangle$, so that atoms can interact with the cooling laser again. Its frequency is locked with a homemade locking system based on Arduino, using a saturated absorption signal obtained with a CoSy (compact saturation spectroscopy) module. On the upper region of Fig. 18 we show the setup of the cooling (blue box) and repump (green box) lasers.

The quadrupole magnetic field necessary for the trapping of the atoms at the region where the light beams intersect is attained with a pair of circular coils in an anti-Helmholtz setting. To shield the experiment from Earth's spurious magnetic field and possibly other fields, we use a set of three pairs of square coils which generate magnetic fields along three orthogonal directions. The atoms are provided by a rubidium alkali metal dispenser (AMD), through which a high electric current is imposed to release the atoms. The released atoms are contained inside the main Rb cell, which is connected to an ionic vacuum pump (VP) from Varian. The pump maintains a very low pressure inside the cell, $\sim 10^{-9}$ Torr, necessary to reduce collisions and increase the lifetime of the cooled atom cloud. At the output end of all fibers of the MOT arms, a telescope is used to increase the beam size and a quarter-wave plate makes them circularly polarized. Inside the cell, the beams intersect far from the glass walls. They are then reflected by a mirror and another $\lambda/4$ plate switches the handedness of their circular polarizations, $\boldsymbol{\sigma}^{\pm} \rightarrow \boldsymbol{\sigma}^{\mp}$, thus creating the configuration needed for the trapping of atoms near the intersection. At the center of Fig. 18 we show the main Rb cell and the $x$ and $y$ MOT

**Figure 18** – Simplified scheme of our magneto-optical trap experimental setup.

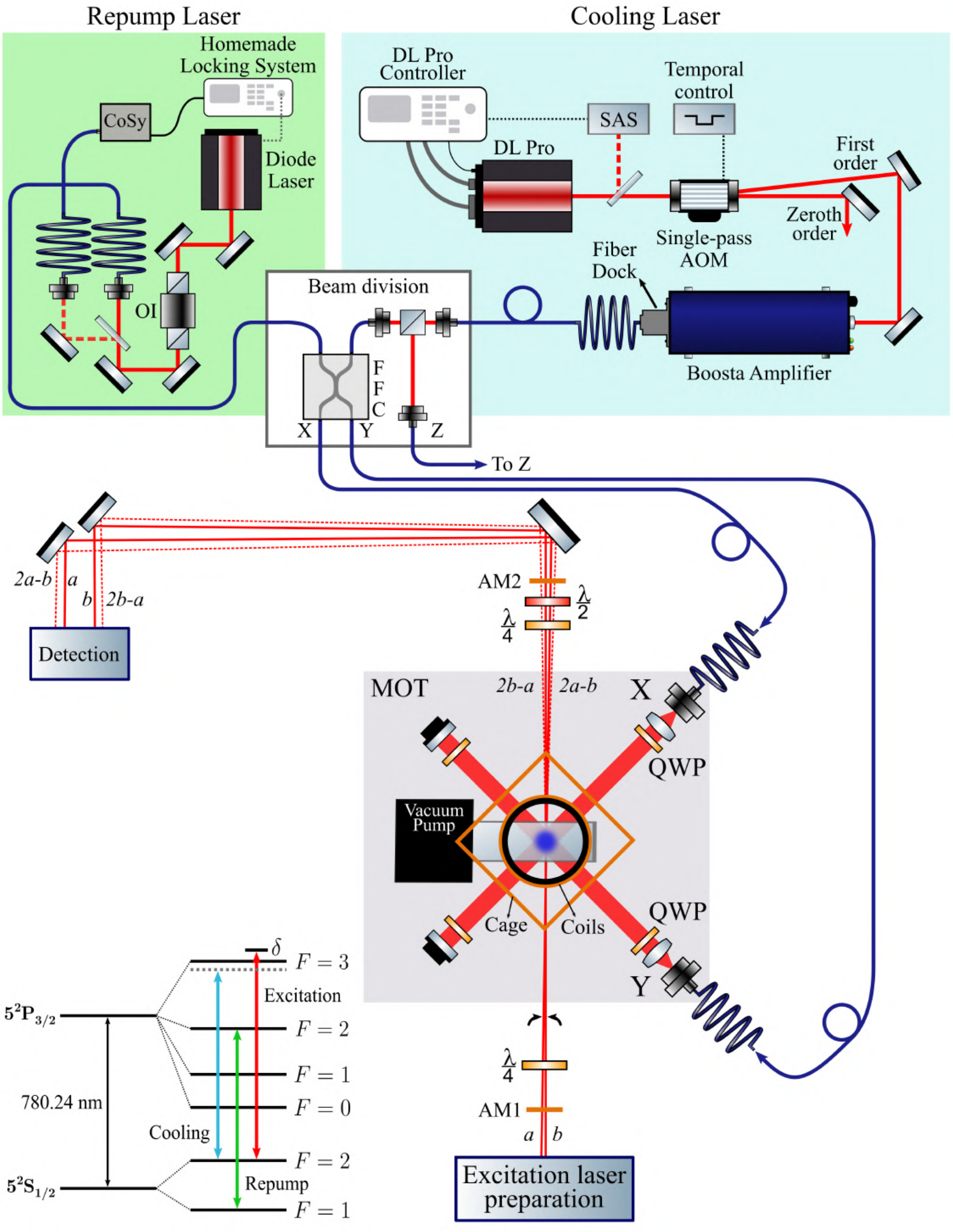

**Source:** The author (2024).

arms (gray box). With the system setup as described so far, we obtain cold atom clouds with an estimated optical depth of $\mathrm{OD} \approx 8$, approximately $10^9$ atoms, and a diameter of $D \approx 3-4$ $\mathrm{mm}$. In Fig. 19 we show a picture of our MOT.

The excitation laser, a homemade diode laser of the same type as the repump, is also tuned to the $|5\mathrm{S}_{1/2}, F_g = 2\rangle \rightarrow |5\mathrm{P}_{3/2}, F_e = 3\rangle$ cycling transition, the same as the cooling laser. For

**Figure 19** – Our magneto-optical trap in operation.

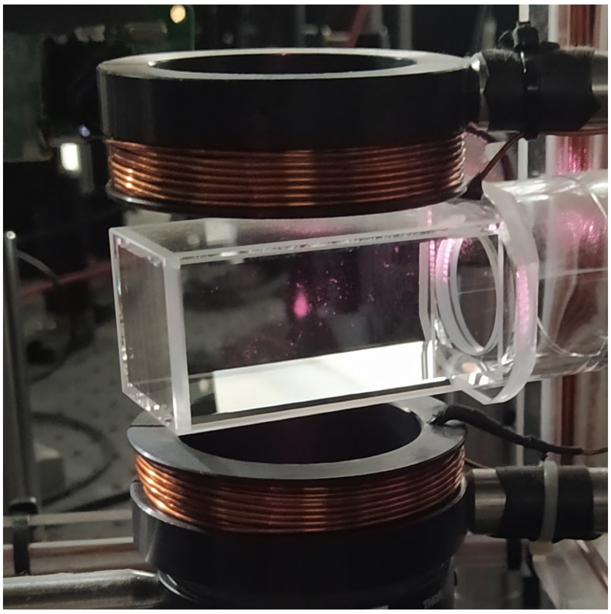

**Source:** The author (2024).

this reason we employ a temporal control scheme that switches off the cooling laser and the trapping magnetic field for $2\ \mathrm{ms}$, and waits a small time interval, of $\sim 100\ \mu s$, before switching on the acquisition time window, when the excitation laser is turned on using the AOM. The time delay before the acquisition time window ensures that the repump laser, which is not turned off, prepares the atoms in the $|F_g = 2\rangle$ state, and is small enough so that the cloud does not move sensibly from the beam intersection position. The excitation laser frequency is locked with the same type of homemade locking system used in the repump laser, and we can vary its frequency by changing the AOM DC voltage. At the bottom left corner of Fig. 18 we show a diagram illustrating the transitions excited by each laser in the experiment.

For the preparation of the excitation beams, we first pass the laser beam through an AOM in a double-pass configuration, allowing for a frequency shift and temporal control. We then divide it into two beams, producing the beams $\mathbf{E}_a$ and $\mathbf{E}_b$. The beam $\mathbf{E}_b$ goes directly to the MOT, and the beam $\mathbf{E}_a$ is sent to the spatial light modulator (SLM). In the upcoming sections we will detail the operation of the SLM. We then align the two beams so that they intersect at the center of the MOT, with a small angle of about $10\ \mathrm{mrad}$ between their wave-vectors. This is done with the aid of alignment masks (AM1 and AM2). In the next Section we will comment more in detail on how this alignment is done. The preparation of the excitation beams is represented in Fig. 20. Depending on the desired configuration of polarizations of the driving fields, some changes must be made to the setup. To excite the atomic cloud with parallel circular polarizations, we send the two beams with parallel linear polarizations through a $50/50$ beam-splitter (BS), and place quarter-wave plates (QWP) at the input and output sides. This is the situation depicted in Figs. 18 and 20. Alternatively, for orthogonal linear polarizations, instead of a BS, we use a PBS and remove the QWPs.

**Figure 20** – Simplified scheme of the preparation of the structured excitation beam in the experiments with the MOT.

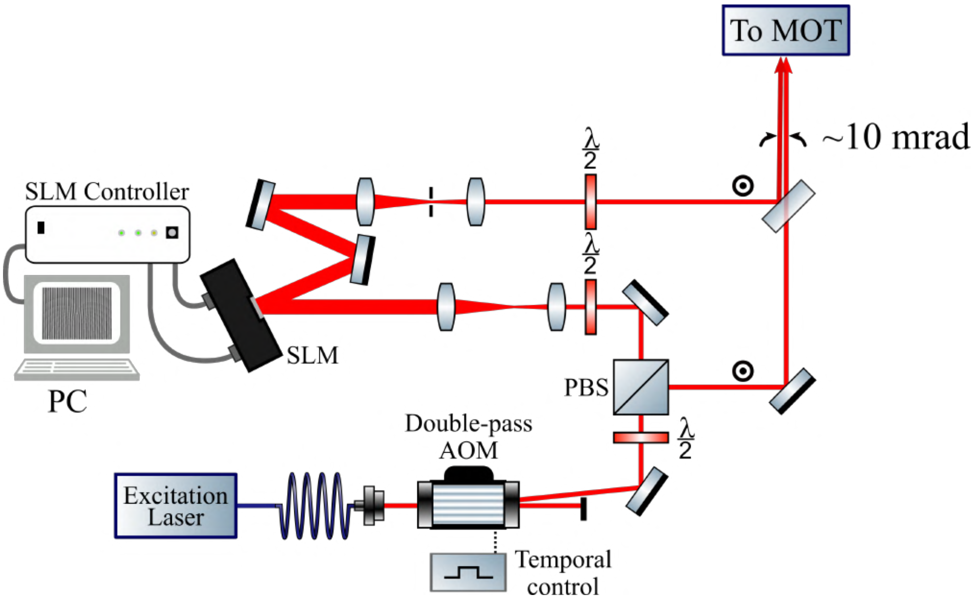

**Source:** The author (2024).

The experiments with the MOT were mainly focused on the correlations between the intensity fluctuations of the participating light fields. In the detection part, we use avalanche photodiodes (APD) from Thorlabs to acquire the intensity fluctuation time-series of the four output signals, the two transmitted beams $a$ and $b$, and the two FWM signals, $2a - b$ and $2b - a$.

## 3.3 HEATED RUBIDIUM VAPOR SETUP

The setup for the experiments on the rubidium vapor cell is relatively simple, in comparison with the MOT setup. A simplified scheme of the experimental arrangement is shown in Fig. 21. We use a homemade tunable diode laser from Sanyo, model $\mathrm{DL7140-201S}$, with homemade electronics for current and temperature control. A small portion of the laser power goes to a saturated absorption (SA) setup to allow for frequency reference, and then it is coupled to a single-mode fiber to correct the initial transverse profile, which is fairly non-Gaussian. At the fiber exit, the beam is split in two by a polarizing beam splitter (PBS). Here, $\mathbf{E}_a$ and $\mathbf{E}_b$

are the transmitted and reflected beams, respectively. Beam $\mathbf{E}_a$ is modulated by the spatial light modulator (SLM), and it can carry any topological charge value or any desired transverse structure. We may pass $\mathbf{E}_b$ through a printed forked grating (FG) mask of order $|\ell| = 1$, allowing us to explore scenarios with structured modes on both incident fields. At the grating output we have the zeroth and first orders, carrying $\ell_b = 0, \pm 1$. The desired diffracted order is selected with a pinhole and sent to the $\mathrm{Rb}$ vapor cell. Before impinging onto the SLM chip, the beam $\mathbf{E}_a$ goes through a telescope (formed by lenses $\mathrm{L1}$ and $\mathrm{L2}$) to increase its size for better modulation. After being diffracted by the SLM, the beam $\mathbf{E}_a$ goes through a reducing telescope (formed by lenses $\mathrm{L3}$ and $\mathrm{L4}$) in which a pinhole is placed at the focal region to select the first diffracted order, the one that carries the desired phase and amplitude modulation. Beam $\mathbf{E}_a$ is then sent to the vapor cell to intersect with beam $\mathbf{E}_b$.

To clean the images of the FWM beams, we use spatial filters to select only the generated signals, blocking the scattered light coming from the incident beams. The spatial filter works as spatial frequency selector. In our setup, the spatial filters are formed by the pairs of lenses $\mathrm{L5}, \mathrm{L6}$ and $\mathrm{L5}, \mathrm{L7}$, with pinholes in between. The first lens projects the 2D Fourier transform of the beam onto the focal plane. As we have seen, the Fourier transform is the transverse wave-vector distribution of a paraxial beam. The pinhole is used to select only the region of the Fourier plane we wish to maintain. In our case, this is the central region, where the smaller spatial frequency components are located. This region represents the profile of the desired beam, which is distributed around $|\mathbf{q}| = 0$, with a characteristic length of $\sim w_0^{-1}$ in wave-vector space. In the physical plane, the overall size of the focused beam is of the order of $w_f = 2f/kw_0$, where $f$ is the lens focal length. The regions blocked are those with the higher frequencies, $|\mathbf{q}| \gg w_0^{-1}$, representing noise, interference, and light from the neighboring beams, which possess larger transverse wave-vector components, as compared to the beam we wish to filter. The second lens, at a symmetric position with respect to the pinhole, brings back the beam to position space.

The two structured beams $\mathbf{E}_a$ and $\mathbf{E}_b$, with wave-vectors $\mathbf{k}_a$ and $\mathbf{k}_b$, respectively, and orthogonal and linear polarization, co-propagate with a small angle of about $6\,\mathrm{mrad}$ inside a $5\,\mathrm{cm}$ long cell containing a natural concentration of rubidium atoms. This angle and the intersection of the beams inside the cell is ensured by a pair of masks we use to aid in the alignment. These masks are placed symmetrically with respect to the cell, and contain 4 equally spaced holes disposed horizontally. We align the transmitted beams, $\mathbf{E}_a, \mathbf{E}_b$, to the two central holes, and two guiding beams for the FWM signals to the two outer holes. There are two options to ensure the crossing at the center: (1) align all the beams parallel to each other, i.e., to the same holes at the input and output masks, and use lenses to focus them at the cell; (2) align the pairs of beams swapping holes at the input and output masks. We use the second method with the two masks separated by a distance $D \approx 68\,\mathrm{cm}$, and the holes spaced by $s = 2\,\mathrm{mm}$, giving the angle $\theta = 2\tan^{-1}(2s/D) \approx 6\,\mathrm{mrad}$ between beams $\mathbf{E}_a$ and $\mathbf{E}_b$. Figure 22 illustrates the situation.

We detect two four-wave mixing signals generated in the $2\mathbf{k}_a - \mathbf{k}_b$ and $2\mathbf{k}_b - \mathbf{k}_a$ directions, denominated as $S_1$ and $S_2$, respectively. Since $\mathbf{E}_a$ and $\mathbf{E}_b$ possess orthogonal polarizations, so do $\mathbf{E}_1$ and $\mathbf{E}_2$. Moreover, $\mathbf{E}_1$ ($\mathbf{E}_2$) is orthogonally polarized with respect to $\mathbf{E}_a$ ($\mathbf{E}_b$). This results in an arrangement at the output where the four signals possess alternating polarizations, and we separate the pairs of beams (transmission + FWM) using a polarizing beam splitter at the output (see Fig. 21).

**Figure 21** – Setup for the experiments of FWM induced by structured light in Rb vapor. The lenses L1, L2, L3, and L4 have focal distances $f_1 = 25.4\,\mathrm{mm}$, $f_2 = 100\,\mathrm{mm}$, $f_3 = 150\,\mathrm{mm}$, $f_4 = 35\,\mathrm{mm}$, giving a magnification factor of $f_2/f_1 \approx 4$ at the input and a similar reduction factor $f_3/f_4$ at the output. The pairs of lenses L5,L6 and L5,L7, together with the pinholes located in between, form the spatial filters for the signals $S_1$ and $S_2$. For the imaging, we may detect either the intensity or the tilted lens profiles of the FWM signals.

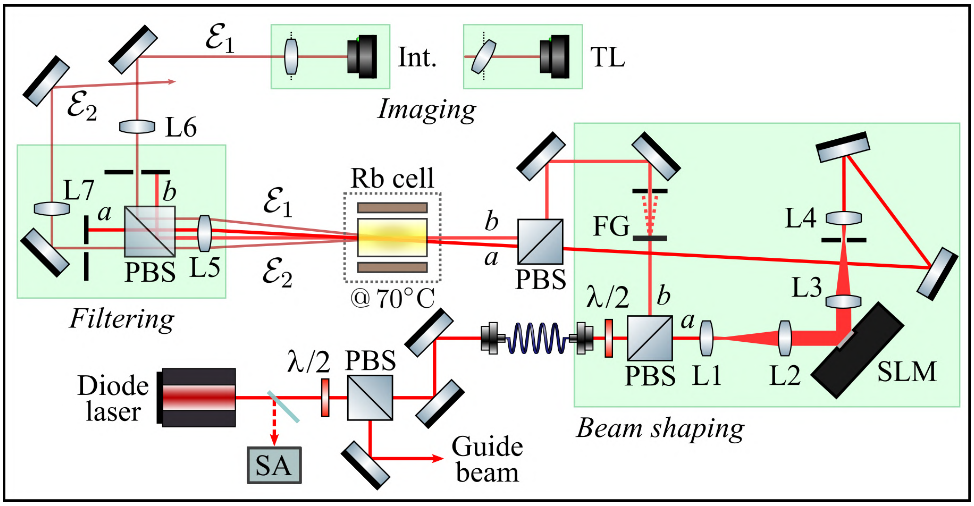

**Source:** The author (2024).

For the results regarding conservation of OAM, we considered the cases $\ell_b = 0, +1$, and varied $\ell_a$ from $-1$ to $3$. In the experiments involving the Poincaré sphere symmetries, we restricted ourselves to the case $\ell_b = 0$, and introduced the nontrivial structure onto the beam $u_a$. For more complex scenarios, one can achieve arbitrary transverse structures for both input beams by modulating them simultaneously with the SLM. However, this results in a greater power loss. To measure the OAM content of the generated signals, we employed the tilted

**Figure 22** – Alignment of the four beams participating in the FWM process with. Namely the two incident beams, to the inner holes of the masks, and the guiding beams for the two FWM signals, to the outer holes. The swapping of the holes between the input and output masks ensures that the beams intersect at the central position, where the vapor cell is located. The masks are separated by a distance $D \approx 68\,\mathrm{cm}$, and the spacing between the holes is $s = 2\,\mathrm{mm}$.

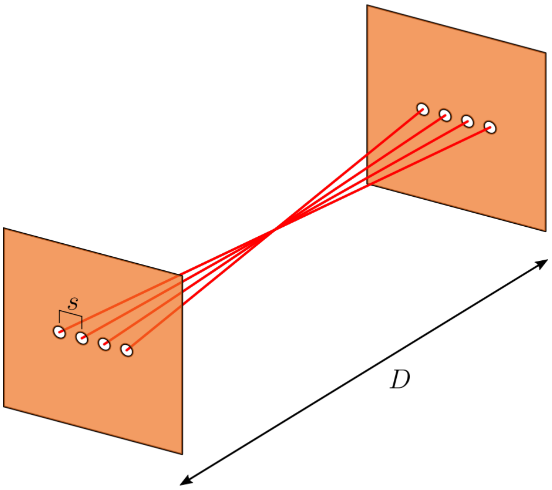

**Source:** The author (2024).

lens technique (VAITY; BANERJI; SINGH, 2013).

In a configuration where both incident beams possess the same power, $P_a/P_b = 1$, the two FWM signals can be generated with equal probabilities, and one may detect both $S_1$ and $S_2$ simultaneously. However, the power conversion from incident to generated beams is very low, and we are limited by the total power of the diode laser ($P \approx 27\,\mathrm{mW}$). Taking into account that for our first studies regarding the transfer of spatial structure we were not concerned with temporal correlations between the two signals, we detected $S_1$ and $S_2$ separately. This allows us to control the power ratio between the two fields, which helps to reduce scattered light, and to obtain better structured fields in general. In our setup, a strong and well-structured output was obtained when $P_a/P_b \approx 2$ for $S_1$ and $P_b/P_a \approx 2$ for $S_2$, and a beam power of the order of $160\ \mu\mathrm{W}$ for the incident field that has two-photon contribution to the process rendered a good compromise between output power and generated signal structure.

We arrange the setup in such a way that the waists of both incident beams are $w_0 \approx 0.5\,\mathrm{mm}$, and located inside the vapor cell, where they intercept. This gives a Rayleigh range of $z_R = \pi w_o^2/\lambda \approx 1\,\mathrm{m}$. For a cell of length $L = 5\,\mathrm{cm}$, we have $L/z_R \approx 0.05$, and we assume that the thin-medium regime ($L/z_R \ll 1$) is always satisfied. The rubidium cell, containing both $^{87}\mathrm{Rb}$ and $^{85}\mathrm{Rb}$ in natural abundances, is heated to about $70\,^{\circ}\mathrm{C}$ to increase atomic density. The atomic density at a temperature $T$ can be estimated by modeling the vapor as an ideal gas, $n_{\mathrm{at}} = P/k_B T$, and using the vapor pressure expression from Ref. (STECK, 2001)

$P_{\mathrm{v}} = 10^{7.193-4040T^{-1}}$. With this, for $T = 70\,^{\circ}\mathrm{C}$, we estimate a density of $n_{\mathrm{at}} \approx 10^9$ atoms/cm$^3$ [see Fig. 23(c)]. Figure 23(a) shows the absorption lines of rubidium obtained by passing an attenuated beam through the sample at different temperatures $T$, as well as the saturated absorption spectrum for reference.

For the experiments, we considered the $|5^2\mathrm{S}_{1/2}, F_g = 3\rangle \rightarrow |5^2\mathrm{P}_{3/2}\rangle$ transition of $^{85}\mathrm{Rb}$. We do not lock the laser frequency, instead we continuously sweep the frequency around the desired resonance, and capture short videos of the FWM signals with $10 - 50$ frames using a CMOS camera. Due to absorption, there is an interchange between scattered light from transmitted beams and nonlinear output arriving at the detection position, and therefore most of the residual scattered light fades away as the frequency approaches the resonance, giving way to the FWM beam. Even so, in all images we performed a background subtraction and applied filters to smooth out interferences. Figure 23(b) shows a typical FWM spectrum and the shaded region represents roughly the detection window.

The problem with scattered light in our system was particularly difficult to deal with,

**Figure 23** – (a) Saturated absorption at room temperature and absorption spectra of the $\mathrm{D}_2$ lines of $^{85}\mathrm{Rb}$ and $^{87}\mathrm{Rb}$ at different temperatures. (b) Absorption spectrum at $T \approx 72\,^{\circ}\mathrm{C}$ in the region of the transitions with $F_g = 2$ of $^{87}\mathrm{Rb}$, and $F_g = 3$ of $^{85}\mathrm{Rb}$. The blue curve shows a typical FWM spectrum, which is stronger at the $^{85}\mathrm{Rb}$ transition. The shaded area indicates the frequency region where we make our measurements. (c) Atomic density of the rubidium vapor as a function of the temperature $T$, calculated considering the sample as an ideal gas. Vertical dashed lines correspond to $T = 50, 60, 70\,^{\circ}\mathrm{C}$,

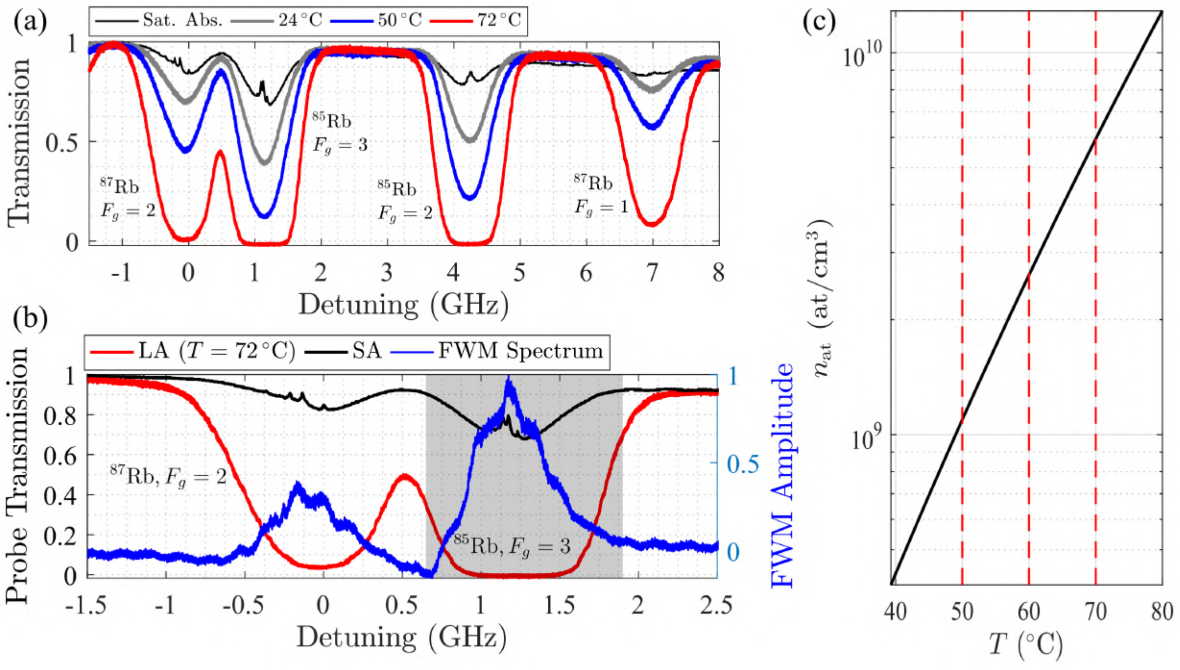

**Source:** The author (2024).

especially because we are dealing with non trivial modes of light. We believe that, among the possible reasons for this, such as multiple reflections and scattering on the cell wall interfaces, propagation inside the vapor, a diffuse sample, and natural diffraction of the input beams, which are much stronger than the generated signals, there is also a matter related to polarization. In a $\chi^{(3)}$ medium, the polarization of a propagating laser field can be rotated due to the presence of a magnetic field (Faraday rotation), and also by polarization self-rotation, in the absence of a magnetic field (HORROM et al., 2011). Therefore, since we rely solely on the angular separation between the light beams and on their polarizations to filter undesired light at the detection positions, polarization rotation of any nature makes this task more difficult.

## 3.4 GENERATING STRUCTURED LIGHT BEAMS IN THE LAB

We have talked a great deal about different structured light modes and their characteristics, but not so much about how to obtain these beams in the first place. This Section is dedicated to a brief description of the methods we employed to generate structured light modes using a phase-only spatial light modulator.

Allen *et al.* discussed the conversion of Hermite-Gaussian beams to LG beams, which is accomplished by employing mode converters composed of astigmatic optical elements (BEIJERSBERGEN et al., 1993). LG modes can also be generated from fundamental Gaussian beams using a spiral phase plate (BEIJERSBERGEN et al., 1994) or a computer generated hologram mask (HECKENBERG et al., 1992). This mask is a diffraction grating with a forked structure at the center that has as many dislocations as the order of the desired singularity, $\ell$. The first order diffracted beam is shown to possess the approximate intensity distribution of an LG beam with topological charge $\ell$ and radial index $p = 0$. It is, in fact, a superposition of modes with the same topological charge and different radial indices. Both spiral phase plates and computer generated holograms can also be used to efficiently generate LG beams with higher radial orders $p \neq 0$ (ARLT et al., 1998; RUFFATO; MASSARI; ROMANATO, 2014). The combination of computer generated holograms and spatial light modulators (SLM) offers a versatile method for the generation of various structured light modes and is vastly employed in many research areas (FORBES; DUDLEY; MCLAREN, 2016).

An SLM is a device used to introduce a spatially dependent phase-modulation to a light beam. Modern SLMs are controlled with computers and the device response is practically immediate, allowing to automatize the wave-front modulation procedure in many ways. Furthermore, the hologram is a gray scale image file that can be easily prepared with any desired transverse phase information and readily uploaded to the SLM chip. There is no need to print the phase mask in any physical form. The intensity of each pixel in the image is translated into voltage in the corresponding pixel of the array, effectively changing the refractive index in that region. With this, the image is "printed" onto the chip and, consequently, onto the phase distribution of the incident beam.

In this work we use the LCOS-SLM (liquid crystal on silicon spatial light modulator) model X10468-02 from Hamamatsu Photonics, shown in Fig. 24 with its main components indicated. The chip dimension of this model is $600 \times 800$ pixels with $20\,\mu\mathrm{m}$ sides. In the LCOS-SLM chip, a nematic liquid crystal (LC) is layered on top of an array of pixels and enclosed by a glass plate [Fig. 25(a)]. The LC molecules are uniaxial, i.e., possess an ordinary and an extraordinary index of refraction, $n_o$ and $n_e$, respectively, in orthogonal directions [Fig. 25(b)]. Their orientation is locally controlled by applying a specific voltage to each pixel. This results in a local change of the index of refraction, that leads to the phase modulation of the incoming light, which is then reflected by a dielectric mirror for the desired wavelengths. Note that due to the geometry of the LC molecules, the phase modulation will only occur if the direction of oscillation of the incoming electric field is parallel to the plane that contains both the ordinary and extraordinary axes, the $x$-$y$ plane (CARVALHO, 2020).

**Figure 24** – LCOS-SLM model X10468-02 from Hamamatsu Photonics with main parts indicated.

**Source:** Modified from (MOTTA, 2021).

### 3.4.1 Generation of optical vortices

In this section we outline the calculation of the field pattern diffracted from a spatial light modulator (SLM), with emphasis on the generation of OAM carrying LG modes with zero radial orders.

**Figure 25** – (a) Elements of the LCOS-SLM chip from Hamamatsu Photonics and (b) depiction of the uniaxial liquid crystal molecule with the indices of refraction $n_o$ and $n_e$ along the $y$ and $x$ directions, respectively.

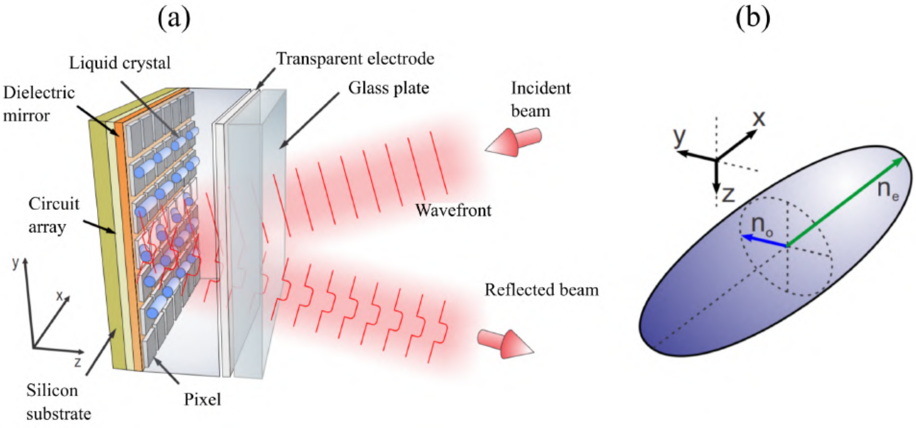

**Source:** Adapted from (CARVALHO, 2020).

Consider an SLM displaying a mask, or a hologram, represented by the 2D function $H(x, y) = \Phi(x, y)$, where $\Phi$ is the phase distribution of the desired field ($x, y$ are discrete coordinates of the SLM pixel sites). We assume that the effect of the SLM on the incident field $\mathcal{E}_{\text{in}}(\mathbf{r}_\perp)$ is the application of the phase factor:

$$T(x, y) = \exp\left[iH(x, y)\right]. \tag{3.4}$$

We can write the field immediately after leaving the chip as $\mathcal{E}_{\text{out}}(\mathbf{r}_\perp) = \mathcal{E}_{\text{in}}(\mathbf{r}_\perp)T(x, y)$, and the far-field diffracted pattern can be obtained by propagating the amplitude $\mathcal{E}_{\text{out}}$ from the plane of the chip to a plane at a large distance $z$.

We consider that the SLM chip is located at $z = 0$, where the minimum waist of the modulated field occurs. To generate an LG mode with topological charge $\ell$, the transmission function can be written in cylindrical coordinates as:

$$T_\ell(r, \phi) = \exp\left(i\ell\phi - i\frac{2\pi}{\Lambda}r\cos\phi\right), \tag{3.5}$$

where $\Lambda$ is the diffraction grating spacing in the $x$ direction. The phase modulation performed by the SLM is not 100% efficient, and therefore the diffraction grating is superimposed to the desired phase pattern to spatially separate the portion of the beam which is successfully modulated, and thus carries the desired OAM content. Defining the period $\kappa = 2\pi/\Lambda$, for an incident Gaussian beam, $\mathcal{E}_{\text{in}} = u_{0,0}$, we may expand the $m$-th diffracted order as (ARLT et al., 1998):

$$\mathcal{E}^{(m)}_{\text{out}}(\mathbf{r}_\perp) = \sum_{l,q} c^{(m)}_{l,q}\, u_{l,q}(\mathbf{r}_\perp)e^{-im\kappa r\cos\phi}, \tag{3.6}$$

where the coefficients are:

$$\begin{aligned} c_{l,q}^{(m)} &= \iint u_{0,0} T_\ell u_{l,q}^* \, e^{im\kappa r \cos\phi} r dr d\phi, \\ &= \int_0^\infty r dr V_0^0(r) V_q^{|l|}(r) \left\{ \int_0^{2\pi} e^{i(\ell-l)\phi - i(1-m)\kappa r \cos\phi} d\phi \right\}. \end{aligned} \tag{3.7}$$

We expect most of the incident power to be converted to the first diffracted order. Then, for $m = 1$ we obtain:

$$c_{l,q}^{(1)} = 2\pi \delta_{l,\ell} \int_0^\infty V_0^0(r) V_q^{|l|}(r) r dr, \tag{3.8}$$

and we see that the first diffracted order is a superposition of multiple radial modes with the same topological charge $l = \ell$. Furthermore, the fidelity with respect to the desired $u_{\ell,0}$ mode can be estimated via[1]:

$$\mathcal{F}_\ell = \frac{c_{\ell,0}^{(1)}}{\sqrt{\sum_q |c_{\ell,q}^{(1)}|^2}}. \tag{3.9}$$

Figures 26(a),(b) show the holograms encoding the azimuthal phase $\ell\phi$, with and without the periodic grating for the spatial separation of the diffracted orders, respectively. Figure 26(c) shows the estimate fidelity $\mathcal{F}_\ell$ calculated using Eq. (3.9) for different values of $\ell$. In Fig. 26(d) we show the intensity profiles of LG modes generated with holograms of the type presented in Fig. 26(b). Although we obtain the characteristic ring-shaped distribution that increases with $|\ell|$, additional outer rings can be seen, and this can be attributed to nonzero $p$ orders present on the output mode, which forbids the mode fidelity to reach the value 1. In the next section we discuss a method to improve the structure of our generated light modes.

### 3.4.2 Amplitude modulation with a phase-only SLM

Here we briefly present an amplitude modulation method using a phase-only SLM. This allows to increase the fidelity of the output mode with respect to the desired field, at the cost of decreasing the power converted to the first diffracted order.

To obtain a better-structured (higher fidelity) desired output field $\mathcal{E}(\mathbf{r}_\perp) = \mathcal{A}(\mathbf{r}_\perp) e^{i\Phi(\mathbf{r}_\perp)}$, the general idea is to include the information from the amplitude $\mathcal{A}$ into the mask encoding the phase $\Phi$. This is especially important when the desired field carries a more intricate transverse

---

[1] This is a rough estimate for our simplified calculation. Rigorously, it would be necessary to propagate the field from a position immediately after leaving the chip, to the far field.

**Figure 26** – (a) Hologram enconding the azimuthal phase $\Phi(x, y) = \phi = \tan^{-1}(y/x)$ ($\ell = 1$) with no periodic grating. (b) Same encoded phase but with gratings in the $x$ and $y$ directions with periods $\Lambda_x = \Lambda_y = 10$ pixels. The inset shows a zoom of the central region where the dislocation can be seen. (c) Estimate of the output beam fidelity $\mathcal{F}_\ell$ for $\ell = -5, ..., +5$. (d) Intensity profiles of LG modes generated with holograms of the type shown in (b) with $\ell = +1, ..., +5$.

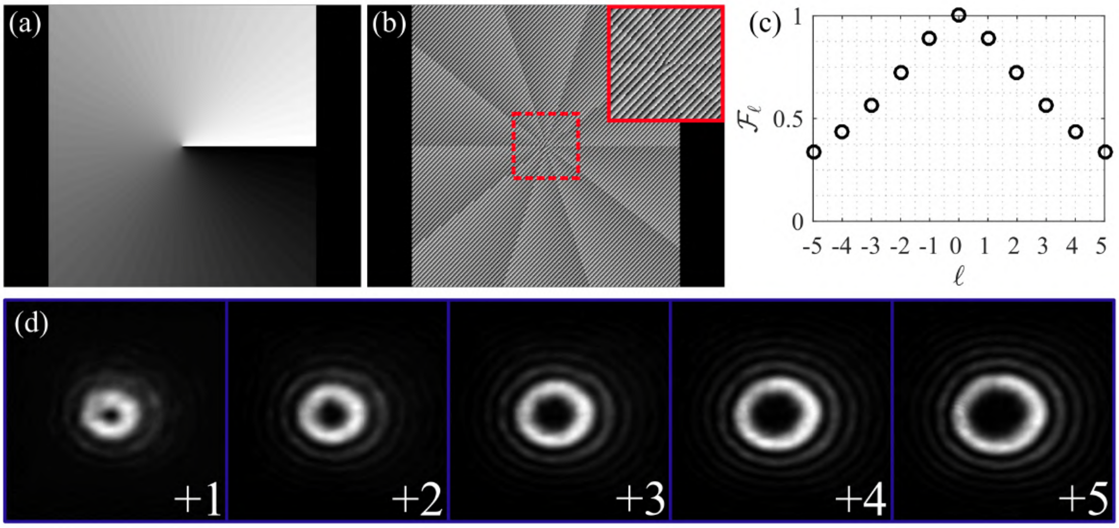

**Source:** The author (2024).

profile. To this end, a number of techniques can be employed (CLARK et al., 2016). Here, our method of choice consists on constructing the modified hologram $\tilde{H}$:

$$\tilde{H} = (1 + \frac{1}{\pi}\mathcal{S})(\Phi - \mathcal{S}), \tag{3.10}$$

where $\mathcal{S} = \mathrm{sinc}^{-1}(\mathcal{A})$. For a detailed description of this method, including the motivation behind it, and the numerical calculation of the inverse of the $\mathrm{sinc}(\cdot)$ function (which can be problematic) please refer to Ref. (AMARAL, 2016). Figure 27 shows the difference between the holograms with and without the amplitude modulation, for a desired field given by the composition of opposite topological charges of the form $u_{+2,0} + u_{-2,0}$.

In Fig. 28 we show the graphical interface we programmed in MATLAB® to generate the holograms used in this work. With this interface, we can work with five different families of modes: HG, LG, IG, as well as the Poincaré sphere and Hermite-Laguerre-Gaussian modes. The latter two will be defined in Chapter 4. We can also introduce gratings both in the $x$ and $y$ directions, and apply the amplitude modulation technique described above.

**Figure 27** – Holograms for generation of an optical mode given by the composition $u_{+2,0} + u_{-2,0}$ with a phase-only method (top), and with the inverse $\mathrm{sinc}$ amplitude modulation technique (bottom), and the corresponding output optical modes obtained in each case. The inset on the intensity graph shows the amplitude ($\propto \sqrt{I}$). In both cases we included linear gratings in both directions with periods $\Lambda_x = \Lambda_y = 10$ pix.

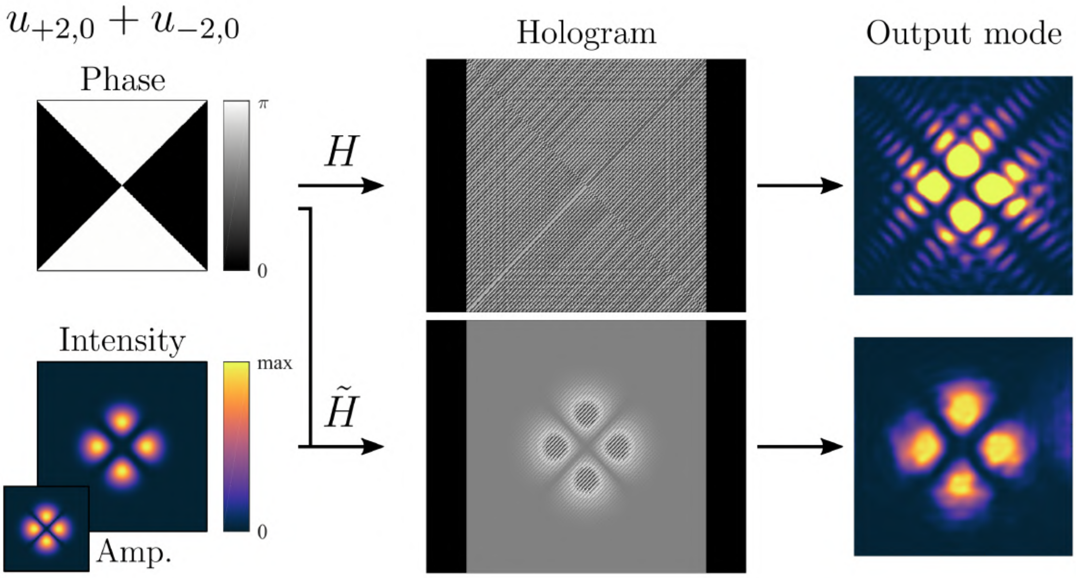

**Source:** The author (2024).

**Figure 28** – *Hologram Creator* interface programmed in MATLAB® using the Graphical User Interface Development Environment (GUIDE) to generate and upload our holograms to the SLM chip.

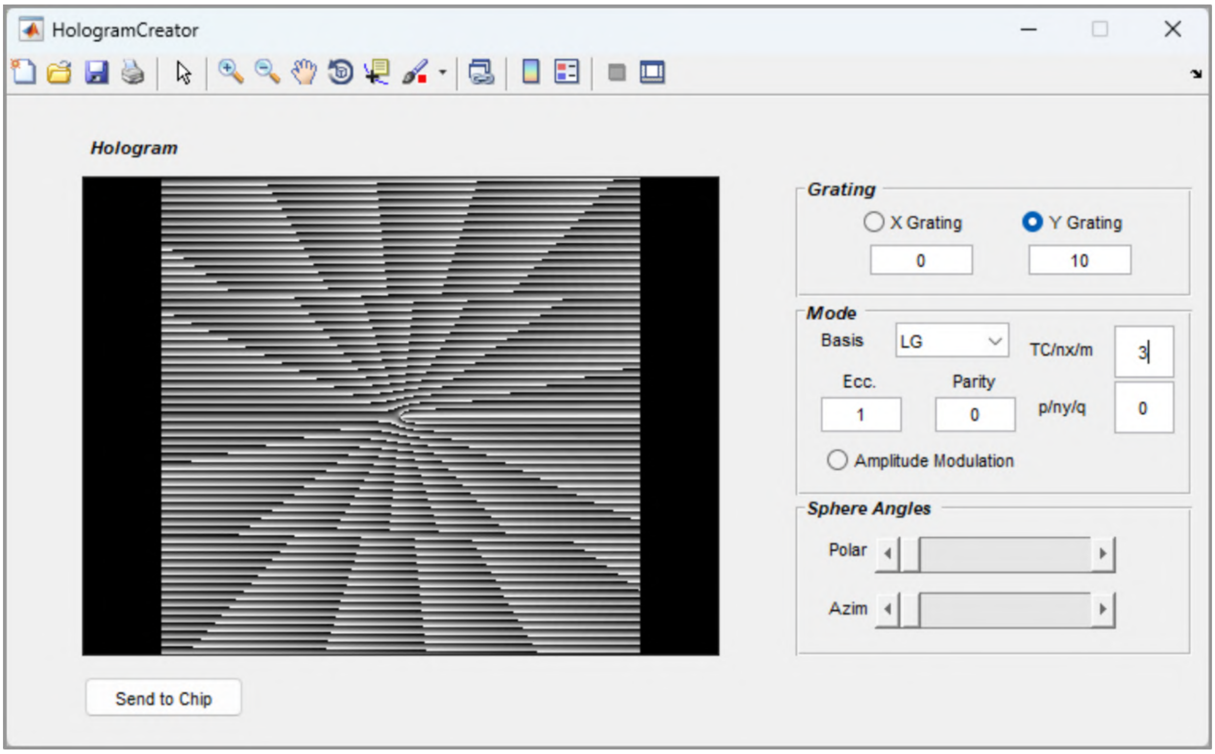

Grating
○ X Grating: 0
● Y Grating: 10

Mode
Basis: LG
TC/nx/m: 3
Ecc.: 1
Parity: 0
p/ny/q: 0
○ Amplitude Modulation

Sphere Angles
Polar
Azim

**Source:** The author (2024).

# 4 TRANSFER OF OPTICAL STRUCTURE VIA FOUR-WAVE MIXING IN RUBIDIUM VAPOR

In this Chapter we present a series of results on manipulations of optical spatial structure via FWM in Rb vapor. We divide the Chapter in three Sections. First, we discuss the tailored conversion of optical modes in a non-degenerate cascade FWM process taking advantage of a unique property of the Hermite-Gaussian basis. We then look at the conservation of OAM in the two-channel degenerate FWM configuration. Finally, we explore the transverse structure dynamics within the context of the OAM Poincaré sphere modes.

## 4.1 OPTICAL MODE CONVERSION IN A NON-DEGENERATE FOUR-WAVE MIXING PROCESS

In this Section we explore the already mentioned connection between the families of HG, LG and IG paraxial modes, beyond a purely mathematical point of view. Despite many similarities between these families of solutions of the paraxial wave-equation (PWE) and the possibility of expressing them in terms of one another (KIMEL; ELIAS, 1993; BANDRES; GUTIéRREZ-VEGA, 2004), they behave differently upon propagation in nonlinear media. Previously, a comparison between HG and parity-defined LG (PDLG) modes propagating in second-order nonlinear medium and undergoing the process of sum-frequency generation was realized (PIRES et al., 2020). It was demonstrated that the HG modes generates an up-converted field with a dominant mode carrying indices $m = m' + m''$ and $n = n' + n''$, where $m', n'$ and $m'', n''$ stand for the indices of the input beams. While the index summation rule cannot be generalized to the PDLG modes, one can use multiple HG modes for the up-conversion into a well-predictable dominant mode to form an LG or an IG mode at the output. This property was found useful to optical mode conversion protocols (PIRES et al., 2019). Importantly, the up-converted field will form a single, pure, mode with indices $m = m' + m''$ and $n = n' + n''$ only in the extended-medium regime, such that $z_R/L \ll 1$. Here $z_R$ is the Rayleigh length of the input modes and $L$ the length of the nonlinear medium (OFFER et al., 2021).

However, the extended-medium regime necessary for achieving high mode purity is not ideal for the $\chi^{(2)}$ processes such as sum-frequency generation (SFG) because efficient phase matching is rather difficult to obtain over the long propagation length (CANKAYA et al., 2014). Since the phase-matching condition across a significant extension is easier to satisfy in a $\chi^{(3)}$

nonlinear medium, here we investigate HG mode interactions and the possibility of the mode symmetry conversion in third-order nonlinear media.

Here we theoretically predict a unique property of the HG basis that allows to generate a highly pure HG mode using a cascade three-level system in $^{85}\mathrm{Rb}$ vapor. Furthermore, we demonstrate the possibility exploiting this property to obtain at the FWM output, modes that carry cylindrical and elliptical symmetries, corresponding to the PDLG and IG modes.

### 4.1.1 Distinct behavior for PDLG and HG modes

Let us consider a frequency up-conversion system consisting of rubidium vapor ($^{85}\mathrm{Rb}$), similar to previous four-wave mixing experiments reported in Refs. (OFFER et al., 2021; WALKER; ARNOLD; FRANKE-ARNOLD, 2012) and depicted in Fig. 29. This process is also named FWM induced by amplified spontaneous emission (ASE) (CHOPINAUD et al., 2018). The input beams consist as two near-infrared fields at $780$ and $776\ \mathrm{nm}$, leading to $5\mathrm{S}_{1/2}{-}5\mathrm{P}_{3/2}$ and $5\mathrm{P}_{3/2}{-}5\mathrm{D}_{5/2}$ transitions, respectively. Through the cascade decay via $6\mathrm{P}_{3/2}$, the atomic system can generate IR ($5.23\ \mu\mathrm{m}$) and blue ($420\ \mathrm{nm}$) coherent light.

**Figure 29** – Schematic illustration of the optical mode conversion under the FWM by amplification of spontaneous emission in Rb vapor. (a) The input HG modes with wave-lengths $780\ \mathrm{nm}$ and $776\ \mathrm{nm}$, $u_{780} = 0.899u^{\mathrm{HG}}_{1,0} - 0.437u^{\mathrm{HG}}_{0,1}$, $u_{776} = 0.899u^{\mathrm{HG}}_{1,0} + 0.437u^{\mathrm{HG}}_{0,1}$, interact to generate an up-converted blue field at $420\ \mathrm{nm}$, and an IR field at $5230\ \mathrm{nm}$. The blue output in this example case emerges as a highly pure Ince-Gaussian mode $\mathrm{IG}^{e}_{2,2}$ with ellipticity $\varepsilon = 2$. (b) Energy-level diagram for the FWM process.

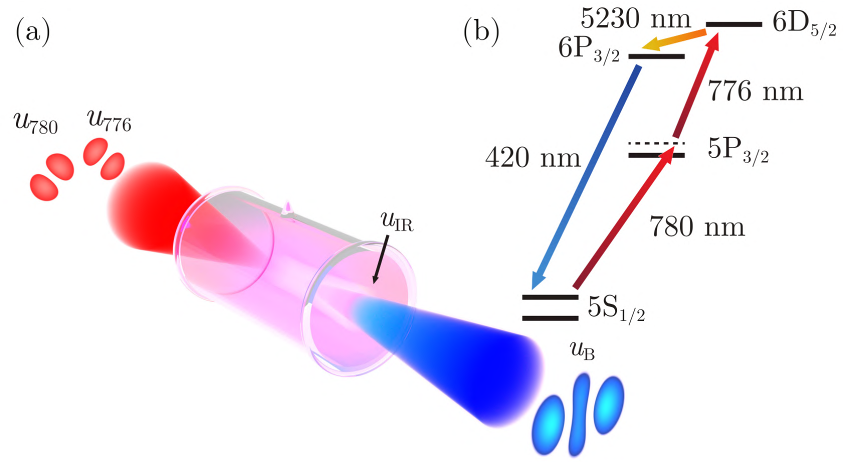

**Source:** Taken from Ref. (ROCHA et al., 2022).

Consider the monochromatic optical field of the generated blue light in the form:

$$\mathbf{E}_{\mathrm{B}}(\mathbf{r}) = \boldsymbol{\epsilon} u_{\mathrm{B}}(\mathbf{r}) e^{-i(k_{\mathrm{B}}z - \omega_{\mathrm{B}}t)} + \mathrm{c.c.}, \tag{4.1}$$

where $k_\mathrm{B}$ is the wave-number, $\omega_\mathrm{B}$ is the frequency, $\boldsymbol{\epsilon}$ is the polarization direction, and $u_\mathrm{B}(\mathbf{r})$ is the slowly varying complex field amplitude. In the paraxial approximation, considering a phase-matched setting, we can write the wave-equation describing the generation and propagation of the blue light mode as:

$$\left(\frac{i}{2k_\mathrm{B}}\nabla_\perp^2 + \frac{\partial}{\partial z}\right) u_\mathrm{B} = \frac{ik_\mathrm{B}}{2\varepsilon_0} P^{(3)}(\omega_\mathrm{B}), \tag{4.2}$$

where $\varepsilon_0$ is the vacuum permittivity, $\nabla_\perp^2$ is the transverse Laplacian and $P^{(3)}(\omega_\mathrm{B})$ is the projected medium polarization at the blue FWM field frequency. For the non degenerate FWM process we are studying, where the pump beams spontaneously generate signal and conjugate beams (in our case, blue and infrared beams, respectively), we may write for the macroscopic polarization:

$$P^{(3)}(\omega_\mathrm{B}) = \varepsilon_0 \chi^{(3)}(\omega_\mathrm{B}) u_{780} u_{776} u_\mathrm{IR}^*. \tag{4.3}$$

The overall efficiency of the FWM is determined by the resonances of the medium described by $\chi^{(3)}$ along with the spatial overlap integral. For reasons already discussed, we shall regard the interaction medium simply as a channel for the nonlinear interaction, and therefore we consider the nonlinear susceptibility $\chi^{(3)}$ a uniform quantity. We know that the solution to Eq. (4.2) can be found in terms of a superposition of paraxial modes, in this case, HG modes. We then write:

$$u_\mathrm{B}(\mathbf{r}) \propto \sum_{m,n} \mathcal{A}_m^n u_{m,n}^\mathrm{HG}(\mathbf{r}), \tag{4.4}$$

where $\mathcal{A}_m^n$ is the full overlap integral on the HG basis, which is responsible for selecting the optical modes that emerge in the superposition of the nonlinear output. The overlap integral in rectangular coordinates as

$$\mathcal{A}_m^n = \int_{-\infty}^{+\infty}\int_{-\infty}^{+\infty}\int_{-L/2}^{L/2} u_{780} u_{776} u_\mathrm{IR}^* u_{m,n}^* dxdydz, \tag{4.5}$$

where $L$ is the vapor cell length. We will assume that the IR field $u_\mathrm{IR}$ can be considered as a fundamental Gaussian mode, $u_\mathrm{IR} \to u_{0,0}^\mathrm{HG}$. For arbitrary pump structures, $u_{780}, u_{776}$, we have already seen that the full overlap integrals becomes a weighted sum of multiple integrals of four HG modes of the form:

$$\mathcal{A}_{mm'm''}^{nn'n''} = \int_{-L/2}^{L/2}\int_{-\infty}^{\infty}\int_{-\infty}^{\infty} u_{m',n'}^\mathrm{HG} u_{m'',n''}^\mathrm{HG} u_{0,0}^{\mathrm{HG}*} u_{m,n}^{\mathrm{HG}*} dxdydz. \tag{4.6}$$

In Chapter 2 we have detailed the calculation of this kind of integral, and studied the associated selection rules in the particular configuration of FWM induced by ASE in an extended interaction medium. Here we shall explore the effective selection rule, resulting from restrictions imposed by the transverse and longitudinal overlaps, the so-named index-sum rule, and show how it can be used to tailor the spatial structure of the blue light output.

To make evident that the HG basis indeed presents a more convenient property of optical mode transfer, let us first compare the nonlinear wave-mixing using as input beams both PDLG and HG modes. The size of the Rb cell considered for the calculations is $L = 7\ \mathrm{cm}$, which is a common length in experimental setups (OFFER et al., 2021; WALKER; ARNOLD; FRANKE-ARNOLD, 2012). The ratio between the Rayleigh range of the reference beam (either of the pump beams at $780$ or $776\ \mathrm{nm}$) and the cell length is $z_R/L \approx 0.098$ ($L/z_R \approx 10$). Since PDLG modes can be seen as superposition of helical LG modes, we can use the same expressions obtained for the LG basis in Chapter 2. Figure 30(a),(b) shows the intensity distribution for the input beams $u_{780} = \mathrm{LG}^{o}_{1,2}, u_{776} = \mathrm{LG}^{o}_{0,1}$, as well as that of the generated beam $u_{\mathrm{B}}$, and the respective histograms for the probabilities of each mode being excited, or the mode weights. The indices $l_{780}, l_{776}, l_{\mathrm{B}}$ and $p_{780}, p_{776}, p_{\mathrm{B}}$ refer to the azimuthal and radial indices for the PDLG superpositions, while $m_{780}, m_{776}, m_{\mathrm{B}}$ and $n_{780}, n_{776}, n_{\mathrm{B}}$ are the indices for the HG case. We see that the index-sum rule is fulfilled.

**Figure 30** – FWM processes using PDLG and HG modes. In the case of PDLG modes, the input beams were taken in the form of (a) $u_{780} = \mathrm{LG}^{o}_{1,2}, u_{776} = \mathrm{LG}^{o}_{0,1}$. In the case of HG modes, the input beams were taken in the form of (c) $u_{780} = u^{\mathrm{HG}}_{1,2}, u_{776} = u^{\mathrm{HG}}_{0,1}$. In both cases, (b,d) represent the histograms with the optical mode weights for PDLG and HG superpositions, respectively.

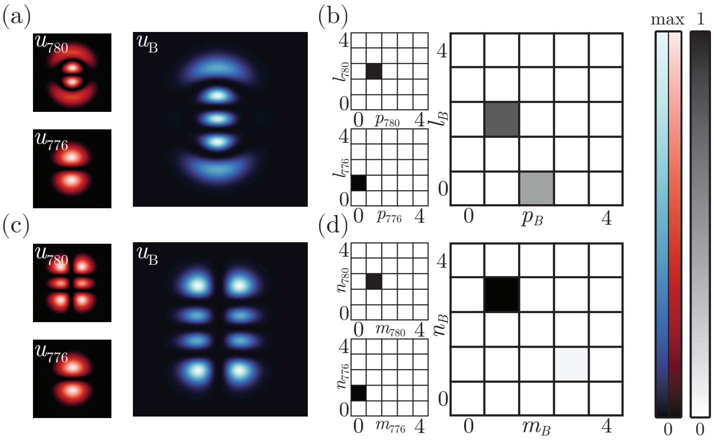

**Source:** Taken from Ref. (ROCHA et al., 2022).

We see that the FWM of LG beams creates a superposition with relevant contributions of two LG modes in the up-converted beam (OFFER et al., 2021; LANNING et al., 2017). In our case, the generated beam carries a superposition of $\mathrm{LG}^{o}_{1,2}$ and $\mathrm{LG}^{o}_{2,0}$. In general, mixing PDLG beams in a third-order nonlinear medium through the process of FWM results in multiple LG modes.

On the other hand, when HG modes are considered as input beams, the behavior is different. In Figure 30 (c),(d) the input beams were taken in the form of $u_{780} = u^{\mathrm{HG}}_{1,2}, u_{776} = u^{\mathrm{HG}}_{0,1}$ together with the histograms for the mode weights. In this case, the FWM field is composed of $u_{\mathrm{B}} = -0.9991 u^{\mathrm{HG}}_{1,3} + 0.0413 u^{\mathrm{HG}}_{3,1}$. Therefore, we conclude that for HG beams taken as input modes, the output field emerges as a nearly pure mode with indices $m = m' + m''$ and $n = n' + n''$, where $m', n'$ and $m'', n''$ are the indices for each input beam. Interestingly, even though both LG and HG modes are solutions of the PWE in different coordinate frames, the response under nonlinear interactions are distinct (PIRES et al., 2020).

### 4.1.2 Tailored generation of PDLG and IG modes at the blue FWM output

Now that we now it is possible generate a highly pure HG mode carrying indices $m = m' + m''$ and $n = n' + n''$, we can tailor the structure of the pump beams to obtain desired optical modes at the FWM output. This is done by preparing the input modes as superpositions of the form:

$$u_{780} = \sum_{m,n} \alpha_{m,n} u^{\mathrm{HG}}_{m,n}, \tag{4.7}$$

$$u_{776} = \sum_{m',n'} \beta_{m',n'} u^{\mathrm{HG}}_{m',n'}, \tag{4.8}$$

with the weights $\alpha_{m,n}, \beta_{m,n}$ carefully set in order to attain a desired spatial mode at the blue light output. Note that the FWM process we study here one of the participating fields is Gaussian, and therefore regarding spatial structure we essentially have a situation analogous to a three-wave interaction. Schematically, we can represent the process as:

$$\left.\begin{array}{c} u_{780} = \sum_{m,n} \alpha_{m,n} u^{\mathrm{HG}}_{m,n} \\ u_{776} = \sum_{m',n'} \beta_{m',n'} u^{\mathrm{HG}}_{m',n'} \end{array}\right\} \Longrightarrow \left\{\begin{array}{c} u_{\mathrm{IR}} = u^{\mathrm{HG}}_{0,0} \\ u_{\mathrm{B}} = \sum_{m_{\mathrm{B}},n_{\mathrm{B}}} \mathcal{A}^{n_{\mathrm{B}}}_{m_{\mathrm{B}}} u^{\mathrm{HG}}_{m_{\mathrm{B}},n_{\mathrm{B}}}. \end{array}\right. \tag{4.9}$$

The procedure to determine the values for these coefficients, as well as limitations of the method, are discussed in Ref. (PIRES et al., 2019) for the optical mode conversion in SFG.

Figure 31 shows the optical mode conversion to PDLG modes, consisting of cylindrically symmetric beams. The left column shows the intensities of the input modes $u_{780}, u_{776}$ together with the up-converted field $u_{\mathrm{B}}$, while the histograms in the right column are associated to the weight of each HG mode for all three interacting fields $u_{780}, u_{776}, u_{\mathrm{B}}$. Here, $m_{780}, m_{776}, m_{\mathrm{B}}$ and $n_{780}, n_{776}, n_{\mathrm{B}}$ stand for the indices of the HG modes composing the optical fields $u_{780}, u_{776}, u_{\mathrm{B}}$

respectively. We show the generation of the optical modes $u_\mathrm{B} = 0.908u^\mathrm{HG}_{1,2} - 0.418u^\mathrm{HG}_{3,0} \simeq \mathrm{LG}^e_{0,3}$ in Fig. 31(a),(b); $u_\mathrm{B} = 0.500u^\mathrm{HG}_{1,2} + 0.866u^\mathrm{HG}_{3,0} \simeq \mathrm{LG}^e_{1,1}$ in Fig. 31(c),(d); and $u_\mathrm{B} = 0.708u^\mathrm{HG}_{1,3} + 0.707u^\mathrm{HG}_{3,1} \simeq \mathrm{LG}^o_{1,2}$ in Fig. 31(e),(f).

The conversion to elliptical beams (IG modes) is displayed in Fig. 32, presented in the same way as the case for PDLG modes. We show the generation of the elliptical modes $u_\mathrm{B} = 0.893u^\mathrm{HG}_{1,3} + 0.450u^\mathrm{HG}_{3,1} \simeq \mathrm{IG}^o_{4,2}$ in Fig. 32(a),(b); $u_\mathrm{B} = 0.265u^\mathrm{HG}_{0,2} - 0.964u^\mathrm{HG}_{2,0} \simeq \mathrm{IG}^e_{2,2}$ in Fig. 32(c),(d); and $u_\mathrm{B} = 0.968u^\mathrm{HG}_{0,3} - 0.253u^\mathrm{HG}_{2,1} \simeq \mathrm{IG}^o_{3,1}$ in Fig. 32(e),(f). All weights $\alpha_{m,n}$ and $\beta_{m,n}$ are normalized such that $\sum_{m,n} |\alpha_{m,n}|^2 = \sum_{m,n} |\beta_{m,n}|^2 = 1$, and the eccentricity parameter for all IG modes is $\varepsilon = 2$.

**Figure 31** – Optical mode conversion to PDLG modes (cylindrical symmetry). The interacting modes are given by: (a) $u_{780} = -0.316u^\mathrm{HG}_{2,0} + 0.948u^\mathrm{HG}_{0,2}$, $u_{776} = u^\mathrm{HG}_{1,0}$, $u_\mathrm{B} = \mathrm{LG}^e_{0,3}$; (c) $u_{780} = 0.707u^\mathrm{HG}_{2,0} + 0.707u^\mathrm{HG}_{0,2}$, $u_{776} = u^\mathrm{HG}_{1,0}$, $u_\mathrm{B} = \mathrm{LG}^o_{1,1}$; (e) $u_{780} = -0.865u^\mathrm{HG}_{3,0} - 0.500u^\mathrm{HG}_{1,2}$, $u_{776} = u^\mathrm{HG}_{0,1}$, $u_\mathrm{B} = \mathrm{LG}^o_{1,2}$. (b),(d),(f) show the histograms with the mode weights shown in (a),(c),(e), respectively.

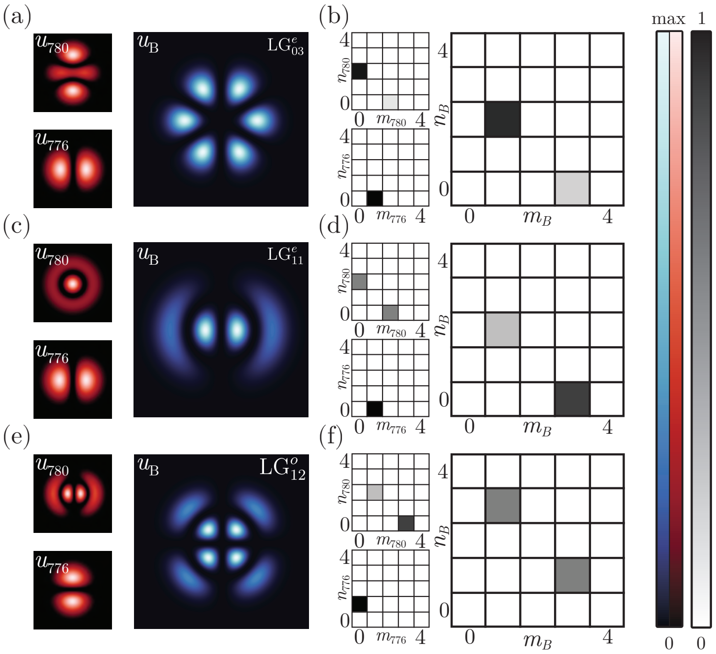

**Source:** Taken from Ref. (ROCHA et al., 2022).

To summarize this Section, we theoretically studied the optical mode up-conversion through the process of the FWM induced by ASE. Using the PDLG and HG modes as input beams, the generated modal superposition was analyzed using analytical and numerical approaches. We found that in the case of PDLG modes, the up-converted beam carries a superposition of modes with different indices. In contrast, when the HG basis is considered, the nonlinear wave-mixing results in the generation of a strongly dominant, almost pure HG mode with indices given by the sums of the input indices, $m = m' + m''$ and $n = n' + n''$. From a fundamental

**Figure 32** – Optical mode conversion to IG modes (elliptical symmetry). The interacting modes were taken in the following form: (a) $u_{780} = -0.471u^{\mathrm{HG}}_{2,0} - 0.881u^{\mathrm{HG}}_{0,2}$, $u_{776} = u^{\mathrm{HG}}_{1,1}$, $u_{\mathrm{B}} = \mathrm{IG}^{o}_{4,2}$; (c) $u_{780} = 0.899u^{\mathrm{HG}}_{1,0} - 0.437u^{\mathrm{HG}}_{0,1}$, $u_{776} = 0.899u^{\mathrm{HG}}_{1,0} + 0.437u^{\mathrm{HG}}_{0,1}$, $u_{\mathrm{B}} = \mathrm{IG}^{e}_{2,2}$; (e) $u_{780} = -0.421u^{\mathrm{HG}}_{2,0} - 0.907u^{\mathrm{HG}}_{0,2}$, $u_{776} = u^{\mathrm{HG}}_{0,1}$, $u_{\mathrm{B}} = \mathrm{IG}^{o}_{3,1}$. (b),(d),(f) show the histograms with the mode weights in (a),(c),(e), respectively.

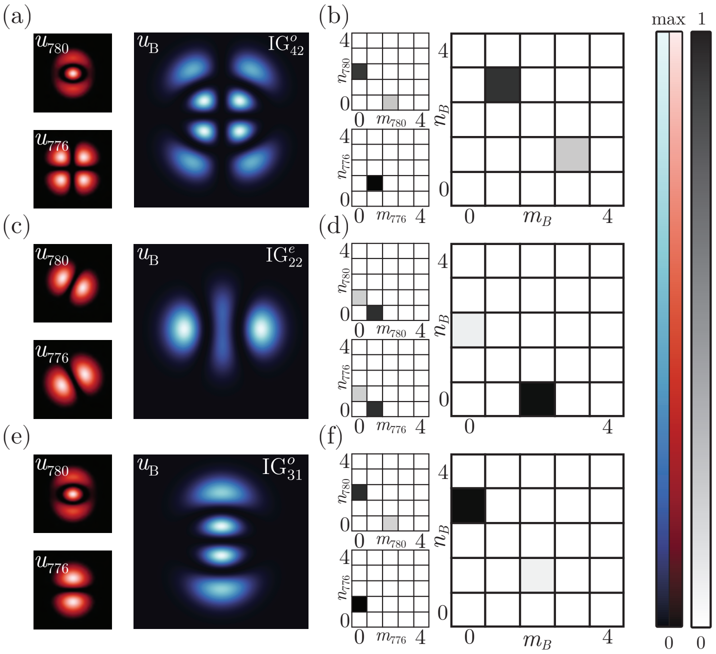

**Source:** Taken from Ref. (ROCHA et al., 2022).

viewpoint, this property highlights important differences between the solutions for the PWE that are revealed in the nonlinear regime of wave propagation. We demonstrated that this property can be exploited to obtain a target mode with high fidelity at the blue light output by precisely adjusting the weights of the input HG mode superpositions. These results may find applications in designing new optical communication protocols, and in the generation of entangled qubits and qudits, where a precise manipulation of optical modes is required (ZHANG et al., 2016; KRENN et al., 2014).

It is important to highlight that our analysis relies on the approximation that the spontaneously generated IR field is purely Gaussian. This has been assumed in other works (WALKER; ARNOLD; FRANKE-ARNOLD, 2012; CHOPINAUD et al., 2018; OFFER et al., 2021), due to the complications associated with the detection of this signal. For the regime we were interested in and the results we sought, we believe that this approximation is appropriate. In reality, the IR and blue light fields are entangled in their OAM degrees of freedom, as was demonstrated in (OFFER et al., 2018). In fact, they are entangled in the transverse spatial degrees of freedom, more generally (BOYER et al., 2008; NIRALA et al., 2023). This means that not only the blue signal, but both fields, which in the quantum level can be seen as a photon-pair generated in the process, occupy several transverse spatial states. This has been taken into account in (LANNING et al., 2017), and subtle differences were noted with respect to the results from (WALKER; ARNOLD; FRANKE-ARNOLD, 2012). In the fully quantum regime, this multi-spatial-mode nature of the photon-pair generated in FWM must be taken into account, just like in the process of PDC, which has been thoroughly investigated over the years.

## 4.2 ORBITAL ANGULAR MOMENTUM CONSERVATION IN A TWO-CHANNEL FWM SETTING

The interaction between light and matter is accompanied by the transfer of linear and angular momentum. The transfer of linear momentum is associated with the radiation pressure on atoms and small particles, which is the key mechanism in the laser cooling of atoms (CHU et al., 1985). The transfer of spin angular momentum from circularly polarized light was first demonstrated almost a century ago by Beth (BETH, 1936). Only after 1992 the transfer of OAM from LG beams to small particles was demonstrated (HE et al., 1995; FRIESE et al., 1996). In both of these works the particles were trapped at the dark focus of an LG beam by the dipole force and set into rotating motion due to the beam's helical phase structure. The quantized nature of the OAM of light has been explored (LEACH et al., 2002) and the transfer of OAM in units of $\ell\hbar$ to atoms was demonstrated in a sodium Bose-Einstein condensate (ANDERSEN et al., 2006). Also, after the first proposals, new possibilities were opened in communications technology, due to the capability of information multiplexing with an additional degree of freedom of light, and the infinite dimensionality of the OAM space (PAN et al., 2019).

Manipulation of light carrying OAM has been performed in the linear and nonlinear regimes. In the nonlinear regime, these beams have been applied to investigate second harmonic generation (SHG) in crystals (DHOLAKIA et al., 1996; COURTIAL et al., 1997), where the beam at the fundamental frequency $\omega$ carries topological charge (TC) $\ell$ and, due to the conservation of OAM, the frequency doubled beam emerges with $2\ell$. This is one key idea when employing OAM beams in nonlinear optics: the transfer of topological charge and transverse structure from incident to generated fields. Today, SHG and other second-order processes offer a highly versatile platform for exploring the transverse degrees of freedom of light.

Another nonlinear optical process that also allowed important studies on light-matter interactions involving the spatial structure of light is the four-wave mixing process, a third-order phenomenon. In this context, a widely explored configuration is FWM induced by ASE in a cascade system in rubidium vapor (VERNIER et al., 2010). As described in Section 4.1, in this process, two incident photons at $776\,\mathrm{nm}$ and $780\,\mathrm{nm}$ interact to generate blue light at $420\,\mathrm{nm}$ with an emission also at $5.23\ \mathrm{\mu m}$. This setting has been used to achieve the transfer of OAM (CHOPINAUD et al., 2018) and intricate beam structures (WALKER; ARNOLD; FRANKE-ARNOLD, 2012) from the incident infrared pumps to the generated blue light beam; to perform operations with the OAM content of the incident beams (AKULSHIN et al., 2016); to evidence the OAM entanglement between the generated blue and infrared beams (OFFER et al., 2018); and the Gouy phase-matching requirement in an extended-medium regime (OFFER et al., 2021). Another atomic level configuration, a double–$\Lambda$ system was used in Ref. (PRAJAPATI et al., 2019) to combine and perform operations with the topological charges of pump and probe beams under a FWM process in hot $\mathrm{Rb}$ vapor.

In this Section, we explore the degenerate FWM in an experimental condition where two nonlinear signals are excited by the same incident fields in a heated sample of $\mathrm{Rb}$ atoms. We employed this setting in previous experiments to investigate a spectral shift of the two FWM signals, also in $\mathrm{Rb}$ vapor (ALVAREZ; ALMEIDA; VIANNA, 2021), and the cross-correlation between the pairs of transmitted beams and FWM signals in a cold $\mathrm{Rb}$ cloud (ALMEIDA; MOTTA; VIANNA, 2023). We also conducted a theoretical study of the spatial shape of the FWM signals and the effects caused by the resonances of the medium (MOTTA; ALMEIDA; VIANNA, 2022).

Here we use this multi-channel FWM setting to combine pairs of OAM values $(\ell_a, \ell_b)$ carried by the two driving beams, and encode this information onto the TCs of the two output beams, $(\ell_1, \ell_2)$. In this context, the incident OAM values can be revealed by measuring the output TCs. We experimentally verify these combinations and discuss scenarios where different pairs of output topological charges are achieved. We first consider a situation where only one of the incident beams carries OAM, while the other one is set as a Gaussian beam. In this case, we verify the transfer of topological charge from the incident to generated signals. Next, we introduce non-zero topological charges in both incident beams and verify the fulfillment of the selection rules dictating the FWM processes. In particular, as the two nonlinear signals are driven by the same fields, the relation between the difference in the incident and outgoing TC is preserved to less than one factor, which in the case of an FWM process is a factor of three.

### 4.2.1 Wave-equations for the two-channel FWM setting

In Chapter 2 we have established the semi-classical modeling of the two simultaneous FWM signals in a two-level atom. This is the case when one has the two pump beams, $\mathbf{E}_a$ and $\mathbf{E}_b$, with parallel circular polarizations. On the other hand, for linearly polarized incident beams with orthogonal polarizations, the interaction can be seen as taking place in a three-level atomic system, constituted of two degenerate ground states $|1\rangle\,, |3\rangle$, and an excited state $|2\rangle$. Of course, to fully describe the atomic response in the temporal and spectral domains, the optical Bloch's equations of the three-level system should be solved with the appropriate considerations. However, as we have repeatedly discussed, the optical modes of the driving fields dominate the transverse structure dynamics, and we may neglect any spatial dependence of the atomic coherence. This allows us to treat the nonlinear susceptibility $\chi^{(3)}$ as a uniform factor that does not affect our overlap integrals. Figure 33(a) shows the spatial orientation of the incident and generated light beams in the two-channel configuration. Each generated signal can be seen as a contribution from two pathways starting from different ground states, as illustrated in Fig. 33(b) for the field $\mathbf{E}_1$.

**Figure 33** – (a) Spatial orientation of incident and generated signals near the interaction region. (b) Two pathways associated with the generation of the $\sigma^{\pm}$ components of the FWM signal $\mathbf{E}_1$ in a three-level atomic system.

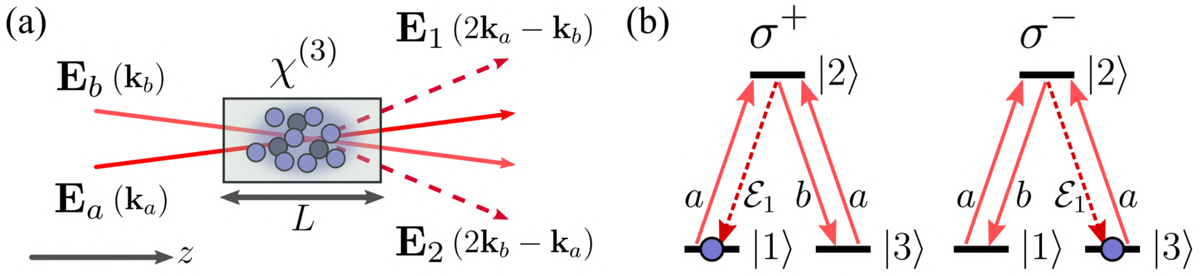

**Source:** The author (2024).

The electric fields of the light beams participating in the FWM processes are written as:

$$\mathbf{E}_i(\mathbf{r},t) = \frac{1}{2}\boldsymbol{\epsilon}_i \mathcal{E}_i(\mathbf{r}) e^{-i(\mathbf{k}_i \cdot \mathbf{r} - \omega_i t)} + \text{c.c.}, \tag{4.10}$$

$i \in \{a, b, 1, 2\}$, where $\boldsymbol{\epsilon}_i$ is the polarization direction, $\mathcal{E}_i$ is the slowly varying field amplitude, $\mathbf{k}_i$ is the wave-vector, and $\omega_i = c|\mathbf{k}_i|$ is the frequency. As we have seen in Chapter 2, the slowly varying amplitudes of the FWM signals, $\mathcal{E}_1$ and $\mathcal{E}_2$, generated in the directions $(2\mathbf{k}_a - \mathbf{k}_b)$ and $(2\mathbf{k}_b - \mathbf{k}_a)$, are calculated by solving the non homogeneous wave equations with source terms given by the corresponding third-order nonlinear polarizations. In the paraxial regime, they read (MOTTA; ALMEIDA; VIANNA, 2022):

$$\left(\frac{i}{2k_1}\nabla_\perp^2 + \frac{\partial}{\partial z}\right)\mathcal{E}_1 = \kappa_1 \mathcal{E}_a^2 \mathcal{E}_b^* e^{-i\Delta k_1 z}, \tag{4.11}$$

$$\left(\frac{i}{2k_2}\nabla_\perp^2 + \frac{\partial}{\partial z}\right)\mathcal{E}_2 = \kappa_2 \mathcal{E}_b^2 \mathcal{E}_a^* e^{-i\Delta k_2 z}, \tag{4.12}$$

where the couplings $\kappa_1$ and $\kappa_2$ are proportional to the nonlinear susceptibilities associated with the two nonlinear processes, $\chi_1$ and $\chi_2$, $\Delta k_1 = |2\mathbf{k}_a - \mathbf{k}_b - \mathbf{k}_1|$ and $\Delta k_2 = |2\mathbf{k}_b - \mathbf{k}_a - \mathbf{k}_2|$ are the phase mismatches. Owing to the orthogonality and completeness of paraxial modes, we can write the solutions to Eqs. (4.11) and (4.12) as general superpositions of the form:

$$\mathcal{E}_1(\mathbf{r}) = \sum_{\ell,p} \alpha_{\ell,p} u_{\ell,p}(\mathbf{r}), \tag{4.13}$$

$$\mathcal{E}_2(\mathbf{r}) = \sum_{\ell,p} \beta_{\ell,p} u_{\ell,p}(\mathbf{r}). \tag{4.14}$$

We consider that the incident fields can be written as $\mathcal{E}_a(\mathbf{r}) = \mathcal{E}_a^0 u_a(\mathbf{r})$ and $\mathcal{E}_b(\mathbf{r}) = \mathcal{E}_b^0 u_b(\mathbf{r})$, where $\mathcal{E}_{a,b}^0$ gives the total power content of each field, $P_{a,b} = \frac{1}{2}c\varepsilon_0|\mathcal{E}_{a,b}^0|^2$, and $u_{a,b}(\mathbf{r})$ carries their spatial structure. Taking into account that the paraxial basis modes $\{u_{\ell,p}\}$ carry the information from the transverse structure of the generated fields $\mathcal{E}_{1,2}$, the problem becomes that of finding the expansion coefficients $\alpha_{\ell,p}$ and $\beta_{\ell,p}$. They are called the full spatial overlap integrals, and can be expressed as (LANNING et al., 2017):

$$\alpha_{\ell,p} = \kappa_1 \mathcal{E}_1^0 \int_{-L/2}^{L/2} \mathcal{A}_{\ell,p}(z) e^{-i\Delta k_1 z} dz, \tag{4.15}$$

$$\beta_{\ell,p} = \kappa_2 \mathcal{E}_2^0 \int_{-L/2}^{L/2} \mathcal{B}_{\ell,p}(z) e^{-i\Delta k_2 z} dz, \tag{4.16}$$

where $\mathcal{E}_1^0 = (\mathcal{E}_a^0)^2(\mathcal{E}_b^0)^*$, $\mathcal{E}_2^0 = (\mathcal{E}_b^0)^2(\mathcal{E}_a^0)^*$ and

$$\mathcal{A}_{\ell,p}(z) = \iint u_a^2 u_b^* u_{\ell,p}^* d^2\mathbf{r}_\perp, \tag{4.17}$$

$$\mathcal{B}_{\ell,p}(z) = \iint u_b^2 u_a^* u_{\ell,p}^* d^2\mathbf{r}_\perp, \tag{4.18}$$

are the transverse overlap integrals of the product of incident beams on the mode basis with waist $w_0$. Since we consider the thin-medium, we can approximate $\alpha_{\ell,p} \simeq \kappa_1 T_1(L)\Lambda_p^\ell(0)$, where $T_1(L) = \int_{-L/2}^{L/2} e^{-i\Delta k_1 z} dz = L\,\mathrm{sinc}(\Delta k_1 L/2)$ is the efficiency measure associated with the phase-matching. Note that the factors $\kappa_1 T_1(L)$ is common for all $(\ell, p)$, and therefore they do not affect the mode superpositions of the generated fields. For this reason we do not carry them further. The same is true for $\beta_{\ell,p}$. The same equations will be used in Section 4.3.

### 4.2.2 Simultaneous OAM transfer to two FWM signals

For incident fields described as pure LG modes with topological charges $\ell_a, \ell_b$, $u_a = u_{\ell_a,0}$ and $u_b = u_{\ell_b,0}$, the azimuthal integrals in the transverse overlaps impose the conditions:

$$\ell_1 = 2\ell_a - \ell_b, \tag{4.19}$$

$$\ell_2 = 2\ell_b - \ell_a, \tag{4.20}$$

over the allowed topological charge values of signals $\mathcal{E}_1$ and $\mathcal{E}_2$, respectively. These are the OAM conservation selections rules in both FWM processes. The generated fields at the detection position, $z_d > L/2$, can be expressed as:

$$\mathcal{E}_1(\mathbf{r}_\perp, z_d) = e^{i(2\ell_a - \ell_b)\phi} A_1(r, z_d), \tag{4.21}$$

$$\mathcal{E}_2(\mathbf{r}_\perp, z_d) = e^{i(2\ell_b - \ell_a)\phi} A_2(r, z_d), \tag{4.22}$$

where the functions $A_{1,2}(r, z)$ describe the radial amplitude distributions and phase profiles:

$$A_1(r, z) = \sum_p \alpha_{\ell_1,p} V_p^{|\ell_1|}(r, z), \tag{4.23}$$

where we write the LG mode function as $u_{\ell,p}(\mathbf{r}) = V_p^{|\ell|}(r, z) e^{i\ell\phi}$, and similarly for $A_2$.

In a first moment, we performed the experiments setting the topological charge of $\mathbf{E}_b$ as zero, $\ell_b = 0$, and varied $\ell_a$. The selection rules thus require that:

$$\ell_1 = 2\ell_a, \tag{4.24}$$

$$\ell_2 = -\ell_a. \tag{4.25}$$

We show in Fig. 34 the intensity profiles of both FWM signals, as well as their tilted lens profiles when $\ell_a = -1, 0, +1$. When $\ell_a = 0$, both generated beams are Gaussian, as expected, and for $\ell_a = \pm 1$, they carry a ring-shaped profile, characteristic of OAM carrying beams. However, only with the information from the intensity distribution, it is hard to distinguish topological charge values, and there is no way to identify the helicity of the vortex. To this end, we employ the tilted lens technique (VAITY; BANERJI; SINGH, 2013). The measured OAM (magnitude and helicity) agrees with that predicted by the conservation rules (4.24) and (4.25) in all cases. These results show that when one of the beams is Gaussian, the generated beams will have topological charges with opposite helicities, and a factor of $2$ between their magnitudes.

**Figure 34** – Far-field intensity distributions (Int.) and tilted lens profiles (TL) for FWM signals $\mathcal{E}_1$ (a) and $\mathcal{E}_2$ (b), when incident beams carry $\ell_b = 0$ and $\ell_a = -1, 0, 1$. We normalized each image separately.

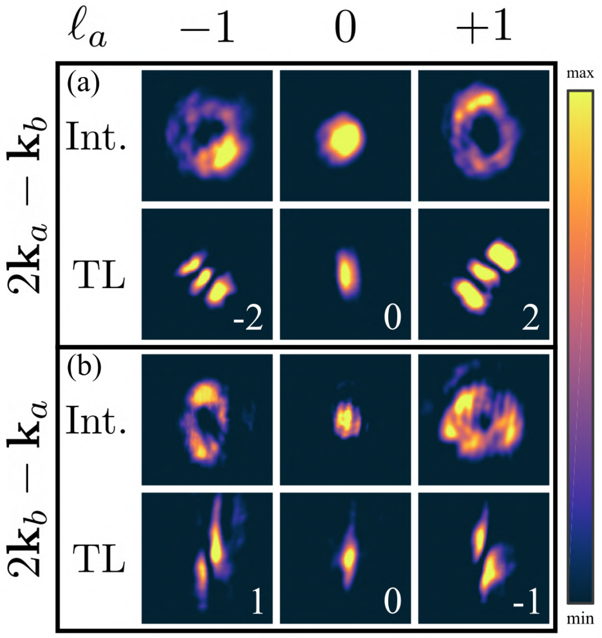

**Source:** The author (2024).

Next, we made $\ell_b = 1$ and varied $\ell_a$ across the same values. The topological charges of signals $\mathcal{E}_1$ and $\mathcal{E}_2$ must therefore satisfy the conditions:

$$\ell_1 = 2\ell_a - 1, \tag{4.26}$$

$$\ell_2 = 2 - \ell_a. \tag{4.27}$$

In Fig. 35, we show the intensity and tilted lens profiles of both generated signals for this case. Even though the ring-shaped intensity profile may not be fully developed in some cases, the measured OAM agrees with the requirements (4.26) and (4.27) in all cases. Note that in this case, when the topological charge of the field $a$ is shifted by one unit, the OAM of signals $2a - b$ and $2b - a$ shift by two units and one unit, respectively. Since $\ell_b = 1$, signal $2a - b$ only emerges with odd-valued TCs. If we make $\ell_b = 2$, then it only emerges with even-valued TCs. Thus, we can produce FWM signals that only carry even- or odd-valued topological charges, depending on the OAM content of the beam that contributes to the nonlinear process with a single photon.

We can highlight some interesting cases regarding the topological charge pairs of the generated beams. When $\ell_a = \ell_b = \ell$, then the two nonlinear signals also emerge with a TC equal to $\ell$. This situation is represented in Fig. 35 when $\ell_a = \ell_b = 1$. However, if the incident beams have TCs with equal magnitude and opposite helicities, $\ell_a = -\ell_b = \ell$, then

**Figure 35** – Far-field intensity distributions and tilted lens profiles for FWM signals $\mathcal{E}_1$ (a) and $\mathcal{E}_2$ (b), when incident beams carry $\ell_b = 1$ and $\ell_a = -1, 0, 1, 2, 3$.

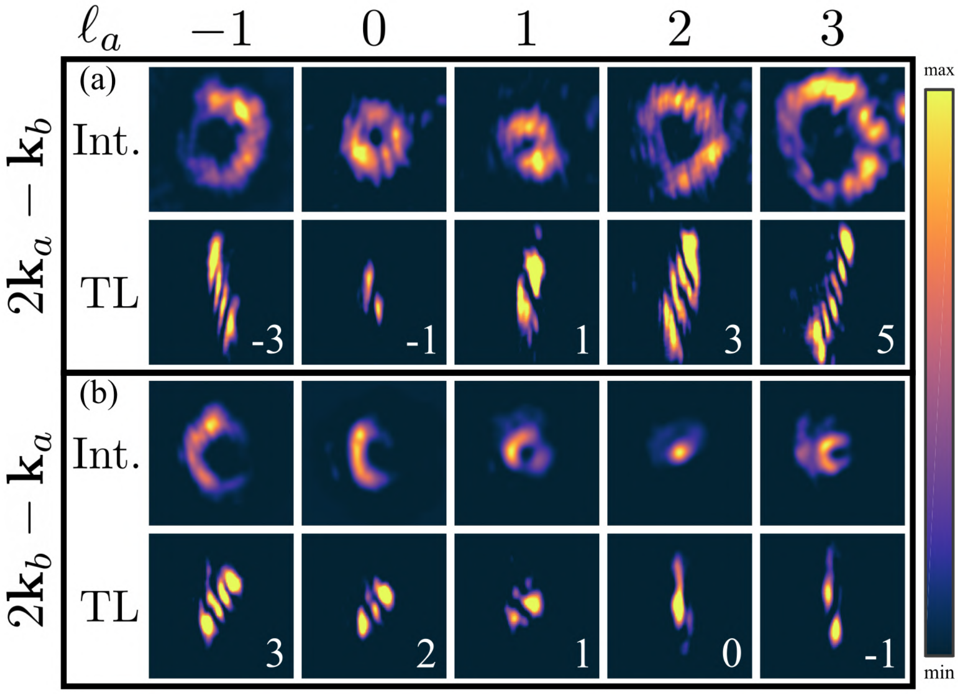

**Source:** The author (2024).

the nonlinear signals are generated with TCs of opposite helicities, but with a three-fold increase in magnitude, $\ell_1 = -\ell_2 = 3\ell$, and this case is shown in Fig. 35 (first column), when $\ell_b = -\ell_a = 1$.

Another interesting case is the one where $(\ell_a, \ell_b) = (2\ell, \ell)$, for which we have at the output one beam with a three-fold increase in OAM, and the other with zero TC, $(\ell_1, \ell_2) = (3\ell, 0)$. This situation is also contained in Fig. 35, when $\ell_a = 2$ and $\ell_b = 1$. Even though signal $\mathcal{E}_2$ carries no topological charge, it emerges with a ring-shaped intensity profile because near the medium exit, the intensity distribution is dictated by the overlap of incident fields, which is dark at the center. This was observed in a cascade system when the incident beams carry opposite OAM (AKULSHIN et al., 2016). However, this distribution is not stable for non-vortex beams, and it will transition into a nearly Gaussian profile under free-propagation outside the interaction medium. This type of transition has been reported in (PEREIRA et al., 2017). Using Eq. (4.21), we can see in Fig. 36 that, with propagation distances of the order of the Rayleigh range, the ring structure fades away. More interestingly, for intermediate positions, where this transition is not yet complete, the beam presents a bright center with an outer light ring. In the lower inset of Fig. 36 we show an experimental image in this situation.

The difference between the input $\Delta\ell_{\text{i}}$ and output $\Delta\ell_{\text{o}}$ topological charges in all cases are

**Figure 36** – Propagation of the FWM signal $\mathcal{E}_2$ $(2b-a)$ outside interaction region for the case $(\ell_a, \ell_b) = (2, 1)$, obtained from Eq. (4.21). The upper insets show the calculated intensity profiles at positions $z/z_R = 0, 0.25, 0.5, 0.75, 1$. The lower inset shows an experimental image taken at a position closer to the medium exit (in comparison with Figs. 34 and 35), where an external light ring can be seen around the central spot.

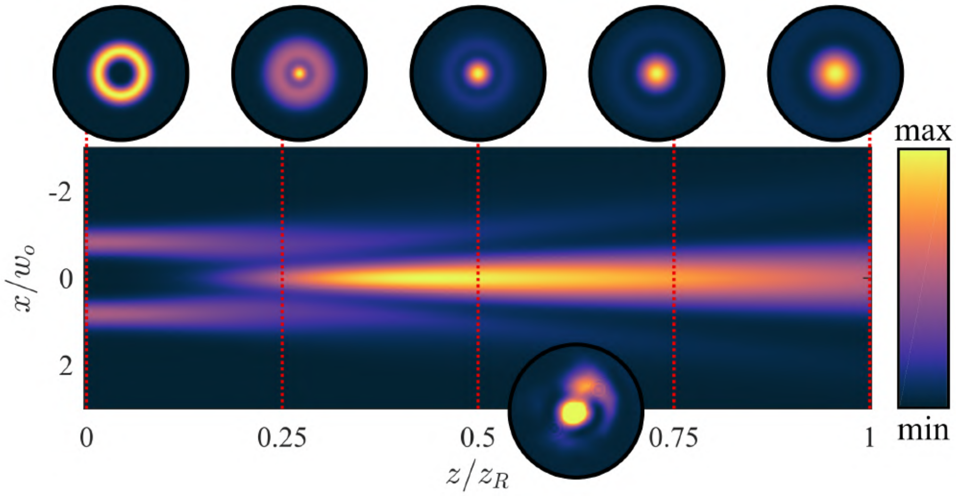

**Source:** The author (2024).

related via

$$\Delta\ell_{\text{o}} = \ell_1 - \ell_2 = 3(\ell_a - \ell_b) = 3\Delta\ell_{\text{i}}. \tag{4.28}$$

The factor of $3$ appears because we are dealing with a third-order process. Considering a fifth-order interaction generating two signals with directions $3\mathbf{k}_a - 2\mathbf{k}_b$ and $3\mathbf{k}_b - 2\mathbf{k}_a$, the OAM conservation would impose $\ell_1^{(5)} = 3\ell_a - 2\ell_b$ and $\ell_2^{(5)} = 3\ell_b - 2\ell_a$, and we would then have $\Delta\ell_{\text{o}} = 5\Delta\ell_{\text{i}}$. It is interesting to note that, with the knowledge of the TC of any two among the four participating signals, the remaining two unknown topological charges can be readily obtained using simple relations. As an example, with the knowledge of the output pair $(\ell_1, \ell_2)$, by inverting Eqs. (4.19), one can determine the incident topological charges $(\ell_a, \ell_b)$ via

$$\ell_a = \frac{1}{3}(2\ell_1 + \ell_2), \tag{4.29}$$

$$\ell_b = \frac{1}{3}(\ell_1 + 2\ell_2). \tag{4.30}$$

To conclude this Section, we explored the process of degenerate FWM induced in a heated sample of $\mathrm{Rb}$ atoms, in a configuration where two nonlinear signals can be detected, and showed that the expected topological charge selection rules are fulfilled. We presented situations where the generated beams can emerge with the same topological charge as the input beams or with a three-fold increase in topological charge magnitude and opposite helicity. We also showed that we can obtain one of the outputs with zero OAM by mixing beams carrying topological charges related by a factor of two.

These results reveal that the proposed experimental setup can be used to control the relations between the OAM content (magnitude and helicity) of two FWM signals by changing the topological charges of the incident beams. Furthermore, this experimental configuration allows us to generate pairs of beams with differences in topological charge coupled to the difference in OAM between the incident beams. The coupling factor between these OAM differences is determined by the nonlinear process that characterizes the interaction with the atomic medium. It is noteworthy that the experimental scheme designed to generate two or more FWM signals, together with the OAM control, is compatible with recent works that explore multiple degrees of freedom, in particular, the spatial degrees of freedom (GUPTA et al., 2016; VERNAZ-GRIS et al., 2018; ZHANG et al., 2020) and those of OAM (PAN et al., 2019; HU et al., 2023).

## 4.3 POINCARÉ SPHERE SYMMETRIES IN FWM

Within the seemingly endless sea of structured light (FORBES; OLIVEIRA; DENNIS, 2021), one finds the optical modes belonging to the so-called OAM Poincaré sphere (PS) (PADGETT; COURTIAL, 1999), named in analogy with the polarization Poincaré sphere. They are given by combinations of Laguerre-Gaussian (LG) modes with topological charges of equal magnitude and opposite handedness, and can be parameterized in terms of polar and azimuthal angles on the sphere. OAM PS modes have been widely employed in three-wave mixing in nonlinear crystals (ROGER et al., 2013; PEREIRA et al., 2017; BUONO et al., 2018; SILVA et al., 2021a). Our aim was to drive higher-order nonlinear optical processes with this family of modes, and investigate the underlying spatial structure dynamics.

This Section can be seen as a generalization of the Section 4.2. When dealing with OAM carrying beams (pure LG modes, in our case), one may think of PS modes restricted to the poles ($\theta = 0, \pi$). With the approach we will present here, it is possible to explore the wave-mixing dynamics driven by any mode on the surface of the Poincaré sphere, significantly expanding the possibilities of spatial structure transfer. In this direction, we experimentally investigate the nonlinear wave mixing induced by OAM PS beams in a heated sample of rubidium atoms, and the underlying rules that dictate the transfer of optical spatial structure. In particular, we consider a forward four-wave mixing (FWM) process in a configuration where two distinct signals are generated, and extend previous studies by analyzing the nonlinear response when the input beams can be described as a combination of LG modes, and going beyond the OAM conservation selection rules. Moreover, we theoretically describe both generated beams and show that, under the usual set of assumptions, they can also be represented as optical modes contained in Poincaré spheres. An interesting point is that, as we shall demonstrate, the PS components of both four-wave mixing outputs satisfy selection rules similar to those verified in three-wave mixing processes, namely, (i) a specular reflection symmetry in the Poincaré sphere, which is observed in the down conversion process (SANTOS et al., 2007; RODRIGUES et al., 2018; RODRIGUES et al., 2022); and (ii) the generation of a radial mode spectrum which has been demonstrated in second harmonic generation (PEREIRA et al., 2017; BUONO et al., 2020). These results indicate that most applications that make use of the OAM degree of freedom of a light beam can be extended to a higher-order nonlinear process. Furthermore, our two-channel FWM configuration allows us to simultaneously detect two nonlinear signals, each exhibiting a characteristic: the reflection symmetry in the Poincaré sphere and the appearance of a radial mode spectrum in the spatial structure, both already explored independently in three-wave mixing processes. The predicted FWM intensity profiles, as well as the consequences of the symmetry properties, are in good agreement with those detected in our experiment.

An arbitrary polarization state, as in any two-level system, can be represented as:

$$|P\rangle = c_{+}\,|+\rangle + c_{-}\,|-\rangle\,, \tag{4.31}$$

where $|+\rangle$ and $|-\rangle$ refer to the positive and negative circular polarization states, and $c_{+,-}$ are complex coefficients satisfying $|c_{+}|^2 + |c_{-}|^2 = 1$. We may parameterize this state by two angles, as:

$$|P\rangle = \cos\frac{\theta}{2}\,|+\rangle + e^{i\phi}\sin\frac{\theta}{2}\,|-\rangle\,. \tag{4.32}$$

In this manner we construct the Poincaré sphere for polarization: any polarization state can be represented by the position vector on the surface of the unit sphere defined by the polar and azimuthal angles given by $\theta$ and $\phi$, respectively. At the poles, there are the positive and negative circular polarization states, and at the equator, the horizontal, vertical, diagonal and anti-diagonal polarizations, as illustrated in Fig. 37(a). At any other point on the surface of the sphere, one finds all the other realizable polarization states.

In analogy with the Poincaré sphere for polarization states of light, we can define an equivalent sphere for OAM modes with topological charge magnitude $|l|$ and radial index $p$

(PADGETT; COURTIAL, 1999). In the OAM sphere $\mathcal{O}(l,p)$, of total order $N_{\ell,p} = 2p + |l|$, we have an arbitrary state $|\theta,\phi\rangle_{l,p}$ characterized by the mode superposition

$$\psi_{l,p}(\theta,\phi) = \cos\frac{\theta}{2}\, u_{l,p} + e^{i\phi}\sin\frac{\theta}{2}\, u_{-l,p}. \tag{4.33}$$

In Fig. 37(b) we represent the OAM Poincaré sphere of first order modes, $\mathcal{O}(1,0)$. For this sphere, the combinations of LG modes at the equator result exactly in HG modes rotated by different angles, passing through positions aligned horizontally, vertically, diagonally, and anti-diagonally. Therefore, the sphere of first order modes bears a direct analogy with the polarization PS. The same is not true for the spheres with $l > 1$, as one can see in Fig. 37(c), where we show modes belonging to the PS sphere $\mathcal{O}(3,1)$. The Poincaré sphere construction applies to two-dimensional complex vector spaces, but there is not a special restriction to the modes used in either input fields $\mathcal{E}_a$ or $\mathcal{E}_b$. This is because even when several modes participate in either three- or four-wave parametric interactions, the interacting modes can be grouped in pairs with opposite OAM, plus the zero OAM modes, when they are present. Each pair of opposite OAM modes builds an independent Poincaré sphere. The geometrical representation of the nonlinear interaction that we will establish, and the associated symmetries, apply to each sphere independently (RODRIGUES et al., 2022). Of course, there is no room for these symmetries in the zero OAM manifold.

We will be interested in the transverse structure dynamics under FWM processes induced by modes belonging to the OAM Poincaré sphere. As will be shown, the effect of the nonlinear light-matter interaction driven by a light field described by Eq. (4.33) can be seen as a transformation of the state vector on the sphere. In fact, the FWM process induced by a field contained in a PS can result in an output mode contained in a different sphere.

In the upcoming Sections, we will explore different scenarios, and try to highlight interesting aspects of the transverse mode dynamics of FWM processes driven by PS modes. Before moving on, we note that for the azimuthal angle on the Poincaré sphere, $\phi$, we use the same letter we have used for the azimuthal angle on the transverse plane throughout this work. Thus, to avoid confusion, in this Chapter we shall rename the transverse azimuthal coordinate as $\gamma$.

**Figure 37** – (a) Polarization Poincaré sphere, (b) OAM Poincaré sphere of first order, $\mathcal{O}(1,0)$, (c) OAM Poincaré sphere $\mathcal{O}(3,1)$. The insets show the intensity profiles of the modes at specific points on the PS.

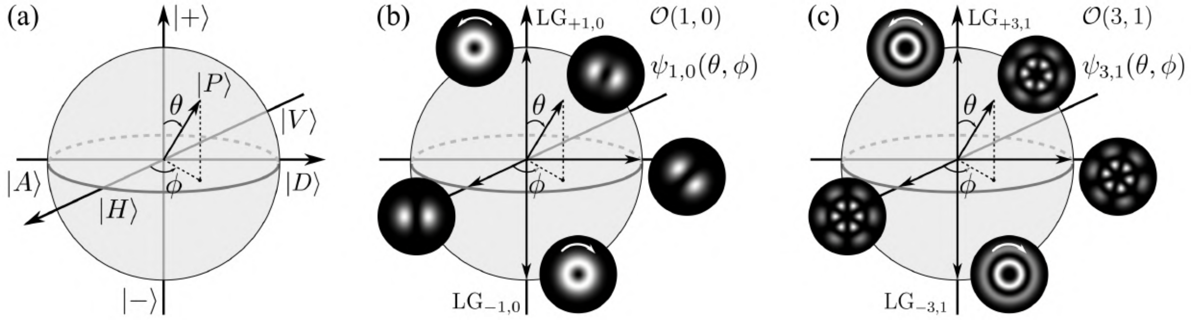

**Source:** The author (2024).

### 4.3.1 FWM driven by a single Poincaré sphere mode

The starting point for the description of the transverse beam structure dynamics is, once again, the pair of wave-equations describing evolution of the slowly varying FWM field envelopes $\mathcal{E}_1$ and $\mathcal{E}_2$, Eqs. (4.11) and (4.12). We write their solutions as general superpositions of LG modes with waist $w_0$:

$$\mathcal{E}_1(\mathbf{r}) = \sum_{\ell,p} \alpha_{\ell,p} u_{\ell,p}(\mathbf{r}), \tag{4.34}$$

$$\mathcal{E}_2(\mathbf{r}) = \sum_{\ell,p} \beta_{\ell,p} u_{\ell,p}(\mathbf{r}). \tag{4.35}$$

As already discussed, with the thin-medium assumption, the coefficients $\alpha_{\ell,p}$ and $\beta_{\ell,p}$ are proportional to the transverse overlap integrals

$$\alpha_{\ell,p} \propto \mathcal{A}_{\ell,p} = \iint u_a^2 u_b^* u_{\ell,p}^* d^2\mathbf{r}_\perp, \tag{4.36}$$

$$\beta_{\ell,p} \propto \mathcal{B}_{\ell,p} = \iint u_b^2 u_a^* u_{\ell,p}^* d^2\mathbf{r}_\perp. \tag{4.37}$$

Now we can explore scenarios where the incident beams $u_a$ and $u_b$ carry different structures. We will focus on the situation where field $u_a$ is given by the composition of LG modes contained in the OAM Poincaré sphere $\mathcal{O}(l,0)$, and $u_b$ is given by a pure Gaussian mode:

$$u_a = \psi_{l,0}(\theta,\phi) = \cos\frac{\theta}{2}\, u_{l,0} + e^{i\phi}\sin\frac{\theta}{2}\, u_{-l,0}, \tag{4.38}$$

$$u_b = u_{0,0}. \tag{4.39}$$

Upon substitution in Eqs. (4.36) and (4.37), we can write the transverse overlap integrals at $z = 0$ as:

$$\mathcal{A}_{\ell,p} = e^{i\phi} \sin\theta \Lambda_{000p}^{l,-l0\ell} + \cos^2 \frac{\theta}{2} \Lambda_{000p}^{ll0\ell} + e^{2i\phi} \sin^2 \frac{\theta}{2} \Lambda_{000p}^{-l,-l0\ell}, \tag{4.40}$$

$$\mathcal{B}_{\ell,p} = \cos \frac{\theta}{2} \Lambda_{000p}^{00l\ell} + e^{-i\phi} \sin \frac{\theta}{2} \Lambda_{000p}^{00,-l\ell}, \tag{4.41}$$

where

$$\Lambda_{qq'np}^{ll'm\ell} = \iint u_{l,q} u_{l',q'} u_{m,n}^* u_{\ell,p}^* \Big|_{z=0} d^2\mathbf{r}_\perp \tag{4.42}$$

is the transverse overlap integral of four LG modes with the same waist $w_0$. The conservation of OAM naturally emerges from the azimuthal integral:

$$\int_0^{2\pi} e^{i(l+l'-m-\ell)\gamma} d\gamma = 2\pi \delta_{\ell,l+l'-m}, \tag{4.43}$$

restricting the possible values for the topological charges contained in the superpositions for $\mathcal{E}_1$ and $\mathcal{E}_2$. For signal $\mathcal{E}_1$, we will have modes with $\ell = \pm 2l$ (first and second terms of Eq. (4.40)), yielding the contribution from a PS of order $N = 2l$, and also from $\ell = 0$; while for signal $\mathcal{E}_2$, we only have the $\ell = \pm l$ components (Eq. (4.41)), associated with a PS of the same order $N = l$ as the input. In principle, there is no such restriction on the radial orders, and an infinite number of $p$ modes can contribute to the superpositions of the fields $\mathcal{E}_1$ and $\mathcal{E}_2$. It is important to note that for the third-order process studied here, the possible values for the topological charges imposed by the azimuthal integral, Eq. (4.43), are the same as those found in second-order processes. In particular, in SHG, where the process is driven by a structured pump, from which two photons are absorbed to generate the up-converted field, as in the case of signal $\mathcal{E}_1$; and in the down-conversion process, where the medium is excited by a Gaussian pump, and the down-converted fields are the ones carrying the spatial structure, a situation analogous to that of signal $\mathcal{E}_2$.

By substituting Eqs. (4.40) and (4.41) into Eqs. (4.34) and (4.35), we can express both generated fields on the $w_0$ mode basis as:

$$\mathcal{E}_1 = \sum_p \Big( a_p \psi_{2l,p}(\vartheta_1, \varphi_1) + e^{i\phi} \sin\theta \, c_p u_{0,p} \Big), \tag{4.44}$$

$$\mathcal{E}_2 = \sum_p b_p \psi_{l,p}(\vartheta_2, \varphi_2), \tag{4.45}$$

where $a_p = \Lambda^{ll0,2l}_{000p} = \Lambda^{-l,-l0,-2l}_{000p}$, $b_p = \Lambda^{00,-ll}_{000p} = \Lambda^{00,l,-l}_{000p}$, $c_p = \Lambda^{l,-l00}_{000p} = \Lambda^{-ll00}_{000p}$, and the output sphere angles are related to the input angles via:

$$\vartheta_1 = 2\tan^{-1}(\tan^2(\theta/2)), \qquad \varphi_1 = 2\phi, \tag{4.46}$$

$$\vartheta_2 = \pi - \theta, \qquad \varphi_2 = \phi. \tag{4.47}$$

The relations given by Eqs. (4.46) and (4.47) are similar to those satisfied in parametric amplification, a second-order nonlinear process (SANTOS et al., 2007; RODRIGUES et al., 2018; RODRIGUES et al., 2022). We note that similar results could be obtained for a zero OAM field with a nonzero radial index $u_b = u_{0,n}$. However, for the simpler situation we study here, regarding the spatial degrees of freedom, the Gaussian field $u_b$ has a passive role in the wave-mixing process, and we essentially have a single field, $u_a$, dictating the transverse mode dynamics. The transformation represented by Eq. (4.47) is more intuitive, and can be seen as a reflection of the input vector on the sphere with respect to the equatorial plane. On the other hand, the visualization and interpretation of Eq. (4.46) is a bit less straightforward. In Fig. 38 we illustrate how the mode vectors are transformed in both FWM processes, according to the rules given by Eqs. (4.46) and (4.47). The inset shows the variation of $\vartheta_1(\theta)$, making evident that $\vartheta_1 < \theta$ ($\vartheta_1 > \theta$) for $\theta < \pi/2$ ($\theta > \pi/2$), and $\vartheta_1 = \theta$ at $\theta = 0, \pi/2, \pi$. Therefore, when the mode vector on the input PS describes a path starting from the north pole and ending on the south pole, the polar angle of the mode vector on the output PS is delayed in the section $0 \to \pi/2$, and advanced in the section $\pi/2 \to \pi$. The magnitude of the rate of change of the vector position ($\boldsymbol{\rho}$) on the input and output spheres is the same for signal $\mathcal{E}_2$, $|\dot{\boldsymbol{\rho}}_2| = |\dot{\boldsymbol{\rho}}_{\text{in}}|$,

**Figure 38** – Representation of the angle symmetries for the FWM signals $\mathcal{E}_1$ and $\mathcal{E}_2$. The inset shows the dependence of the output angle $\vartheta_1$ with $\theta$.

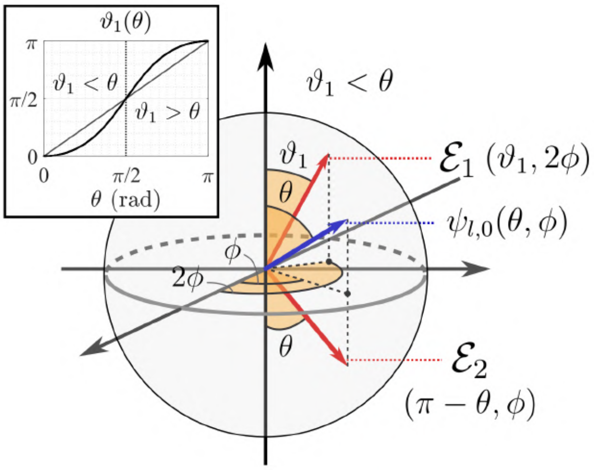

**Source:** The author (2024).

but not for signal $\mathcal{E}_1$, $|\dot{\boldsymbol{\rho}}_1| \neq |\dot{\boldsymbol{\rho}}_{\rm in}|$, where the dot indicates the derivative with respect to a parameter $t$. Namely, we have $\dot{\vartheta}_j = \frac{\partial \vartheta_j}{\partial \theta}\dot{\theta}$, $\dot{\varphi}_j = \frac{\partial \varphi_j}{\partial \phi}\dot{\phi}$, and using Eqs. (4.46), (4.47), we get:

$$\dot{\vartheta}_1 = \frac{2\sin(\theta)}{1+\cos^2(\theta)}\dot{\theta}, \quad \dot{\varphi}_1 = 2\dot{\phi}, \tag{4.48}$$

$$\dot{\vartheta}_2 = -\dot{\theta}, \quad \dot{\varphi}_2 = \dot{\phi}. \tag{4.49}$$

We show in Fig. 39 the paths followed by the PS components of the fields $\mathcal{E}_1$ and $\mathcal{E}_2$ as a result of the FWM processes driven by an input mode that follows a closed path on the PS. In the inset we show the dependence of $\vartheta_1$ and $\dot{\vartheta}_1/\dot{\theta}$ with $\theta$. One interesting possibility is to consider fluctuations of the position vector $\boldsymbol{\rho}(t)$ on the input PS $(\theta, \phi)$, and how they are transferred to the output spheres (SANTOS; DECHOUM; KHOURY, 2009).

**Figure 39** – Closed path $(\theta, \phi)$ followed by an input PS mode, describing a solid angle $\Omega$, and resulting paths followed by $\mathcal{E}_1$ and $\mathcal{E}_2$, $(\vartheta_1, \varphi_1)$, and $(\vartheta_2, \varphi_2)$, respectively. The inset shows the dependence of $\vartheta_1$ and $\dot{\vartheta}_1/\dot{\theta}$ with $\theta$. The transformed paths define solid angles $\Omega_1 > \Omega$, and $\Omega_2 = \Omega$.

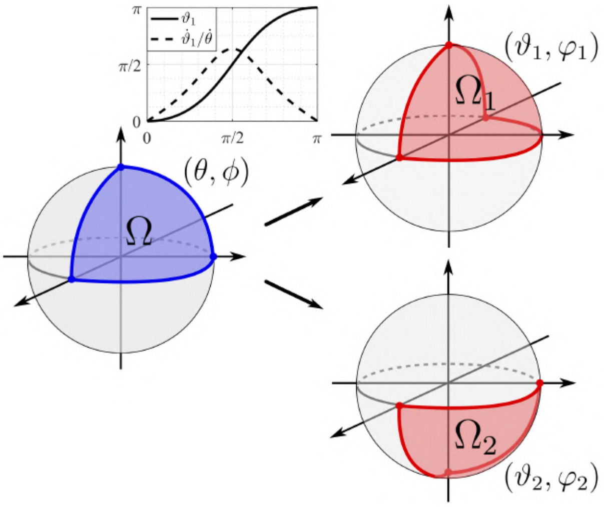

**Source:** The author (2024).

If we rewrite the products of incident fields as:

$$\mathcal{E}_1 : (u_a^2)u_b^* \rightarrow U_1 u_b^*, \tag{4.50}$$

$$\mathcal{E}_2 : (u_b^2)u_a^* \rightarrow U_2 u_a^*, \tag{4.51}$$

we see that the FWM processes driven by fields $u_a, u_b$ can, indeed, be seen as three-wave mixing processes driven by the effective fields $U_1 = u_a^2$ ($\mathcal{E}_1$), and $U_2 = u_b^2$ ($\mathcal{E}_2$), as illustrated in Fig. 40. The difference between the two cases is that for $\mathcal{E}_1$ the pump carries the non-trivial mode, and its structure is completely transferred to the generated signal, and for $\mathcal{E}_2$, the pump is Gaussian, and the structured field acts to stimulate an emission in its mode, generating the

**Figure 40** – Four-wave mixing processes generating signals $\mathcal{E}_1 \sim u_a^2 u_b^*$ and $\mathcal{E}_2 \sim u_b^2 u_a^*$ seen as three-wave mixing processes driven by the effective fields $U_1 = u_a^2$ and $U_2 = u_b^2$. In our specific case, $U_1$ is the structured field, given by the square of a PS mode, and $U_2$ is the square of a Gaussian mode. A two-level system was considered for this illustrative example.

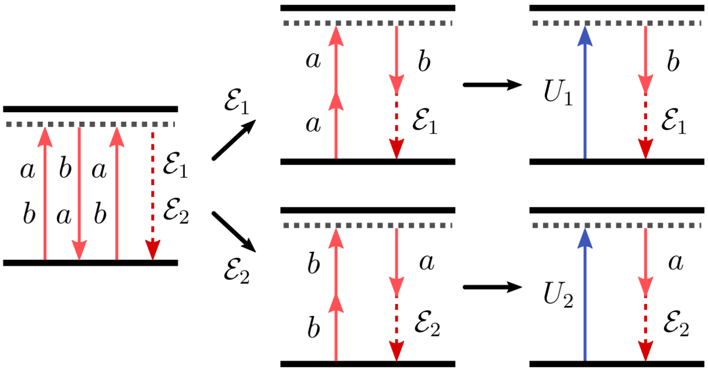

**Source:** The author (2024).

FWM field. We can therefore associate these two situations with SHG and down-conversion, respectively.

The FWM fields are generated with a smaller overall size as compared with the input beams, since the generated field amplitudes are dictated by the spatial overlap of the incident modes. This can be understood intuitively in the case of Gaussian inputs, when we make:

$$\mathcal{E}_{1,2} \sim u_{0,0}^2 u_{0,0}^* \sim \exp\left(-\frac{r^2}{w_0^2/3}\right). \tag{4.52}$$

When dealing with a thin-medium, only the transverse degrees of freedom play an important role, and we don't need to account for the longitudinal propagation of the beams inside the interaction region. In other words, the Boyd criterion is relaxed. As a consequence, we gain the freedom to set the beam waist parameter of our basis modes. By choosing a basis with the appropriate (reduced) waist $\tilde{w} = w_0/\xi$, the number of modes required to represent the FWM fields is reduced (OLIVEIRA et al., 2023). In fact, for $\xi = \sqrt{3}$, the following restriction on the $p$ orders is established: the sphere modes in $\mathcal{E}_1$ and $\mathcal{E}_2$ are limited to $p = 0$ only, while the contribution from the non-vortex modes in $\mathcal{E}_1$ is bound to $0 \leq p \leq |l|$. We may then write the output fields in the final form:

$$\mathcal{E}_1 = \tilde{a}_0 \tilde{\psi}_{2l,0}(\vartheta_1(\theta), 2\phi) + e^{i\phi} \sin\theta \sum_{p=0}^{|l|} \tilde{c}_p \tilde{u}_{0,p}, \tag{4.53}$$

$$\mathcal{E}_2 = \tilde{b}_0 \tilde{\psi}_{l,0}(\pi - \theta, \phi), \tag{4.54}$$

where $\tilde{u}$ and $\tilde{\psi}$ are the LG and OAM PS modes with the modified waist $\tilde{w} = w/\sqrt{3}$, $\tilde{a}_0 = \tilde{\Lambda}_{0000}^{ll0,2l}(\sqrt{3})$, $\tilde{b}_0 = \tilde{\Lambda}_{0000}^{00,-ll}(\sqrt{3})$, $\tilde{c}_p = \tilde{\Lambda}_{000p}^{l,-l00}(\sqrt{3})$. The transverse overlap integral on the modified waist basis is

$$\tilde{\Lambda}^{ll'm\ell}_{qq'np}(\xi) = \iint u_{l,q}u_{l',q'}u^{*}_{m,n}\tilde{u}^{*}_{\ell,p}\Big|_{z=0} d^2\mathbf{r}_{\perp}, \\ = \sum_{s}\Lambda^{ll'm\ell}_{qq'ns}\lambda^{\ell}_{s,p}(\xi), \tag{4.55}$$

and $\lambda^{\ell}_{s,p}(\xi)$ are the coefficients for the change of basis $\{u(w_0)\} \to \{u(w_0/\xi)\}$ (OLIVEIRA et al., 2023):

$$\lambda^{\ell}_{s,p}(\xi) = \iint u_{\ell,s}\tilde{u}^{*}_{\ell,p}\Big|_{z=0} d^2\mathbf{r}_{\perp}. \tag{4.56}$$

We then see that, to represent the output fields on the reduced waist basis, we can either calculate directly $\tilde{\Lambda}$ on the $\tilde{w}$ basis, or calculate $\Lambda$ on the $w_0$ basis and perform the transformation using the coefficients $\lambda$. In the Appendix B we give analytical expressions for the relevant overlap integrals on the reduced waist basis, given by the first line of Eq. (4.55), making explicit the radial mode restriction, and in Appendix C we calculate the change of basis coefficients.

First, we performed experiments by setting field $\mathcal{E}_a$ as a mode on the equator ($\theta = \pi/2$) of the PS $\mathcal{O}(\ell, 0)$, $\psi^{(a)}_{\ell,0}(\pi/2, 0)$ with $\ell = 1, 2, 3$ [see Fig. 41(a)], and field $\mathcal{E}_b$ as a pure Gaussian beam. Figures 41(b) and 41(c) show the calculated and measured far-field intensity profiles of the generated signals, $\mathcal{E}_1$ and $\mathcal{E}_2$, respectively. We see that for signal $2a - b$ [Fig. 41(b)] we obtain more intricate figures, while the structure of signal $2b - a$ [Fig. 41(c)] seems to be dominated by that of the pump in each case. This is due to the fact that signal $\mathcal{E}_1$ has two contributions from the structured pump, and the nonlinear polarization associated with its generation is proportional to $(\psi^{(a)}_{\ell,0})^2$. On the other hand, for $\mathcal{E}_2$, which has only one contribution from $\mathcal{E}_a$, the macroscopic polarization is proportional to $(\psi^{(a)}_{\ell,0})^*$. The central spots present in signal $\mathcal{E}_1$ are due to the contribution from the $\ell = 0$ modes arising from the crossed term in the product $(\psi^{(a)}_{\ell,0})^2$. They only develop in the far-field because of the different Gouy phases carried by the $2\ell$ PS mode and the radial modes. The Gouy phase of the PS mode is proportional to $(1 + 2|\ell|)\tan^{-1}(z/z_R)$, while those of the radial modes with $0 < p < |\ell|$ are proportional to $(1 + 2p)\tan^{-1}(z/z_R)$. This becomes evident when one looks at the near-field intensity distributions of the FWM signal $\mathcal{E}_1$ for $\ell = 1, 2$, shown in Fig. 41(d). This type of transition of the transverse structure has been verified in other situations (PEREIRA et al., 2017; AKULSHIN et al., 2016; ZHANG et al., 2022). This behavior is not verified for signal $\mathcal{E}_2$, since it only contains the PS mode with total order $N = |l|$, and therefore its shape is stable under propagation. Finally, it is worth commenting on the distortions seen in the experimental images. This is due

**Figure 41** – (a) Calculated intensity profiles of modes $\psi_{\ell,0}(\pi/2,0)$, for $\ell=1,2,3$, alongside the corresponding beams prepared in the experiment near the interaction region. Calculated and detected far-field intensity profiles of the FWM signals (b) $\mathcal{E}_2$ and (c) $\mathcal{E}_1$, resulting from the mixing of $u_a$ given by the modes shown in (a) and $u_b$ given by a Gaussian mode. (d) Calculated and detected near-field intensity profiles of the FWM signal $\mathcal{E}_1$ for the cases $\ell=1,2$.

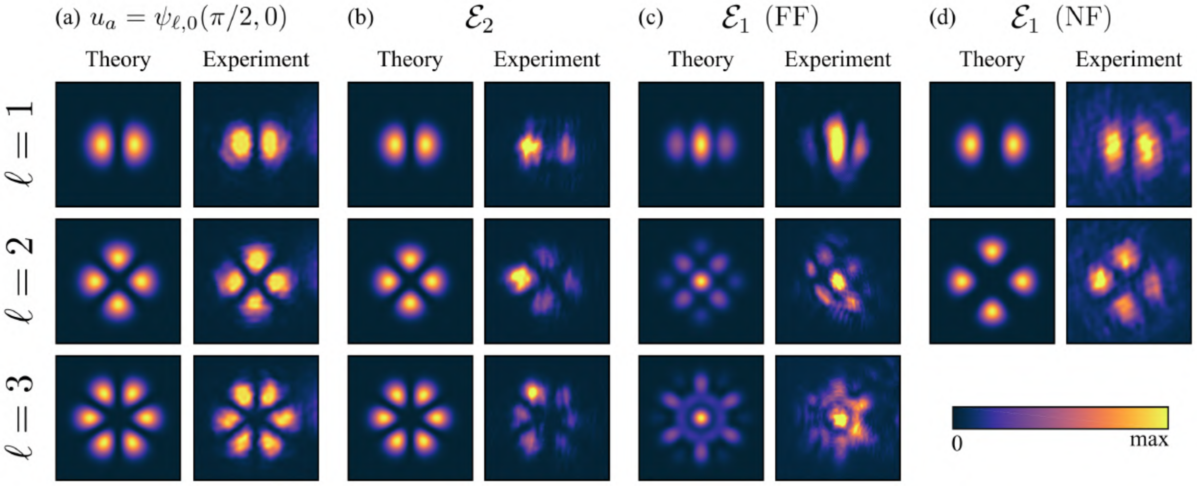

**Source:** The author (2024).

to the degenerate configuration we are working with, which makes it difficult to completely filter the scattered light superimposed to the spatial profiles of the generated signals.

In Fig. 42 we show the coefficient distributions of the calculated output mode superpositions on the original $(w_0)$ and reduced $(\tilde{w}=w_0/\xi)$ waist bases, to evidence the constraint on the radial spectrum of the generated fields $\mathcal{E}_1$ and $\mathcal{E}_2$ that is derived in the Appendix B. Let us look at the modification of the mode distribution with the chosen waist basis a little more in detail. For an arbitrary basis with $\tilde{w}=w_0/\xi$, we may write the radial spectrum as $P_p$ of the generated fields $\mathcal{E}_i$, $i=1,2$:

$$P_p(\xi)=\sum_{\ell}|\langle\mathcal{E}_i(w_0)|\tilde{u}_{\ell,p}(\xi)\rangle|^2=\begin{cases}|\tilde{a}_p|^2+\sin^2\theta|\tilde{c}_p|^2, & \text{for } \mathcal{E}_1,\\ |\tilde{b}_p|^2, & \text{for } \mathcal{E}_2,\end{cases} \tag{4.57}$$

where the sum runs over all values of $\ell$ present in $\mathcal{E}_i$, i.e., $\{-2l,0,2l\}$ for $\mathcal{E}_1$, and $\{-l,l\}$ for $\mathcal{E}_2$. We may define the width of the radial spectrum as:

$$\Delta p(\xi)=\sqrt{\sum_p P_p(\xi)p^2-\left(\sum_p P_p(\xi)p\right)^2}. \tag{4.58}$$

In Fig. 43 we show the spectrum of radial modes $P_p$ of the generated fields $\mathcal{E}_1$ and $\mathcal{E}_2$ for the input waist $w_0$ and the modified waist $\tilde{w}=w/\sqrt{3}$, and for increasing value of the input PS order $l$, as well as the width of the radial spectrum as a function of the waist ratio $\xi$. Looking at the graphs for the widths $\Delta p$, we see that for signal $\mathcal{E}_1$ the radial spectrum is narrower

**Figure 42** – Coefficients of the mode superpositions of the output fields shown in figure 41 on the original and reduced waist bases. The radial spectrum is significantly narrowed on the $w_0/\sqrt{3}$ basis, and complies with the analytical mode restriction.

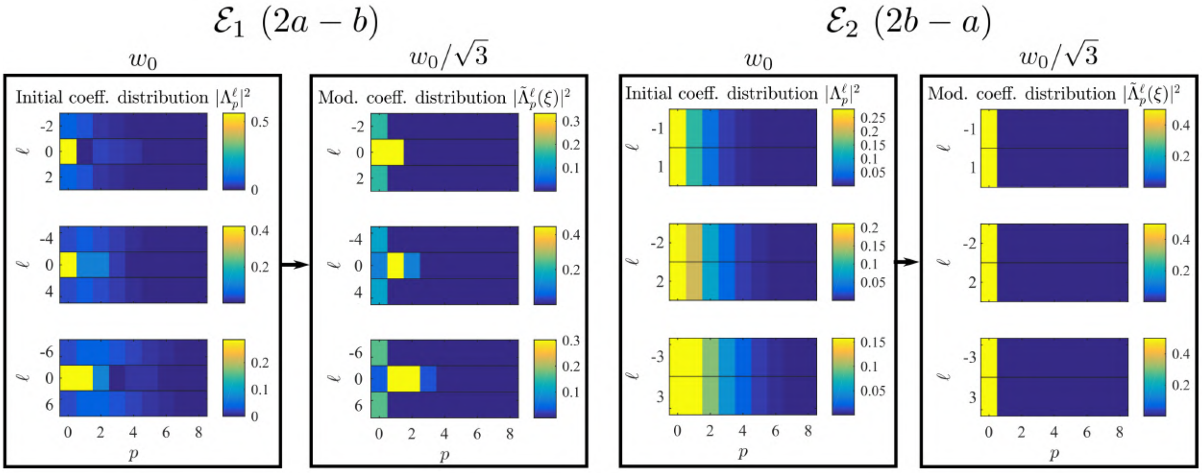

**Source:** The author (2024).

**Figure 43** – Spectrum of radial modes of the FWM signals $\mathcal{E}_1$ (top) and $\mathcal{E}_2$ (bottom) for an input PS mode of order (a),(f) $l = 1$; (b),(g) $l = 2$; (c),(h) $l = 3$; (d),(i) $l = 4$ considering the input $w_0$ and modified $\tilde{w} = w_0/\sqrt{3}$ waist bases. In (a)-(d) the blue shaded region indicates the interval $0 \leq p \leq |l|$, representing the exact bound for the value $\xi = \sqrt{3}$. In (e) and (j) we show the width $\Delta p(\xi)$ of the radial spectra as a function of the ratio $\xi$. The vertical lines indicate the value $\xi = \sqrt{3}$.

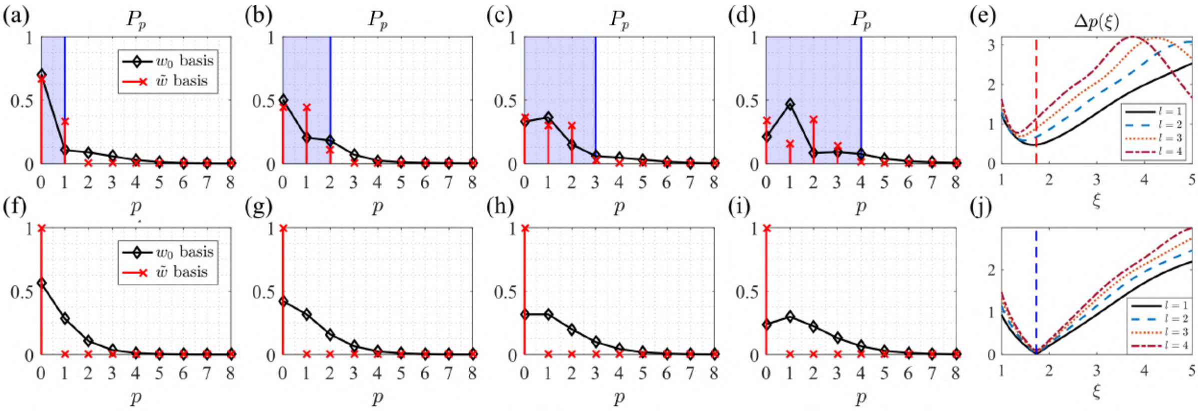

**Source:** The author (2024).

around $\xi = \sqrt{3}$ as compared to $\xi = 1$, while for signal $\mathcal{E}_2$ its radial spectrum collapses at the value $\xi = \sqrt{3}$.

We also made the pump field $u_a$ occupy different positions on the PS. First we consider $u_a$ following a path starting on the positive pole, $(\theta, \phi) = (0, 0)$, going to $(\pi/2, 0)$ on the equator, and then to $(\pi/2, \pi/2)$. We call these points $1, 2,$ and $3$, respectively [see Fig. 44(a)]. The incident modes in these positions are $\psi_{1,0}(0,0) = u_{1,0}$, $\psi_{1,0}(\pi/2) = (u_{1,0} + u_{-1,0})/\sqrt{2}$, and $\psi_{1,0}(\pi/2, \pi/2) = (u_{1,0} + iu_{-1,0})/\sqrt{2}$. Figure 44(b) shows the corresponding path followed by the PS component of the FWM field $\mathcal{E}_1$ on the output sphere $\mathcal{O}(2,0)$. In Fig. 44(c), we

**Figure 44** – (a) Incident field modes along a path described by points $1, 2, 3$ on the first order sphere $\mathcal{O}(1,0)$. (b) Corresponding modes on the output sphere $\mathcal{O}(2,0)$ for the FWM signal $\mathcal{E}_1$, when $u_b = u_{0,0}$. Insets show the intensity profiles of the sphere modes on the indicated positions. (c) Measured (top) and calculated (bottom) FWM intensity profiles for signal $\mathcal{E}_1$ on the points $1, 2, 3'$.

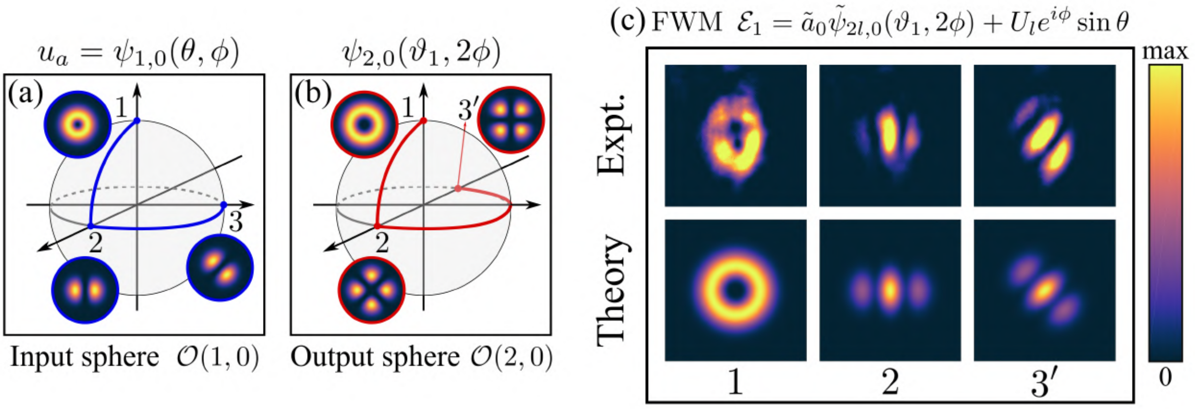

**Source:** The author (2024).

show the experimental and theoretical far-field intensity profiles of signal $\mathcal{E}_1$ in this case. For the point 1, where $u_a$ is a pure $u_{1,0}$ mode, the field $\mathcal{E}_1$ emerges as a pure $u_{2,0}$ mode, and we are essentially performing OAM addition (MOTTA; ALMEIDA; VIANNA, 2023). As we leave the pole, we can employ the PS geometric representation to interpret the behavior of the FWM output field structure. We see that the actual FWM intensity profiles differ from those expected solely from a PS mode $\psi_{2,0}$ on the points $2$ and $3$, corresponding to the first term on the right-hand-side (r.h.s.) of Eq. (4.53). This is due to the contribution from the radial modes in the superposition $\mathcal{E}_1$, which becomes maximum when $\theta = \pi/2$, as seen from the second term on the r.h.s. of Eq. (4.53).

What is remarkable from these results is that the variation of the azimuthal angle $\phi$ on the input sphere results in a rigid rotation of the FWM intensity profile that is equal to the rotation of the intensity profile of $u_a$. This is not obvious since, as already mentioned, (i) the azimuthal angle on the output sphere is doubled, $\varphi_1 = 2\phi$, and (ii) there are radial modes contributing to the FWM field mode structure. In fact, this net effect is precisely a result of the combination of these two aspects. To explain this, we first look at the rotation of the intensity profile of the input PS mode $\psi_{l,0}(\theta,\phi)$, $\mathcal{I}_l(\mathbf{r}_\perp;\theta,\phi) = |\psi_{l,0}(\theta,\phi)|^2$, which can be understood when we write

$$\mathcal{I}_l(\mathbf{r}_\perp;\theta,\phi) = |u_{l,0}|^2 \left\{1 + \sin\theta\cos\left[2l\left(\gamma - \frac{\phi}{2l}\right)\right]\right\}. \tag{4.59}$$

We see that the PS azimuthal angle $\phi$ shifts the origin of the transverse azimuthal coordinate

$\gamma$ as:

$$\mathcal{I}_l(\mathbf{r}_\perp;\theta,\phi) = \mathcal{I}_l(r,\gamma-\phi/2l;\theta,0), \tag{4.60}$$

thus rotating the intensity profile by $+\phi/2l$. This can be verified by looking at figures 44(a) and 44(b), where we see the intensity profiles of the modes on the spheres $\mathcal{O}(1,0)$ and $\mathcal{O}(2,0)$ rotate by 45 degrees when the azimuthal angles vary by 90 and 180 degrees, respectively. The intensity profile of the FWM field $\mathcal{E}_1$, $I_1 = |\mathcal{E}_1|^2$, can be found as:

$$\begin{aligned} I_1(\mathbf{r}_\perp;\theta,\phi) = |U_l|^2\sin^2\theta + |\tilde{a}_0|^2|\tilde{u}_{2l,0}|^2\left\{1+\sin\vartheta_1\cos\left[4l\left(\gamma-\frac{\phi}{2l}\right)\right]\right\}+ \\ +2\sqrt{2}\tilde{a}_0\tilde{V}_0^{|2l|}U_l\sin\theta\sin\left(\frac{\vartheta_1}{2}+\frac{\pi}{4}\right)\cos\left[2l\left(\gamma-\frac{\phi}{2l}\right)\right], \end{aligned} \tag{4.61}$$

where the LG radial amplitude $\tilde{V}_p^{|\ell|}(r)$ is defined via $\tilde{u}_{\ell,p}(r,\gamma) = \tilde{V}_p^{|\ell|}(r)e^{i\ell\gamma}$, and $U_l = \sum_{p=0}^{|l|}\tilde{c}_p\tilde{u}_{0,p}$ is the term from Eq. (4.53) containing the superposition of radial modes. Thus, we see that just like in Eq. (4.59), $I_1$ presents a shift of the transverse azimuthal coordinate by the amount $\phi/2l$, equal to that of the input PS mode $\psi_{l,0}$:

$$I_1(r,\gamma;\theta,\phi) = I_1(r,\gamma-\phi/2l;\theta,0). \tag{4.62}$$

Next we analyze the FWM signal $\mathcal{E}_2$ for a similar path on the input sphere $\mathcal{O}(1,0)$, going through points $1,2,3$ and ending at point $4$, the negative pole, $(\theta,\phi) = (\pi,\pi/2)$. On this position, the incident mode is $\psi_{1,0}(\pi,\pi/2) = u_{-1,0}$. In Fig. 45(a) we show the paths followed by the $u_a = \psi_{1,0}(\theta,\phi)$ (left), and by the generated field $\mathcal{E}_2 \propto \psi_{1,0}(\pi-\theta,\phi)$ (right). We divide the complete path $1-4$ into three sections, and in Fig. 45(b) we illustrate how the incident and generated mode vectors change on the sphere in each section. In Fig. 45(c) we show the detected images of the intensity profiles of the incident field $u_a$ at each position $1,...,4$ (top) and the resulting FWM signal $\mathcal{E}_2$ in each case (bottom). For the points $1$ and $4$ the insets show the tilted lens (TL) profiles, indicating that in these positions the input and FWM fields possess opposite OAM. Along the arc $2-3$ the input and generated field modes are degenerate in the sense that the position vector on the first order sphere is the same. These results indicate the fulfilment of the reflection symmetry for signal $\mathcal{E}_2$.

In conclusion, we investigated the transfer of spatial structures from the input pump fields to the converted fields in a FWM degenerated process in a Rb vapor cell. We showed that the whole interaction can be seen as a two-channel three-wave mixing process, whose spatial structures for the converted fields are independently driven by the square of one input field

**Figure 45** – (a) Path followed by the input mode $u_a = \psi_{1,0}(\theta,\phi)$ passing through points $1,2,3,4$ on the sphere $\mathcal{O}(1,0)$, and the corresponding path followed by the FWM signal $\mathcal{E}_2 \propto \psi_{1,0}(\pi-\theta,\phi)$, going through points $1',2,3,4'$. The path on the generated field sphere is a reflection of the path on the input sphere with respect to the equatorial plane. (b) Sections $1,1'-2$, $2-3$, and $3-4,4'$ and the variation of the mode vectors of $u_a$ and $\mathcal{E}_2$ in each one. (c) Detected far-field intensity profiles of the input and FWM signals at the points $1,1',2,3,4,4'$. For points $1,1'$ and $4,4'$ we also show in the insets the tilted lens (TL) profiles, indicating opposite OAM between input and FWM fields.

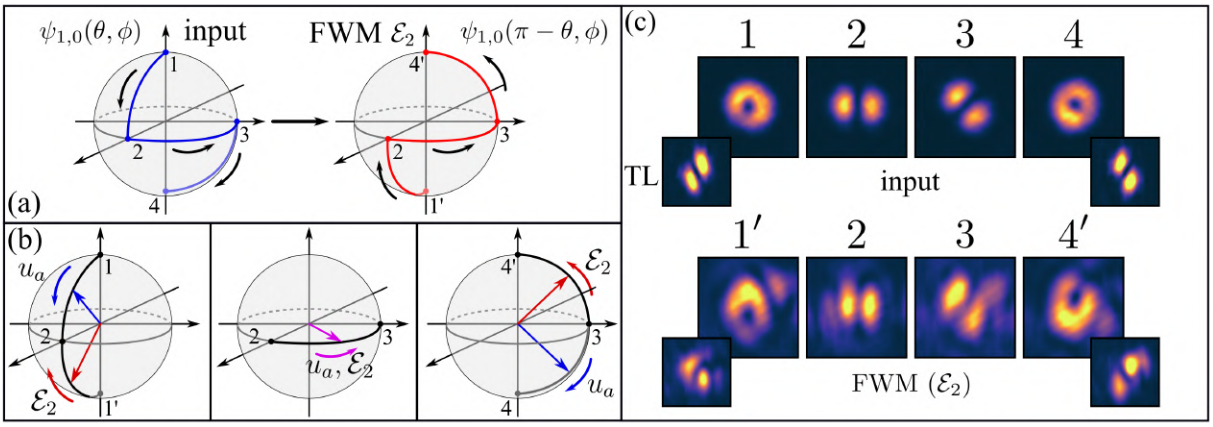

**Source:** The author (2024).

times the conjugate of the other field. By setting one of the input fields in a fundamental Gaussian mode, we have shown that the spatial structure of each conversion channel, in a thin medium, will be equivalent to what takes place in a second harmonic generation (SHG) and in a parametric down-conversion (PDC) for the fields $\mathcal{E}_1$ and $\mathcal{E}_2$, respectively.

This allowed us to simultaneously explore the symmetries previously reported for these nonlinear processes (RODRIGUES et al., 2018; RODRIGUES et al., 2022), by structuring the other input field in an OAM Poincaré sphere $\mathcal{O}(l,0)$. In particular, it was possible to observe the specular reflection symmetry for the field $\mathcal{E}_2$ with respect to the equatorial plane in the OAM sphere. We have also shown that the spatial structure of the other channel ($\mathcal{E}_1$) is a combination of two effects: the generation of radial order modes, and an inner symmetry for the OAM components, similar to what was predicted for a three-wave mixing process (RODRIGUES et al., 2022). This simultaneous two-channel symmetry of spatial modes can be useful for parallel generation and transmission of correlated fields for quantum information.

### 4.3.2 Superposition of Poincaré spheres – Hermite-Laguerre-Gaussian modes and the generalized Poincaré sphere

Another interesting path to follow is to investigate what happens when we combine two or more spheres in the superposition of the structured field $u_a = u_{a'}$. We can, for example, restrict ourselves the subspace of $N = 3$ spheres, $\mathcal{S}_3$, composed of the modes $\{\psi_{3,0}, \psi_{1,1}\}$ (RODRIGUES et al., 2022), to write:

$$u_a = c_{3,0}\psi_{3,0}(\Omega_{3,0}) + c_{1,1}\psi_{1,1}(\Omega_{1,1}), \tag{4.63}$$

where $c_{3,0}, c_{1,1}$ are complex coefficients, and we use $\Omega_{l,q} \equiv (\theta, \phi)_{l,q}$ to denote the angular coordinates in each sphere. Figure 46 shows an example of a combination of this kind. We may define subspaces of PS modes with definite order $N$ as:

$$\mathcal{S}_N = \{\psi_{N,0}\} \oplus \{\psi_{N-2,1}\} \oplus ... \oplus \operatorname{mod}(N,2)\{\psi_{1,(N-1)/2}\} \oplus \varepsilon_N\{u_{0,N/2}\}, \tag{4.64}$$

where $\varepsilon_N = 1 - \operatorname{mod}(N,2)$. For example, for the subspaces $N = 1, 2, 3, 4$, we have (RODRIGUES et al., 2022):

$$\begin{aligned}
N = 1 &: \mathcal{S}_1 = \{\psi_{1,0}\}, \\
N = 2 &: \mathcal{S}_2 = \{\psi_{2,0}\} \oplus \{u_{0,1}\}, \\
N = 3 &: \mathcal{S}_3 = \{\psi_{3,0}\} \oplus \{\psi_{1,1}\}, \\
N = 4 &: \mathcal{S}_4 = \{\psi_{4,0}\} \oplus \{\psi_{2,1}\} \oplus \{u_{0,2}\}.
\end{aligned} \tag{4.65}$$

It is interesting to work in these subspaces because, apart from an overall scaling of the beams due to diffraction, the optical modes are unchanged upon propagation.

**Figure 46** – Combination of optical modes on the Poincaré spheres of order $N = 3$, $u_a = \psi_{3,0}(\pi/4, \pi/4) + \psi_{1,1}(3\pi/4, \pi/2)$.

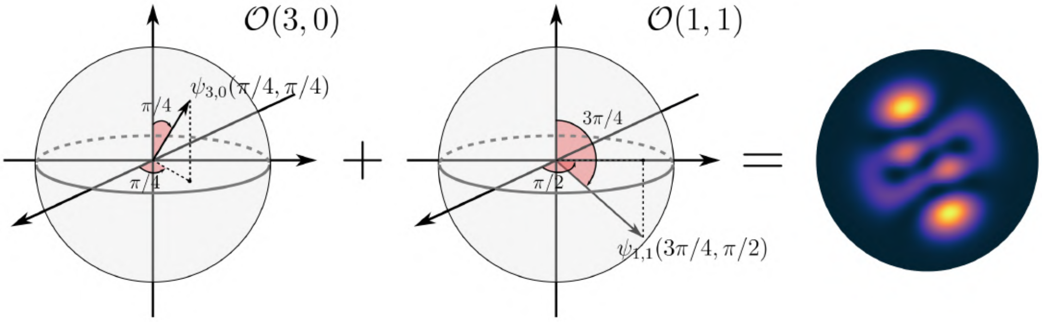

**Source:** The author (2024).

Let us treat the general case where $u_a$ is given by an arbitrary composition of PS modes with independent position vectors, and possibly radial modes, not necessarily with a well-defined mode order $N$:

$$u_a = \sum_{n \geq 0} d_n u_{0,n} + \sum_{i=1}^{M} c_i \psi_{l_i,q_i}(\theta_i, \phi_i), \tag{4.66}$$

where $M$ is total number of spheres, and $c_i, d_n$ are complex coefficients. In this case, the analytical treatment for the calculation of signal $\mathcal{E}_1$ becomes a bit cumbersome, since we must account for all of the combinations that arise from the product $u_a^2$; but for $\mathcal{E}_2$, which only has one contribution from $u_a$, the problem is still tractable. For $u_b = u_{0,0}$[1], we may obtain for the generated field:

$$\mathcal{E}_2 = \sum_{p=0}^{\infty} \left( \sum_{n \geq 0} d_{n,p} u_{0,p} + \sum_{i=1}^{M} c_{i,p} \psi_{l_i,p}(\vartheta_i, \varphi_i) \right), \tag{4.67}$$

where $d_{n,p} = d_n \Lambda_{00np}^{0000}$, $c_{i,p} = c_i \Lambda_{00q_ip}^{00-l_il_i} = c_i \Lambda_{00q_ip}^{00l_i,-l_i}$, and the transformed angles are given by relations (4.46) and (4.47), but for each sphere $\mathcal{O}(l_i, p)$ separately:

$$\vartheta_i = \pi - \theta_i, \tag{4.68}$$

$$\varphi_i = \phi_i. \tag{4.69}$$

In other words, the specular reflection symmetry holds in each individual sphere (RODRIGUES et al., 2022). In what follows we will apply this treatment for the particular case of the so-called generalized Hermite-Laguerre-Gaussian modes, which are stable solutions to the PWE, and can be understood as belonging to the generalized Poincaré sphere (CALVO; PICÓN; BAGAN, 2006; DENNIS; ALONSO, 2017). It is easy to see that for the signal $\mathcal{E}_1$, the associated symmetry should not hold valid in each sphere separately, since the vector angles on the various spheres $(\theta_i, \phi_i)$ get mixed due to the square of $u_a$.

The definition for a Poincaré sphere in the context of structured light presented in Eq. (4.33) is not the only one. In fact, there are many different definitions (DENNIS; ALONSO, 2017; SHEN et al., 2020; SHEN, 2021; HE; SHEN; FORBES, 2022), even mixing the amplitude, polarization, and other degrees of freedom (SHEN; ROSALES-GUZMÁN, 2022). One interesting definition is the Poincaré sphere associated with the so-called Hermite-Laguerre-Gaussian (HLG) modes, which can be seen as a generalization of the OAM PS. The HLG mode of order $N$ belongs to the subspace $\mathcal{S}_N$, and it is given by (CALVO; PICÓN; BAGAN, 2006; DENNIS;

---

[1] The discussion follows in the same manner for $u_b$ with nonzero radial order.

ALONSO, 2017; SHEN et al., 2020; SHEN, 2021):

$$\Psi_{\ell,N}(\theta,\phi) = i^{\frac{\ell-N}{2}} \sum_{\mu=-N}^{N} C^{\mu}_{\ell,N}(\theta,\phi)\, u_{\mu,(N-|\mu|)/2}, \tag{4.70}$$

where $N$ is the mode order, index $\mu$ runs in steps of $2$, the coefficients $C^{\mu}_{\ell,N}(\theta,\phi)$ are:

$$C^{\mu}_{\ell,N}(\theta,\phi) = (-1)^{\frac{\mu-|\mu|}{2}} d^{\frac{N}{2}}_{\frac{\ell}{2},\frac{\mu}{2}}(\theta)\, e^{-i\frac{\mu}{2}\phi}, \tag{4.71}$$

and $d^{j}_{m,n}(\theta)$ is the Wigner $d$-function, denoted as:

$$\begin{aligned} d^{j}_{m,n}(\theta) = & \sqrt{(j+m)!\,(j-m)!\,(j+n)!\,(j-n)!}\times \\ & \times \sum_{s=s_{\min}}^{s_{\max}} \frac{(-1)^{m-n+s}\left(\cos\frac{\theta}{2}\right)^{2j+n-m-2s}\left(\sin\frac{\theta}{2}\right)^{m-n+2s}}{(j+n-s)!\,s!\,(m-n+s)!\,(j-m-s)!}, \end{aligned} \tag{4.72}$$

where $s_{\min} = \max(0, n-m)$ and $s_{\max} = \min(j+n, j-m)$. At the poles of the generalized PS ($\theta = 0, \pi$) we also have pure LG modes, but at the equator ($\theta = \pi/2$) we always have HG modes, for any order $N$. At intermediate $\theta$ angles, they present more exotic distributions (see Fig. 47). Among many interesting properties, the HLG modes have an exact Wigner distribution function (CALVO, 2005; CALVO; PICÓN; BAGAN, 2006).

Note that the HLG mode, defined on the generalized Poincaré sphere, $\mathcal{O}_g(\ell, N)$, is a superposition of multiple LG modes with the same order $N$, but it can also be seen as a superposition of modes belonging to different OAM Poincaré spheres with order $N$, $\mathcal{O}(\mu, (N-|\mu|)/2)$. In terms of the modes $\psi_{l,p}$, we can write:

$$\Psi_{\ell,N}(\theta,\phi) = i^{\frac{\ell-N}{2}} \left( \varepsilon_N C^{0}_{\ell,N}(\theta,\phi)\, u_{0,N/2} + \sum_{\mu=1-\varepsilon_N}^{N} e^{i\frac{\mu}{2}\phi} \alpha_\mu \psi_{\mu,(N-\mu)/2}(\tilde{\theta}_\mu, \phi) \right), \tag{4.73}$$

**Figure 47** – Generalized Poincaré spheres for the Hermite-Laguerre-Gaussian modes. (a) $\mathcal{O}_g(3,3)$ and (b) $\mathcal{O}_g(2,4)$. Insets show the intensity profiles on specific points of the spheres.

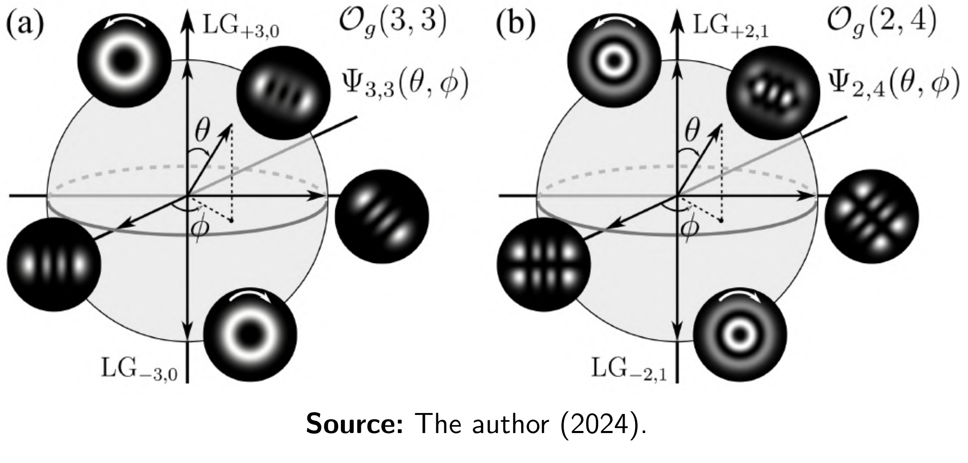

**Source:** The author (2024).

where $\varepsilon_N = [1 - \mathrm{mod}(N,2)]$, $\alpha_\mu = (|C^{\mu}_{\ell,N}(\theta,0)|^2 + |C^{-\mu}_{\ell,N}(\theta,0)|^2)^{\frac{1}{2}}$, and the modified polar angle is $\tilde{\theta}_\mu = 2\tan^{-1}[C^{-\mu}_{\ell,N}(\theta,0)/C^{\mu}_{\ell,N}(\theta,0)]$. The lowest order modes on the OAM and generalized spheres coincide, $\Psi_{1,1} = \psi_{1,0}$.

Note that Eq. (4.73 has the same form as Eq. (4.66), and thus the FWM signal $\mathcal{E}_2$ induced as a result of the interaction between $u_a = \Psi_{\ell,N}(\theta,\phi)$ and $u_b = u_{0,0}$ can be expressed as in Eq. (4.67):

$$\mathcal{E}_2 = \sum_p \left( d_p u_{0,p} + \sum_{\mu=1-\varepsilon_N}^{N} c_{\mu,p}\psi_{\mu,p}(\pi - \tilde{\theta}_\mu, \phi) \right), \tag{4.74}$$

where we neglected the global factor $i^{\frac{\ell-N}{2}}$, and the coefficients are:

$$d_p = \varepsilon_N C^{0}_{\ell,N}(\theta,\phi)\Lambda^{0000}_{00N/2,p}, \tag{4.75}$$

$$c_{\mu,p} = e^{i\frac{\mu}{2}\phi}\alpha_\mu \Lambda^{00-\mu\mu}_{00(N-\mu)/2,p}. \tag{4.76}$$

Therefore, by separating the different OAM PS contributions of the generalized HLG mode, the geometrical interpretation of the FWM process generating the field $\mathcal{E}_2$ can be applied, and the reflection symmetry holds valid in each individual sphere.

### 4.3.3 Pump fields as independent Poincaré spheres

Let us now investigate a FWM process driven by the product $u_a u_{a'} u_b^*$, where we have two independent Poincaré spheres, $u_a = \psi_{l,q}(\theta,\phi)$, $u_{a'} = \psi_{l',q'}(\theta',\phi')$, and the stimulated field is an arbitrary LG mode $u_b = u_{m,n}$. The product $u_a u_{a'}$ can be written as:

$$\begin{aligned} u_a u_{a'} &= \psi_{l,q}(\theta,\phi)\psi_{l',q'}(\theta',\phi'), \\ &= \cos\frac{\theta}{2}\cos\frac{\theta'}{2}\, u_{l,q}u_{l',q'} + e^{i\phi'}\cos\frac{\theta}{2}\sin\frac{\theta'}{2}\, u_{l,q}u_{-l',q'} + \\ &+ e^{i\phi}\sin\frac{\theta}{2}\cos\frac{\theta'}{2}\, u_{-l,q}u_{l',q'} + e^{i(\phi+\phi')}\sin\frac{\theta}{2}\sin\frac{\theta'}{2}\, u_{-l,q}u_{-l',q'}. \end{aligned} \tag{4.77}$$

The full overlap integral (including the longitudinal integration) in this case is:

$$\begin{aligned} \mathcal{A}^{\ell}_{p} &= \cos\frac{\theta}{2}\cos\frac{\theta'}{2}\,\mathcal{A}^{ll'm\ell}_{qq'np} + e^{i\phi'}\cos\frac{\theta}{2}\sin\frac{\theta'}{2}\,\mathcal{A}^{l,-l'm\ell}_{qq'np} + \\ &+ e^{i\phi}\sin\frac{\theta}{2}\cos\frac{\theta'}{2}\,\mathcal{A}^{-ll'm\ell}_{qq'np} + e^{i(\phi+\phi')}\sin\frac{\theta}{2}\sin\frac{\theta'}{2}\,\mathcal{A}^{-l,-l'm\ell}_{qq'np}. \end{aligned} \tag{4.78}$$

We recall that, in principle, the radial spectrum is unrestricted, and thus multiple $p$ orders can be generated. To proceed, let us consider $m = 0$, i.e., $u_b$ given by a pure radial mode. In this case, it is straightforward to identify the Poincaré sphere modes at the output. We may write:

$$\mathcal{A}_p^{\ell} = A\mathcal{A}_{qq'np}^{ll'0\ell} + B\mathcal{A}_{qq'np}^{l,-l'0\ell} + C\mathcal{A}_{qq'np}^{-ll'0\ell} + D\mathcal{A}_{qq'np}^{-l,-l'0\ell}, \tag{4.79}$$

with the coefficients

$$A = \cos(\theta/2)\cos(\theta'/2), \tag{4.80}$$

$$B = e^{i\phi'}\cos(\theta/2)\sin(\theta'/2), \tag{4.81}$$

$$C = e^{i\phi}\sin(\theta/2)\cos(\theta'/2), \tag{4.82}$$

$$D = e^{i(\phi+\phi')}\sin(\theta/2)\sin(\theta'/2). \tag{4.83}$$

The first and fourth terms in Eq. (4.79) are associated with the generation of modes belonging to Poincaré spheres $\mathcal{O}(|l+l'|,p)$, while the middle terms are related with the generation of modes belonging to Poincaré spheres $\mathcal{O}(|l-l'|,p)$, and we may write:

$$\mathcal{E}_{a+a'+b} = \sum_p \left\{ A_p\psi_{l+l',p}(\vartheta_3,\varphi_3) + e^{i\phi'}B_p\psi_{l-l',p}(\vartheta_4,\varphi_4)\right\}, \tag{4.84}$$

where $A_p = \mathcal{A}_{qq'np}^{ll'0,l+l'} = \mathcal{A}_{qq'np}^{-l,-l'0,-l-l'}$, $B_p = \mathcal{A}_{qq'np}^{l,-l'0,l-l'} = \mathcal{A}_{qq'np}^{-l,l'0,l'-l}$, and the angles $(\vartheta_3,\varphi_3)$, $(\vartheta_4,\varphi_4)$ are:

$$\vartheta_3 = 2\tan^{-1}\left(\tan(\theta/2)\tan(\theta'/2)\right), \qquad \varphi_3 = \phi+\phi', \tag{4.85}$$

$$\vartheta_4 = 2\tan^{-1}\left(\tan(\theta/2)\cot(\theta'/2)\right), \qquad \varphi_4 = \phi-\phi'. \tag{4.86}$$

It can be readily verified that when $(\theta',\phi')\to(\theta,\phi)$, the relations (4.85) become those shown in Eq. (4.46), but we still have the possibility of working with two independent spheres ($l\neq l'$, $q\neq q'$). For relations (4.86), in this case we obtain $(\vartheta_4,\varphi_4)\to(\pi/2,0)$, i.e., the second term of the sum in Eq. (4.84) becomes $\frac{1}{\sqrt{2}}e^{i\phi}B_p(u_{l-l',p}+u_{-(l-l'),p})$. On the other hand, if $l=l'$, the sphere associated with the OAM difference $(l-l')$ is not well-defined anymore, and we may rewrite the FWM field (4.84) as:

$$\mathcal{E}_{a+a'+b} = \sum_p \left\{ A_p\psi_{2l,p}(\vartheta_3,\varphi_3) + C_p(\theta,\phi;\theta',\phi')u_{0,p}\right\}, \tag{4.87}$$

where now

$$C_p(\theta,\phi;\theta',\phi') = \mathcal{A}_{qq'np}^{l,-l00}\left[e^{i\phi'}\cos(\theta/2)\sin(\theta'/2) + e^{i\phi}\sin(\theta/2)\cos(\theta'/2)\right], \tag{4.88}$$

and for $(\theta',\phi')\to(\theta,\phi)$, the term inside square brackets becomes $e^{i\phi}\sin\theta$, equivalent to the case in Eq. (4.53). Thus, we see that the analysis we applied in the previous Section can be easily extended to more complicated scenarios.

### 4.3.4 Extended-medium regime – restrictions imposed by the Gouy phase-matching

In this section we explore a few outcomes predicted in the extended-medium regime. It is not an easy task to achieve this condition in the experiment, especially in the degenerate setting, where we can only count on the directions of the wave-vectors, and the polarizations of the fields, to filter the generated light output. We will revisit some of the scenarios we considered up to this point. Recalling what we saw in Chapter 2, when $L/z_R \to \infty$, for the full overlap integral $\mathcal{A}_{qq'np}^{ll'm\ell}$ to be nonzero, it must satisfy simultaneously the OAM conservation and the Gouy phase-matching (GPM) conditions:

$$\ell = l + l' - m, \tag{4.89}$$

$$p = q + q' - n + \frac{1}{2}(|l| + |l'| - |m| - |\ell|). \tag{4.90}$$

The GPM condition automatically narrows the radial spectrum of the FWM signal to a single possible value. However, this may not be so easily satisfied in some cases. Let us consider the situation studied in Section 4.3.1, where we looked at the two FWM signals $\mathcal{E}_1$ and $\mathcal{E}_2$, driven by $u_a = \psi_{l,0}(\theta, \phi)$, and $u_b = u_{0,0}$. Taking into account now the fact that we need to integrate on the longitudinal coordinate over the medium extension $L$, we rewrite Eqs. (4.44) and (4.45) as:

$$\mathcal{E}_1 = \sum_p \left\{ \overline{a}_p \psi_{2l,p}(\vartheta_1, \varphi_1) + e^{i\phi} \sin\theta \, \overline{c}_p u_{0,p} \right\}, \tag{4.91}$$

$$\mathcal{E}_2 = \sum_p \overline{b}_p \psi_{l,p}(\vartheta_2, \varphi_2), \tag{4.92}$$

where the transformed angles are not affected, and now the coefficients are given by the full overlap integrals:

$$\{\overline{a}_p, \overline{b}_p, \overline{c}_p\} = \left\{ \mathcal{A}_{000p}^{ll0,2l}, \mathcal{A}_{000p}^{00,-ll}, \mathcal{A}_{000p}^{l,-l00} \right\}. \tag{4.93}$$

We emphasize that since we are not in a thin-medium setting, we cannot change between bases with different beam waists. Now, for $L/z_R \to \infty$, we must have:

$$\{\overline{a}_p, \overline{b}_p, \overline{c}_p\} \to \{\overline{a}_0, \overline{b}_0, \overline{c}_l\}, \tag{4.94}$$

since these are the only coefficients that comply with the GPM requirement, according to Eq. (4.90), and we rewrite the FWM fields as

$$\mathcal{E}_1 = \overline{a}_0 \psi_{2l,0}(\vartheta_1, \varphi_1) + e^{i\phi} \sin\theta \, \overline{c}_l u_{0,l}, \tag{4.95}$$

$$\mathcal{E}_2 = \overline{b}_0 \psi_{l,0}(\vartheta_2, \varphi_2). \tag{4.96}$$

We then see the main difference with respect to the result obtained previously [Eqs. (4.53) and (4.54)]: the radial spectrum is automatically restricted on the basis of modes with waist $w_0$ to $p = 0$ for the PS components of both fields $\mathcal{E}_1$ and $\mathcal{E}_2$, and to $p = l$ for the zero TC component of $\mathcal{E}_1$. The Table 1 shows the bounds to the radial index $p$ contributing to the field $\mathcal{E}_1$ in the thin- and extended-medium regimes.

**Table 1** – Synthesis of the $p$ values constituting the radial spectrum of signal $\mathcal{E}_1$ in the thin- and extended-medium regimes, when the pump beams are given by OAM PS modes $\psi_{l,0}(\theta, \phi)$, and the corresponding mode bases in which these selection rules are verified.

| Medium length | $\mathcal{E}_1$ radial spectrum | Comment |
|---|---|---|
| Thin, $L/z_R \ll 1$ | $0 \leq p \leq \lvert l \rvert$ | Only on the reduced waist basis, $\tilde{w} = w_0/\sqrt{3}$ |
| Extended, $L/z_R \gg 1$ | $p = \lvert l \rvert$ | Automatically on the input waist basis, $w_0$ |

**Source:** The author (2024).

Note that the radial integral in the coefficient $\bar{c}_l$ falls onto the case we detailed in Section 2.3.3.4, and it is therefore equal to zero for *odd* $l$ values [see Eq. (2.177)]:

$$\bar{c}_l \propto \mathcal{R}^{l,-l00}_{000l} \overset{\mathrm{odd}\, l}{=} 0. \tag{4.97}$$

With this, we obtain a peculiar dependence of the non-vortex component of $\mathcal{E}_1$ with the parity of the pump Poincaré sphere order $N = l$. If $N$ is even, we will have a contribution from the $u_{0,l}$ radial mode; but if $N$ is odd, we obtain a pure OAM PS mode $\psi_{2l,0}$ at the output. We must emphasize that this is only true in a degenerate configuration. This is the reason why, in our configuration, we expect to obtain qualitatively different results with respect to those obtained in Ref. (WALKER; ARNOLD; FRANKE-ARNOLD, 2012), where the nondegenerate FWM by amplified spontaneous emission scheme was used. More specifically, the zero OAM component of the output superposition is completely suppressed when the incident pumps are given by combinations of odd valued $\pm l$. The Table 2 presents the combinations of LG modes contributing to the total FWM field driven by the pumps shown in Fig. 4 of Ref. (WALKER; ARNOLD; FRANKE-ARNOLD, 2012), and the corresponding results considering a degenerate setting. In Fig. 48 we show the FWM intensity profiles obtained in both settings for all cases $\#1 - 5$ of Table 2. We highlight that all images are up to scale, and this evidences the fact that in the cascade configuration, the generated blue light field emerges with a smaller overall size with respect to the pump beam size, as compared to the degenerate case. Namely, $w_{0,\mathrm{B}} = w_0/\xi_{\mathrm{B}}$, with $\xi_{\mathrm{B}} = \sqrt{780/420} \approx 1.36$, and $w_{0,\mathrm{deg}} = w_0$.

Let us now take a closer look at signal $\mathcal{E}_2$. It is interesting to note that in this case, the generation of signal $\mathcal{E}_2$ is suppressed, $\bar{b}_0 \to 0$, since the only radial index for the coefficient

**Table 2** – Comparison between the output mode superpositions obtained in the extended-medium regime ($L/z_R \to \infty$) for the nondegenerate FWM scheme of Ref. (WALKER; ARNOLD; FRANKE-ARNOLD, 2012) and in the degenerate FWM configuration considered in our work. For $\#1, 5$, where the pump is composed of odd $\pm l$, the contribution from the radial mode $u_{0,l}$ to the FWM field in the degenerate setting is exactly zero.

| $\#$ | Pump mode | Nondegenerate (Walker, 2012) | Degenerate |
|---|---|---|---|
| 1 | $\frac{1}{\sqrt{2}}(u_{1,0} + u_{-1,0})$ | $0.52(u_{2,0} + u_{-2,0}) - 0.68u_{0,1}$ | $\frac{1}{\sqrt{2}}(u_{2,0} + u_{-2,0})$ |
| 2 | $\frac{1}{\sqrt{2}}(u_{1,0} + u_{-2,0})$ | $0.66u_{2,0} + 0.53u_{-4,0} - 0.53u_{-1,1}$ | $0.77u_{2,0} + 0.33u_{-4,0} + 0.54u_{-1,1}$ |
| 3 | $\frac{1}{\sqrt{2}}(u_{2,0} + u_{-2,0})$ | $0.66(u_{4,0} + u_{-4,0}) + 0.37u_{0,2}$ | $0.46(u_{4,0} + u_{-4,0}) - 0.76u_{0,2}$ |
| 4 | $\frac{1}{\sqrt{2}}(u_{2,0} + u_{-3,0})$ | $0.74u_{4,0} + 0.63u_{-6,0} + 0.22u_{-1,2}$ | $0.73u_{4,0} + 0.33u_{-6,0} - 0.60u_{-1,2}$ |
| 5 | $\frac{1}{\sqrt{2}}(u_{3,0} + u_{-3,0})$ | $0.70(u_{6,0} + u_{-6,0}) - 0.11u_{0,3}$ | $\frac{1}{\sqrt{2}}(u_{6,0} + u_{-6,0})$ |

**Source:** The author (2024).

**Figure 48** – Comparison between the FWM intensity profiles obtained in the extended-medium regime, for the nondegenerate setting of Ref. (WALKER; ARNOLD; FRANKE-ARNOLD, 2012), and those predicted for a degenerate situation.

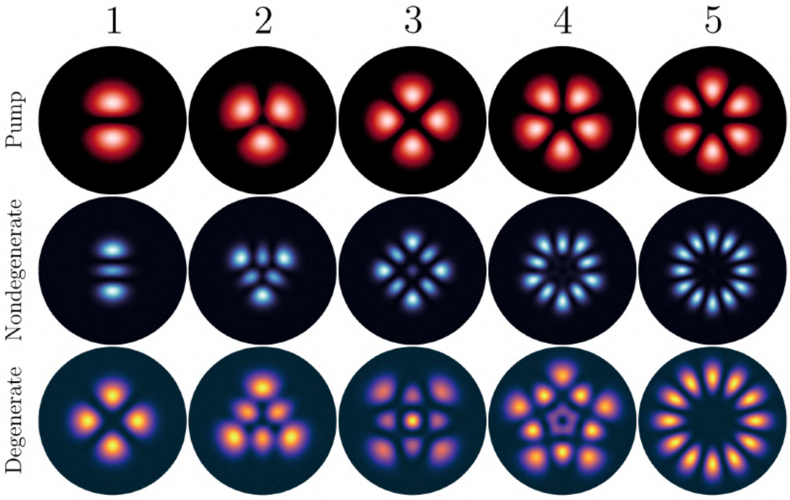

**Source:** The author (2024).

$\mathcal{A}^{00,-ll}_{000p}$ that complies with Eq. (4.90) is negative: $p = -|l|$, which is not allowed. To obtain an output in the direction $(2\mathbf{k}_b - \mathbf{k}_a)$, the GPM condition for this overlap integral must result in positive $p$ values. To this end, we must resort to a non-Gaussian $u_b$ field. Let us consider $u_b = u_{0,n}$[2], and that the PS for $u_a$ may carry a nonzero radial index, $\psi_{l,q}$. In this manner, we may rewrite the FWM fields as:

$$\mathcal{E}_1 = \mathcal{A}^{ll0,2l}_{qqnP}\psi_{2l,P}(\vartheta_1, \varphi_1) + e^{i\phi}\sin\theta\mathcal{A}^{l-l00}_{qqnP'}u_{0,P'}, \tag{4.98}$$

$$\mathcal{E}_2 = \mathcal{A}^{00,-l,l}_{nnqP''}\psi_{l,P''}(\vartheta_2, \varphi_2), \tag{4.99}$$

where $P = 2q - n, P' = 2q - n + |l|, P'' = 2n - q - |l|$. Another curious selection rule arises

---

[2] If $u_b$ carries topological charge, the analysis is still possible, but the definition of the output PS may not be as straightforward.

here. The radial integral

$$\mathcal{R}^{00\pm l\mp l}_{nnqP''} = \int_0^\infty \rho^{2|l|} \left[L_n^0(\rho^2)\right]^2 L_q^{|l|}(\rho^2) L_{P''}^{|l|}(\rho^2) e^{-2\rho^2} \rho d\rho, \tag{4.100}$$

is null for certain combinations of the indices $(n, q, l)$, even if the resulting $P'' = 2n - q - |l|$ has an allowed (positive) value. The FWM field $\mathcal{E}_2$ is therefore completely suppressed. This restriction is not as clear as the selection rule obtained for the case with structured pumps with odd topological charges with opposite handedness [Eq. (2.176)], that we used previously. By analyzing the calculated values of the normalized overlap integral $\overline{\mathcal{A}}^{00\pm l\mp l}_{nnqP''} = \mathcal{A}^{00\pm l\mp l}_{nnqP''}/\mathcal{A}^{0000}_{0000}$ for several cases, we verify that it is null for odd $l$, which also makes $N_{l,q}$ odd.

Restrictions of this kind are not exclusive to situations involving PS modes. Much simpler scenarios, even ones involving pure LG modes, may result in the complete suppression of one of the signals $\mathcal{E}_1$ or $\mathcal{E}_2$. As a simple example, consider the FWM induced by $u_a = u_{l,0}$, $u_b = u_{0,0}$. For signal $\mathcal{E}_2$ the OAM conservation imposes the output TC to be $\ell = -l$, and the GPM condition restricts the output radial index to be $p = -|l|$, which is not possible. If $u_b$ has a possibly nonzero radial index, $u_b = u_{0,n}$, then $p = 2n - |l|$, and the $\mathcal{E}_2$ output is expected to be generated for $2n \geq |l|$.

It must be noted that in our experiment it is extremely difficult to access the extended-medium regime. This is because the degenerate frequency configuration only leaves the propagation direction and polarization degrees of freedom to work with in order to filter the FWM signals. Regarding polarization, we know that with input orthogonal linear polarizations, we can use polarizing beam splitters to separate the signal pairs at the output. But these components have their success rate, measured by the extinction ratio. Since the pumps are orders of magnitude stronger than the FWM signals, in practice it is not possible to completely eliminate the scattered light arriving at the detection positions. This is why we always work with non co-linear input beams. The small angle between their wave-vectors allows to separate the four output signals. At a significant propagation distance, it becomes easier to detect the two FWM signals. This works well for the thin-medium regime, but it becomes troublesome when we try to achieve the extended-medium regime, as the necessary separation angle makes it impossible to maintain the physical overlap of the pump beams inside the cell across a significant extension.

# 5 SPATIAL CORRELATIONS IN FWM

A multitude of processes take place when two driving laser beams intersect inside an atomic sample and generate the two FWM outputs. To track and account for all of them is a tough task. To this day in our lab we looked at phenomena associated with the spectral, temporal, and more recently, the spatial degrees of freedom of light. In general, and in the most fundamental aspects of the light-matter interaction, all of these degrees of freedom are coupled to one another. What we usually do is to perform approximations that allow us to decouple the degrees of freedom we want to focus on, from all the others.

So far in this Thesis we explored the two-channel FWM configuration looking at the outputs independently. This allowed to establish and verify well-defined rules dictating the transfer of spatial structure of the input to the output light fields. A natural sequence to our studies, and one that aligns with the current advances in the area, is to investigate the correlations between the participating fields. In particular, the spatial correlations associated with the multi-mode structure of the light fields.

The study of correlations, in a general sense, has been of paramount importance in the development of modern physics. Spatial correlations of the photon pairs generated in parametric down-conversion have been exhaustively investigated in the last decades (WALBORN et al., 2010). In four-wave mixing, it has been shown that the entanglement, measured by the level of multi-mode squeezing, between the generated signal pair presents a transverse position dependence (BOYER et al., 2008). The squeezing measured when the entirety of the output signals were detected can be seen as an overall measure of the localized squeezing between the smaller regions of the beams. This can only be achieved in the presence of a spatially multi-mode light state (KOLOBOV, 2007). The idea of studying the dependence of squeezing on the different regions of the generated beams was also employed in other work from this same group (BOYER; MARINO; LETT, 2008; MARINO et al., 2008). In a 2018 work, the spiral bandwidth of cascade FWM generating blue light in Rb vapor was studied (OFFER et al., 2018), and it was shown that the OAM states of the output light fields are entangled. More recently, in Ref. (NIRALA et al., 2023), it was shown that the spatial information carried by the driving pump field can be transferred to the spatial cross-correlation between the generated twin beams. In this manner, to successfully access the information carried by the pump field, one must simultaneously detect the probe and conjugate signals.

It is well-known that in a single FWM process, it is expected that the spontaneously generated probe and conjugate signals are spatially correlated. The description in terms of the biphoton state, well-established in PDC within the context of structured light (WALBORN et al., 2010), encompasses these spatial correlations in FWM as well (NIRALA et al., 2023). In a two FWM channel setting, such as ours, where we have four light fields in total, it is reasonable to expect correlations between the possible pairs of signals. However, the detection of such correlations can be challenging, and we don't have experience in this area.

What we present in this Chapter, as the last bit of this Thesis, is our attempt to comprehend fundamental aspects concerning spatial correlations in FWM, and to establish guiding lines for what we believe may be interesting to explore in the future.

## 5.1 PHASE FLUCTUATIONS OF DIODE LASERS AND TEMPORAL CORRELATIONS

Our investigations of correlations in FWM actually started with the study of temporal correlations between the light beams participating in the process. These correlations can be explained semi-classically, and they originate from the conversion of the phase-noise inherent to diode lasers, to amplitude-noise, as a result of the interaction with the atomic medium (ARIUNBOLD et al., 2010). In this context, in a recent work (ALMEIDA; MOTTA; VIANNA, 2023) we showed that the intensity correlations between transmitted signals, and between FWM signals, oscillate with a frequency dictated by the generalized Rabi frequency. We verified this experimentally by varying the detuning of the incident fields and looking at the dominant oscillation frequency of the intensity fluctuation cross-correlation curves $g^{(2)}(\tau)$. We were able to reproduce this behavior in the calculations by numerically solving the optical Bloch's equations taking into account the fluctuating phase $\phi(t)$ of the driving fields:

$$\mathbf{E}_i(\mathbf{r},t) = \frac{1}{2}\boldsymbol{\epsilon}_i\mathcal{E}_i e^{-i[\mathbf{k}_i\cdot\mathbf{r}-\omega_i t+\phi_i(t)]} + \text{c.c.}, \tag{5.1}$$

where the subscript $i = a, b$ labels the pump fields. For the calculations we considered beams with uniform spatial profiles. The random phase $\phi_i(t)$ is described by a Wiener-Levy diffusion process, and satisfies

$$\overline{\langle\dot{\phi}_i(t)\dot{\phi}_j(t')\rangle} = 2D\delta_{i,j}\delta(t-t'), \tag{5.2}$$

where $D$ is the diffusion coefficient, and the bar indicates stochastic averaging. It is important to note that we only expect correlations between the outgoing signals since we consider a single driving field, which is split into two beams, and therefore carry the same fluctuating phase, $\phi_a(t) = \phi_b(t) = \phi(t)$. If the two beams originated from two different laser sources, the fluctuations would be uncorrelated. The numerical solution to the OBEs with the stochastic phase fluctuation of the pump beams yields the time varying elements of the atomic density matrix $\hat{\rho}(t)$. It can be said that the fluctuating phase acts as a driving term in the highly coupled set of equations that describes the atomic response associated with the absorption of transmitted signals and the generation of the FWM fields (and possibly other processes). This can be seen as an explanation to the mechanism that converts the phase fluctuations to intensity fluctuations as a result of the light-atom interaction. We can then use the coherences associated with the generation of the FWM signal or the absorption of the pump beams, to calculate the theoretical intensity correlation curves (ARIUNBOLD et al., 2010; ALMEIDA; MOTTA; VIANNA, 2023).

The experiment consisted in passing the Gaussian laser beams $a$ and $b$ through the cold atom cloud and detecting intensity time series of the transmitted and generated signals with avalanche photo detectors (APD). Figure 49 illustrates the idea. To detect the fluctuations of the transmitted beams, we need to work in a low intensity regime (too much power saturates the medium, and the medium-driven amplitude fluctuations are not seen); while to generate and detect the FWM signals we need high intensities. Due to this conflict between the intensity regimes necessary to observe the fluctuations of the transmitted and FWM signals, it is not possible to detect all of them simultaneously. Therefore, we cannot compute transmission-FWM correlations. In Fig. 50(a) we show a $1\ \mu\text{s}$ interval of a $150\ \mu\text{s}$ time series of the intensity fluctuations of the transmitted signals $a$ and $b$, while in Fig. 50(b) we show the corresponding cross-correlation $g^{(2)}_{a,b}(\tau)$, calculated taking into account the full time-series.

The intensity fluctuation correlation curves for both the experimental and numerical data

**Figure 49** – Simplified scheme for the detection of the intensity fluctuation time-series of the transmision and FWM signals.

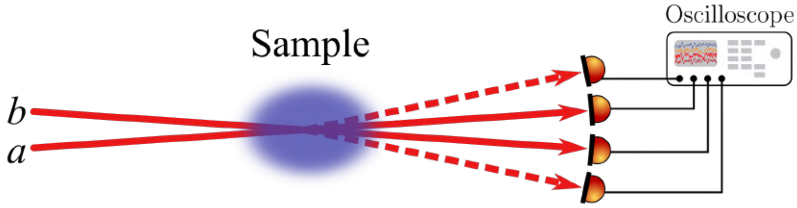

**Source:** The author (2024).

**Figure 50** – (a) Measured time series of the intensity fluctuations of the two Gaussian beams, $a$ and $b$, transmitted through the cold atom cloud. (b) Corresponding cross-correlation between the intensity fluctuations. The two incident beams were detuned by $\delta \approx -5$ MHz, and their power was $P \approx 5$ µW. The correlation at zero delay is $\approx 0.87$.

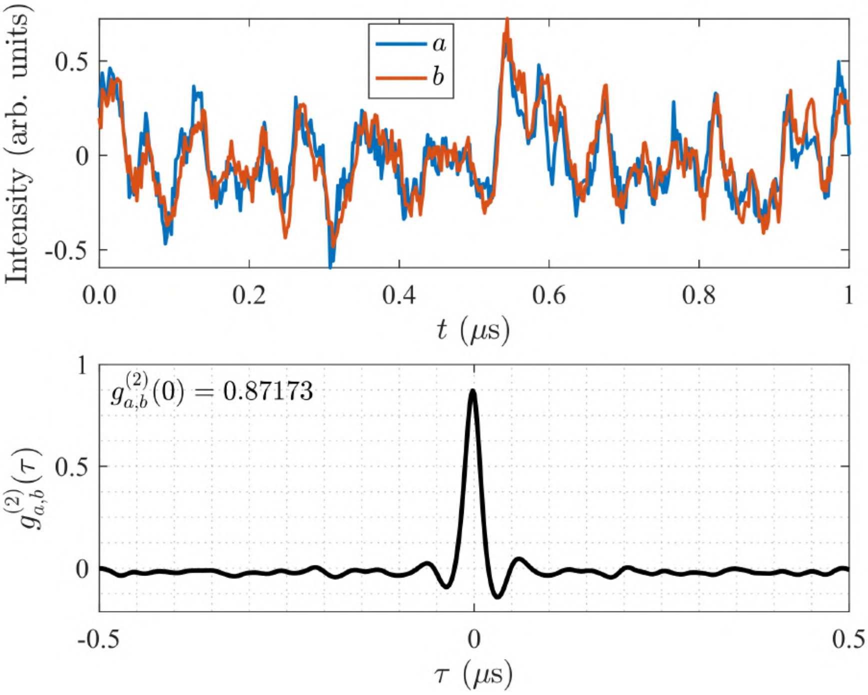

**Source:** The author (2024).

are calculated via:

$$g^{(2)}_{i,j}(\tau) = \frac{\langle f_i(t) f_j(t+\tau)\rangle}{[\langle f_i^2(t)\rangle \langle f_j^2(t)\rangle]^{\frac{1}{2}}}, \tag{5.3}$$

where in our case $f_i(t) = I_i(t) - \langle I_i \rangle$ denotes the intensity fluctuation of the signal $i$ around the mean (DC) value $\langle I_i \rangle$. In fact we can also subtract slow temporal envelopes to study only the fast intensity fluctuations. Therefore, the correlation functions presented here satisfy the bound $-1 \leq g^{(2)}(0) \leq 1$, where positive, negative and null values indicate correlated, anti-correlated, and uncorrelated signals, respectively. For the experimental results, $I_i(t)$ is given by the measured intensity time-series, and for the theoretical results, $I_i(t)$ is connected to the calculated atomic coherences. The time averaging of the product of two real functions of time is defined as $\langle f_i(t) f_j(t+\tau)\rangle \equiv \frac{1}{T}\int_{t-T/2}^{t+T/2} f_i(t') f_j(t'+\tau) dt'$, which for large sample times $T$, with respect to the dominant frequencies of the signals $f_{i,j}$, can be calculated by means of their Fourier transforms, $\tilde{f}_{i,j}$, as:

$$\langle f_i(t) f_j(t+\tau)\rangle = \frac{\pi}{T}\mathcal{F}^{-1}\{\tilde{f}_i(\omega)\tilde{f}_j^*(\omega)\}(\tau) = \frac{\pi}{T} G_{i,j}(\tau). \tag{5.4}$$

With this, we may write:

$$g_{i,j}^{(2)}(\tau) = \frac{G_{i,j}(\tau)}{\sqrt{G_{i,i}(0)G_{j,j}(0)}}. \tag{5.5}$$

We can perform the same measurements using hot rubidium vapor as the interaction medium. In this case, there are multiple velocity groups contributing to the interaction dynamics, contrary to the cold atom cloud where we essentially have atoms with zero velocity. We are currently conducting a study on the influence of the non-negligible velocity distribution on the behavior of the correlation curves. To demonstrate that the intensity fluctuations only become correlated as a result of the light-atom interaction, we show in Fig. 51(a) the time series and correlation curves obtained with no interaction medium. Furthermore, we show in Fig. 51(b) the results obtained with a heated Rb sample as the nonlinear medium but using a laser source that does not present the stochastic phase fluctuations. The fluctuations are completely uncorrelated in both cases.

**Figure 51** – Intensity time-series of transmitted signals and cross-correlation curves (a) without an interaction medium to promote the phase- to amplitude-noise conversion; and (b) with a heated rubidium sample, but using a grating stabilized diode laser, which does not present stochastic phase-fluctuations.

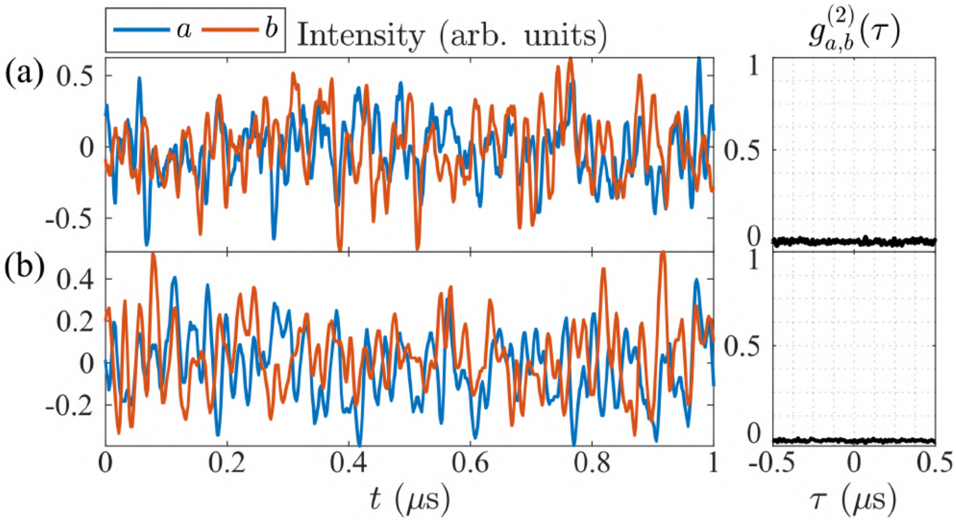

**Source:** The author (2024).

## 5.2 COUPLED SPATIAL AND TEMPORAL CORRELATIONS

One follow-up path was to explore possible spatial dependencies in these correlations. The correlations between transmitted beams are much stronger and easier to detect in comparison with the correlations between FWM signals. For this reason we started with the transmissions.

The idea was to measure intensity time series, just like the ones we did originally, but with a spatially resolved detection scheme. The spatial resolution is introduced by placing pinholes with translation degrees of freedom in front of the detectors. Figure 52(a) illustrates this detection scheme. In this manner, we can select the regions of the beam profile that will impinge onto the detectors, and possibly distinguish between areas that carry stronger or weaker correlations. This idea was taken from detection schemes that were employed to study spatial correlations in the photon-pair generated in PDC (WALBORN et al., 2010). What we get as a result is a the matrix $g^{(2)}_{a,b}(X_a, X_b; \tau)$, that contains all of the correlation curves between the signals measured when the pinholes were positioned at $(X_a, X_b)$, as represented in Fig. 52(b). The dimension of this correlation matrix is $N_a \times N_b \times N_\tau$, where $N_a, N_b$ are the number of positions where the pinholes are placed during the measurements, determining the spatial resolution, and $N_\tau$ is the number of points on the time axis. Visualizing all of the information in such a quantity is not simple. We are usually interested in some parameters that encompass the behavior of the correlation curves, such as the Pearson coefficient, the width (or correlation time) and the characteristic oscillation frequency. We can then define more convenient $N_a \times N_b$ matrices carrying these parameters at each position $(X_a, X_b)$. In Fig. 53 we show a result from such a measurement performed in our cold atom setup. On the left we present the $g^{(2)}$ values at $\tau = 0$, and on the right we show the mean frequency $\langle f \rangle$ of the Fourier distribution, as functions of the pinhole positions in front of the transmitted beams $a$ and $b$. The diameters of the beams near the detection position was $\sim 2$ mm, and the diameter of the pinholes was $500$ µm.

We must highlight, however, that the spatial correlations studied in PDC originate essentially from the conservation of transverse linear momentum, and not from the stochastic phase fluctuations of the input light source. Another important distinction that must be made is that the correlations in PDC and FWM are expected between conjugate signal pairs, i.e., light fields that are emitted in a single parametric process. This is not the case of the transmission signals we are studying, and neither of the two FWM signals. Nonetheless, we wondered if a coupling between spatial and temporal correlations could be verified in our experiment. We believe that a signature of spatial dependencies in the correlations we measure would give us information about the spatial dependence of the phase fluctuation itself. For example, if instead of being a uniform quantity over the transverse beam profile, it may be expressed as $\phi(\mathbf{r}, t)$, indicating a coupling between the spatial and temporal degrees of freedom. Or even, if there is any kind of cross-talk between the two incident light beams mediated by the atomic sample that can

**Figure 52** – (a) Depiction of the spatially resolved detection of the intensity fluctuation time-series of the transmitted signals. The pinholes with a translation degree of freedom in the horizontal direction select the regions of the beam profile that impinge onto the detectors. (b) Representation of the resulting correlation matrix $g^{(2)}_{a,b}(X_a, X_b; \tau)$. The different colors of the correlation curves are meant to aid the visualization.

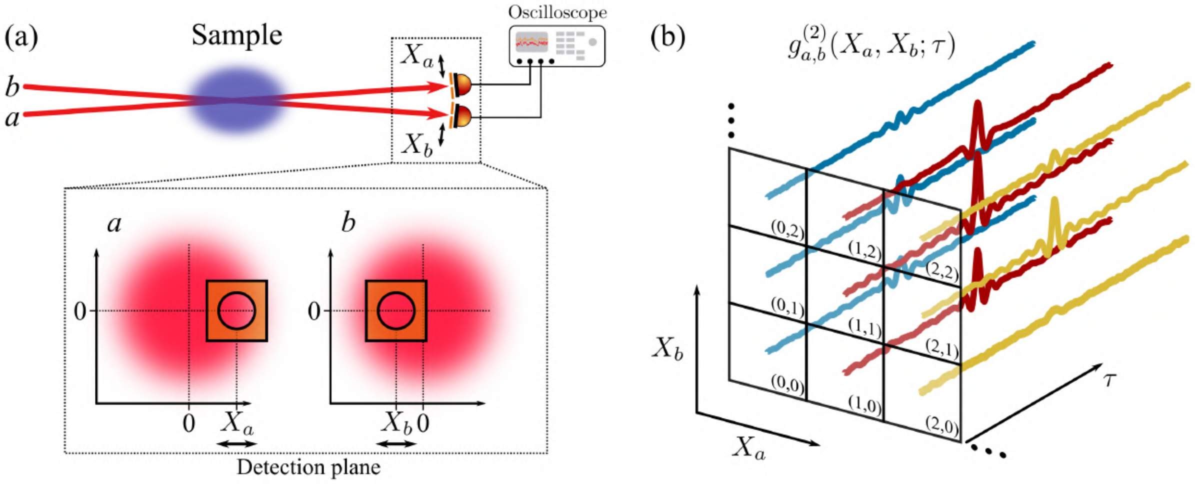

**Source:** The author (2024).

**Figure 53** – Pearson coefficient $g^{(2)}(\tau = 0)$ (left) and mean frequency of the Fourier spectrum $\langle f \rangle$ (right) of the fluctuation correlation functions $g^{(2)}$ obtained by detecting localized portions of the beams transmitted through the cold atom cloud, as a function of the pinhole positions $(X_a, X_b)$. In all of the measurements, the detuning was $\delta \approx -5$ MHz and the power in each beam was $P \approx 5$ µW.

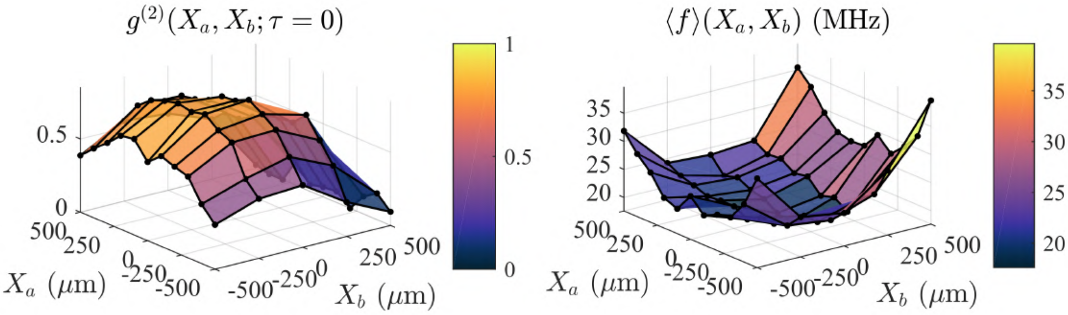

**Source:** The author (2024).

be revealed by the correlations between the localized portions of the beam profiles.

From our experience with this arrangement both in hot and cold samples, we know that depending on the pump intensities, the two light fields may influence one-another. One example is the absorption spectra of the transmitted signals when we have a single beam passing through the sample, compared to when we make the two beams intersect inside the medium. Modifications can be verified when we compare the two cases, and they become more evident for higher intensities. Also, small differences can be noted in the aforementioned correlation curves when we compare these two cases. We believe these modifications may be caused by linear and nonlinear effects. The strong beams influence the effective index of refraction in an intricate way, and this influence may be position-dependent by itself. When we have a spatial overlap between the two beams, we can argue that some of their power is allocated to participate in the four-wave mixing processes. The discussion so far only considered Gaussian beams, but we can also reason considering any other structure of the pump beams, which was our initial objective.

## 5.3 QUANTUM SPATIAL CORRELATIONS IN FWM

The quantum theory for spatial correlations in FWM in the regime of a classical pump bears great similarity with the theory for parametric-down conversion (PDC), which is already well-established (WALBORN et al., 2010). In very simple terms, in both processes a pump beam excites the nonlinear medium and a pair of correlated photons is generated. The difference is that in PDC, a single photon is absorbed from the pump, while in FWM two photons are absorbed. Of course, this is a general comparison from a fundamental point of view, and more specific aspects must be considered when studying each process in their many configurations. Nonetheless, many concepts and calculations translate almost effortlessly to FWM. An interesting capability thoroughly explored in PDC is to engineer the spatial correlations between the photon-pair by modifying the pump structure. Despite that, to the best of our knowledge, only recently this approach was employed to encode information in the spatial correlations between the FWM twin-beams with a high degree of control (NIRALA et al., 2023).

In this section, we explore the quantum-mechanical picture of FWM induced by structured light, evidencing the multi-spatial mode nature of the generated light state, and the associated spatial correlations. We start with a simplified quantization procedure of a paraxial optical field, which so far has only been treated a classical quantity. We then proceed to establish the nonlinear interaction Hamiltonian describing the FWM process. The solution to Schrödinger's equation with the interaction Hamiltonian leads to the biphoton state, which can be cast in the position and momentum (wave-vector) spaces. We discuss both descriptions. We calculate the spatial coincidence count rate with respect to the biphoton state, and show that the transfer of the pump angular spectrum to the coincidence count profile, a well-known result in PDC (MONKEN; RIBEIRO; PÁDUA, 1998), is also verified in FWM. This is an expected result, due to the similarity in the description of the two processes. Lastly, we briefly discuss concepts such as the spiral bandwidth of the biphoton state and other measures of entanglement.

### 5.3.1 Quantization of the electromagnetic field in the paraxial regime

To establish a quantum description of the FWM process that contemplates the spatial degrees of freedom of light, we must represent the paraxial light fields within a second-quantized framework. Therefore, here we outline the quantization of a paraxial electromagnetic field. For a more rigorous procedure, one may consult Refs. (AIELLO; WOERDMAN, 2005; CALVO; PICÓN; BAGAN, 2006). We start with the electric field in free-space expanded in terms of plane-waves[1]:

$$\mathbf{E}(\mathbf{r},t) = -i\sum_{\sigma,\mathbf{k}}\sqrt{\frac{\omega_{\mathbf{k}}}{2\varepsilon_0 V}}\Big(\boldsymbol{\epsilon}_{\sigma,\mathbf{k}}\mathfrak{a}_{\sigma,\mathbf{k}}e^{-i(\mathbf{k}\cdot\mathbf{r}-\omega_{\mathbf{k}}t)} - \boldsymbol{\epsilon}^*_{\sigma,\mathbf{k}}\mathfrak{a}^*_{\sigma,\mathbf{k}}e^{i(\mathbf{k}\cdot\mathbf{r}-\omega_{\mathbf{k}}t)}\Big), \tag{5.6}$$

where $V$ is the volume of the region in space, $\boldsymbol{\epsilon}_{\sigma,\mathbf{k}}$, with $\sigma = 1, 2$, denotes a particular polarization basis orthogonal to the wave-vector $\mathbf{k}$, $\mathfrak{a}_{\sigma,\mathbf{k}}$ is the complex amplitude of the field component with polarization $\sigma$ and wave-vector $\mathbf{k}$, and $\omega_{\mathbf{k}} = c|\mathbf{k}|$ is the frequency. We separate the electric field into positive and negative frequency components, $\mathbf{E}(\mathbf{r},t) = \mathbf{E}^{(+)}(\mathbf{r},t) + \mathbf{E}^{(-)}(\mathbf{r},t)$, where:

$$\mathbf{E}^{(+)}(\mathbf{r},t) = -i\sum_{\sigma,\mathbf{k}}\sqrt{\frac{\omega_{\mathbf{k}}}{2\varepsilon_0 V}}\boldsymbol{\epsilon}_{\sigma,\mathbf{k}}\mathfrak{a}_{\sigma,\mathbf{k}}e^{-i(\mathbf{k}\cdot\mathbf{r}-\omega_{\mathbf{k}}t)}, \tag{5.7}$$

and $\mathbf{E}^{(-)} = [\mathbf{E}^{(+)}]^*$. Now we write the wave-vector as $\mathbf{k} = k\mathbf{e}_z + \mathbf{q}$, where $\mathbf{q}$ is the transverse wave-vector ($\mathbf{q}\cdot\mathbf{e}_z = 0$). In this manner, we obtain:

$$\mathbf{E}^{(+)}(\mathbf{r},t) = \frac{-i}{\sqrt{2\varepsilon_0 V}}\sum_{\sigma,\mathbf{k}}\sqrt{\omega_{\mathbf{k}}}\boldsymbol{\epsilon}_{\sigma,\mathbf{k}}\mathfrak{a}_{\sigma,\mathbf{k}}e^{-i(kz+\mathbf{q}\cdot\mathbf{r}_\perp-\omega_{\mathbf{k}}t)}. \tag{5.8}$$

Now, the transverse position-momentum exponential $e^{i\mathbf{q}\cdot\mathbf{r}_\perp}$ can be expressed in terms of the following closure relation between the LG mode and its angular spectrum:

$$\begin{aligned} e^{i\mathbf{q}\cdot\mathbf{r}_\perp} &= \iint e^{i\mathbf{q}\cdot\mathbf{r}'_\perp}\delta^{(2)}(\mathbf{r}_\perp - \mathbf{r}'_\perp)d^2\mathbf{r}'_\perp, \\ &= \sum_{\ell,p}\iint e^{i\mathbf{q}\cdot\mathbf{r}'_\perp}u_{\ell,p}(\mathbf{r}'_\perp,z)u^*_{\ell,p}(\mathbf{r}_\perp,z)d^2\mathbf{r}'_\perp, \\ &= 2\pi\sum_{\ell,p}\mathcal{L}_{\ell,p}(\mathbf{q},z;k)u^*_{\ell,p}(\mathbf{r}_\perp,z;k), \end{aligned} \tag{5.9}$$

where the completeness relation of the LG modes (Eq. (2.52)) was used. Equation (5.9) is useful to us because it allows to change from a momentum representation on the continuous variable $\mathbf{q}$, to a paraxial mode representation on the discrete indices $(\ell, p)$. Substituting into

---

[1] More generally, we can perform the described procedure to quantize the vector potential $\mathbf{A}$ in a completely analogous manner.

Eq. (5.8), we get:

$$\mathbf{E}^{(+)}(\mathbf{r},t) = \frac{-2\pi i}{\sqrt{2\varepsilon_0 V}} \sum_{\mathbf{k}} \sum_{\sigma,\ell,p} \sqrt{\omega_{\mathbf{k}}} \boldsymbol{\epsilon}_{\sigma,\mathbf{k}} \mathfrak{a}_{\sigma,\mathbf{k}} \mathcal{L}^*_{\ell,p}(\mathbf{q},z;k) u_{\ell,p}(\mathbf{r};k) e^{-i(kz-\omega_{\mathbf{k}}t)}. \tag{5.10}$$

Now, considering a continuous spectrum of wave-vectors, the summation becomes an integral as:

$$\sum_{\mathbf{k}} \rightarrow \frac{V}{(2\pi)^3} \int d^3\mathbf{k}, \tag{5.11}$$

and separating the transverse and longitudinal integrals as $\int d^3\mathbf{k} = \iint d^2\mathbf{q} \int_{-\infty}^{+\infty} dk$, we can write:

$$\begin{aligned} \mathbf{E}^{(+)}(\mathbf{r},t) = -i\sqrt{\frac{V}{2\varepsilon_0}} \frac{1}{(2\pi)^2} \sum_{\sigma=1,2} \sum_{\ell,p} \iint d^2\mathbf{q} \int_{-\infty}^{\infty} dk \\ \times \sqrt{\omega_{\mathbf{k}}} \boldsymbol{\epsilon}_{\sigma,\mathbf{k}} \mathfrak{a}_{\sigma}(\mathbf{q},k) \mathcal{L}^*_{\ell,p}(\mathbf{q},0) u_{\ell,p}(\mathbf{r}_\perp,z;k) e^{-i[k(1+\vartheta_{\mathbf{k}}^2)z - c|\mathbf{k}|t]}, \end{aligned} \tag{5.12}$$

where $\vartheta_{\mathbf{k}} \equiv |\mathbf{q}|/\sqrt{2}k$. In the paraxial limit, $\vartheta_{\mathbf{k}} \ll 1$, and $\boldsymbol{\epsilon}_{\sigma,\mathbf{k}} \simeq \boldsymbol{\epsilon}_\sigma$ ($\boldsymbol{\epsilon}_\sigma^{(*)} \cdot \mathbf{e}_z = 0$), $\omega_{\mathbf{k}} \simeq ck = \omega_k$. We then define (CALVO; PICÓN; BAGAN, 2006)

$$\mathfrak{a}_{\sigma,\ell,p}(k) \equiv \frac{1}{(2\pi)^2} \iint \mathfrak{a}_\sigma(\mathbf{q},k) \mathcal{L}^*_{\ell,p}(\mathbf{q}) d^2\mathbf{q}, \tag{5.13}$$

as the amplitude of a field component with polarization $\sigma$ and wave-number $k$ that is described by an LG mode with indices $\ell$ and $p$. Then, defining the re-scaled amplitudes $a_{\sigma,\ell,p}(k) \equiv \sqrt{\omega_k}\mathfrak{a}_{\sigma,\ell,p}(k)$ we can write:

$$\mathbf{E}^{(+)}(\mathbf{r},t) = -i\sqrt{\frac{V}{2\varepsilon_0}} \sum_{\sigma,\ell,p} \int dk\, \boldsymbol{\epsilon}_\sigma a_{\sigma,\ell,p}(k) u_{\ell,p}(\mathbf{r};k) e^{-i(kz-\omega_k t)}. \tag{5.14}$$

Starting with a general plane-wave expansion, Eq. (5.6), which satisfies the Helmholtz equation, we arrived at a superposition of field components propagating in the $z$ direction characterized by polarization ($\sigma$), transverse mode satisfying the PWE ($\ell,p$), and wave-number ($k$). The amplitudes $a_{\sigma,\ell,p}(k)$, that give the weight of each component, in general couple all of the mentioned degrees of freedom.

The electric field given by Eq. (5.14) is now suitable to become a quantum-mechanical operator. To this end, we promote the complex amplitudes $a^{(*)}$ to bosonic annihilation and creation operators as:

$$a^{(*)} \rightarrow \sqrt{\hbar}\,\hat{a}^{(\dagger)}, \tag{5.15}$$

which satisfy the commutation relations:

$$[\hat{a}_{\sigma,\ell,p}(k), \hat{a}^\dagger_{\sigma',\ell',p'}(k')] = \delta_{\sigma,\sigma'}\delta_{\ell,\ell'}\delta_{p,p'}\delta(k-k'). \tag{5.16}$$

The electric field amplitude thus becomes an operator:

$$\mathbf{E}^{(+)} \rightarrow \hat{\mathbf{E}}, \tag{5.17}$$

$$\mathbf{E}^{(-)} \rightarrow \hat{\mathbf{E}}^{\dagger}, \tag{5.18}$$

and the photon number states can be represented as:

$$\begin{aligned} \left|\{n_{\sigma,\ell,p}(k)\}\right\rangle &\equiv \left|n_1, n_2, ...\right\rangle, \\ &= \prod_i \frac{(\hat{a}^{\dagger}_{g_i})^{n_i}}{\sqrt{n_i!}} \left|0, 0, ...\right\rangle, \end{aligned} \tag{5.19}$$

where $g_i = \{\sigma, \ell, p; k\}_i$ labels a particular combination of polarization, paraxial mode indices, and wave-number value, and $n_i$ is the number of photons in the mode $g_i$. The results are analogous if one considers another paraxial basis $\{u_{m,n}\}$.

### 5.3.2 The nonlinear interaction Hamiltonian

We write the Hamiltonian of our system as $\hat{H} = \hat{H}_0 + \hat{H}_I$, where $\hat{H}_0 = \hat{H}_{\mathrm{A}} + \hat{H}_{\mathrm{F}}$ is the unperturbed Hamiltonian, taking into account the atomic, $\hat{H}_{\mathrm{A}}$, and light field, $\hat{H}_{\mathrm{F}} = \frac{\varepsilon_0}{2} \int_{\mathbb{V}} (\hat{\mathbf{E}}^{\dagger} \cdot \hat{\mathbf{E}} + \mathrm{h.c.}) d^3\mathbf{r}$, contributions. Here $\hat{\mathbf{E}}$ ($\hat{\mathbf{E}}^{\dagger}$) is the positive (negative) frequency component of the total electric field operator of light. The interaction Hamiltonian can be written as:

$$\hat{H}_I = \frac{1}{2} \int_{\mathbb{V}} \left( \hat{\mathbf{E}}^{\dagger} \cdot \hat{\mathbf{P}} + \mathrm{h.c.} \right) d^3\mathbf{r}, \tag{5.20}$$

where $\hat{\mathbf{P}}$ is the macroscopic polarization, composed of the linear and nonlinear polarizations, $\hat{\mathbf{P}} = \hat{\mathbf{P}}_L + \hat{\mathbf{P}}_{NL}$. In our configuration, where we have two incident fields, $a$ and $b$, interacting to generate a four-wave mixing field, $s$, we have:

$$\hat{\mathbf{P}}_L = \boldsymbol{\epsilon}_s \varepsilon_0 \chi^{(1)} \hat{E}_s, \tag{5.21}$$

$$\hat{\mathbf{P}}_{NL} = \boldsymbol{\epsilon}_s \varepsilon_0 \chi^{(3)} \hat{E}_a^2 \hat{E}_b^{\dagger}. \tag{5.22}$$

The linear and nonlinear polarizations lead to the linear and nonlinear contributions to the Hamiltonian, $\hat{H}_I = \hat{H}_L + \hat{H}_{NL}$. The nonlinear term is the one we are interested in, and thus we write:

$$\hat{H}_I = \frac{\varepsilon_0}{2} \int_{\mathbb{V}} d^3\mathbf{r} \left( \chi^{(3)} \cdot \hat{E}_s^{\dagger} \hat{E}_a \hat{E}_b^{\dagger} \hat{E}_a + \mathrm{h.c.} \right). \tag{5.23}$$

We consider that field $a$ is a strong pump with wave-vector $\mathbf{k}_a$ parallel to the $\mathbf{e}_z$ direction, such that it can be written as a classical monochromatic wave of the form

$$\hat{E}_a(\mathbf{r},t) \to E_a(\mathbf{r},t) = \mathcal{E}_a^0 \mathcal{V}(\mathbf{r}) e^{-i(k_a z - \omega_a t)}, \tag{5.24}$$

with $\mathcal{V}(\mathbf{r}) = \sum_{l,q} c_{l,q} u_{l,q}(\mathbf{r})$, $\sum_{l,q} |c_{l,q}|^2 = 1$, and, for simplicity, $\mathcal{E}_a^0 = 1$. The stimulated and generated fields, $b$ and $s$, are in turn regarded as operators, and we write them in the general form:

$$\hat{E}(\mathbf{r},t) = -i \sum_{\mathbf{k}} \sqrt{\frac{\hbar\omega_{\mathbf{k}}}{2\varepsilon_0 V}} \hat{\mathfrak{a}}_{\mathbf{k}} e^{-i(\mathbf{k}\cdot\mathbf{r} - \omega_{\mathbf{k}} t)}, \tag{5.25}$$

where $\hat{\mathfrak{a}}_{\mathbf{k}}^{(\dagger)}$ is the annihilation (creation) operator for a photon with wave-vector $\mathbf{k}$, satisfying $[\hat{\mathfrak{a}}_{\mathbf{k}}, \hat{\mathfrak{a}}_{\mathbf{k}'}^\dagger] = \delta^{(3)}(\mathbf{k} - \mathbf{k}')$, and $\omega_{\mathbf{k}} = c|\mathbf{k}|$. We write the wave-vectors as $\mathbf{k} = k\cos\theta \mathbf{e}_z + \mathbf{q}$, with $\theta$ being the separation angle between the pump $a$ and seed $b$ fields in the experimental configuration[2]. Note that no polarization labels are present, since we consider a well-defined polarization for all fields: circular polarization, $\boldsymbol{\epsilon}_i = \boldsymbol{\sigma}^+$, in a way that we may think of a two-level atom. We can then write the Hamiltonian as:

$$\hat{H}_I = -\frac{\hbar}{4V} \sum_{\mathbf{k}_1,\mathbf{k}_2} \left( \sqrt{\omega_{\mathbf{k}_1}\omega_{\mathbf{k}_2}} \hat{\mathfrak{a}}_{\mathbf{k}_1}^\dagger \hat{\mathfrak{a}}_{\mathbf{k}_2}^\dagger e^{i\delta\omega t} \int_{\mathbb{V}} d^3\mathbf{r} \chi^{(3)} \mathcal{V}^2(\mathbf{r}) e^{-i(2\mathbf{k}_a - \mathbf{k}_1 - \mathbf{k}_2)\cdot\mathbf{r}} + \mathrm{h.c.} \right), \tag{5.26}$$

where $\delta\omega = 2\omega_a - \omega_1 - \omega_2$. For simplicity, we define the re-scaled operators $\hat{a}_{\mathbf{k}}^\dagger \equiv \sqrt{\omega_{\mathbf{k}}} \hat{\mathfrak{a}}_{\mathbf{k}}^\dagger$, to write:

$$\hat{H}_I = -\frac{\hbar}{4V} \sum_{\mathbf{k}_1,\mathbf{k}_2} \left( \hat{a}_{\mathbf{k}_1}^\dagger \hat{a}_{\mathbf{k}_2}^\dagger e^{i\delta\omega t} \int_{-L/2}^{L/2} dz \iint d^2\mathbf{r}_\perp \chi^{(3)} \mathrm{V} e^{-i\Delta k z} e^{i(\mathbf{q}_1 + \mathbf{q}_2)\cdot\mathbf{r}_\perp} + \mathrm{h.c.} \right), \tag{5.27}$$

where $\mathrm{V}(\mathbf{r}) = \mathcal{V}^2(\mathbf{r})$ is the pump function, and $\Delta k = 2k_a - (k_1 + k_2)\cos\theta$ is the longitudinal phase mismatch. Now we use the closure relation between LG modes and their angular spectrum, Eq. (5.9), to rewrite the exponential $e^{i(\mathbf{q}_1+\mathbf{q}_2)\cdot\mathbf{r}_\perp}$. This is the first step to switch from the continuous space of transverse momentum variables $(\mathbf{q}_1, \mathbf{q}_2)$ to the discrete space of paraxial mode indices. In this manner, we can write:

$$\hat{H}_I = -\frac{\hbar\pi^2}{V} \sum_{\mathbf{k}_1,\mathbf{k}_2} \sum_{\ell_b,p_b} \sum_{\ell_s,p_s} \left( \hat{a}_{\mathbf{k}_1}^\dagger \hat{a}_{\mathbf{k}_2}^\dagger \mathcal{L}_{\ell_b,p_b}(\mathbf{q}_1) \mathcal{L}_{\ell_s,p_s}(\mathbf{q}_2) e^{i\delta\omega t} \mathcal{A}_{p_b,p_s}^{\ell_b,\ell_s}(\mathbf{k}_1,\mathbf{k}_2) + \mathrm{h.c.} \right), \tag{5.28}$$

where

$$\mathcal{A}_{p,q}^{\ell,l}(\mathbf{k}_1,\mathbf{k}_2) = \int_{-L/2}^{L/2} dz\, e^{-i\Delta k z} e^{i(k_1\vartheta_{\mathbf{k}_1}^2 + k_2\vartheta_{\mathbf{k}_2}^2)z} \iint d^2\mathbf{r}_\perp \chi^{(3)}(\mathbf{r};\omega) \mathrm{V}(\mathbf{r}) u_{\ell,p}^*(\mathbf{r}) u_{l,q}^*(\mathbf{r}), \tag{5.29}$$

---

[2] We consider that the wave-vectors of the plane-wave modes of fields $b$ and $s$ are described in reference frames rotated by the small angles $\pm\theta$ around the $x$-axis of the reference frame of field $a$.

is the full spatial overlap integral. In what follows, we shall assume the paraxial condition ($|\vartheta^2_{\mathbf{k}_i}| = |\mathbf{q}_i|^2/2k_i^2 \ll 1$) to be valid. Next, taking the discrete summations on the wave-vectors into integrals, $\sum_{\mathbf{k}_i} \to \frac{V}{(2\pi)^3}\iint d^2\mathbf{q}_i \int dk_i$, and restricting ourselves to the thin-medium approximation, we arrive at:

$$\hat{H}_I = A\int dk_2 dk_1 e^{i\delta\omega t}\mathrm{sinc}\left(\frac{\Delta kL}{2}\right)\sum_{\ell_b,p_b}\sum_{\ell_s,p_s} C^{\ell_b,\ell_s}_{p_b,p_s}(\omega)\,\hat{a}^{\dagger}_{\ell_s,p_s}(k_2)\,\hat{a}^{\dagger}_{\ell_b,p_b}(k_1) + \mathrm{h.c.}, \tag{5.30}$$

where $A = -2\pi^3\hbar LV$, $\omega$ represents $\{\omega_a, \omega_1, \omega_2\}$, the creation operator of a photon in the mode $(\ell, p)$ with longitudinal wave-number $k_j$ is $\hat{a}^{\dagger}_{\ell,p}(k_j) = \frac{1}{(2\pi)^2}\iint \hat{a}^{\dagger}(\mathbf{q}, k_j)\mathcal{L}_{\ell,p}(\mathbf{q})d^2\mathbf{q}$, satisfying $[\hat{a}_{\ell,p}(k), \hat{a}^{\dagger}_{\ell',p'}(k')] = \delta_{\ell,\ell'}\delta_{p,p'}\delta(k-k')$, and:

$$\begin{aligned} C^{\ell_b,\ell_s}_{p_b,p_s}(\omega) &= \iint \chi^{(3)}(\mathbf{r}_\perp,\omega)\mathcal{V}^2(\mathbf{r}_\perp)u^*_{\ell_b,p_b}u^*_{\ell_s,p_s}\Big|_{z=0} d^2\mathbf{r}_\perp, \\ &= \sum_{l,q}\sum_{l',q'} c_{l,q}c_{l',q'}C^{l,l',\ell_b,\ell_s}_{q,q',p_b,p_s}(\omega), \end{aligned} \tag{5.31}$$

is the transverse overlap integral, where:

$$C^{l,l',\ell_b,\ell_s}_{q,q',p_b,p_s}(\omega) = \iint \chi^{(3)}(\omega)u_{l,q}u_{l',q'}u^*_{\ell_b,p_b}u^*_{\ell_s,p_s}\Big|_{z=0} d^2\mathbf{r}_\perp. \tag{5.32}$$

We then see that the spatial overlap integral of four paraxial modes also appears in the quantized treatment of FWM. Here, besides containing the selection rules that dictate the allowed modes in the generated fields, it has an important role in quantifying their squeezing and entanglement properties (LANNING et al., 2018; OFFER et al., 2018). Furthermore, the spatial dependence of the nonlinear susceptibility $\chi^{(3)}$ couples the spatial and spectral degrees of freedom. This dependence may come from the fields themselves, as we have already discussed (MOTTA; ALMEIDA; VIANNA, 2022), and also from the shape of the sample, such as the distribution of atoms in a cloud of cold atoms (OSORIO et al., 2008). For simplicity, we shall consider a spatially uniform susceptibility over the interaction volume, and in this manner, it factors out of the integral in Eq. (5.32):

$$C^{l,l',\ell_b,\ell_s}_{q,q',p_b,p_s}(\omega) = \chi^{(3)}(\omega)\Lambda^{l,l',\ell_b,\ell_s}_{q,q',p_b,p_s}, \tag{5.33}$$

and we may use the same expression for the transverse overlap we obtained in Chapter 2.

### 5.3.3 The biphoton state in position space

In what follows we consider a quasi phase-matched configuration, $\Delta k \approx 0$. The state $|\psi\rangle$, describing the generated light state at time $t$ can be written as:

$$|\psi(t)\rangle = \hat{U}(t)\,|\psi(0)\rangle\,, \tag{5.34}$$

where the quantum mechanical evolution operator is:

$$\begin{aligned}\hat{U}(t) &= \exp\left(-\frac{i}{\hbar}\int_0^t \hat{H}_I(\tau)d\tau\right), \\ &\simeq \mathbb{1} - \frac{i}{\hbar}\int_0^t \hat{H}_I(\tau)d\tau. \end{aligned} \tag{5.35}$$

If we suppose that the interaction lasts for a time interval much longer than any relevant time scale of the system, we can extend the integration limits to $\pm\infty$, to get $\int_{-\infty}^{\infty} e^{i(2\omega_a-\omega_1-\omega_2)\tau}d\tau = 2\pi\delta(2\omega_a-\omega_1-\omega_2)$. With the initial state as the vacuum, $|\psi(0)\rangle = |0\rangle$, the first-order approximation to the state at time $t$, $|\psi(t)\rangle$, can be written as:

$$|\psi(t)\rangle = |0\rangle + \mathcal{A}\int d\omega_1 \sum_{\ell_b,p_b}\sum_{\ell_s,p_s} C_{p_b,p_s}^{\ell_b,\ell_s}(\omega_1)\,|\ell_b,p_b;\omega_1\rangle\,|\ell_s,p_s;\omega_1'\rangle\,, \tag{5.36}$$

where $\mathcal{A}$ is a constant and $\omega_1' = 2\omega_a - \omega_1$. With the substitution $\omega_1 = \omega_b + \Omega$, we can write:

$$|\psi(t)\rangle = |0\rangle + \mathcal{A}\int d\Omega \sum_{\ell_b,p_b}\sum_{\ell_s,p_s} C_{p_b,p_s}^{\ell_b,\ell_s}(\Omega)\,|\ell_b,p_b;\omega_b+\Omega\rangle\,|\ell_s,p_s;\omega_s-\Omega\rangle\,, \tag{5.37}$$

where $\omega_s = 2\omega_a - \omega_b$. We now assume that the nonlinear process is spectrally narrow around $\omega_b$, or $\Omega = 0$, to write $|\psi\rangle = |0\rangle + \mathcal{A}'\,|\Psi\rangle$, where $|\Psi\rangle$ is the biphoton state:

$$|\Psi\rangle = \sum_{\ell_b,p_b}\sum_{\ell_s,p_s} C_{p_b,p_s}^{\ell_b,\ell_s}\,|\ell_b,p_b;\omega_b\rangle_b\,|\ell_s,p_s;\omega_s\rangle_s\,. \tag{5.38}$$

We can now evaluate operator averages with respect to the state $|\psi\rangle$.

### 5.3.4 The coincidence count rate

The intensity correlation function, or coincidence count rate, between the fields $b$ and $s$ is:

$$\begin{aligned}C(\mathbf{r}_b,\mathbf{r}_s) &= \langle\psi|\hat{E}_b^\dagger(\mathbf{r}_b)\hat{E}_s^\dagger(\mathbf{r}_s)\hat{E}_s(\mathbf{r}_s)\hat{E}_b(\mathbf{r}_b)|\psi\rangle, \\ &= |\,\langle 0|\hat{E}_s(\mathbf{r}_s)\hat{E}_b(\mathbf{r}_b)|\Psi\rangle\,|^2, \\ &\propto |\Psi(\mathbf{r}_b,\mathbf{r}_s)|^2, \end{aligned} \tag{5.39}$$

where the spatial mode function is:

$$\begin{aligned}\Psi(\mathbf{r}_b,\mathbf{r}_s) &= \langle\mathbf{r}_b,\mathbf{r}_s|\Psi\rangle\,, \\ &= \sum_{\ell_b,p_b}\sum_{\ell_s,p_s} C_{p_b,p_s}^{\ell_b,\ell_s} u_{\ell_p,p_b}(\mathbf{r}_b)u_{\ell_s,p_s}(\mathbf{r}_s). \end{aligned} \tag{5.40}$$

Suppose that we detect signal $b$ in its entirety, then the measured coincidence rate can be written as:

$$\begin{aligned} g(\mathbf{r}_s) &= \int C(\mathbf{r}_b, \mathbf{r}_s) d^2\mathbf{r}_b, \\ &\propto \sum_{\ell_b,p_b} \sum_{\ell_s,p_s} \sum_{\ell'_s,p'_s} C^{\ell_b,\ell_s}_{p_b,p_s} (C^{\ell_b,\ell'_s}_{p_b,p'_s})^* u_{\ell_s,p_s}(\mathbf{r}_s) u^*_{\ell'_s,p'_s}(\mathbf{r}_s), \\ &= \sum_{\ell_s,p_s} \sum_{\ell'_s,p'_s} D^{\ell_s,\ell'_s}_{p_s,p'_s} u_{\ell_s,p_s}(\mathbf{r}_s) u^*_{\ell'_s,p'_s}(\mathbf{r}_s), \end{aligned} \tag{5.41}$$

where $D^{\ell_s,\ell'_s}_{p_s,p'_s} = \sum_{\ell_b,p_b} C^{\ell_b,\ell_s}_{p_b,p_s} (C^{\ell_b,\ell'_s}_{p_b,p'_s})^*$. It is interesting to note that, although not explicit, the transfer of the pump distribution to the coincidence rate profile, a known result in PDC (MONKEN; RIBEIRO; PÁDUA, 1998; WALBORN et al., 2010), also occurs here. This can be demonstrated by analyzing the biphoton state in momentum space. More generally, for arbitrary aperture functions for the detection of the fields $b$ and $s$, $\mathrm{A}_b, \mathrm{A}_s$, we can write:

$$g(\mathbf{u}_b, \mathbf{u}_s) = \int \mathrm{A}_b(\mathbf{r}_b; \mathbf{u}_b) \mathrm{A}_s(\mathbf{r}_s; \mathbf{u}_s) C(\mathbf{r}_b, \mathbf{r}_s) d^2\mathbf{r}_b d^2\mathbf{r}_s, \tag{5.42}$$

where $\mathbf{u}_{b,s}$ are the set of parameters characterizing the detection scheme of each output. Consider now that we wish to detect only the circular region of radius $r_c$ centered at $\mathbf{R}$. For a really small aperture size ($r_c \ll w_0$) at $\mathbf{R} = (X, 0)$, representing a situation where we place a tight pinhole in front of the beam with a translational degree of freedom in the $x$–direction (see Fig. 54), we may write:

$$\mathrm{A}_b(\mathbf{r}_b; X_b) = \delta(x_b - X_b)\delta(y_b), \tag{5.43}$$

$$\mathrm{A}_s(\mathbf{r}_s; X_s) = \delta(x_s - X_s)\delta(y_s), \tag{5.44}$$

and the coincidence rate becomes:

$$g(X_b, X_s) = C(X_b, 0; X_s, 0). \tag{5.45}$$

In these steps, it was assumed that both signals are detected at the same longitudinal position $z \geq L/2$. It is interesting to note that the coincidence profile evolves with the propagation distance outside the interaction medium, as we show in Fig. 55. At the medium exit, we see a positive inclination of the correlation profile. This is because the two photons are generated at the same transverse position. As we move the detection position to larger distances, allowing the fields to propagate in free-space, the inclination of the coincidence profile becomes negative. This is a signature of the conservation of transverse of linear momentum. Figure 56 shows the

**Figure 54** – Simplified scheme for obtaining the coincidence count map $g(X_b, X_s)$, where $(X_b, X_s)$ are the horizontal positions of the pinholes with respect to the center of the $b$ and $s$ fields. The separation angle $\theta$ is small such that the distance from the exit of the interaction medium to the detectors is approximately equal to that measured on the pump beam axis. C - photon coincidence counting system.

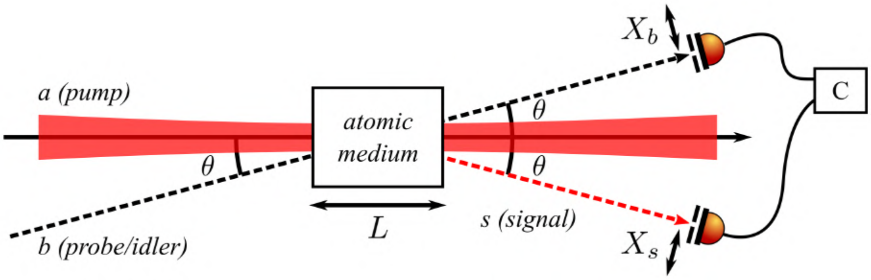

**Source:** The author (2024).

**Figure 55** – Coincidence count profile on the $(X_b, X_s)$ plane (top) for a Gaussian pump in a nonlinear medium of length $L = 3\,\mathrm{mm}$, and diagonal and anti-diagonal line profiles (bottom) as a function of the propagation distance outside the interaction medium (from left to right).

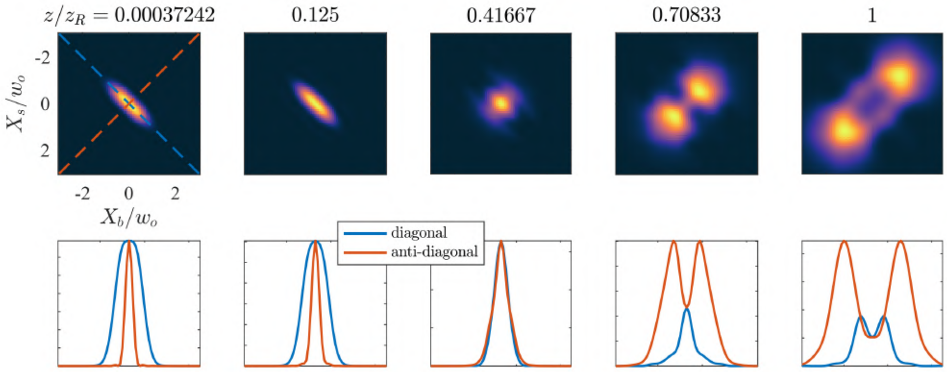

**Source:** The author (2024).

**Figure 56** – (a) Normalized mode distribution $|C^{\ell_b,\ell_s}_{p_b,p_s}|^2$ of the two-photon state for the configuration considered in Fig. 55. (b) Corresponding $\ell$–distribution, $P_{\ell_b,-\ell_b}$, evidencing a finite spiral bandwidth $\Delta\ell$.

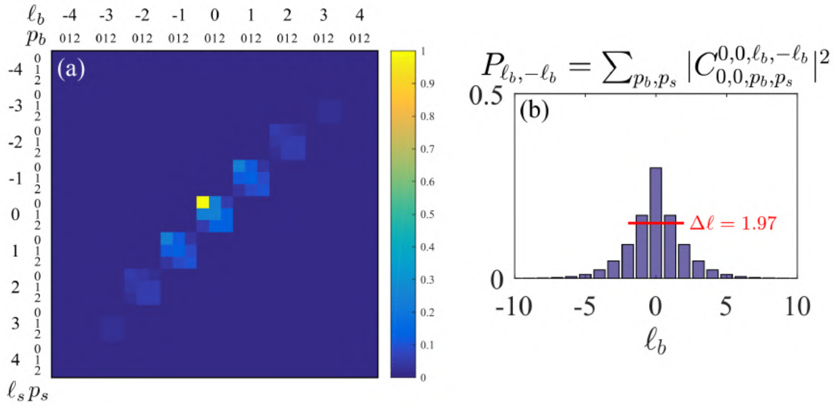

**Source:** The author (2024).

spatial mode distribution of the biphoton state and the corresponding $\ell-$distribution, defined as:

$$P_{\ell_b,\ell_{\mathrm{T}}-\ell_b} \equiv \sum_{p_b,p_s} |C^{\ell_b,\ell_{\mathrm{T}}-\ell_b}_{p_b,p_s}|^2, \tag{5.46}$$

where $\ell_{\mathrm{T}}$ is the total OAM pumped into the system.

We may employ a classical model for the intensity correlation function, to serve as a proof of concept, and see if we can reproduce the behavior of the correlation profiles we obtained in the quantum picture. Suppose we want to calculate the classical intensity correlation function, at zero time delay, between signal and conjugate beams generated in a FWM process:

$$g^{(2)}_{s,c}(\mathbf{r}_s, \mathbf{r}_c; z) \propto \langle I_s(\mathbf{r}_s, z; t) I_c(\mathbf{r}_c, z; t)\rangle, \tag{5.47}$$

where $z$ is the longitudinal position at which the fields are detected. To calculate the intensity distributions, $I_j = |E_j|^2$, $j \in \{s, c\}$, we must first propagate the field amplitudes $E_j$ from the source position, $z = 0$, to $z$. The conservation of linear momentum dictates that the two fields be generated with the wave-vectors:

$$\begin{aligned} \mathbf{k}_j &\simeq k_j(\mathbf{e}_z \pm \mathbf{e}_x\theta), \\ &= \mathbf{k}^z_j + \mathbf{k}^{\perp}_j, \end{aligned} \tag{5.48}$$

where the small angle approximation was employed, and $\mathbf{k}^z_j, \mathbf{k}^{\perp}_j$ are the longitudinal and transverse components of the wave-vectors $\mathbf{k}_j$, respectively. We can then write the field propagated to $z$ as

$$E_j(\mathbf{r}_{\perp}, z; t) = \mathcal{F}^{-1}\Big\{\tilde{\mathcal{A}}_j(\mathbf{q}, 0) e^{i\frac{|\mathbf{q}|^2}{2k_j}z}\Big\} e^{-i(k_j z - \omega_j t)}, \tag{5.49}$$

where $\tilde{\mathcal{A}}_j(\mathbf{q}, 0)$ is the Fourier transform of the field amplitude at $z = 0$

$$\mathcal{A}_j(\mathbf{r}_{\perp}, 0) = \mathcal{E}_j(\mathbf{r}_{\perp}, 0) e^{-i\mathbf{k}^{\perp}_j \cdot \mathbf{r}_{\perp}}. \tag{5.50}$$

Equation (5.50) takes into account that the propagation directions of the beams $s$ and $c$ are not parallel to the $z$ direction. We highlight that $\mathbf{k}^{\perp}_j$, being the transverse component of the physical wave-vector $\mathbf{k}_j$, must not to be confused with the Fourier space coordinate $\mathbf{q}$. In order to encompass the statistical nature of the signal pair generation process, we modify the transverse component of the wave-vectors to read:

$$\mathbf{k}^{\perp}_j = \pm\mathbf{e}_x k_j(\theta + \varphi), \tag{5.51}$$

where $\varphi$ is a deviation from the gross beam direction, and it is a statistical quantity that obeys a Gaussian probability distribution:

$$p(\varphi) = \frac{1}{\sqrt{\pi}\sigma_\varphi} e^{-\varphi^2/\sigma_\varphi^2}, \tag{5.52}$$

with $\sigma_\varphi$ being a measure of the angular uncertainty, or spread, of the signal emission around $\theta$. With this, the averages $\langle \cdot \rangle$ in Eq. (5.47) can be approximated as:

$$\langle o(\mathbf{r}_s, \mathbf{r}_c, z; t) \rangle \simeq \frac{1}{N} \sum_i o_i(\mathbf{r}_s, \mathbf{r}_c, z), \tag{5.53}$$

where the index $i$ labels the $N$ different realizations of the random angle deviation $\varphi$. Then, in a configuration where we have a 1D translational degree of freedom on the detectors of both signals, which are point-like, we can estimate the correlation function as:

$$\langle I_s(X_s, 0, z; t) I_c(X_c, 0, z; t) \rangle \simeq \frac{1}{N} \sum_i \{I_s(X_s, 0, z) I_c(X_c, 0, z)\}_i. \tag{5.54}$$

Figure 57(a) illustrates the situation and Fig. 57(b) shows the correlation profiles calculated with Eq. (5.54) for different $\sigma_\varphi$ and propagation distances. For larger spread widths $\sigma_\varphi$ and propagation distances we see the formation of a pattern rotated in the same direction as that seen in the far-field quantum-mechanical coincidence profile shown in Fig. 55, indicating the expected spatial correlation due to transverse momentum conservation. But at the near-field, we don't see an inclination to the opposite direction.

**Figure 57** – (a) Generation of a signal-conjugate pair due to the nonlinear interaction in an atomic sample. The pump beam wave-vector is parallel to the $z$ direction. (b) Coincidence profiles obtained by generating several realizations of the random angle $\varphi$. The angular uncertainty $\sigma_\varphi$ around the gross beam direction $\theta$ gives rise to spatial correlations in a similar manner to those obtained in the quantum picture.

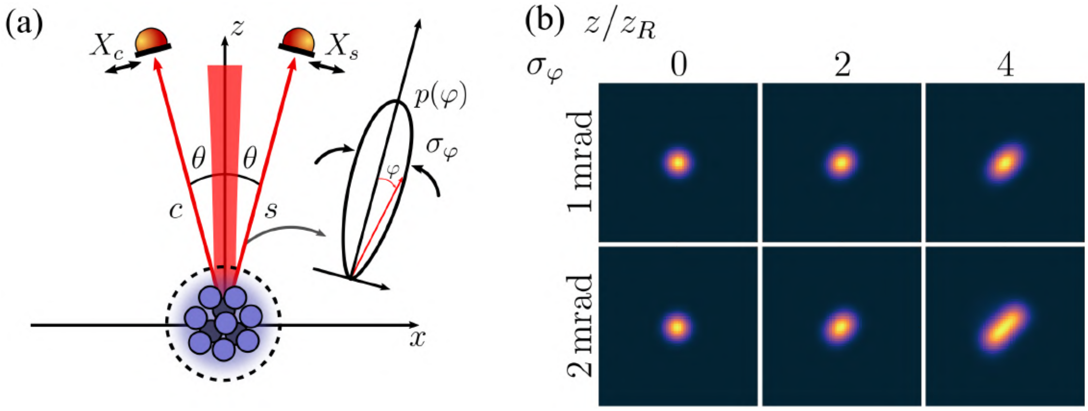

**Source:** The author (2024).

### 5.3.5 The biphoton state in momentum space

Now, let us go back to Eq. (5.27), and outline a treatment in momentum space. We define the pump angular spectrum via $\mathrm{V}(\mathbf{r}) \equiv \mathcal{V}^2(\mathbf{r}) = \iint \widetilde{\mathrm{V}}(\mathbf{q}, z) e^{-i\mathbf{q}\cdot\mathbf{r}_\perp} d^2\mathbf{q}$. Then, we may write:

$$\hat{H}_I = -B \sum_{\mathbf{k}_1,\mathbf{k}_2} \left( \hat{a}^\dagger_{\mathbf{k}_1} \hat{a}^\dagger_{\mathbf{k}_2} e^{i\delta\omega t} \int dz d^2\mathbf{r}_\perp d^2\mathbf{q}' \, \widetilde{\mathrm{V}}(\mathbf{q}', z) e^{-i\Delta k z} e^{-i(\mathbf{q}'-\mathbf{q}_1-\mathbf{q}_2)\cdot\mathbf{r}_\perp} + \mathrm{h.c.} \right), \quad (5.55)$$

where $B = \hbar\chi^{(3)}/4V$ and $\chi^{(3)}$ was considered spatially uniform. Performing the integration on the transverse position vector, we obtain:

$$\hat{H}_I \propto \sum_{\mathbf{k}_1,\mathbf{k}_2} \left( \hat{a}^\dagger_{\mathbf{k}_1} \hat{a}^\dagger_{\mathbf{k}_2} e^{i\delta\omega t} \int dz d^2\mathbf{q}' \, \widetilde{\mathrm{V}}(\mathbf{q}', z) e^{-i\Delta k z} \delta(\mathbf{q}' - \mathbf{q}_1 - \mathbf{q}_2) + \mathrm{h.c.} \right). \quad (5.56)$$

Upon integrating in the $\mathbf{q}'$ coordinate, we are imposing the transverse linear momentum conservation in the parametric process. Neglecting the slow longitudinal variation of $\widetilde{\mathrm{V}}$, we get:

$$\begin{aligned} \hat{H}_I &\propto \sum_{\mathbf{k}_1,\mathbf{k}_2} \left( \hat{a}^\dagger_{\mathbf{k}_1} \hat{a}^\dagger_{\mathbf{k}_2} e^{i\delta\omega t} \widetilde{\mathrm{V}}(\mathbf{q}_1 + \mathbf{q}_2) \, \mathrm{sinc}\left( \frac{\Delta k L}{2} \right) + \mathrm{h.c.} \right), \\ &\propto \int d^3\mathbf{k}_1 d^3\mathbf{k}_2 \left\{ \hat{a}^\dagger(\mathbf{k}_1) \hat{a}^\dagger(\mathbf{k}_2) \Phi(\mathbf{q}_1, \mathbf{q}_2; k_1, k_2) e^{i\delta\omega t} + \mathrm{h.c.} \right\}, \end{aligned} \quad (5.57)$$

where the biphoton amplitude:

$$\Phi(\mathbf{q}_1, \mathbf{q}_2; k_1, k_2) = \widetilde{\mathrm{V}}(\mathbf{q}_1 + \mathbf{q}_2) \mathrm{sinc}\left( \frac{\Delta k L}{2} \right), \quad (5.58)$$

carries the information from the pump structure and the phase mismatch (LAW; EBERLY, 2004; SCHNEELOCH; HOWELL, 2016). The quantum mechanical state at time $t$, $|\tilde{\psi}(t)\rangle = \hat{U}(t)|0\rangle$, in the first order approximation, can be expressed as:

$$|\tilde{\psi}(t)\rangle = |0\rangle + \mathcal{B} \int d\omega_1 \iint d^2\mathbf{q}_1 d^2\mathbf{q}_2 \Phi(\mathbf{q}_1, \mathbf{q}_2; \omega_1) |\mathbf{q}_1, \omega_1\rangle_b |\mathbf{q}_2, \omega'\rangle_s, \quad (5.59)$$

where $\omega' = 2\omega_a - \omega_1$ and $\mathcal{B}$ is a constant. We may now use $|\mathbf{q}, kc\rangle = \hat{a}^\dagger(\mathbf{q}, k)|0\rangle$, along with the inverse of relation (5.13) in its quantum version, which on the LG basis reads:

$$\hat{a}^\dagger(\mathbf{q}, k) = (2\pi)^2 \sum_{\ell,p} \hat{a}^\dagger_{\ell,p}(k) \mathcal{L}^*_{\ell,p}(\mathbf{q}), \quad (5.60)$$

to write:

$$|\tilde{\psi}(t)\rangle = |0\rangle + \mathcal{B}' \int d\omega_1 \sum_{\ell_b,p_b} \sum_{\ell_s,p_s} \widetilde{C}^{\ell_b,\ell_s}_{p_b,p_s}(\omega_1) |\ell_b, p_b; \omega_1\rangle_b |\ell_s, p_s; \omega'\rangle_s. \quad (5.61)$$

Note that with expression (5.60) we have changed from the momentum to the LG representation. Considering the nonlinear process narrow around $\omega_1 = \omega_b$ (making $\omega' = 2\omega_a - \omega_b = \omega_s$), as we have done in position space, we identify the momentum space biphoton state as:

$$|\tilde{\Psi}\rangle = \sum_{\ell_b,p_b}\sum_{\ell_s,p_s} \widetilde{C}^{\ell_b,\ell_s}_{p_b,p_s} \left|\ell_b, p_b; \omega_b\right\rangle_b \left|\ell_s, p_s; \omega_s\right\rangle_s , \tag{5.62}$$

where the momentum transverse overlap is:

$$\widetilde{C}^{\ell_b,\ell_s}_{p_b,p_s} = \iint d^2\mathbf{q}_1 d^2\mathbf{q}_2 \Phi(\mathbf{q}_1,\mathbf{q}_2)\mathcal{L}^*_{\ell_b,p_b}(\mathbf{q}_1)\mathcal{L}^*_{\ell_s,p_s}(\mathbf{q}_2), \tag{5.63}$$

with $k' = \omega'/c$. Note that the integration is in two transverse momentum vectors. Also, considering the argument of the $\mathrm{sinc}(\cdot)$ function negligible, $\Phi(\mathbf{q}_1,\mathbf{q}_2) \simeq \widetilde{\mathrm{V}}(\mathbf{q}_1+\mathbf{q}_2) = \mathcal{F}\{\mathcal{V}^2\}(\mathbf{q}_1+\mathbf{q}_2)$, $\widetilde{C}^{\ell_b,\ell_s}_{p_b,p_s}$ does not become the overlap integral of four LG modes in momentum variables, or sums of such integrals, as is the case in position space. The Fourier transform of the squared Gaussian distribution can be obtained as $\mathcal{F}\{u^2_{0,0}\} = \frac{1}{2\pi}e^{-\rho^2 w_0^2/8}$, and thus:

$$\widetilde{\mathrm{V}}(\mathbf{q}_1+\mathbf{q}_2) = \frac{1}{2\pi}\exp\left(-\frac{w_0^2}{8}|\mathbf{q}_1+\mathbf{q}_2|^2\right). \tag{5.64}$$

With the small angle approximation, we may write the longitudinal phase mismatch as (SCHNEELOCH; HOWELL, 2016):

$$\Delta k = \frac{k_a}{4k_b^2}|\mathbf{q}_1-\mathbf{q}_2|^2, \tag{5.65}$$

and thus in the degenerate setting ($k_a = k_b$), we get:

$$\Phi(\mathbf{q}_1,\mathbf{q}_2) = \frac{1}{2\pi}\exp\left(-\frac{w_0^2}{8}|\mathbf{q}_1+\mathbf{q}_2|^2\right)\mathrm{sinc}\left(\frac{L}{8k}|\mathbf{q}_1-\mathbf{q}_2|^2\right). \tag{5.66}$$

The $\mathrm{sinc}(\cdot)$ function can be troublesome if used directly, and we can take a step back and write it alternatively as:

$$\mathrm{sinc}\left(\frac{L}{8k}|\mathbf{q}_1-\mathbf{q}_2|^2\right) = \frac{1}{L}\int_{-L/2}^{L/2} e^{-i\frac{s}{4k}|\mathbf{q}_1-\mathbf{q}_2|^2}ds. \tag{5.67}$$

Now, using $|\mathbf{q}_1 \pm \mathbf{q}_2|^2 = \rho_1^2+\rho_2^2 \pm 2\rho_1\rho_2\cos(\phi_1-\phi_2)$, we can write:

$$\widetilde{C}^{\ell_b,\ell_s}_{p_b,p_s} \propto \int_{-L/2}^{L/2} T^{\ell_b,\ell_s}_{p_b,p_s}(s)ds, \tag{5.68}$$

where, with $\alpha^2_{\pm}(s) \equiv (w_0^2/8 \pm is/4k)$, we have:

$$T^{\ell_b,\ell_s}_{p_b,p_s}(s) = \iint e^{-(\rho_1^2+\rho_2^2)\alpha_+^2(s)-2\rho_1\rho_2\alpha_-^2(s)\cos(\varphi_1-\varphi_2)}\mathcal{L}^*_{\ell_b,p_b}(\mathbf{q}_1)\mathcal{L}^*_{\ell_s,p_s}(\mathbf{q}_2)d^2\mathbf{q}_1 d^2\mathbf{q}_2. \tag{5.69}$$

With this we can numerically calculate the coefficients of the biphoton state in momenutm space. Note that here, even though we only have integrals on the transverse momentum coordinates, the information regarding the extension of the interaction medium is included in the calculations. We can use a measure of distance between the biphoton states in position and in momentum space via (BAGHDASARYAN; STEINLECHNER; FRITZSCHE, 2021):

$$D(|\tilde{\Psi}\rangle, |\Psi\rangle) = \sqrt{1 - |\langle\tilde{\Psi}|\Psi\rangle|^2}, \tag{5.70}$$

to probe the influence of the medium length $L$ or the beam waist $w_0$ on the biphoton state mode distribution. We identify in Eq. (5.70) the fidelity $F(|\tilde{\Psi}\rangle, |\Psi\rangle) \equiv |\langle\tilde{\Psi}|\Psi\rangle|^2$. In fact, in the thin-medium limit, $L/z_R \to 0$, it is expected that $|\tilde{\Psi}\rangle \to |\Psi\rangle$, and therefore $D \to 0$. This also means that the overlap integrals in position and in momentum space should become the same, $\widetilde{C}^{\ell_b,\ell_s}_{p_b,p_s} \to C^{\ell_b,\ell_s}_{p_b,p_s}$ (BAGHDASARYAN; STEINLECHNER; FRITZSCHE, 2021). In Fig. 58 we show the dependence of the distance $D$ with the medium extension $L$ and the beam waist $w_0$. This computation was performed by calculating $\widetilde{C}$ numerically using Eqs. (5.68) and (5.69), and using the expression for the overlap integral in position space for $C$ given in Chapter 2. With this result we can determine the configurations where the phase-matching function is relevant for the calculations.

As a last remark, we note that the major difference in the calculations for FWM with respect to PDC lies in the fact that the pump contributes twice to the process. In this man-

**Figure 58** – Trace distance $D = \sqrt{1 - |\langle\tilde{\Psi}|\Psi\rangle|^2}$ as a function of $L$ and $w_0$. The dashed lines represent the $D = 0.1$ (upper) and $D = 0.5$ (lower) contours, and these correspond to curves of the form $w_0 \propto \sqrt{L}$.

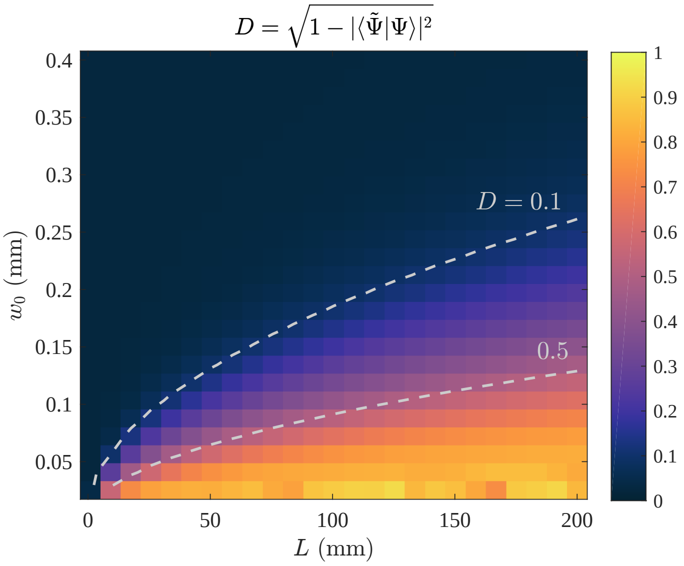

**Source:** The author (2024).

ner, we have two main changes: the width of the phase-matching function is modified; and the pump function is equal to the square of the pump mode, $\mathrm{V}(\mathbf{r}_\perp) = \mathcal{V}^2(\mathbf{r}_\perp)$, effectively changing the width of the pump function both in position and in momentum space. We could therefore adapt the calculations from Refs. (MIATTO; YAO; BARNETT, 2011; BAGHDASARYAN et al., 2022) to obtain an (almost) analytical expression for $\widetilde{C}^{\ell_b,\ell_s}_{p_b,p_s}$, and even extend the treatment to accommodate an arbitrary pump structure.

### 5.3.6 Transfer of the pump angular spectrum to the coincidence profile

To show that the pump structure is transferred to the coincidence rate profile of the generated photon-pair, a known result in PDC (MONKEN; RIBEIRO; PÁDUA, 1998; WALBORN et al., 2010), we will work with the biphoton state in momentum space:

$$|\Psi\rangle = \iint d^2\mathbf{q}_1 d^2\mathbf{q}_2 \Phi(\mathbf{q}_1,\mathbf{q}_2) \left|\mathbf{q}_1, k_b\right\rangle_b \left|\mathbf{q}_2, k_s\right\rangle_s , \tag{5.71}$$

where $\Phi(\mathbf{q}_1,\mathbf{q}_2) = \widetilde{\mathrm{V}}(\mathbf{q}_1+\mathbf{q}_2)\Delta(\mathbf{q}_1-\mathbf{q}_2)$, with $\Delta(\cdot)$ being the phase-matching function. The coincidence count can be written as:

$$\begin{aligned} C(\mathbf{r}_b,\mathbf{r}_s;z_b,z_s) &= |\left\langle 0\right| \hat{E}_s(\mathbf{r}_s,z_s)\hat{E}_b(\mathbf{r}_b,z_b)\left|\Psi\right\rangle|^2, \\ &= |\Psi(\mathbf{r}_b,\mathbf{r}_s;z_b,z_s)|^2, \end{aligned} \tag{5.72}$$

where we can write the spatial mode function $\Psi$ explicitly as:

$$\begin{aligned} &\Psi(\mathbf{r}_b,\mathbf{r}_s;z_b,z_s) \\ &\propto \int d^2\mathbf{q}_1 d^2\mathbf{q}_2 \Phi(\mathbf{q}_1,\mathbf{q}_2) \sum_{\mathbf{k},\mathbf{k}'} \underbrace{\left\langle 0\right|\left\langle 0\right| \hat{a}_{\mathbf{k}}\hat{a}_{\mathbf{k}'}\left|\mathbf{q}_1,k_b\right\rangle\left|\mathbf{q}_2,k_s\right\rangle}_{=\delta(\mathbf{q}-\mathbf{q}_1)\delta(\mathbf{q}'-\mathbf{q}_2)\delta(k-k_b)\delta(k'-k_s)} e^{-i(\mathbf{q}\cdot\mathbf{r}_b+\mathbf{q}'\cdot\mathbf{r}_s)} e^{i\left(\frac{z_b}{2k}|\mathbf{q}|^2+\frac{z_s}{2k'}|\mathbf{q}'|^2\right)}, \\ &\to \int d^2\mathbf{q}_1 d^2\mathbf{q}_2 \widetilde{\mathrm{V}}(\mathbf{q}_1+\mathbf{q}_2)\Delta(\mathbf{q}_1-\mathbf{q}_2) e^{-i(\mathbf{q}_1\cdot\mathbf{r}_b+\mathbf{q}_2\cdot\mathbf{r}_s)} e^{i\left(\frac{z_b}{2k_b}|\mathbf{q}_1|^2+\frac{z_s}{2k_s}|\mathbf{q}_2|^2\right)}, \\ &\propto \int d^2\mathbf{q}_+ d^2\mathbf{q}_- \widetilde{\mathrm{V}}(\mathbf{q}_+)\Delta(\mathbf{q}_-) e^{-i\mathbf{q}_+\cdot(\mathbf{r}_b+\mathbf{r}_s)-i\mathbf{q}_-\cdot(\mathbf{r}_b-\mathbf{r}_s)} e^{i\left(\frac{z_b}{2k_b}|\mathbf{q}_++\mathbf{q}_-|^2+\frac{z_s}{2k_s}|\mathbf{q}_+-\mathbf{q}_-|^2\right)}, \end{aligned} \tag{5.73}$$

with $\mathbf{q}_\pm = (\mathbf{q}_1 \pm \mathbf{q}_2)/2$. For $z_b = z_s = z$, $k_b = k_s = k$, and using $|\mathbf{q}_+ \pm \mathbf{q}_-|^2 = q_+^2 + q_-^2 \pm 2q_+q_-\cos(\varphi_+ - \varphi_-)$, the last exponential in the last line of Eq. (5.73) becomes $e^{i\frac{z}{k}\left(q_+^2+q_-^2\right)}$, and therefore:

$$\Psi(\mathbf{r}_b,\mathbf{r}_s;z) \propto \int \widetilde{\mathrm{V}}(\mathbf{q}_+) e^{i\frac{z}{k}q_+^2} e^{-i\mathbf{q}_+\cdot(\mathbf{r}_b+\mathbf{r}_s)} d^2\mathbf{q}_+ \int \Delta(\mathbf{q}_-) e^{i\frac{z}{k}q_-^2} e^{-i\mathbf{q}_-\cdot(\mathbf{r}_b-\mathbf{r}_s)} d^2\mathbf{q}_- . \tag{5.74}$$

Note that $\widetilde{\mathrm{V}}(\mathbf{q}_+)e^{i\frac{z}{k}q_+^2} = \widetilde{\mathrm{V}}(\mathbf{q}_+, 2z)$, and $\Delta(\mathbf{q}_-)e^{i\frac{z}{k}q_-^2} = \Delta(\mathbf{q}_-, 2z)$ are the pump angular spectrum and the phase-matching function propagated to $2z$. Thus,

$$\Psi(\boldsymbol{\xi}_+, \boldsymbol{\xi}_-, z) \propto \mathrm{V}(\boldsymbol{\xi}_+, 2z)M(\boldsymbol{\xi}_-, 2z), \tag{5.75}$$

where $\boldsymbol{\xi}_\pm \equiv (\mathbf{r}_b \pm \mathbf{r}_s)/2$, and $M(\mathbf{R}, z) \equiv \iint \Delta(\mathbf{q}, z)e^{-i\mathbf{q}\cdot\mathbf{R}}d^2\mathbf{q}$. Considering the thin-medium limit, $\Delta(\mathbf{q})$ may be approximated by unity, and at $z = 0$, $M(\mathbf{r}_b - \mathbf{r}_s, 0) \to \delta(\mathbf{r}_b - \mathbf{r}_s)$. With this, we arrive at

$$C(\mathbf{r}_b, \mathbf{r}_s, 0) \propto |\mathrm{V}(\mathbf{r}_b + \mathbf{r}_s, 0)|^2\delta(\mathbf{r}_b - \mathbf{r}_s), \tag{5.76}$$

and the coincidence count profile obtained when the signal $b$ is detected entirely, Eq. (5.41), becomes:

$$\begin{aligned} g(\mathbf{r}_s, 0) &= \int C(\mathbf{r}_b, \mathbf{r}_s, 0)d^2\mathbf{r}_b, \\ &\propto |\mathrm{V}(2\mathbf{r}_s, 0)|^2. \end{aligned} \tag{5.77}$$

Recall that $\mathrm{V}(\mathbf{r}_\perp) = \mathcal{V}^2(\mathbf{r}_\perp)$. In Fig. 59 we show the transfer of the pump structure to the coincidence count for different pump modes, and also the biphoton amplitudes in each case. The coincidence profiles were calculated using Eq. (5.41) considering the subspace $\ell_{b,s} = l_a - 4, ..., l_a + 4$, $p_{b,s} = 0, ..., 3$. We see that the mode distribution is sensibly affected when we vary the pump structure. One effect that can be noted is the broadening of the spiral bandwidth $\Delta\ell$ with increasing $l_a$. This is a signature of the increase in spatial entanglement of the bipartite light state, and we will discuss this more in detail shortly.

We highlight that performing these calculations on a discrete basis of paraxial modes is convenient because it circumvents the need to evaluate multidimensional integrals. However, this convenience is rapidly out-weighted by the number of modes that must be taken into account when we increase the order of the pump field. This can be verified from Fig. 59, where the matrices showing the mode weights get highly populated, as compared to the Gaussian pump case.

### 5.3.7 Measures of spatial entanglement of the biphoton state

The spiral bandwidth (SBW), or the $\ell$–distribution standard deviation, of the two-photon state is associated with the amount of entanglement between the two conjugate signals, in our case, $b$ and $s$, and it is directly related to the number of modes contributing to the entangled

**Figure 59** – Transfer of the pump structure to the coincidence count profile for different pump modes $u_{l_a,p_a}$. The upper, middle and lower rows show respectively the pump intensity profile $|\mathcal{V}(\mathbf{r}_\perp)|^2$, the corresponding coincidence profile $g(X_s, Y_s)$, and the distribution of normalized amplitudes $C^{\ell_b,\ell_s}_{p_b,p_s}$ for the subspace, $\ell_{b,s} = l_a - 4, ..., l_a + 4$, $p_{b,s} = 0, ..., 3$, with the inset showing in more detail the subspace $\ell_{b,s} = l_a - 1, l_a, l_a + 1$.

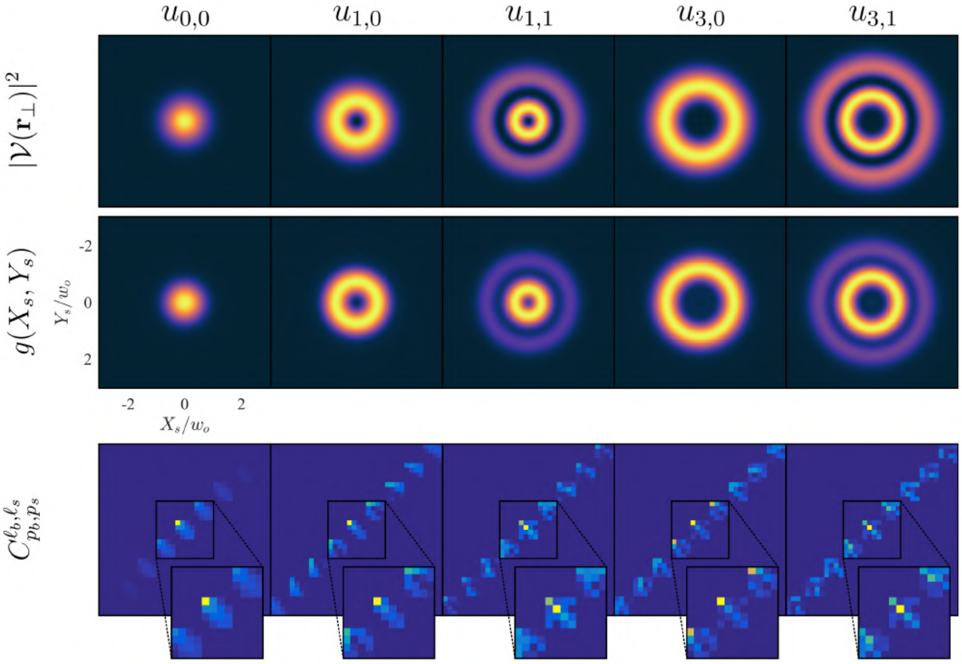

**Source:** The author (2024).

photon state. The SBW of the photon-pair generated in parametric down-conversion has been extensively studied (TORRES; ALEXANDRESCU; TORNER, 2003; MIATTO; YAO; BARNETT, 2011; YAO, 2011), while in FWM it was investigated in Ref. (OFFER et al., 2018). The SBW can be expressed as:

$$\Delta\ell(\ell_\mathrm{T}) = \sqrt{\sum\nolimits_{\ell_s} \ell_s^2 P_{\ell_\mathrm{T}-\ell_s,\ell_s} - \left(\sum\nolimits_{\ell_s} \ell_s P_{\ell_\mathrm{T}-\ell_s,\ell_s}\right)^2}, \tag{5.78}$$

where $P_{l,l'} = \sum_{p_b,p_s} |C^{l,l'}_{p_b,p_s}|^2$ and $\ell_\mathrm{T} = \ell_b + \ell_s$ is the total OAM pumped into the system, which in the case of a pure LG mode for the pump $\mathcal{E}_a$, is $\ell_\mathrm{T} = 2\ell_a$, and for a Gaussian pump, $\ell_\mathrm{T} = 0$. One may study the dependence of the SBW with any system parameter, such as phase-mismatch, medium length, beam waist, etc. In Fig. 60 we show the variation of $\Delta\ell$ with the total pumped OAM, $\ell_\mathrm{T}$.

We can also examine the entanglement between the two generated photons by evaluating the purity of the partially traced biphoton state:

$$\begin{aligned} \mathcal{P} &= \mathrm{tr}_b(\hat{\rho}_b^2), \\ &= \sum C^{\ell_b,\ell_s}_{p_b,p_s} (C^{\ell'_b,\ell_s}_{p'_b,p_s})^* C^{\ell'_b,\ell'_s}_{p'_b,p'_s} (C^{\ell_b,\ell'_s}_{p_b,p'_s})^*, \end{aligned} \tag{5.79}$$

**Figure 60** – $\ell-$distributions of the biphoton state for pump modes $u_{l_a,0}$ with $l_a = 0, 1, 2, 3$ (top) and the dependence of the SBW $\Delta\ell$ with the total pumped OAM $\ell_{\mathrm{T}} = 2l_a$ (bottom).

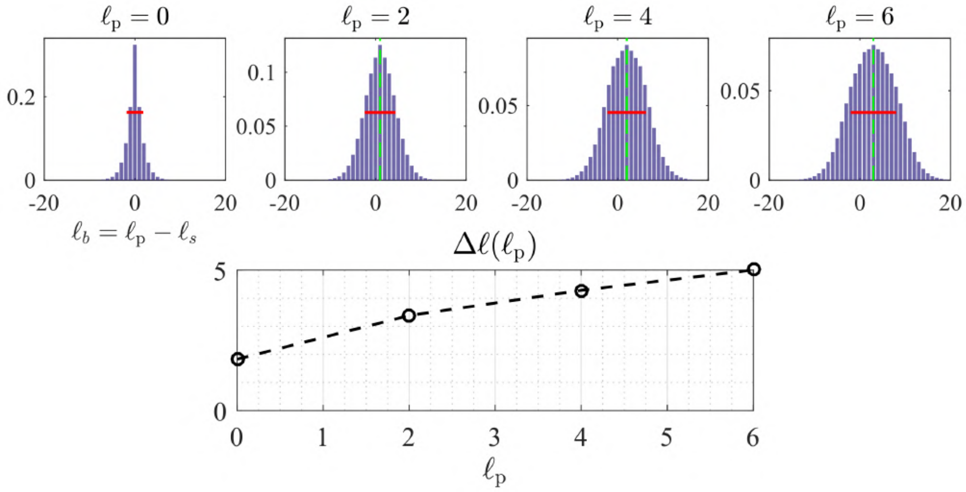

**Source:** The author (2024).

where the summation is performed over all indices on the right-hand side, $\hat{\rho}_b = \mathrm{tr}_s(\hat{\rho})$, with $\hat{\rho} = |\Psi\rangle\langle\Psi|$ being the biphoton density operator. The less pure (or more mixed) the partial state, the more entangled is the full state. The purity $\mathcal{P}$ is in turn related to the Schmidt number $K$ via:

$$\mathcal{P} = 1/K. \tag{5.80}$$

The Schmidt number is the number nonzero coefficients of the Schmidt decomposition of the quantum state (LAW; EBERLY, 2004; WALBORN et al., 2010; SCHNEELOCH; HOWELL, 2016), and it quantifies the degree of entanglement between the system parts (NIELSEN; CHUANG, 2010). In Ref. (LAW; EBERLY, 2004) the Schmidt number of the biphoton state generated in PDC was estimated by approximating the $\mathrm{sinc}(\cdot)$ phase-matching function as a Gaussian. In doing so, the following analytical form for $K$ can be found:

$$K_G = \frac{1}{4}\left(b\sigma_\perp + \frac{1}{b\sigma_\perp}\right)^2, \tag{5.81}$$

where $\sigma_\perp$ and $b^{-1}$ are the widths of the Gaussian pump function in wave-vector space $\widetilde{\mathrm{V}}(\mathbf{q})$, and of the approximate Gaussian phase-matching function, respectively. The entanglement in this Gaussian approximation serves as a lower bound (WALBORN et al., 2010).

As we have seen throughout the last Sections, the calculations for the biphoton state generated in the FWM process are very similar, with some differences arising mainly due to the fact that the pump and phase-matching functions are dictated by a squared contribution of the pump field. These differences manifest precisely on the widths of the pump angular spectrum

($\sigma_\perp$), and phase-matching function ($b$). For this reason, here we utilize the expressions obtained for the $K_G$ in PDC, taking into account the relevant modifications on the widths, to estimate $K_G$ for the FWM process. In the case of PDC, $\sigma_\perp = 4/w_0 = \sqrt{8k/z_R}$, $b \simeq \gamma\sqrt{L/4k}$, where the factor $\gamma \approx 0.257$ ensures that the $\mathrm{sinc}(\cdot)$ and Gaussian functions have the same width at half maximum (WALBORN; PIMENTEL, 2012). In our case, of a degenerate FWM process, we have $\sigma_\perp = \sqrt{8}/w_0 = \sqrt{4k/z_R}$, $b \simeq \gamma\sqrt{L/8k}$. We may encompass both cases by writing the widths $(\sigma_\perp, b)$ as:

$$\sigma_\perp = \sqrt{\frac{16}{n}}\frac{1}{w_0} = \sqrt{\frac{8k}{nz_R}}, \tag{5.82}$$

$$b = \gamma\sqrt{\frac{L}{4nk}}, \tag{5.83}$$

with $n = 1$ for PDC, and $n = 2$ for FWM. Thus, the Schmidt number, given by Eq. (5.81), can be expressed as:

$$K_G = \frac{\gamma^2}{4n^2}\left(\sqrt{\frac{L}{z_R}} + \frac{n^2}{\gamma^2}\sqrt{\frac{z_R}{L}}\right)^2. \tag{5.84}$$

We then see that the ratio $L/z_R$, which was important for us in the classical picture to establish different regimes of restriction on the FWM mode components, is also connected with the entanglement properties of the photon pair generated in the quantum description. In fact, there is an equivalence here. Larger medium extensions, in comparison with the characteristic longitudinal lengths, accommodate less transverse momentum modes of light. The uncertainty on the direction of the wave-vectors of the accepted modes is reduced, as compared with the situation in a thin-medium. The Gouy phase matching can be seen an interpretation of this restriction within the discrete basis of paraxial modes.

In our studies of the quantum-mechanical theory of FWM we also delved into the squeezing properties of the generated light state and examined the two-channel setting. The possibilities in multi-channel configurations, in particular regarding quantum spatial correlations, are interesting routes to follow in future work. While we have laid the foundation and provided initial insights in this Chapter, there is room for deeper discussions and the careful development of these ideas. Therefore, we shall not go into further detail. We believe that what has been exposed here was sufficient to initiate exploration into this promising subject.

# 6 CONCLUSIONS

In this work, we have investigated several aspects of four-wave mixing processes driven by structured light in atomic media. We focused on two main themes: the dynamics of optical modes and the correlations between the participating light fields.

Regarding the first one, we considered two different configurations in rubidium vapor. We initially explored the possibility to perform a controlled conversion of optical modes in a nondegenerate FWM process, taking advantage of the selection rules associated with the Hermite-Gaussian basis in the extended-medium regime. Next, we switched to a configuration where two degenerate FWM signals are generated by the same pump beams. In this system we verified the simultaneous transfer of orbital angular momentum to both generated FWM fields, which allows to encode the pair of input topological charges onto the two wave-mixing channels. This served as a simple demonstration of what may be achieved in multi-channel configurations. We then introduced more intricate field structures to one of the pump beams, in the form of modes contained in the orbital angular momentum Poincaré sphere. This allowed to interpret the transverse mode dynamics in light of a geometrical representation, and establish the rules that dictate the transformations of the state vectors in the sphere. We showed that the two FWM signals present characteristics already verified in parametric amplification and second-harmonic generation, drawing a clear parallel between second- and third-order nonlinear processes. We also explored interesting scenarios, such as the combination of multiple Poincaré spheres, and the additional restrictions that appear in the extended-medium regime.

In the last part of the Thesis we dealt with the subject of correlations in four-wave mixing. We started with a study on correlations between the intensity fluctuations of the pump beams transmitted through the atomic sample. Considering a sample of cold atoms as the interaction medium, we sought to identify spatial dependencies on these correlations. We argue that these dependencies may originate from the fluctuations themselves, or even from cross-talk processes between the intersecting light fields. Finally, we explored many aspects of the theory of quantum spatial correlations between the photon-pair generated in four-wave mixing. In particular, we calculated the spatial intensity correlation and showed that the transfer of the pump structure to the coincident count, a known result in PDC, also occurs in FWM. At the end, we looked at measures of spatial entanglement of the generated light state. We highlighted the role of the ratio between the medium extension and the Rayleigh range in the estimate of the number of spatial modes contributing to the biphoton state. This ratio was important for us in the classical picture to distinguish between different regimes of optical mode transfer.

An interesting route to follow from this point is to further investigate the spatial correlations in FWM, even exploring effects related to the Poincaré sphere symmetries studied here, for example. The spatial correlations between the two FWM channels can also be a very promising subject to study in greater detail.

# REFERENCES

ABRAMS, R. L.; LIND, R. C. Degenerate four-wave mixing in absorbing media. *Optics Letters*, Optica Publishing Group, v. 2, n. 4, p. 94–96, 1978.

AGARWAL, G.; NAYAK, N. Effects of collisions and saturation on multiphoton processes and nonlinear mixing in the field of two pumps. *Physical Review A*, APS, v. 33, n. 1, p. 391, 1986.

AIELLO, A.; WOERDMAN, J. Exact quantization of a paraxial electromagnetic field. *Physical Review A*, APS, v. 72, n. 6, p. 060101, 2005.

AKULSHIN, A. M.; MCLEAN, R. J.; MIKHAILOV, E. E.; NOVIKOVA, I. Distinguishing nonlinear processes in atomic media via orbital angular momentum transfer. *Optics Letters*, Optica Publishing Group, v. 40, n. 6, p. 1109–1112, 2015.

AKULSHIN, A. M.; NOVIKOVA, I.; MIKHAILOV, E. E.; SUSLOV, S. A.; MCLEAN, R. J. Arithmetic with optical topological charges in stepwise-excited Rb vapor. *Optics Letters*, Optica Publishing Group, v. 41, n. 6, p. 1146–1149, 2016.

ALLEN, L.; BEIJERSBERGEN, M. W.; SPREEUW, R.; WOERDMAN, J. Orbital angular momentum of light and the transformation of Laguerre-Gaussian laser modes. *Physical Review A*, APS, v. 45, n. 11, p. 8185, 1992.

ALMEIDA, A. de; MOTTA, M. da; VIANNA, S. Intensity correlations in the forward four-wave mixing driven by a single pump. *Physical Review A*, APS, v. 107, n. 2, p. 023515, 2023.

ALVAREZ, A.; ALMEIDA, A. de; VIANNA, S. Two symmetric four-wave mixing signals generated in a medium with anomalous refractive index. *Journal of Physics B: Atomic, Molecular and Optical Physics*, IOP Publishing, v. 54, n. 4, p. 045403, 2021.

ALVES, G. B.; BARROS, R. F.; TASCA, D. S.; SOUZA, C. E. R.; KHOURY, A. Z. Conditions for optical parametric oscillation with a structured light pump. *Physical Review A*, APS, v. 98, n. 6, p. 063825, 2018.

AMARAL, A. M. *Transverse optical phenomena with Gaussian beams and optical vortices*. Phd Thesis (PhD Thesis) — Universidade Federal de Pernambuco, 2016.

ANDERSEN, M.; RYU, C.; CLADÉ, P.; NATARAJAN, V.; VAZIRI, A.; HELMERSON, K.; PHILLIPS, W. D. Quantized rotation of atoms from photons with orbital angular momentum. *Physical Review Letters*, APS, v. 97, n. 17, p. 170406, 2006.

ANDREWS, D. L.; BABIKER, M. *The Angular Momentum of Light*. [S.l.]: Cambridge University Press, 2012.

ARIUNBOLD, G. O.; ROSTOVTSEV, Y. V.; SAUTENKOV, V. A.; SCULLY, M. O. Intensity correlation and anti-correlations in coherently driven atomic vapor. *Journal of Modern Optics*, Taylor & Francis, v. 57, n. 14-15, p. 1417–1427, 2010.

ARLT, J.; DHOLAKIA, K.; ALLEN, L.; PADGETT, M. The production of multiringed Laguerre–Gaussian modes by computer-generated holograms. *Journal of Modern Optics*, Taylor & Francis, v. 45, n. 6, p. 1231–1237, 1998.

BAGHDASARYAN, B.; SEVILLA-GUTIÉRREZ, C.; STEINLECHNER, F.; FRITZSCHE, S. Generalized description of the spatio-temporal biphoton state in spontaneous parametric down-conversion. *Physical Review A*, APS, v. 106, n. 6, p. 063711, 2022.

BAGHDASARYAN, B.; STEINLECHNER, F.; FRITZSCHE, S. Justifying the thin-crystal approximation in spontaneous parametric down-conversion for collinear phase matching. *Physical Review A*, APS, v. 103, n. 6, p. 063508, 2021.

BANDRES, M. A.; GUIZAR-SICAIROS, M. Paraxial group. *Optics Letters*, Optica Publishing Group, v. 34, n. 1, p. 13–15, 2009.

BANDRES, M. A.; GUTIéRREZ-VEGA, J. C. Ince–Gaussian modes of the paraxial wave equation and stable resonators. *Journal of the Optical Society of America A*, Optica Publishing Group, v. 21, n. 5, p. 873–880, 2004.

BARREIRO, S.; TABOSA, J. W. R. Generation of light carrying orbital angular momentum via induced coherence grating in cold atoms. *Physical Review Letters*, APS, v. 90, n. 13, p. 133001, 2003.

BARREIRO, S.; TABOSA, J. W. R.; TORRES, J. P.; DEYANOVA, Y.; TORNER, L. Four-wave mixing of light beams with engineered orbital angular momentum in cold cesium atoms. *Optics Letters*, Optica Publishing Group, v. 29, n. 13, p. 1515–1517, 2004.

BEIJERSBERGEN, M.; COERWINKEL, R.; KRISTENSEN, M.; WOERDMAN, J. Helical-wavefront laser beams produced with a spiral phaseplate. *Optics Communications*, Elsevier, v. 112, n. 5-6, p. 321–327, 1994.

BEIJERSBERGEN, M. W.; ALLEN, L.; VEEN, H. Van der; WOERDMAN, J. Astigmatic laser mode converters and transfer of orbital angular momentum. *Optics Communications*, Elsevier, v. 96, n. 1-3, p. 123–132, 1993.

BERžANSKIS, A.; MATIJOšIUS, A.; PISKARSKAS, A.; SMILGEVIčIUS, V.; STABINIS, A. Sum-frequency mixing of optical vortices in nonlinear crystals. *Optics Communications*, v. 150, n. 1, p. 372–380, 1998. ISSN 0030-4018.

BETH, R. A. Mechanical detection and measurement of the angular momentum of light. *Physical Review*, APS, v. 50, n. 2, p. 115, 1936.

BOYD, G.; KLEINMAN, D. Parametric interaction of focused Gaussian light beams. *Journal of Applied Physics*, American Institute of Physics, v. 39, n. 8, p. 3597–3639, 1968.

BOYD, R. *Nonlinear Optics*. [S.l.]: Academic Press, 2020.

BOYD, R. W.; RAYMER, M. G.; NARUM, P.; HARTER, D. J. Four-wave parametric interactions in a strongly driven two-level system. *Physical Review A*, APS, v. 24, n. 1, p. 411, 1981.

BOYER, V.; MARINO, A.; LETT, P. Generation of spatially broadband twin beams for quantum imaging. *Physical Review Letters*, APS, v. 100, n. 14, p. 143601, 2008.

BOYER, V.; MARINO, A. M.; POOSER, R. C.; LETT, P. D. Entangled images from four-wave mixing. *Science*, American Association for the Advancement of Science, v. 321, n. 5888, p. 544–547, 2008.

BRANSDEN, B. H.; JOACHAIN, C. J. *Physics of Atoms and Molecules*. [S.l.]: Pearson Education India, 2003.

BUONO, W. T.; PETERS, C.; TAU, J.; NAPE, I.; FORBES, A. Eigenmodes of aberrated systems: the tilted lens. *Journal of Optics*, IOP Publishing, v. 24, n. 12, p. 125602, 2022.

BUONO, W. T.; SANTIAGO, J.; PEREIRA, L. J.; TASCA, D. S.; DECHOUM, K.; KHOURY, A. Z. Polarization-controlled orbital angular momentum switching in nonlinear wave mixing. *Optics Letters*, Optica Publishing Group, v. 43, n. 7, p. 1439–1442, 2018.

BUONO, W. T.; SANTOS, A.; MAIA, M. R.; PEREIRA, L. J.; TASCA, D. S.; DECHOUM, K.; RUCHON, T.; KHOURY, A. Z. Chiral relations and radial-angular coupling in nonlinear interactions of optical vortices. *Physical Review A*, APS, v. 101, n. 4, p. 043821, 2020.

CALVO, G. F. Wigner representation and geometric transformations of optical orbital angular momentum spatial modes. *Optics Letters*, Optica Publishing Group, v. 30, n. 10, p. 1207–1209, 2005.

CALVO, G. F.; PICÓN, A.; BAGAN, E. Quantum field theory of photons with orbital angular momentum. *Physical Review A*, APS, v. 73, n. 1, p. 013805, 2006.

CANKAYA, H.; CALENDRON, A.-L.; SUCHOWSKI, H.; KÄRTNER, F. X. Highly efficient broadband sum-frequency generation in the visible wavelength range. *Optics Letters*, Optica Publishing Group, v. 39, n. 10, p. 2912–2915, 2014.

CARVALHO, A. J. A. *Rota para absorção de fótons individuais ultracurtos por um meio atômico*. Phd Thesis (PhD Thesis) — Universidade Federal de Pernambuco, 2020.

CHOPINAUD, A.; JACQUEY, M.; VIARISDELESEGNO, B.; PRUVOST, L. High helicity vortex conversion in a rubidium vapor. *Physical Review A*, APS, v. 97, n. 6, p. 063806, 2018.

CHU, S.; HOLLBERG, L.; BJORKHOLM, J. E.; CABLE, A.; ASHKIN, A. Three-dimensional viscous confinement and cooling of atoms by resonance radiation pressure. *Physical Review Letters*, APS, v. 55, n. 1, p. 48, 1985.

CLARK, T. W.; OFFER, R. F.; FRANKE-ARNOLD, S.; ARNOLD, A. S.; RADWELL, N. Comparison of beam generation techniques using a phase only spatial light modulator. *Optics express*, Optica Publishing Group, v. 24, n. 6, p. 6249–6264, 2016.

COURTIAL, J.; DHOLAKIA, K.; ALLEN, L.; PADGETT, M. Second-harmonic generation and the conservation of orbital angular momentum with high-order Laguerre-Gaussian modes. *Physical Review A*, APS, v. 56, n. 5, p. 4193, 1997.

DENNERY, P.; KRZYWICKI, A. *Mathematics for physicists*. [S.l.]: Courier Corporation, 1996.

DENNIS, M. R.; ALONSO, M. A. Swings and roundabouts: optical Poincaré spheres for polarization and Gaussian beams. *Philosophical Transactions of the Royal Society A: Mathematical, Physical and Engineering Sciences*, The Royal Society Publishing, v. 375, n. 2087, p. 20150441, 2017.

DHOLAKIA, K.; SIMPSON, N.; PADGETT, M.; ALLEN, L. Second-harmonic generation and the orbital angular momentum of light. *Physical Review A*, APS, v. 54, n. 5, p. R3742, 1996.

DING, D. S.; ZHOU, Z. Y.; SHI, B. S.; GUO, G. C. Single-photon-level quantum image memory based on cold atomic ensembles. *Nature Communications*, Nature Publishing Group UK London, v. 4, n. 1, p. 2527, 2013.

FLEISCHHAUER, M.; IMAMOGLU, A.; MARANGOS, J. P. Electromagnetically induced transparency: Optics in coherent media. *Reviews of Modern Physics*, v. 77, n. 2, p. 633, 2005.

FOOT, C. J. *Atomic Physics*. [S.l.]: Oxford University Press, 2005.

FORBES, A.; DUDLEY, A.; MCLAREN, M. Creation and detection of optical modes with spatial light modulators. *Advances in Optics and Photonics*, Optica Publishing Group, v. 8, n. 2, p. 200–227, 2016.

FORBES, A.; OLIVEIRA, M. de; DENNIS, M. R. Structured light. *Nature Photonics*, Nature Publishing Group UK London, v. 15, n. 4, p. 253–262, 2021.

FRANKEN, e. P.; HILL, A. E.; PETERS, C.; WEINREICH, G. Generation of optical harmonics. *Physical Review Letters*, APS, v. 7, n. 4, p. 118, 1961.

FRIEDMANN, H.; WILSON-GORDON, A. Dispersion profiles of the absorptive response of a two-level system interacting with two intense fields. *Physical Review A*, APS, v. 36, n. 3, p. 1333, 1987.

FRIESE, M.; ENGER, J.; RUBINSZTEIN-DUNLOP, H.; HECKENBERG, N. R. Optical angular-momentum transfer to trapped absorbing particles. *Physical Review A*, APS, v. 54, n. 2, p. 1593, 1996.

GRYNBERG, G.; MAÎTRE, A.; PETROSSIAN, A. Flowerlike patterns generated by a laser beam transmitted through a rubidium cell with single feedback mirror. *Physical Review Letters*, APS, v. 72, n. 15, p. 2379, 1994.

GUPTA, P.; HORROM, T.; ANDERSON, B. E.; GLASSER, R.; LETT, P. D. Multi-channel entanglement distribution using spatial multiplexing from four-wave mixing in atomic vapor. *Journal of Modern Optics*, Taylor & Francis, v. 63, n. 3, p. 185–189, 2016.

HAMEDI, H. R.; RUSECKAS, J.; JUZELIŪNAS, G. Exchange of optical vortices using an electromagnetically-induced-transparency–based four-wave-mixing setup. *Physical Review A*, APS, v. 98, n. 1, p. 013840, 2018.

HARTER, D.; BOYD, R. Nearly degenerate four-wave mixing enhanced by the ac stark effect. *IEEE Journal of Quantum Electronics*, IEEE, v. 16, n. 10, p. 1126–1131, 1980.

HE, C.; SHEN, Y.; FORBES, A. Towards higher-dimensional structured light. *Light: Science & Applications*, Nature Publishing Group UK London, v. 11, n. 1, p. 205, 2022.

HE, H.; FRIESE, M.; HECKENBERG, N.; RUBINSZTEIN-DUNLOP, H. Direct observation of transfer of angular momentum to absorptive particles from a laser beam with a phase singularity. *Physical Review Letters*, APS, v. 75, n. 5, p. 826, 1995.

HECKENBERG, N.; MCDUFF, R.; SMITH, C.; WHITE, A. Generation of optical phase singularities by computer-generated holograms. *Optics Letters*, Optica Publishing Group, v. 17, n. 3, p. 221–223, 1992.

HORROM, T.; LEZAMA, A.; BALIK, S.; HAVEY, M. D.; MIKHAILOV, E. E. Quadrature noise in light propagating through a cold 87Rb atomic gas. *Journal of Modern Optics*, Taylor & Francis, v. 58, n. 21, p. 1936–1941, 2011.

HU, Q.; WANG, X.; ZHANG, R.; REN, Y.; LIU, S.; JING, J. Enhancing and flattening multiplexed quantum entanglement by utilizing perfect vortex modes. *Optics Letters*, Optica Publishing Group, v. 48, n. 7, p. 1782–1785, 2023.

JACKSON, J. D. *Classical electrodynamics*. [S.l.]: American Association of Physics Teachers, 1999.

KARIMI, E.; BOYD, R.; HOZ, P. D. L.; GUISE, H. D.; ŘEHÁČEK, J.; HRADIL, Z.; AIELLO, A.; LEUCHS, G.; SÁNCHEZ-SOTO, L. L. Radial quantum number of Laguerre-Gauss modes. *Physical Review A*, APS, v. 89, n. 6, p. 063813, 2014.

KIMEL, I.; ELIAS, L. R. Relations between Hermite and Laguerre Gaussian modes. *IEEE Journal of Quantum Electronics*, IEEE, v. 29, n. 9, p. 2562–2567, 1993.

KOGELNIK, H.; LI, T. Laser beams and resonators. *Applied Optics*, Optica Publishing Group, v. 5, n. 10, p. 1550–1567, 1966.

KOLOBOV, M. I. *Quantum Imaging*. [S.l.]: Springer Science & Business Media, 2007.

KRENN, M.; HUBER, M.; FICKLER, R.; LAPKIEWICZ, R.; RAMELOW, S.; ZEILINGER, A. Generation and confirmation of a (100×100)-dimensional entangled quantum system. *Proceedings of the National Academy of Sciences*, National Academy of Sciences, v. 111, n. 17, p. 6243–6247, 2014.

LANNING, R. N.; XIAO, Z.; ZHANG, M.; NOVIKOVA, I.; MIKHAILOV, E. E.; DOWLING, J. P. Gaussian-beam-propagation theory for nonlinear optics involving an analytical treatment of orbital-angular-momentum transfer. *Physical Review A*, APS, v. 96, n. 1, p. 013830, 2017.

LANNING, R. N.; XIAO, Z.; ZHANG, M.; NOVIKOVA, I.; MIKHAILOV, E. E.; DOWLING, J. P. Quantized nonlinear Gaussian-beam dynamics: Tailoring multimode squeezed-light generation. *Physical Review A*, APS, v. 98, n. 4, p. 043824, 2018.

LAW, C.; EBERLY, J. Analysis and interpretation of high transverse entanglement in optical parametric down conversion. *Physical Review Letters*, APS, v. 92, n. 12, p. 127903, 2004.

LEACH, J.; PADGETT, M. J.; BARNETT, S. M.; FRANKE-ARNOLD, S.; COURTIAL, J. Measuring the orbital angular momentum of a single photon. *Physical Review Letters*, APS, v. 88, n. 25, p. 257901, 2002.

MAIMAN, T. H. Stimulated optical radiation in ruby. *Nature*, v. 187, p. 493–494, 1960.

MALLICK, N. S.; DEY, T. N. Four-wave mixing-based orbital angular momentum translation. *Journal of the Optical Society of America B*, Optica Publishing Group, v. 37, n. 6, p. 1857–1864, 2020.

MARINO, A. M.; BOYER, V.; POOSER, R. C.; LETT, P. D.; LEMONS, K.; JONES, K. Delocalized correlations in twin light beams with orbital angular momentum. *Physical Review Letters*, APS, v. 101, n. 9, p. 093602, 2008.

MAXWELL, J. C. A dynamical theory of the electromagnetic field. *Philosophical transactions of the Royal Society of London*, The Royal Society London, n. 155, p. 459–512, 1865.

MIATTO, F. M.; YAO, A. M.; BARNETT, S. M. Full characterization of the quantum spiral bandwidth of entangled biphotons. *Physical Review A*, APS, v. 83, n. 3, p. 033816, 2011.

MOLINA-TERRIZA, G.; TORRES, J. P.; TORNER, L. Twisted photons. *Nature Physics*, Nature Publishing Group, v. 3, n. 5, p. 305–310, 2007.

MONKEN, C. H.; RIBEIRO, P. S.; PÁDUA, S. Transfer of angular spectrum and image formation in spontaneous parametric down-conversion. *Physical Review A*, APS, v. 57, n. 4, p. 3123, 1998.

MORETTI, D.; FELINTO, D.; TABOSA, J. W. R. Collapses and revivals of stored orbital angular momentum of light in a cold-atom ensemble. *Physical Review A*, APS, v. 79, n. 2, p. 023825, 2009.

MOTTA, M. da; ALMEIDA, A. de; VIANNA, S. Combinations of orbital angular momentum in two degenerate four-wave mixing processes in Rb vapor. *Journal of Optics*, IOP Publishing, v. 25, n. 9, p. 095501, 2023.

MOTTA, M. R. da; ALMEIDA, A. A. de; VIANNA, S. S. Spatial distribution of two symmetric four-wave-mixing signals induced by Gaussian beams. *Physical Review A*, APS, v. 106, n. 5, p. 053502, 2022.

MOTTA, M. R. L. *Two symmetric four-wave mixing signals induced by beams with nonuniform distributions*. Master's Thesis (Master's Thesis) — Universidade Federal de Pernambuco, 2021.

MOTTA, M. R. L. da; ALVES, G. B.; KHOURY, A. Z.; VIANNA, S. S. Poincaré-sphere symmetries in four-wave mixing with orbital angular momentum. *Physical Review A*, APS, v. 109, n. 1, p. 013506, 2024.

NIELSEN, M. A.; CHUANG, I. L. *Quantum computation and quantum information*. [S.l.]: Cambridge university press, 2010.

NIRALA, G.; PRADYUMNA, S. T.; KUMAR, A.; MARINO, A. M. Information encoding in the spatial correlations of entangled twin beams. *Science Advances*, American Association for the Advancement of Science, v. 9, n. 22, p. eadf9161, 2023.

OFFER, R. F.; DAFFURN, A.; RIIS, E.; GRIFFIN, P. F.; ARNOLD, A. S.; FRANKE-ARNOLD, S. Gouy phase-matched angular and radial mode conversion in four-wave mixing. *Physical Review A*, APS, v. 103, p. L021502, 2021.

OFFER, R. F.; STULGA, D.; RIIS, E.; FRANKE-ARNOLD, S.; ARNOLD, A. S. Spiral bandwidth of four-wave mixing in Rb vapour. *Communications Physics*, Nature Publishing Group, v. 1, n. 1, p. 1–8, 2018.

OLIVEIRA, M. G. de; PEREIRA, L.; SANTOS, A.; DECHOUM, K.; BRAMATI, A.; KHOURY, A. Radial-angular coupling in self-phase-modulation with structured light. *Physical Review A*, APS, v. 108, n. 1, p. 013503, 2023.

OSORIO, C. I.; BARREIRO, S.; MITCHELL, M. W.; TORRES, J. P. Spatial entanglement of paired photons generated in cold atomic ensembles. *Physical Review A*, APS, v. 78, n. 5, p. 052301, 2008.

PADGETT, M. J.; COURTIAL, J. Poincaré-sphere equivalent for light beams containing orbital angular momentum. *Optics Letters*, Optica Publishing Group, v. 24, n. 7, p. 430–432, 1999.

PAN, X.; YU, S.; ZHOU, Y.; ZHANG, K.; ZHANG, K.; LV, S.; LI, S.; WANG, W.; JING, J. Orbital-angular-momentum multiplexed continuous-variable entanglement from four-wave mixing in hot atomic vapor. *Physical Review Letters*, APS, v. 123, p. 070506, 2019.

PEREIRA, L. J.; BUONO, W. T.; TASCA, D. S.; DECHOUM, K.; KHOURY, A. Z. Orbital-angular-momentum mixing in type-ii second-harmonic generation. *Physical Review A*, APS, v. 96, p. 053856, 2017.

PIRES, D.; ROCHA, J.; JESUS-SILVA, A.; FONSECA, E. Optical mode conversion through nonlinear two-wave mixing. *Physical Review A*, APS, v. 100, n. 4, p. 043819, 2019.

PIRES, D.; ROCHA, J.; JESUS-SILVA, A.; FONSECA, E. Suitable state bases for nonlinear optical mode conversion protocols. *Optics Letters*, Optica Publishing Group, v. 45, n. 14, p. 4064–4067, 2020.

PLICK, W. N.; KRENN, M. Physical meaning of the radial index of Laguerre-Gauss beams. *Physical Review A*, APS, v. 92, n. 6, p. 063841, 2015.

PRAJAPATI, N.; SUPER, N.; LANNING, N. R.; DOWLING, J. P.; NOVIKOVA, I. Optical angular momentum manipulations in a four-wave mixing process. *Optics Letters*, Optica Publishing Group, v. 44, n. 4, p. 739–742, 2019.

ROCHA, J.; PIRES, D.; MOTTA, M.; LITCHINITSER, N.; VIANNA, S.; FONSECA, E.; FERRAZ, J. Controlled conversion of transverse symmetries in a four-wave mixing process. *Journal of Optics*, IOP Publishing, v. 24, n. 4, p. 045505, 2022.

RODRIGUES, R.; ALVES, G.; BARROS, R.; SOUZA, C.; KHOURY, A. Generalized orbital angular momentum symmetry in parametric amplification. *Physical Review A*, APS, v. 105, n. 1, p. 013510, 2022.

RODRIGUES, R.; GONZALES, J.; SILVA, B. P. da; HUGUENIN, J.; MARTINELLI, M.; ARAÚJO, R. M. de; SOUZA, C.; KHOURY, A. Orbital angular momentum symmetry in a driven optical parametric oscillator. *Optics Letters*, Optica Publishing Group, v. 43, n. 11, p. 2486–2489, 2018.

ROGER, T.; HEITZ, J. J. F.; WRIGHT, E. M.; FACCIO, D. Non-collinear interaction of photons with orbital angular momentum. *Scientific Reports*, Nature, v. 3, p. 3491, 2013.

RUBINSZTEIN-DUNLOP, H.; FORBES, A.; BERRY, M. V.; DENNIS, M. R.; ANDREWS, D. L.; MANSURIPUR, M.; DENZ, C.; ALPMANN, C.; BANZER, P.; BAUER, T. et al. Roadmap on structured light. *Journal of Optics*, IOP Publishing, v. 19, n. 1, p. 013001, 2016.

RUFFATO, G.; MASSARI, M.; ROMANATO, F. Generation of high-order Laguerre–Gaussian modes by means of spiral phase plates. *Optics Letters*, Optica Publishing Group, v. 39, n. 17, p. 5094–5097, 2014.

SANTOS, B. C. D.; DECHOUM, K.; KHOURY, A. Continuous-variable hyperentanglement in a parametric oscillator with orbital angular momentum. *Physical Review Letters*, APS, v. 103, n. 23, p. 230503, 2009.

SANTOS, B. C. dos; SOUZA, C. E. R.; DECHOUM, K.; KHOURY, A. Z. Phase conjugation and adiabatic mode conversion in a driven optical parametric oscillator with orbital angular momentum. *Physical Review A*, APS, v. 76, n. 5, p. 053821, 2007.

SCHNEELOCH, J.; HOWELL, J. C. Introduction to the transverse spatial correlations in spontaneous parametric down-conversion through the biphoton birth zone. *Journal of Optics*, IOP Publishing, v. 18, n. 5, p. 053501, 2016.

SCHWOB, C.; COHADON, P. F.; FABRE, C.; MARTE, M.; RITSCH, H.; GATTI, A.; LUGIATO, L. Transverse effects and mode couplings in opos. *Applied Physics B*, Springer, v. 66, n. 6, p. 685–699, 1998.

SHEN, Y. Rays, waves, SU(2) symmetry and geometry: toolkits for structured light. *Journal of Optics*, IOP Publishing, v. 23, n. 12, p. 124004, 2021.

SHEN, Y.; ROSALES-GUZMÁN, C. Nonseparable states of light: from quantum to classical. *Laser & Photonics Reviews*, Wiley Online Library, v. 16, n. 7, p. 2100533, 2022.

SHEN, Y.; WANG, Z.; FU, X.; NAIDOO, D.; FORBES, A. SU(2) Poincaré sphere: A generalized representation for multidimensional structured light. *Physical Review A*, APS, v. 102, n. 3, p. 031501, 2020.

SILVA, B. P. da; BUONO, W. T.; PEREIRA, L. J.; TASCA, D. S.; DECHOUM, K.; KHOURY, A. Z. Spin to orbital angular momentum transfer in frequency up-conversion. *Nanophotonics*, De Gruyter, v. 11, n. 4, p. 771–778, 2021.

SILVA, B. P. da; MARQUES, B.; RODRIGUES, R.; RIBEIRO, P. S.; KHOURY, A. Machine-learning recognition of light orbital-angular-momentum superpositions. *Physical Review A*, APS, v. 103, n. 6, p. 063704, 2021.

STECK, D. A. Rubidium 87 d line data. 2001.

TABOSA, J. W. R.; PETROV, D. V. Optical pumping of orbital angular momentum of light in cold cesium atoms. *Physical Review Letters*, APS, v. 83, n. 24, p. 4967, 1999.

TACHÉ, J. Derivation of abcd law for Laguerre-Gaussian beams. *Applied Optics*, Optica Publishing Group, v. 26, n. 14, p. 2698–2700, 1987.

TORRES, J.; ALEXANDRESCU, A.; TORNER, L. Quantum spiral bandwidth of entangled two-photon states. *Physical Review A*, APS, v. 68, n. 5, p. 050301, 2003.

VAITY, P.; BANERJI, J.; SINGH, R. Measuring the topological charge of an optical vortex by using a tilted convex lens. *Physics Letters A*, Elsevier, v. 377, n. 15, p. 1154–1156, 2013.

VALLONE, G.; PARISI, G.; SPINELLO, F.; MARI, E.; TAMBURINI, F.; VILLORESI, P. General theorem on the divergence of vortex beams. *Physical Review A*, APS, v. 94, n. 2, p. 023802, 2016.

VERNAZ-GRIS, P.; HUANG, K.; CAO, M.; SHEREMET, A. S.; LAURAT, J. Highly-efficient quantum memory for polarization qubits in a spatially-multiplexed cold atomic ensemble. *Nature Communications*, Nature Publishing Group UK London, v. 9, n. 1, p. 363, 2018.

VERNIER, A.; FRANKE-ARNOLD, S.; RIIS, E.; ARNOLD, A. Enhanced frequency up-conversion in Rb vapor. *Optics Express*, Optica Publishing Group, v. 18, n. 16, p. 17020–17026, 2010.

WALBORN, S.; PIMENTEL, A. Generalized Hermite–Gauss decomposition of the two-photon state produced by spontaneous parametric down conversion. *Journal of Physics B: Atomic, Molecular and Optical Physics*, IOP Publishing, v. 45, n. 16, p. 165502, 2012.

WALBORN, S. P.; MONKEN, C.; PÁDUA, S.; RIBEIRO, P. S. Spatial correlations in parametric down-conversion. *Physics Reports*, Elsevier, v. 495, n. 4-5, p. 87–139, 2010.

WALKER, G.; ARNOLD, A. S.; FRANKE-ARNOLD, S. Trans-spectral orbital angular momentum transfer via four-wave mixing in Rb vapor. *Physical Review Letters*, APS, v. 108, n. 24, p. 243601, 2012.

WEBER, H. Collins' integral for misaligned optical elements. *Journal of Modern Optics*, Taylor & Francis, v. 53, n. 18, p. 2793–2801, 2006.

WILSON-GORDON, A.; FRIEDMANN, H. Saturation-induced distortion of four-wave-mixing spectra in a two-level system. *Physical Review A*, APS, v. 38, n. 8, p. 4087, 1988.

YAO, A. M. Angular momentum decomposition of entangled photons with an arbitrary pump. *New Journal of Physics*, IOP Publishing, v. 13, n. 5, p. 053048, 2011.

YAO, A. M.; PADGETT, M. J. Orbital angular momentum: origins, behavior and applications. *Advances in Optics and Photonics*, Optica Publishing Group, v. 3, n. 2, p. 161–204, 2011.

YARIV, A. *Quantum Electronics*. [S.l.]: John Wiley & Sons, 1989.

YARIV, A.; PEPPER, D. M. Amplified reflection, phase conjugation, and oscillation in degenerate four-wave mixing. *Optics Letters*, Optica Publishing Group, v. 1, n. 1, p. 16–18, 1977.

YU, C.; WANG, Z. Engineering helical phase via four-wave mixing in the ultraslow propagation regime. *Physical Review A*, APS, v. 103, n. 1, p. 013518, 2021.

ZHANG, K.; WANG, W.; LIU, S.; PAN, X.; DU, J.; LOU, Y.; YU, S.; LV, S.; TREPS, N.; FABRE, C. et al. Reconfigurable hexapartite entanglement by spatially multiplexed four-wave mixing processes. *Physical Review Letters*, APS, v. 124, n. 9, p. 090501, 2020.

ZHANG, Y.; PRABHAKAR, S.; ROSALES-GUZMÁN, C.; ROUX, F. S.; KARIMI, E.; FORBES, A. Hong-ou-mandel interference of entangled Hermite-Gauss modes. *Physical Review A*, APS, v. 94, n. 3, p. 033855, 2016.

ZHANG, Z.; GAO, Y.; LI, X.; WANG, X.; ZHAO, S.; LIU, Q.; ZHAO, C. Second harmonic generation of laser beams in transverse mode locking states. *Advanced Photonics*, Society of Photo-Optical Instrumentation Engineers, v. 4, n. 2, p. 026002–026002, 2022.

ZHOU, Y.; WANG, Z. Helical phase steering via four-wave mixing in a closely cycled double-ladder atomic system. *Journal of Applied Physics*, AIP Publishing, v. 133, n. 17, 2023.

# APPENDIX A – LIST OF JOURNAL PUBLICATIONS

1. J. C. A. Rocha, D. G. Pires, **M. R. L. Motta**, N. M. Litchinitser, S. S. Vianna, E. J. S. Fonseca, J. Ferraz. Controlled conversion of transverse symmetries in a four-wave mixing process. *Journal of Optics*, 24(4), 045505 (2022).
2. **M. R. L. Motta**, A. A. C. Almeida, S. S. Vianna. Spatial distribution of two symmetric four-wave-mixing signals induced by Gaussian beams. *Physical Review A*, 106(5), 053502 (2022).
3. A. A. C. Almeida, **M. R. L. Motta**, S. S. Vianna. Intensity correlations in the forward four-wave mixing driven by a single pump. *Physical Review A*, 107(2), 023515 (2023).
4. **M. R. L. Motta**, A. A. C. Almeida, S. S. Vianna. Combinations of orbital angular momentum in two degenerate four-wave mixing processes in Rb vapor. *Journal of Optics*, 25(9), 095501 (2023).
5. **M. R. L. Motta**, G. B. Alves, A. Z. Khoury, S. S. Vianna. Poincaré-sphere symmetries in four-wave mixing with orbital angular momentum. *Physical Review A*, 109(1), 013506 (2024).

# APPENDIX B – OVERLAP INTEGRALS ON THE REDUCED WAIST BASIS - RADIAL MODE RESTRICTION

As mentioned in the last Section of Chapter 4, with the appropriate choice of the beam waist of the LG mode basis, it is possible to restrict the number of radial orders contained in the output mode superpositions. In this Appendix we outline the calculation of the overlap integrals on the reduced beam waist basis, and make this restriction explicit. The transverse overlap integral on the $\tilde{w} = w/\xi$ mode basis is

$$\tilde{\Lambda}^{ll'm\ell}_{qq'np}(\xi) = \iint u_{l,q} u_{l',q'} u^*_{m,n} \tilde{u}^*_{\ell,p}\Big|_{z=0} d^2\mathbf{r}_\perp. \tag{B.1}$$

We now look at three different cases, corresponding to the coefficients $\tilde{a}_0, \tilde{b}_0$ and $\tilde{c}_p$ in Eqs. (4.53) and (4.54).

Let us focus first on the case $q = q' = m = n = 0$:

$$\begin{aligned}\tilde{\Lambda}^{ll'0\ell}_{000p}(\xi) &= \iint u_{l,0} u_{l',0} u^*_{0,0} \tilde{u}^*_{\ell,p}\Big|_{z=0} d^2\mathbf{r}_\perp, \\ &= 2\pi \delta_{\ell,l+l'} C_{l,0} C_{l',0} C_{0,0} C_{\ell,p} \xi^{|\ell|+1} \frac{1}{w^4} \\ &\times \int_0^\infty (r_w)^{|l|+|l'|+|\ell|} L_p^{|\ell|}(\xi^2 r_w^2) e^{-r_w^2(3+\xi^2)/2} r dr,\end{aligned} \tag{B.2}$$

where $r_w = \sqrt{2}r/w$. The choice $\xi = \sqrt{3}$ will be most interesting for us because it allows to establish a maximum value for the possibly coupled $p$ orders. The only nonzero coefficients are those with $\ell = l + l'$,

$$\begin{aligned}\tilde{\Lambda}^{ll'0,l+l'}_{000p}(\sqrt{3}) &= \frac{8}{\pi w^4}\sqrt{\frac{p!\,3^{1-|l|-|l'|}}{|l|!\,|l'|!\,(p+|l+l'|)!}} \\ &\times \int_0^\infty (3r_w^2)^{|l+l'|}(3r_w^2)^P L_p^{|l+l'|}(3r_w^2) e^{-3r_w^2} r dr,\end{aligned} \tag{B.3}$$

where $P = (|l| + |l'| - |l + l'|)/2$. Then

$$\tilde{\Lambda}^{ll'0,l+l'}_{000p}(\sqrt{3}) = \frac{4}{\pi w^2}\sqrt{\frac{p!\,3^{-1-|l|-|l'|}}{|l|!\,|l'|!\,(p+|l+l'|)!}} \int_0^\infty x^{|l+l'|} x^P L_p^{|l+l'|}(x) e^{-x} dx. \tag{B.4}$$

## B.1 COEFFICIENTS $\tilde{a}_0$ FOR THE SPHERE MODES CONTAINED IN $\mathcal{E}_1$

For $l \cdot l' \geq 0$, $P = 0$, and we can substitute $x^P$ by $L_0^{|l+l'|}(x) = 1$. Using the orthogonality relation of the associated Laguerre polynomials, $\int_0^\infty x^\alpha L_p^\alpha(x) L_q^\alpha(x) e^{-x} dx = \frac{\Gamma(p+\alpha+1)}{p!}\delta_{p,q}$, we can write

$$\tilde{\Lambda}_{000p}^{ll'0,l+l'}(\sqrt{3}) = \begin{cases} \frac{4}{\sqrt{3}\pi w^2}\sqrt{\frac{|l+l'|!}{|l|!\,|l'|!\,3^{|l|+|l'|}}}, & \text{for} \quad p = 0, \\ 0, & \text{for} \quad p > 0. \end{cases} \tag{B.5}$$

We then see that no radial order $p > 0$ is generated.

## B.2 COEFFICIENTS $\tilde{c}_p$ FOR THE RADIAL MODES CONTAINED IN $\mathcal{E}_1$

Now, for $l \cdot l' < 0$, $P = \min(|l|, |l'|)$, and we expand the monomial $x^P$ in terms of Laguerre polynomials as $x^n = n! \sum_{j=0}^{n} (-1)^j \binom{n+\alpha}{n-j} L_j^\alpha(x) = n! \sum_{j=0}^{n} b_{j,n}^{\alpha} L_j^\alpha(x)$, with $\alpha = |l+l'|$, to write

$$\begin{aligned} \tilde{\Lambda}_{000p}^{ll'0,l+l'}(\sqrt{3}) = \frac{4}{\pi w^2}\sqrt{\frac{p!\,3^{-1-|l|-|l'|}}{|l|!\,|l'|!\,(p+|l+l'|)!}}P! \\ \times \sum_{j=0}^{P} b_{j,P}^{|l+l'|} \int_0^\infty x^{|l+l'|} L_j^{|l+l'|}(x) L_p^{|l+l'|}(x) e^{-x} dx. \end{aligned} \tag{B.6}$$

The $x$ integral is once again the orthogonality relation of the associated Laguerre polynomials. Finally, we obtain

$$\tilde{\Lambda}_{000p}^{ll'0,l+l'}(\sqrt{3}) = \frac{4}{\pi w^2}\frac{(-1)^p}{(P-p)!}\sqrt{\frac{3^{-1-|l|-|l'|}}{|l|!\,|l'|!\,p!(p+|l+l'|)!}}P!(P+|l+l'|)!, \tag{B.7}$$

for $p \leq P$, and $\tilde{\Lambda}_{000p}^{ll'0,l+l'}(\sqrt{3}) = 0$, for $p > P$. This result is simplified in the case $l' = -l$, which makes $P = |l|$, and we get

$$\tilde{\Lambda}_{000p}^{l,-l00}(\sqrt{3}) = \begin{cases} \frac{4}{\sqrt{3}\pi w^2}\frac{(-1)^p}{(|l|-p)!}\frac{|l|!}{p!\,3^{|l|}}, & \text{for} \quad p \leq |l|, \\ 0, & \text{for} \quad p > |l|. \end{cases} \tag{B.8}$$

## B.3 COEFFICIENTS $\tilde{b}_0$ FOR THE SPHERE MODES CONTAINED IN $\mathcal{E}_2$

Next, for $l = l' = q = q' = n = 0$, we have

$$\begin{aligned} \tilde{\Lambda}_{000p}^{00m\ell}(\xi) = \iint u_{0,0}^2 u_{m,0}^* \tilde{u}_{\ell,p}^*\Big|_{z=0} d^2\mathbf{r}_\perp = 2\pi\delta_{\ell,-m} C_{0,0}^2 C_{m,0} C_{\ell,p} \xi^{|\ell|+1}\frac{1}{w^4} \\ \times \int_0^\infty (r_w)^{|m|+|\ell|} L_p^{|\ell|}(\xi^2 r_w^2) e^{-r_w^2(3+\xi^2)/2} r dr. \end{aligned} \tag{B.9}$$

The OAM conservation dictates $\ell = -m$, and thus for $\xi = \sqrt{3}$, we can arrive at the expression

$$\tilde{\Lambda}_{000p}^{00m,-m}(\sqrt{3}) = \frac{4}{\pi w^2}\sqrt{3^{-1-|m|}}\frac{(2|m|)!}{(|m|!)^2}\delta_{p,0}. \tag{B.10}$$

# APPENDIX C – COEFFICIENTS FOR CHANGING WAIST BASIS

We may expand the mode $u_{\ell,p}$, with waist $w$, on the basis of modes $\tilde{u}_{l,q}$, with waist $\tilde{w} = w/\xi$ as:

$$u_{\ell,p} = \sum_{l,q} \lambda^{\ell,l}_{p,q}(\xi)\tilde{u}_{l,q}, \tag{C.1}$$

where the expansion coefficients are:

$$\lambda^{\ell,l}_{p,q}(\xi) = \iint u_{\ell,p}\tilde{u}^*_{l,q}\Big|_{z=0} d^2\mathbf{r}_\perp. \tag{C.2}$$

Since we must have $\ell = l$, we drop one of the upper indices, to write:

$$\lambda^{\ell}_{p,q}(\xi) = \frac{\pi}{2} C_{\ell,p}C_{\ell,q}\xi^{|\ell|+1} \int_0^\infty x^{|\ell|} L^{|\ell|}_p(x) L^{|\ell|}_q(\xi^2 x) e^{-x(1+\xi^2)/2} dx, \tag{C.3}$$

where we made the change of variable $x = 2r^2/w^2$. For $\xi = 1$, we obtain $\lambda^\ell_{p,q}(1) = \delta_{p,q}$, which is expected. To obtain an analytical expression, we can employ the generating function for the Laguerre polynomials $\sum_{n=0}^\infty t^n L^\alpha_n(x) = (1-t)^{-(\alpha+1)} e^{-tx/(1-t)}$. Differentiating $p$ times with respect to $t$, and making $t = 0$, we get:

$$L^\alpha_p(x) = \frac{1}{p!}\frac{\partial^p}{\partial t^p}\left[\frac{e^{-tx/(1-t)}}{(1-t)^{\alpha+1}}\right]\Bigg|_{t=0}, \tag{C.4}$$

and we can rewrite the integral in (C.3) as:

$$\begin{aligned}\frac{1}{p!q!}\frac{\partial^p}{\partial t^p}\frac{\partial^q}{\partial t'^q}\frac{1}{[(1-t)(1-t')]^{|\ell|+1}}\int_0^\infty x^{|\ell|} e^{-b(t,t')x} dx = \\ = \frac{|\ell|!}{p!q!}\frac{\partial^p}{\partial t^p}\frac{\partial^q}{\partial t'^q}\frac{1}{[b(t,t')(1-t)(1-t')]^{|\ell|+1}}\Bigg|_{t,t'=0},\end{aligned} \tag{C.5}$$

with $b(t,t') = \frac{1+\xi^2}{2} + t/(1-t) + \xi^2 t'/(1-t')$. For $\ell = p = q = 0$, we obtain simply:

$$\lambda^0_{0,0}(\xi) = \frac{2\xi}{1+\xi^2}. \tag{C.6}$$

Let us call $S = b(1-t)(1-t') = \frac{1+\xi^2}{2}(1-t)(1-t') + t(1-t') + \xi^2 t'(1-t)$. For $\ell, p, q \neq 0$, noting that $\partial^n_t S = \partial^n_{t'} S = 0$ for $n > 1$, we have:

$$\frac{\partial^p}{\partial t^p}\frac{1}{S^c} = (-1)^p \frac{(c+p-1)!}{(c-1)!}\frac{1}{S^{c+p}}\left(\frac{\partial S}{\partial t}\right)^p. \tag{C.7}$$

Also, with $\partial_t \partial_{t'} S = -\frac{(1+\xi^2)}{2} = J$, we can write[1]:

$$\begin{aligned}
\frac{\partial^p}{\partial t^p}\frac{\partial^q}{\partial t'^q}\frac{1}{S^{|\ell|+1}} &= \frac{\partial^p}{\partial t^p}\left[(-1)^q \frac{(|\ell|+q)!}{|\ell|!}\frac{1}{S^{|\ell|+q+1}}\left(\frac{\partial S}{\partial t'}\right)^q\right], \\
&= (-1)^q \frac{(|\ell|+q)!}{|\ell|!}\left[\sum_{n=0}^{p}\frac{q!\binom{p}{n}J^{p-n}}{(q-p+n)!}\frac{\partial^n}{\partial t^n}\left(\frac{1}{S^{|\ell|+q+1}}\right)\left(\frac{\partial S}{\partial t'}\right)^{q-p+n}\right], \\
&= \frac{(-1)^q q!}{|\ell|!}\left[\sum_{n=0}^{p}(-1)^n J^{p-n}\binom{p}{n}\frac{(|\ell|+q+n)!}{(q-p+n)!}\frac{(\partial_t S)^n\,(\partial_{t'}S)^{q-p+n}}{S^{|\ell|+q+n+1}}\right].
\end{aligned} \tag{C.8}$$

Finally, making $t, t' \to 0$, $S \to \frac{1+\xi^2}{2}, \partial_t S \to \frac{1-\xi^2}{2}, \partial_{t'} S \to -\frac{1-\xi^2}{2}$, and we obtain:

$$\begin{aligned}
\lambda^{\ell}_{p,q}(\xi) = &\sqrt{\frac{p!q!}{(|\ell|+p)!(|\ell|+q)!}}\left(\frac{2\xi}{1+\xi^2}\right)^{|\ell|+1} \\
&\times \sum_{n=0}^{p}\frac{(-1)^n(|\ell|+q+n)!}{n!(p-n)!(q-p+n)!}\left(\frac{1-\xi^2}{1+\xi^2}\right)^{q-p+2n}.
\end{aligned} \tag{C.9}$$

---

[1] Note that the expression given here for the basis conversion factor $\lambda^{\ell}_{p,q}(\xi)$ is applicable when $q \geq p$ only.